CRANFIELD UNIVERSITY

DAVID BACCI

TRANSONIC AERO-ACOUSTICS OF WEAPON BAYS

CENTRE FOR DEFENCE ENGINEERING

Aeromechanical Systems Group

PhD

Academic Year: 2017-2018

Supervisors: Dr Saddington, A. J. and Dr Bray, D.

September 2017

CRANFIELD UNIVERSITY

CENTRE FOR DEFENCE ENGINEERING

Aeromechanical Systems Group

PhD

Academic Year: 2017-2018

DAVID BACCI

TRANSONIC AERO-ACOUSTICS OF WEAPON BAYS

Supervisors: Dr Saddington, A. J. and Dr Bray, D.

September 2017

This thesis is submitted in partial fulfilment of the requirements for the degree of PhD

(NB. This section can be removed if the award of the degree is based solely on examination of the thesis)

ABSTRACT

The requirement for modern combat aircraft to have low radar cross sections and improved aerodynamic performance has introduced the necessity to incorporate weapons bays in almost every new military aircraft design project. This, on its own, has led to a renewed interest in the field of cavity flows, especially during transonic and supersonic speed regimes. Although considerable data already exist on the fundamental physical aspects of cavity flows, whenever a cavity is integrated in an aircraft design, various other related issues must also be considered. Airframe aerodynamics requirements may impose changes on the shape of the cavity, while flight dynamics parameters, like incidence and sideslip, may prompt a different response of such a non-linear phenomenon. A study was therefore conducted in order to assemble knowledge and understanding of some of the main aspects related to weapon bay design. A representative cavity, exposed to a typically representative transonic Mach number, was tested to determine the effects of the introduction of typical stealth design features. These included the saw-toothing of the leading and trailing edges of the bay and the indentations of the doors accompanying the cavity. Such features were tested with and without the presence of a model of a representative store inside the bay. Subsequently, these aspects were tested, in numerical models, by installing the cavity on a representative stealthy airframe, which was used to explore incidence angle effects of the flow characteristics. Finally, an innovative solution, designed to mitigate the adverse aspects of the flow was tested.

Due to the extreme complexity of the aero-acoustic environment typical of cavity flows, a technique based on the complementary use of frequency-domain and time-frequency domain linear and non-linear analyses was used to process the pressure histories recorded. Such a procedure was able to highlight the complexity of the flow, which, in accordance with previous studies, was rich in non-statistical stationary phenomena, like amplitude modulation, frequency modulation, and mode switching.

KEYWORDS

Aeroacoustics, Cavity Flows, CFD, Joint Frequency and Time-Frequency Analysis, UCAV, Wavelet Analysis, Wind Tunnel.

ACKNOWLEDGEMENTS

I am grateful to my supervisors, Dr Alistair Saddington and Dr Derek Bray, for their guidance and encouragement. I also thank Professor Kevin Knowles of the PhD committee for his suggestions during the review meetings.

Special thanks to Dr Mark V. Finnis. His support was fundamental in the planning and execution of all wind tunnel experiments contained in this work.

I acknowledge the contribution of the Shrivenham's workshop team, which built the models for the wind tunnel campaign.

Life during these years of research has been hard but the privilege to meet people like Sqn. Ldr. Ioannis Vagias, Dr Adam Zagorecki, Dr Alessio Balleri, Dr Paolo Palmieri, Dr Luke Roberts, and Lt Stefano Rizzo, alleviated the burden and make me feel like part of a big family.

Special thanks must go also to Sifu Benjamin Gash and all my mates of Swindon Kung-Fu academy that instilled in my spirit the equilibrium and the strength necessary to deal with everyday challenges.

Thanks also to Dr Claudia Brighenti whom 4 years ago pushed my desire for a better life and supported my decision to apply for this PhD.

Last but not least thanks to my family. Mother, father, brother, grandpas, grannies, it would have been impossible for me to accomplish all this without your support and your love. You are the pillars of my life.

Chi ha provato il volo camminerà guardando il cielo, perché là è stato e là vuole tornare.

He, who tried the flight, will walk looking at the sky, because there he was and there he wishes to go back.

Leonardo da Vinci

TABLE OF CONTENTS

LIST OF ABBREVIATIONS

AOA	=	angle of attack
AVT	=	averaged variance trend [dB]
BC	=	bi-coherence
BP	=	bi-phase [rad]
BS	=	bi-spectrum
CFD	=	computational fluid dynamics
CFL	=	Courant–Friedrichs–Lewy condition
DES	=	detached eddy simulation
DFT	=	discrete Fourier transform
FFT	=	fast Fourier transform
FPL	=	fluctuating pressure level [dB]
GWS	=	global wavelet spectrum
GWSP	=	global wavelet spectral power [dB]
HOSA	=	high order spectral analysis
HPC	=	high performance computer
IDDES	=	improved delayed detached eddy simulation
ISA	=	international standard atmosphere
JFTFA	=	joint frequency and time-frequency analysis
LIC	=	line integral convolution
OAFPL	=	overall fluctuating pressure level [dB]
OASPL	=	overall sound pressure level [dB]
PR	=	persistence index of a signal
PSD	=	power spectral density
RCS	=	radar cross section
SNR	=	signal-to-noise ratio
SPL	=	sound pressure level [dB]
UCAV	=	unmanned combat air vehicle
WAVT	=	wavelet averaged variance trend [dB]
WBC	=	wavelet bi-coherence
WBP	=	wavelet bi-phase [rad]
WLCC	=	wavelet local correlation coefficient
WLCP	=	wavelet local correlation phase [rad]
WPS	=	wavelet power spectrum
WSP	=	wavelet spectral power [dB]

LIST OF SYMBOLS

a_∞	=	sound speed in undisturbed flow [m/s]
c	=	wave propagation speed [m/s]
C_p	=	pressure coefficient
D	=	cavity depth [m]
f	=	frequency [Hz]
F_r	=	frequency resolution [Hz]
F_s	=	sampling frequency [Hz]
H	=	altitude [m]
Hm_{Mn}	=	m^{th} harmonic of n^{th} Rossiter-Heller mode
i	=	imaginary unit
k	=	wavenumber [rad/m] $(2\pi/\lambda)$
k_∞	=	turbulent kinetic energy at far-field [m^2/s^2]
L	=	cavity length [m]
M_∞	=	Mach number in undisturbed flow
Mn	=	n^{th} Rossiter-Heller mode
p_∞	=	air pressure in undisturbed flow [Pa]
Q	=	second invariant of the velocity gradient tensor [$1/s^2$]
Re_∞	=	Reynolds number based on cavity length
Shm_{Mn}	=	m^{th} sub-harmonic of n^{th} Rossiter-Heller mode
$Sb_{Mp\pm Mq}$	=	sub-mode created by the non-linear interaction of p^{th} mode and q^{th} mode
St	=	Strouhal number $(f \cdot L/U_\infty)$
t_{Char}	=	characteristic time of cavity [s] (L/U_∞)
T_∞	=	air temperature in undisturbed flow [K]
U_∞	=	free stream speed in undisturbed flow [m/s]
W	=	cavity width [m]
$\bar{x}$	=	time averaged value of the discrete time series x_n $(\sum_{j=1}^{N} x_j/N)$
$\langle x_n \rangle$	=	expected value of the discrete time series x_n $(\lim_{n\to\infty} \sum_{j=1}^{N} x_j/N)$
$\vec{X}$	=	vector quantity
$\bar{\bar{X}}$	=	tensor quantity
$\hat{X}$	=	discrete Fourier transform of the variable x
X^*	=	complex conjugate of the variable X
y^+	=	boundary layer non-dimensional height
α	=	angle of attack [deg]
β	=	angle of sideslip [deg]
γ	=	ratio of specific heats (1.4 for air)
λ	=	wavelength [m] (c/f)
μ	=	mean value
μ_∞	=	dynamic viscosity in undisturbed flow [kg/ms]
ν_∞	=	kinematic viscosity in undisturbed flow [m^2/s]
σ	=	root mean square
ρ_∞	=	air density in undisturbed flow [kg/m^3]
ϕ	=	angular phase [rad]
ω	=	angular velocity [rad/s] $(2\pi \cdot f)$
ω_∞	=	turbulent specific dissipation rate at far-field [1/s]

LIST OF FIGURES

1 INTRODUCTION

This chapter is dedicated to the literature review, which will address the main problems and research performed to date regarding the aero-acoustic phenomena associated with transonic cavity flows. Once defined, the basic nature of the problem will be introduced, including the scope and the overarching reasons for wishing to carry out this research. Finally, a description of the thesis layout will be introduced.

1.1 OVERVIEW

Design requirements of modern combat aircraft often place a high emphasis on radar cross section reduction. Moreover, characteristics like transonic and supersonic persistence[1] have become mandatory features in recent generations of military aircraft. A particular outcome of such requirements is the consequential adoption of a weapons bay into the aircraft configuration (Figure 1.1).

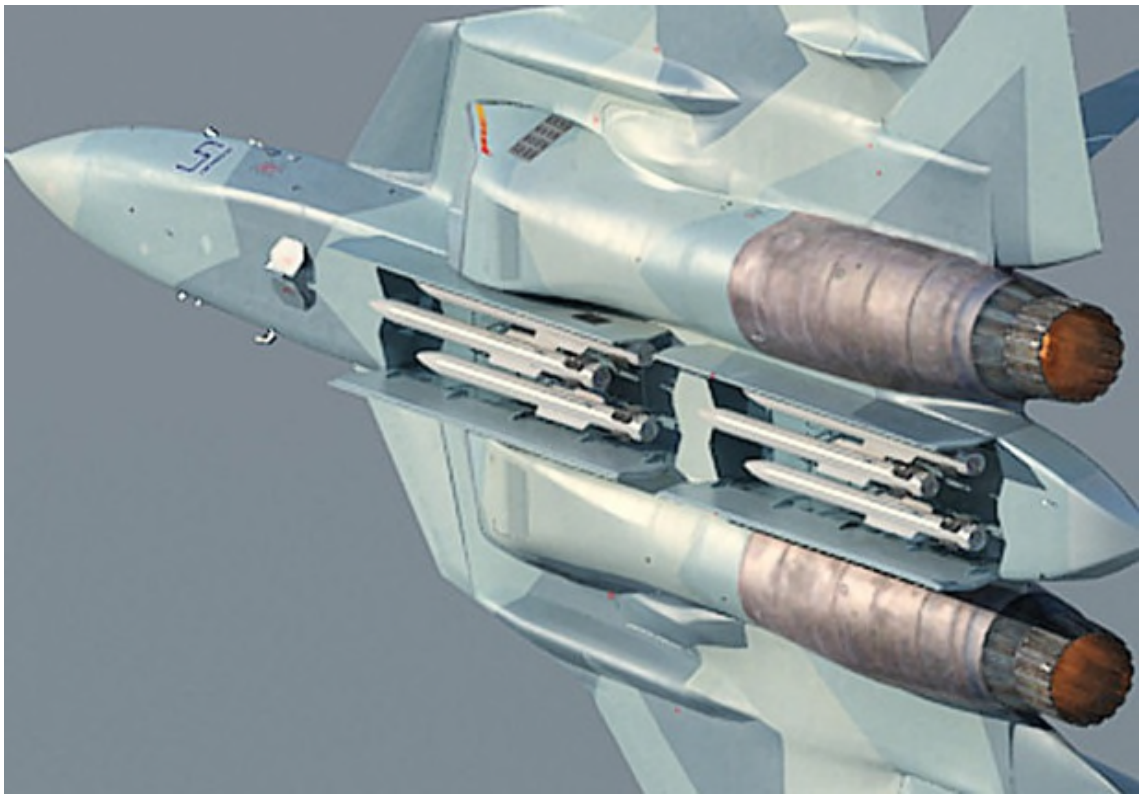

Figure 1.1 - Weapon bay installation on 5th generation fighter prototype Sukhoi T50 (Image source: Google Images®).

[1] This last aspect is usually applied only in air-dominance platforms.

Many current and future bombers, fighters, and UCAV configurations will normally have to carry their weapons loads internally in order to reduce signatures and to reduce form drag. Nevertheless, one of the major drawbacks of this design choice comes whenever the bay is opened in order to release the store. The typical weapon bay operational environment is highly demanding. Usually the store is released in transonic and/or supersonic speed regimes and the associated cavity flow field will develop the following, usually undesirable, characteristics:

- Unsteady Flow Field: The store is subjected to periodic and random oscillations during the release and separation procedures from the aircraft.
- Longitudinal Pressure Gradient: The store, once released, may experience pitch-up moments altering the drop trajectory and potentially even causing impact of the store within the cavity of the parent aircraft.
- Heavy Acoustic Loads: Resonant tones, with sound pressure levels up to 180 dB, and broadband noise with SPL values in excess of 120 dB, are developed inside the cavity, leading to acoustic fatigue phenomena and avionics equipment damage to the payload being launched and the parent aircraft.

It is clear that, for the correct operational use of a weapon bay, all these aspects have to be resolved, or, at least, must be controlled in a way to make the store release as safe as possible. Therefore, cavity flow problems have become a critical design point in many current military aeronautical applications.

1.2 AIMS AND OBJECTIVES

The object of this study was to address some of the uncertainties that inevitably arise by considering results generated only through the use of simple rectangular transonic cavities. More realistic data is required in order to predict the installation of a weapon bay on a real aircraft airframe subjected to the design requirements of current and next generation combat aircraft. In doing so, the following aims were identified:

- Identify the effects of the adoption in the geometry of bay doors and cavity leading and trailing edge of a typical RCS reduction design guideline (45 degree saw tooth pattern) in a cavity installed in an inert environment, i.e. surrounded by a flat surface.
- Identify the effects of the adoption in the geometry of bay doors and cavity leading and trailing edge of a typical RCS reduction design guideline (45 degrees saw tooth

pattern) in a cavity installed on a representative military aircraft, to determine the effects on the flow of the surrounding airframe.

- Explore angle of attack effects on cavity flows installed in an airframe.
- Analyse the cavity response to the introduction of a store model.
- Analyse the effects of the introduction of an innovative passive control method (collar).
- Explore the effects on the flow due to bay door dynamics.

The principal approach to the study was experimental and consisted of various wind tunnel campaigns. However, computational methods were used too, whenever it was not possible to test a condition due to tunnel constraints and limitations (such as exploring angle of attack effects and/or analysing full aircraft/cavity configurations).

1.3 THESIS DESCRIPTION

The thesis is divided into 9 chapters. Chapter 1 covers the introduction, the aims and objectives and the thesis description. Chapter 2 covers the literature review and the scope of the work. Chapter 3 contains a description of the experimental techniques adopted in this study for both CFD numerical simulations and wind tunnel testing. Chapters 4, 5 6, and 7, contain the results, their analysis and a discussion of all of the experiments conducted. The work was divided into three phases. In phase one, starting from the simple rectangular geometry, additional geometrical details were included, such as bay doors, and the indentation of leading and trailing edges for RCS reduction. The analyses were conducted via experimental methods, with the utilisation of a transonic wind tunnel. Once the analysis of the effects of doors and cavity geometry were completed, simulations were conducted via computational methods, using CFD techniques, to explore the same cavity geometry configurations with the cavity installed onto a representative UCAV airframe. In this case, it was necessary to utilise CFD methodologies since, due to size restrictions, it was not possible to test a full aircraft configuration in the wind tunnel. The second phase (Chapter 6) was oriented towards the analysis of angle of attack effects on cavity flows, a parameter that has never previously been discussed in the open literature. In this case, due to limitations of the wind tunnel apparatus, the analysis was performed only with CFD methods. The third phase (Chapter 7) was dedicated to the study of the effects induced by a typical store, constructed starting from a GBU39-JDAM bomb. In addition, an innovative flow-control method, based on the insertion of collars inside the cavity, was tested. In this case, the analyses were performed only in the wind tunnel. A similar investigation utilising

CFD simulation required, due to the increased complexity of the geometry, computational resource capacities not available at the time of the experiments. Finally, Chapters 8 and 9 are dedicated to the conclusions and the discussion and recommendations for future work into the subject area.

2 LITERATURE REVIEW

Weapon bay aerodynamics is a part of the branch of fluid dynamics dedicated to cavity flows. The study of this particular aspect dates back to the 19th Century with Helmholtz (1895) studies on the flow resonance process.

2.1.1 PHYSICS OF THE PHENOMENON

Cavity flows are a particular case of unsteady flows. Indeed, they are characterised by both coherent and incoherent motions at various scales. As stated by Hussain (1986), to encompass the whole range of motions, the flow field should be de-composed into a mean and a fluctuating motion. Hence, the first classification of cavity flow is done by analysing its mean characteristics before switching to the fluctuating phenomena.

TIME-AVERAGED FLOW FIELD

Despite the fact that cavity flows are, by nature, highly unsteady, some characteristic information can be extracted by the measured time-averaged flow pattern and pressure distribution. In their wind tunnel campaign, Tracy & Plentovich (1993) identified three different types of flow configuration depending on the ratio of cavity length to cavity depth (L/D). As shown in Figure 2.1 it is then possible to define the configuration as open, transitional, or closed.

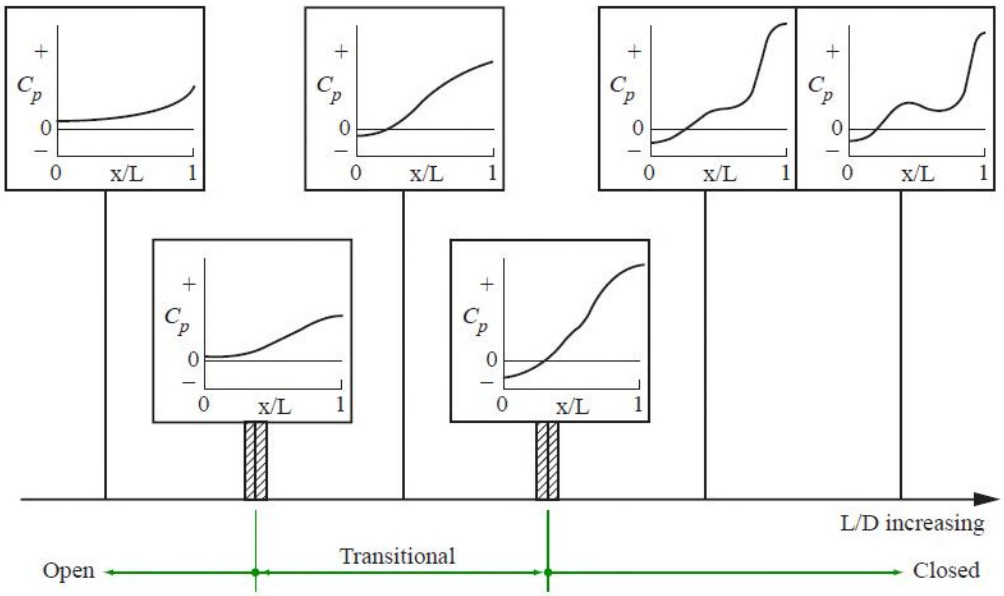

Figure 2.1 - Cavity flow classification with varying length to depth ratio (Tracy & Plentovich (1993)).

Increasing *L/D* ratio has a marked effect on the mean pressure coefficient along the cavity. At low *L/D* values, the mean pressure gradient is shallow and always positive, with a slight increase towards the end of the cavity. Such a configuration, generally called “open”, is usually maintained up to *L/D* values of six. At higher ratios, the curve begins to evolve from a purely concave shape, to a concave-convex form, with an inflection point placed somewhere around the middle of the cavity. The mean pressure coefficient is still positive. An additional increase of the *L/D* ratio introduces a new cavity regime, called “transitional”. Such configuration is usually maintained for values of *L/D* between 6 and 15. The concave-convex shape is maintained, but in this configuration, the mean pressure coefficient is usually negative in the front part of the bay. The final regime, called “closed”, appears for *L/D* values from 15 onwards. Here the pressure gradient has a marked shallow central part that, with an increase of the *L/D* ratio, tends to transform the profile into a local peak and dip curve.

From the point of fluid structure organisation, open cavity flows are characterised by a shear layer that, upon detaching from the bay leading edge, bridges the whole cavity and reattaches at the trailing edge, forming a large eddy inside the bay. A schematic of the flow field structure is given in Figure 2.2.

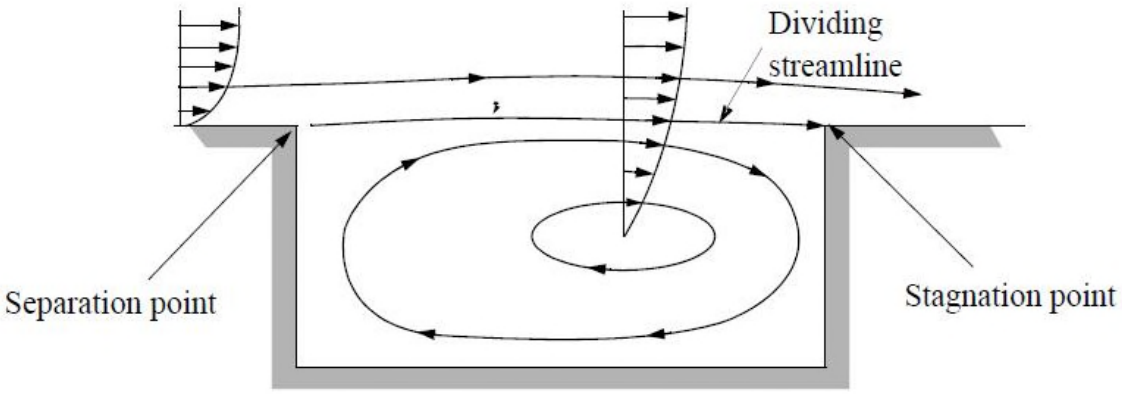

Figure 2.2 - Open cavity flow structure (Tracy & Plentovich (1993)).

Closed cavity flow (Figure 2.3) is characterised by the shear layer that, after detaching from the bay leading edge, reattaches along the floor of the cavity and then separates again before the trailing edge. This produces two distinct eddies, responsible for the “peak and dip” form of the pressure gradient, as shown in Figure 2.1.

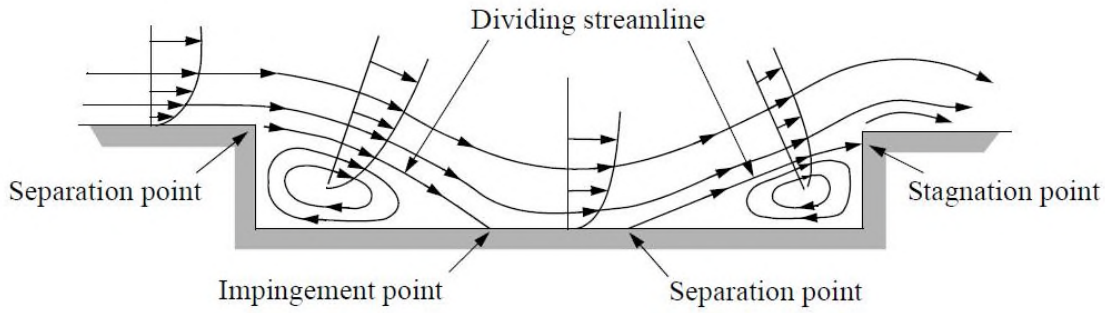

Figure 2.3 - Closed cavity flow structure (Tracy & Plentovich (1993)).

Transitional cavity flow, as its name states, is the link between the open and the closed types and the phenomena involved are a mix of the two previously discussed. The pressure gradient is not favourable, as exists for the open category, but it shows clearly the rising towards positive values, typical of an open cavity. If an open cavity configuration is taken as the starting point, as the *L/D* ratio is increased, it is possible to observe that, somewhere in the middle of the bay, the shear layer tends to drop, moving towards the floor, until the point at which it collides with the floor, reattaches and immediately separates. Such a configuration usually marks the boundary between "open" and "transitional" flow regimes. Figure 2.4 identifies the difference between a transitionally open flow, where the shear layer drops but does not contact with the cavity floor, and the transitionally closed flow, where instead attachment occurs.

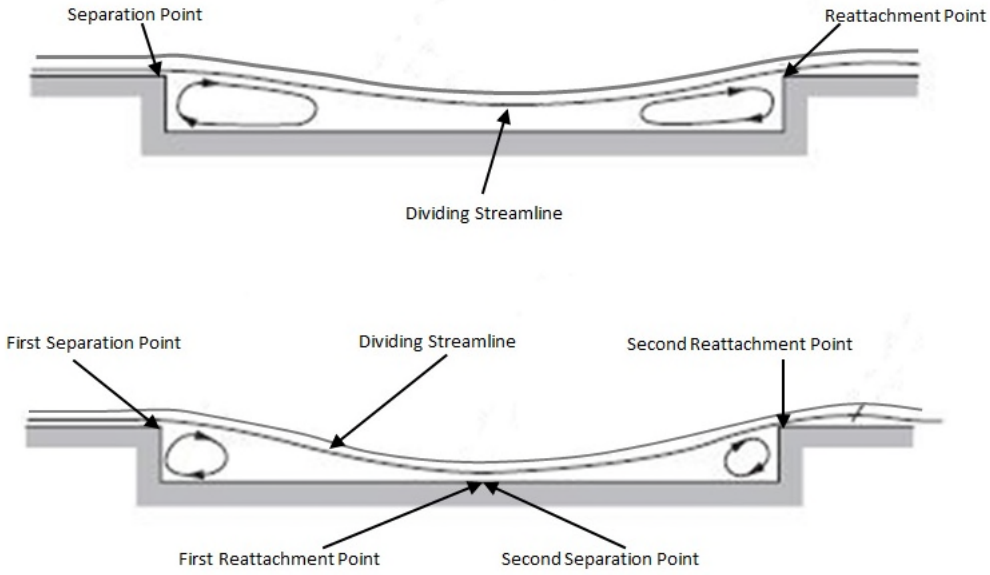

Figure 2.4 - Transitional open (upper) and transitional closed (lower) flow structures (Tracy & Plentovich (1993)).

NON-STATIONARY FLOW FIELD

The fundamental aspect that characterises a cavity flow is its unsteadiness, formed by a combination of both periodic and random pressure fluctuations. In certain combinations of geometries and external flows, resonance mechanisms occur, known as cavity resonance modes, which increase the adverse effect due to a worsening of the pressure fluctuations. The first study on cavity oscillation mechanisms in incompressible flow dates back to the work of Rossiter (1966) in which he derived an empirical formula for the determination of the possible resonance frequencies that may arise in cavities. He proposed a feedback loop in which the shear layer was represented as a series of vortices separating from the cavity leading edge, travelling downstream at a constant speed. Upon colliding with the trailing edge these vortices produce acoustic waves, which propagate at the local speed of sound. When these waves collide with the upstream lip, they trigger the production of new vortices, thus closing the loop. Based upon on this simple mechanism, Rossiter developed the following formula to define the resonance frequency modes (f_n):

$$f_n = \frac{U_\infty}{L} \cdot \left(\frac{n - \alpha}{M_\infty + {}^1/_k} \right) \quad n = 1,2,3 \ldots \tag{2-1}$$

Here L is the length of the cavity, k is the ratio of disturbance velocity in the shear layer to the free stream velocity, equal to 0.57, and α is an empirical constant that takes into account the phase lag between the passage of an eddy disturbance past the trailing edge and the formation of an upstream traveling disturbance. This constant depends on cavity geometry:

$$\alpha = 0.062 \cdot \left(\frac{L}{D} \right) \tag{2-2}$$

The variable D is the cavity depth. Equation (2-1) is valid for subsonic Mach numbers only because it does not take into account the temperature recovery inside the cavity, which modifies the speed of sound and hence the propagation of the disturbance waves. Heller (1971) proposed a modified formula to include such compressibility effects:

$$f_n = \frac{U_\infty}{L} \cdot \left(\frac{n - \alpha}{M_\infty \cdot \left[1 + \frac{\gamma - 1}{2} \cdot M_\infty^2 \right]^{-0.5} + {}^1/_k} \right) \quad n = 1,2,3 \ldots \tag{2-3}$$

Equation (2-3) is known as the "Rossiter-Heller" formula, and it predicts, with good accuracy, the tones at which eventual self-sustained oscillations may occur. Its derivation is based on the fact that the speed of sound inside the cavity (a_c) can be expressed as (Heller (1971)):

$$a_c = a_\infty \left[1 + r \cdot \frac{\gamma - 1}{2} \cdot M_\infty^2\right]^{0.5} \quad \textbf{(2-4)}$$

Here r is the temperature recovery factor inside the cavity. It was determined to be equal to 0.9 and 0.95 respectively at Mach 0.8 and 3.0 indeed it has been postulated to use a value of 1 in the hypersonic regime, with an assumed negligible error (Heller (1971)). Equation (2-3) can be obtained from Equation (2-1) replacing, at the denominator, the value $M_\infty = U_\infty / a_\infty$, with the equivalent cavity Mach number, $M_c = U_\infty / a_c$, where a_c has been calculated using Equation (2-4), assuming $r = 1$. An additional correction has to be applied when dealing with very low L/D values. Larcheveque, et al. (2003) proposed a new expression, derived experimentally, for the parameter α, accounting for this aspect:

$$\alpha = 0.58 \cdot e^{-\left(\frac{L/D - 10}{6}\right)^2} \quad \textbf{(2-5)}$$

This expression gives results more accurate for $L/D < 0.2$ with respect to the original Rossiter-Heller formulation.

Using the Schlieren technique, which is based on the visualisation of density gradients, it is possible to provide visual evidence for all the phases of the Rossiter-Heller tones

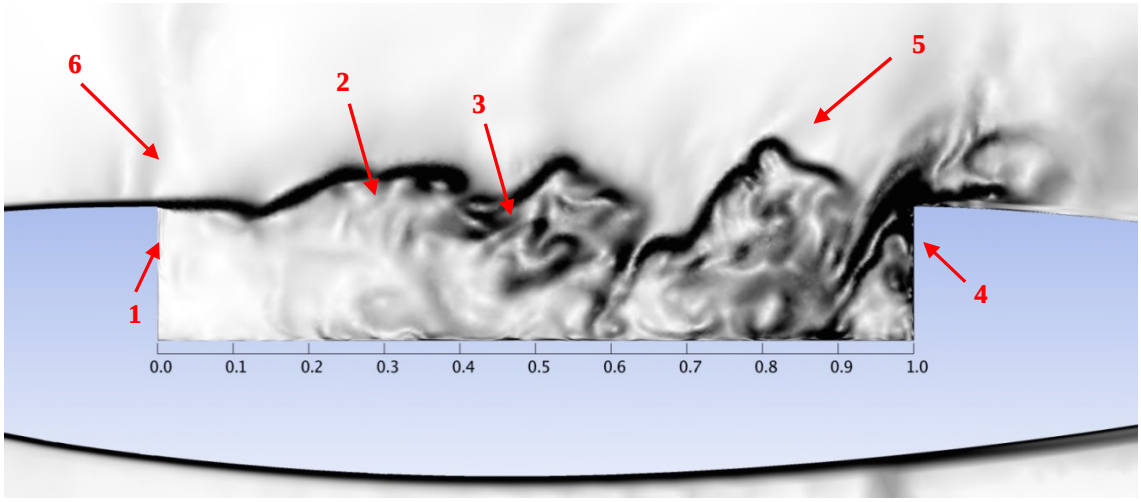

Figure 2.5 - Schlieren picture of a transonic cavity flow field. *Mach number is 0.85. Flow from left to right.*

Figure 2.5, which was generated at a transonic Mach number of 0.85, shows an instantaneous visualisation of the flow structures present in a cavity with an L/D ratio of five. Here, it is possible to observe the detachment of the shear layer (1), the destabilisation and transition to turbulent flow conditions (2), with the subsequent formation of vortices (3), the impact of these structures with the rear wall of the cavity (4), and the generation of sound waves (5), which travel upstream closing the loop (6).

Even if the term of self-sustained oscillation is in itself reasonably self-explanatory, its underlying nature is complex and many studies have been conducted to understand the fundamental fluid mechanics associated. The oscillatory mechanism is also variable, as described in the study of Rockwell & Naudasher (1978). They identified three different oscillation types, fluid-dynamic, fluid-resonant and fluid-elastic.

Fluid-dynamic oscillations are typical of cavities with dimensions small compared to the acoustic wavelength or, expressed in terms of resonant frequencies, the following equation must be satisfied:

$$f_n \ll \frac{a_c}{L} \tag{2-6}$$

The primary mechanism of these oscillations is the amplification of the vorticity fluctuation inside the cavity shear layer. This amplification is enhanced by the presence of the bay rear wall; this generates a feedback loop capable of sustaining the oscillation that otherwise would decay as every free-stream turbulence phenomenon.

Fluid-resonant oscillations occur if one of the cavity dimensions is of the same order or greater than the acoustic wavelength and hence can be length, width or depth-related as shown in Equation (2-7). They are characterised by standing waves, along the major bay dimension, that continually displace the shear layer and create a feedback loop changing the impingement point or the cavity rear face.

$$f_n \geq \frac{a_c}{\max[L, W, D]} \tag{2-7}$$

Fluid-elastic oscillations appear whenever one or more cavity walls deform elastically to an extent such to influence the feedback mechanism. This is a typical problem of structure-flow interaction and is strongly dependant of the geometry of the cavity as well its constitutive materials.

Frequency domain analysis of pressure signals, recorded inside cavities, produce spectra that again are dependent on the *L/D* parameter. For open-flow topology, the frequency analysis is characterised by the presence, on the sound pressure level (SPL) plots, of peaks in correspondence of the Rossiter-Heller modes (Figure 2.6).

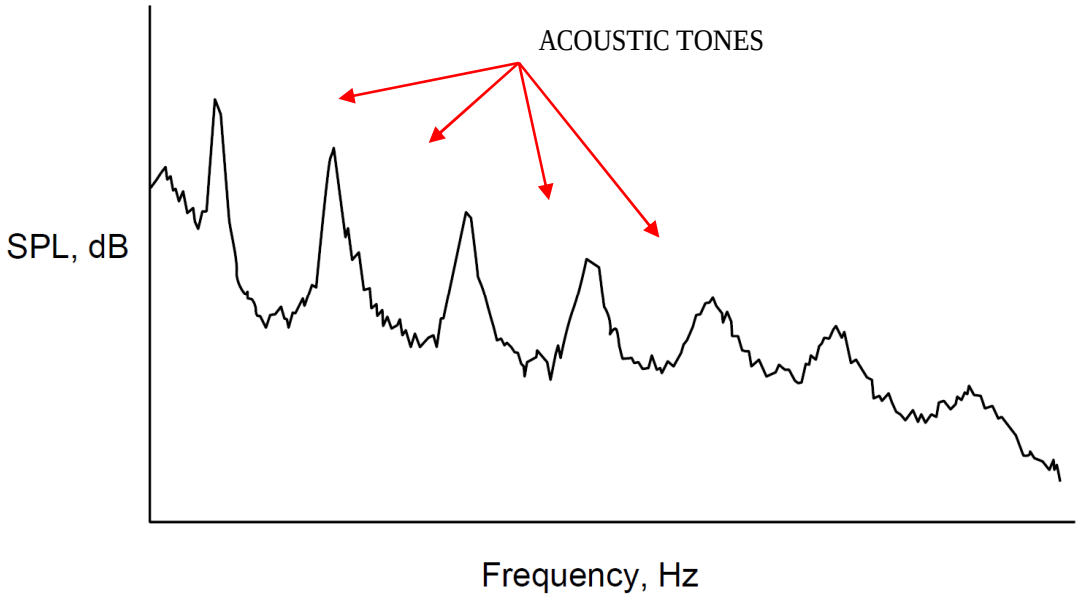

Figure 2.6 - Open cavity flow typical fluctuating pressure spectrum (Tracy & Plentovich (1993)).

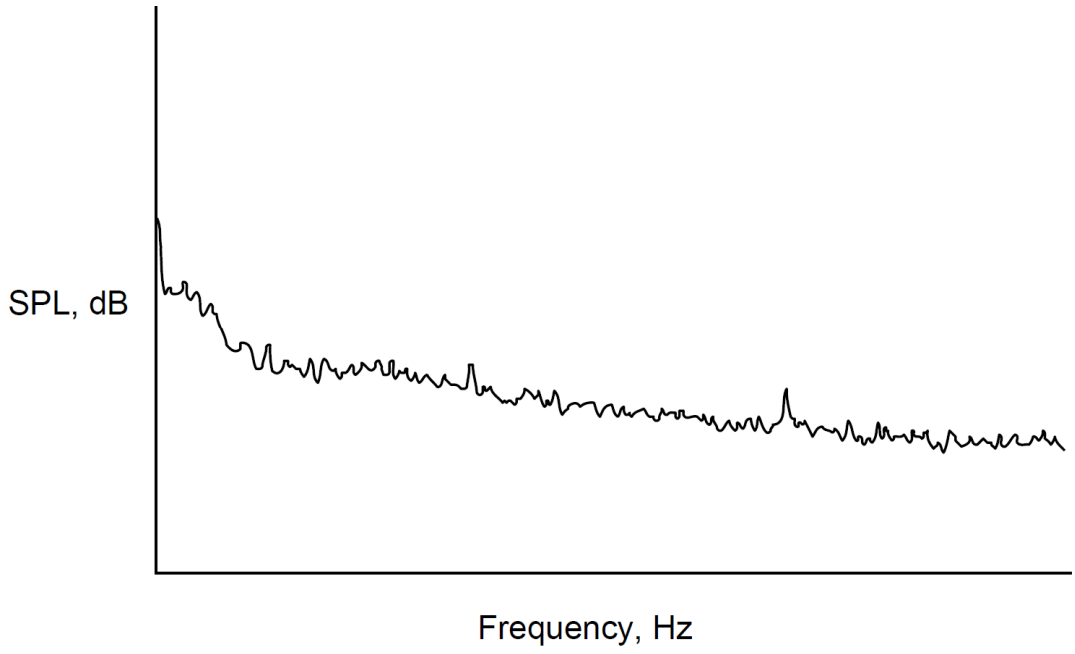

Figure 2.7 - Closed cavity flow typical fluctuating pressure spectrum (Tracy & Plentovich (1993)).

The dominant mode varies from case to case but is usually the first or the second, with the power of the subsequent tones decreasing as the mode number is increased. Background noise also has the form of a red-type spectrum, i.e. power decreasing with increasing frequency. Closed-type cavity flow is instead characterised by a SPL plot with just broadband noise (Figure 2.7). Finally, as in the case of the time-averaged flow, transitional-type cavities have spectra typical of the open and closed type characteristics (Figure 2.8). While acoustic tones are still present they appear to be more smeared and shifted toward higher frequencies.

The expansion of the analysis in the time-frequency domain, work pioneered by Kengerise, et al (2004), has unveiled additional levels of complexity in nature of the non-steady flow field. The adoption of short-time Fourier transform (STFT) and wavelet transform analysis routines demonstrated that the nature of Rossiter-Heller modes is non-stationary from a statistical point of view. The tones and, in general, the supporting structure of the acoustic vibrations, are, in fact, subjected to a phenomenon called *mode switching*, i.e. a process whereby the dominant energy shifts from one resonant tone to another as the signal evolves in time. Additionally, it has been discovered that the flow is also affected by non-linarites such as quadratic frequency and phase coupling. This last aspect can be attributed to the studies of Yen (1971) , in that the generation of sub-harmonics is acoustic in nature; a process, described as occurring whenever a potentially non-linear medium is subjected to extreme high amplitude perturbations.

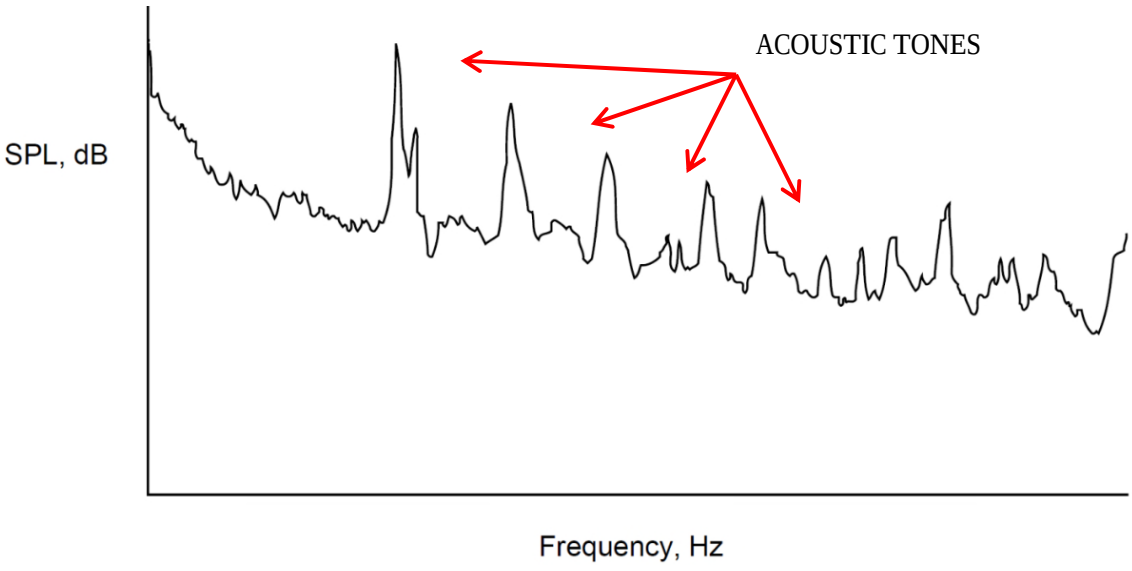

Figure 2.8 - Transitional cavity flow typical fluctuating pressure spectrum (Tracy & Plentovich (1993)).

OTHER FACTORS AFFECTING CAVITY FLOWS

As shown in previous paragraphs, the *L/D* ratio is considered the main parameter influencing cavity flows. However, various studies have also demonstrated that factors such as *W/D* ratio, leading-edge sweep, Mach number, incoming boundary layer thickness and temperature are also capable of influencing the flow configuration; hence, they will all be discussed in this section.

Ahuja & Mendoza (1995) conducted wind tunnel studies investigating the effect of *W/D* ratio, finding that changing the width of the cavity did not affect significantly the resultant flow. The parameter only begins to have an effect when it is reduced below unity. Dropping below this threshold, sound pressure levels increase asymptotically towards a limit defined by 2-dimensional flow configurations. This can be explained by the fact that a 3-dimensional aerodynamic flow has one more dimension to relieve the phenomena and it is implicit that a 2-dimensional flow produces effects more pronounced, whether of an aerodynamic and/or aero-acoustic nature. Finally, Plentovich et al. (1993) found that decreasing cavity width tends to reduce the critical value of length to depth ratio at which closed cavity flow configuration conditions begin to appear.

Effects of leading edge sweep have been studied by Tracy et al. (2012). This parameter was found to have only small effects in transitional and closed type cavities, merely reducing the effective *L/D* ratio, but a much stronger effect on open cavity flows. Increasing the yaw angle of the leading edge makes the shear layer roll up around itself, very similar to the formation of a delta wing vortex. This vortex changes completely the flow topology and virtually eliminates the major Rossiter peaks usually found in the spectrum. However, the introduction of this new coherent structure creates two new adverse effects that are not present in cavities with straight leading edges. The first is the introduction of cross flow instabilities that could lead to the destabilization of any payload in all three directions of motion. The second adverse effect is due to the strong suction generated by the vortex core in the front part of the bay, leading to a store experiencing a pronounced pitching moment during release. There is a consistent reduction of the pressure noise due to the disruption of the Rossiter modes. The instabilities are now governed by the behaviour of the formed vortices. As the vortex starts forming and growing in force due to sweepback angle increase, the shear-layer resonance phenomenon is weakened until approximately 40 degrees of sweep is reached. Then there is another rise, most probably caused by the increased strength of the rolled vortex formed at the

leading edge. Passing this peak, at around 55 degrees the resonance strength is once again reduced. In fact, progressing further with increased sweep angle, the flow closes to the limit of 90 degrees, in which once again a closed cavity flow type forms.

Mach number is the second main dependence parameter. Increasing its value increases the resonant frequency because the shear layer disturbances are transported downstream with greater speed. In transonic and supersonic regimes, expansion and compression stages of the shear layer create shock waves and expansion fans that increase drag and lead to shock-boundary layer interactions that further destabilize and complicate the flow.

The nature of the boundary layer has a strong effect on the flow, directly controlling the amount and the state of vorticity shed in the shear layer. Ahuja & Mendoza (1995) found that increasing boundary layer thickness decreases the cavity tones, as well as the pressure gradients, up to the point where all tones are eliminated. A thicker boundary layer has its vorticity spread over a greater thickness, tending therefore to generate a weaker shear layer that, firstly, has less energy to devote to the resonance mechanism and, secondly, its impact on the cavity rear wall generates a lower amplitude disturbance, thus weakening the feedback mechanism described by Rossiter. Thangamani et al. (2014) investigated the effect of scale, using the parameter L/δ, that is the ratio between bay length to incoming boundary layer thickness. They found that increasing this ratio tends to increase the tones of the oscillations due to the increased time that the shear layer is allowed to travel in free air. In fact, in this case the shear layer has more time to grow and acquire coherence, thus gaining more energy at the trailing edge. This effect could also spoil the efficiency of some palliative mechanisms like the usage of spoilers. In their conclusion, the authors recommend, during wind tunnel trials, to scale the parameter L/δ to obtain the same environment experienced in flight.

Yet more problems are encountered when the obtained experimental results are extrapolated in the case of the design of weapon bays installed in real combat aircraft, which seldom can be represented as a simple rectangular cavity surrounded by a constant ambient environment. Only limited work has been published in open literature. Studies like the ones of Clark (1979), Kannepalli, et al. (2011), and Morton, et al. (2012), were related to the analysis of already existing combat aircraft designs, while the papers of Lawson & Barakos (2010), Chaplin & Birch (2012), and Hallissy & Hariharan (2014), oriented toward the analysis of a UCAV platform with weapons bay installed. Other authors such Ukeiley, et al. (2008), Murray & Jansen (2012), and Casper, et al. (2016),

focused on analysing some geometrical features, always present in modern designs, such as bay doors, indented leading and trailing edges and non-flat surfaces on the front of the cavity.

The general effect of the presence of bay doors is that the SPL curve is translated towards higher decibel values, usually from between 2 dB to 5 dB; however, the signal to noise ratio (SNR) of the peaks with respect to the broadband noise is reduced compared with the no-doors case. In fact, while the doors' presence tends to impede the formation of the Rossiter-Heller tones, the tunnelling effect promotes the oscillation energy creating the noise. The situation changes if, in the case of double doors installed on opposite sides of the cavity, one is kept closed and one is opened. In this case, the signal-to-noise ratio of the modes increases sharply, sometimes by as much as 100%, while the SPL curve is shifted towards lower values, usually decreasing by 4 dB to 8 dB. The presence of the closed door prevents a part of the flow from entering the cavity, thus reducing the broadband noise level; however, the empty air space between the closed door and cavity's floor is a perfect resonator that intensifies the acoustic vibrations of the tones.

Other geometrical details, typical of cavities used on actual combat aircraft, have also been investigated, such as the work of Casper, et al. (2016). However, the data available is too limited to introduce general rules and hence it will not be discussed further in this section.

2.1.2 CAVITY FLOW CONTROL TECHNIQUES

Since its discovery, palliatives to the phenomenon of cavity oscillation have been developed in order to reduce adverse effects and to ensure a safer environment for store release. Usually, the most common studied solution is the passive method because of its simplicity. More advanced solutions, like active blowing, have been investigated in recent years but they have not yet been reported as being used due to the complexity of their installation, as well as to the programming of the control laws. Recently, the trend is to use more than one passive mechanism to keep the complexity low but to maintain a satisfactory width of envelope usage. In fact, one of the major drawbacks of the passive palliatives is that they are point-designed, and in different flight conditions can lead to a worsening of the situation.

Many control methods have been developed for the attenuation of the phenomena. A first subdivision can be made with passive and active categories. Passive methods are considered to be those involving any geometry modifications, like chamfers, slots etc.

These modify the phenomena by interfering with the formation mechanisms, without adding any energy to the flow. On the other hand, an active flow control mechanism, using moving parts, suction or blowing of air, aims to modify directly the flow field.

PASSIVE CONTROL METHODS

Passive control methods are easy to implement and this has contributed to their proliferation. However, their range of operation is limited and in some configurations their benefits can be denied, or even worse, could introduce disadvantages across some sections of the aircraft's flight envelope.

The most common mechanism utilized is the installation of a spoiler at the cavity leading edge. Its role is to disrupt the mechanism of interaction that originates the resonance phenomenon, altering the incoming boundary layer, diverting it away from the cavity or splitting its vorticity. Many forms of spoiler have been investigated in various studies. The shape of the spoiler plays a crucial role, as well its height and thickness ratios with respect to the incoming boundary layer thickness. This is the major drawback of this solution because it can be optimised only for a specific working point of the envelope of the aircraft. Usually the height of the spoiler shall be of the order of magnitude of the boundary layer thickness at the cavity leading edge to obtain the maximum tone reduction on the first three wave modes. In addition, saw-toothed spoilers (triangular, square and wedge forms) have shown good behaviour, their key strength being their ability to disrupt the incoming eddies, reducing the amount of energy contained in the larger scales of the shed turbulence. Thangamani et al. (2013) found that the greatest reduction of sound levels at transonic speeds was obtained with squared saw-tooth spoilers with a maximum reduction of 10 dB in the first three dominant frequencies at Mach 0.7. However, this beneficial effect tends to decrease when the flow becomes supersonic and, at higher Mach numbers, saw-toothed spoilers tend to have a detrimental effect, increasing the sound levels. This behaviour has been investigated by Tripton (1980). In his studies on a real aircraft geometry, the Rockwell B1-B Lancer bomber, he showed that spoilers, even if providing positive benefits in the subsonic-transonic regime, lose their effectiveness at supersonic speeds. He also found that, for porous spoiler configurations, the effect is even more detrimental.

Another passive control method studied in the literature has been the modification of the cavity wall and edges. The most common features are leading-edge and trailing-edge steps and chamfers as well as front and rear wall slants. A good survey of the effects of these

geometry modifications can be found in Thangamani et al. (2013). The authors discovered that the most promising mechanism seems to be the wall slant, more precisely the leading-edge wall slant. In fact, the forward wall slant is the only modification capable of swallowing the longitudinal pressure gradient in its entirety. Furthermore, the OASPL is reduced by 5 dB with respect to the clean cavity case. Finally, the forward wall slant eliminates the third Rossiter mode, reduces the second by 3 dB but increases the first by 1 dB, probably indicating a redistribution of the energy between modes instead of a proper suppression.

Another passive mechanism, based on Helmholtz resonators, is the adoption of porous walls inside the cavity, specifically designed to work as resonant absorbers. The more common and promising solution of this kind is the perforation of the front and rear wall of the cavities. It is believed that the oscillating air masses in the holes of the walls create viscous forces that dissipate the acoustic energy produced by the resonant mechanism. Roberts (2013) demonstrated that a properly designed perforated wall could produce a reduction of 26 dB in supersonic flow conditions and 17 dB in transonic conditions, the largest effects produced by installing absorbers on both the front and rear walls.

ACTIVE CONTROL METHODS

Active control methods have the advantage of being tuneable to different settings in order to cover a greater spectrum of the flight envelope. However, their considerable complexity has prevented their adoption so far. The most studied mechanisms have involved mass flow injection and moving actuators, usually placed at the cavity leading edge.

Mass injection methods can be divided into open-loop and closed-loop categories. The first involves constant or pulsed blowing at frequencies different to the Rossiter values, the second is a more advanced solution that can auto-adjust to the phenomena. The most common injection is from the leading edge of the cavity, both parallel and angled to the incoming flow, with an achievable reduction of pressure levels around 10 dB for the former and around 5 dB for the latter, as demonstrated by the studies of Sarno & Franke (1994). The basic principle of operation is to move the impingement point aft of the rear wall, by pushing the shear layer away from the cavity. In the pulsing method, the mechanism is different, the idea being to disrupt the feedback mechanism by altering the resonant frequencies, and shifting them to higher values. The system can auto-adjust to the changing flight conditions. However, this approach is far from easy to implement in the real world; in fact, it requires additional levels of complexity such as feedback sensors,

micro actuators, and a dedicated pressure air reservoir. These reasons have prevented the adoption of this palliative to date.

Moving actuators are the mechanical counterpart of the mass injection method. Usually a small flap is placed at the leading edge of the bay and is moved accordingly to disrupt the feedback mechanism. This solution shares all of the drawbacks of the mass injection mechanism and adds a moving mechanical part, which is a further complication of the structure. Up to now, it has not gone further than wind tunnel experiments, where in transonic Mach numbers it has demonstrated (Kergerise et al. (2002)) a peak reduction in sound pressure levels of between 5 to 10 decibels.

2.1.3 AIRFRAME INSTALLATION SOLUTIONS

The discussion, so far, has been focused on the analysis of cavities in isolated environments. However, when weapon bays are considered, the integration on the airframe is of paramount importance. In fact, the cavity is no more surrounded by a flat surface but has to cope with the influence of the aircraft's geometry, which can greatly modify the response of the system. Moreover, not all cavity flow-control techniques can be integrating in the airplane design, be it for complexity reduction, and/or drag and weight issues.

Weapon bays began to appear in bomber designs a decade before the outbreak of the Second World War. Prior to that, the entire weapons payload was carried outside the aeroplane, under the fuselage and/or under the wing. At that time, cavities were simply cut-outs incorporated into an aeroplane's fuselage.

Figure 2.9 - B29 weapon bay. (Image source: Google Images®)

Little was known about the phenomenon of cavity aeroacoustics and the essence of a bomber's tactical warfare, which consisted of carpet-bombing[2], did not require a stable separation of the store from the airframe and so no care was given to an eventual tumbling of the bomb induced by the turbulent flow. Moreover, aircraft speeds at ordnance launch were well below transonic Mach numbers, implying less adverse effects. After the Second World War, aircraft knowledge and complexity increased in many ways but the problem of cavity aero-acoustic phenomena was essentially ignored. This may be explained by the fact that a weapon bay was a characteristic feature present only in bombers, where typical *L/D* ratios exceeded values of 10. In this situation, the main adverse phenomenon was the pronounced pressure gradient. However, in such long bays, usually the ratio of the store length to cavity length is in the order of 0.2-0.3, so the effective gradient, felt by the weapon, was virtually non-existent. The problem was therefore left unresolved, since it was of secondary importance, also because there was still no requirement for precision bombing, and the release trajectory was therefore of minimal importance.

Up to the second decade of the Cold War, weapon bays were still only present in bombers. The only exceptions, at that time, were the Convair F-102 Delta Dagger and F-106 Delta Dart supersonic fighters. In these aircraft, the weapon bays had to accommodate small missiles and the *L/D* dropped to values appropriate to open flow configurations. Here, adverse phenomena were more pronounced and the correct employment of the air-to-air load-out required a better control of the release sequence, so the problem was given more attention.

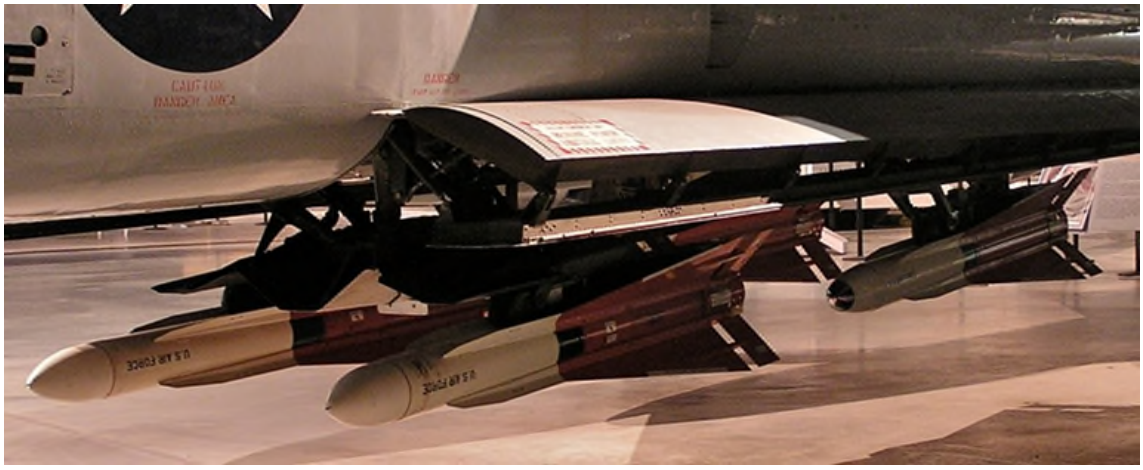

[2] Carpet-bombing consists of the indiscriminate attack of a selected area of land, without aiming to strike a particular target inside it, but to cover the whole area with the maximum damage possible.

Figure 2.10 – Convair F-106 missile rail launchers. (Image source: Google Images®)

The developed solution (Figure 2.10) at that time was the adoption of an extendible rail that exposed the missile to the undisturbed airflow before launch.

Bomber aircraft bays, however, still had no particular "flow alleviation" solution adopted due to the high *L/D* values. The only issue was to streamline the bay doors and the cavity's profile in order to present a smooth flow and reduce drag, as shown by the Vulcan bomber (Figure 2.11).

Figure 2.11 – Avro Vulcan weapon bay. (Image source: Google Images®)

Practical studies and applications started to appear in the 1970s. The operational framework and doctrine, by then, had changed. The new requirements demanded more accurate weapons delivery at both transonic and supersonic launch Mach numbers. Examples are given in the studies of Clark (1979); he analysed various spoiler configurations to reduce the randomness of the stores deployment from the bay of the General Dynamics F-111 fighter-bomber.

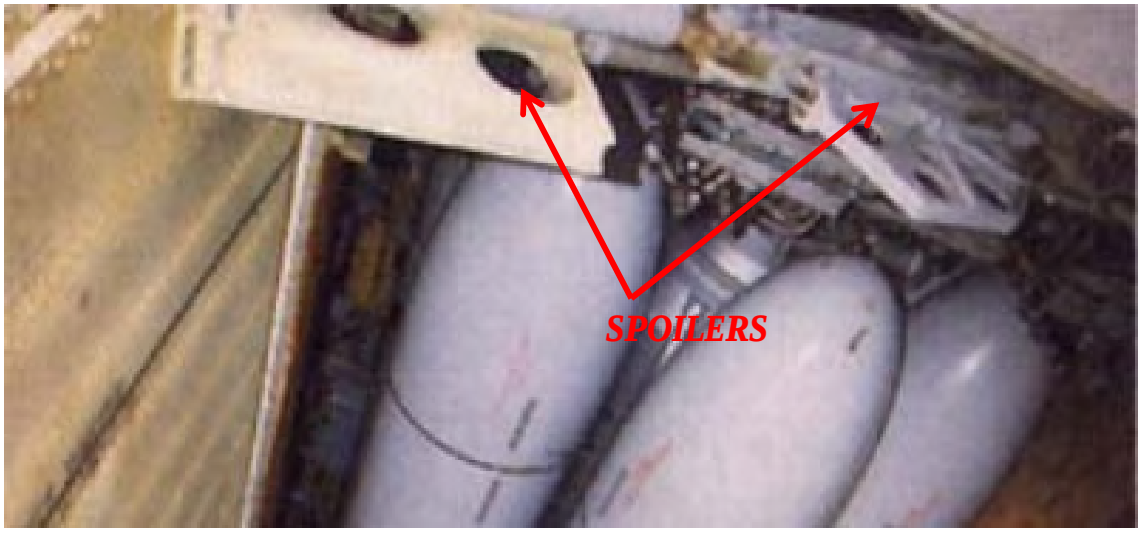

Figure 2.12 – Tu-160 perforated spoiler installation on the front weapon bay. (Image source: Google Images®)

The first series of aircraft designed with built-in suppression mechanisms were the Rockwell B1-B Lancer and Tupolev Tu-160 Blackjack supersonic bombers (Figure 2.12). An accurate study of the perforated spoiler configuration of the B1-B was conducted by Tripton (1980). He examined the behaviour of such a mechanism in various parts of the flight envelope of the aircraft, proving its effectiveness.

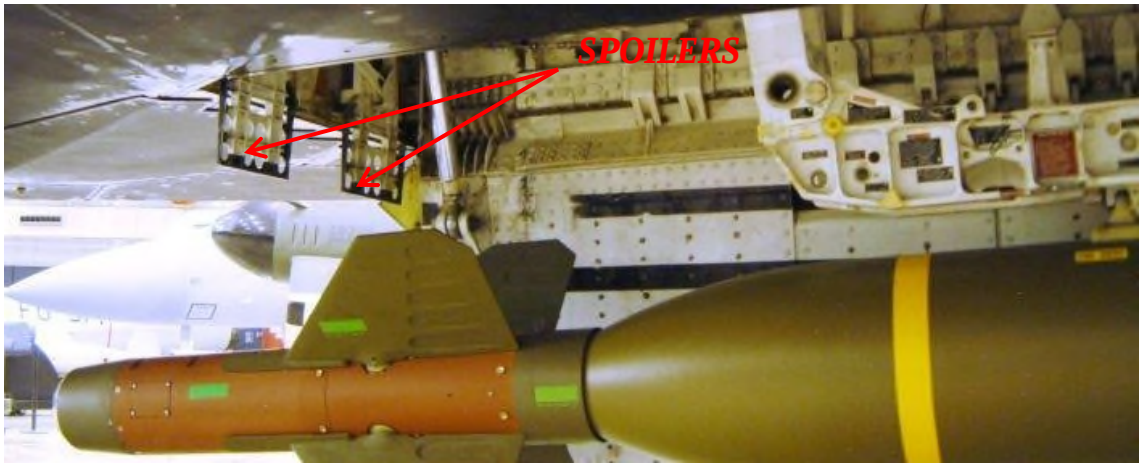

Figure 2.13 - View of F-117 weapon bay with spoilers extended. (Image source: Google Images®)

With the advent of the first stealth projects like the Lockheed F-117 and the Northrop Grumman B-2 bombers, the problem was complicated by the primary demand of RCS reduction, which required the serration of the transverse edges of the bays. The most adopted “adverse phenomena” reduction technique still was the deployable spoiler

(located at the leading edge of the bay), since it did not seem to affect the overall stealth characteristics of the airframe. The solution used on the F-117 (Figure 2.13) was quite simple but offered an improvement on the flow, simply by making the shear layer deflect away from the bay trailing-edge, thus reducing the resonance and oscillatory phenomena.

The adoption of a perforated spoiler helped to reduce the drag of the mechanism and avoid any eventual unsteady wake development, which would be typical of that produced by immersing a plate perpendicular to the oncoming flow. Moreover, the designer opted for the installation of two small separate devices in order to reduce the exposed area, mainly for drag reduction reasons.

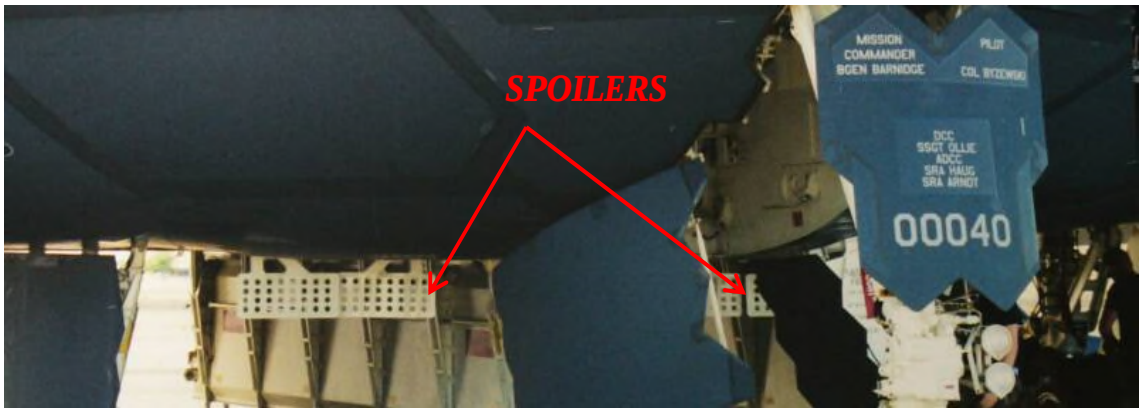

Figure 2.14 - View of B-2 weapon bay with spoilers extended. (Image source: Google Images®)

Recent aircraft, such as the B-2 stealth bomber (Figure 2.14) and the Lockheed F-22 supersonic fighter, have retained the adoption of such a spoiler. In the latter case, the spoiler was modified from a perforated plate to a small winglet (Figure 2.15), with an inclination of 30 degrees, to deflect the flow outside the bay without excessively increasing the drag. The cavity also included a slanted ramp on the rear wall (Figure 2.16). The effect in this case was to relieve the impact of the free shear layer on the trailing edge, facilitating its ejection outside the cavity, and reducing the strength of the emitted sound waves.

Figure 2.15 - View of the F-22 main weapon bay with spoiler extended. (Image source: Google Images®)

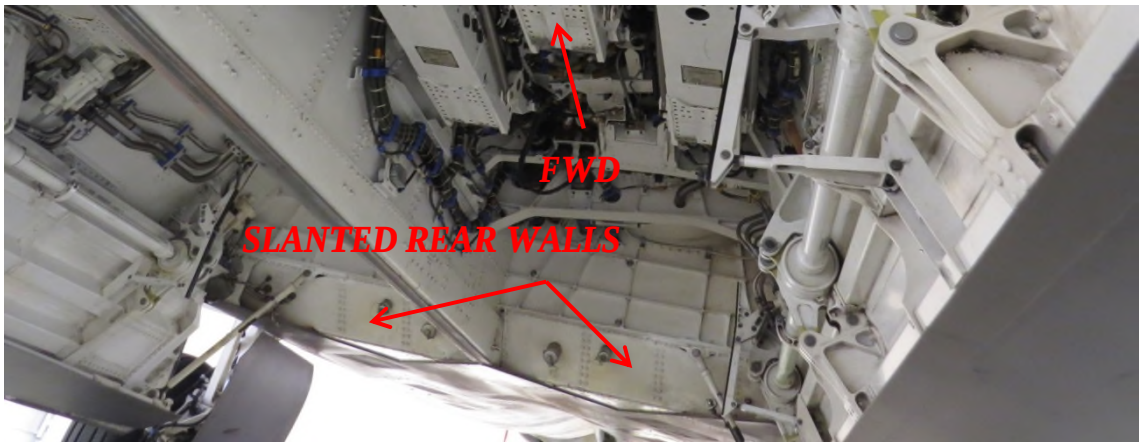

Figure 2.16 – F-22 main weapon bay showing rear slanted walls. (Image source: Google Images®)

In more recent configurations, like the Lockheed F-35 (Figure 2.17), the adoption of a full-depth swept weapon bay leading edge, seemed to have removed the necessity for the spoiler. This matched well in accordance with the findings of Tracy et al. (2012) as well as the analyses of Thangamani et al. (2013). A combination of leading-edge sweep and rear slant walls should have been enough to keep the adverse effects at a level considered acceptable by the airplane's designers.

This brief survey on the solutions adopted for the integration of the weapon bays with the parent airframes provides sufficient evidence to suggest that the integration problem is a major consideration for this discipline. Cavity aero-acoustics is a highly non-linear phenomenon and even a small change in the surrounding environment can have

pronounced effects. Hence, it is of extreme importance, that, when a new weapon bay is designed, airframe integration issues are contemplated from the outset.

Figure 2.17 – Close-Up view of the F-35 weapon bay. (Image source: Google Images®)

2.2 SCOPE OF THE WORK

The major part of the research done so far has concentrated upon simple geometries to establish the influence of geometrical and flight parameters. However, when such experimental results are extrapolated to the design of weapon bays installed in real combat aircraft, which seldom can be represented as rectangular nor surrounded by a simple environment, additional problems may arise.

Limited work has been published in the open literature regarding studies on complete airframes, such as Clark (1979) with the F-111 fighter-bomber and Tripton (1980) with the B1-B bomber. More recently 5th generation aircraft have been analysed by Kannepalli, et al. (2011) (F-35A fighter-bomber), and Morton, et al. (2012) (F-22 fighter). Additional studies such as Lawson & Barakos (2010), Chaplin & Birch (2012), and Hallissy & Hariharan (2014), oriented towards the analysis of a UCAV platform with a weapons bay installed, a likely logical development with the future increased use of such aircraft in air warfare. This new approach, however, has generated a new set of problems because real aircraft will not have cavity geometries that will be of a simple rectangular shape. In some cases, it is even difficult to calculate parameters like length to depth ratio due to the irregular shape of the volume. Moreover, other factors, such as the presence of the store

contained within, and other geometry details, may influence flow behaviour. This is especially true when radar cross section (RCS) reduction guidelines are incorporated into the design, which often result in indentations being made to the bay's leading and trailing edge, altering the shear layer responsible for the acoustic phenomena. Additionally, during the store release, other factors must be considered. Primarily, a normal weapon employment routine encompasses a quick opening of the bay, the ejection of the missile/bomb, and the closure of the cavity. Such a process is typically completed as quickly as possible, in just a few seconds, and dynamic effects must be considered too. Secondly, the airframe, during the store launch may be manoeuvring, and may assume incidence and sideslip angles completely different to those existing during steady level flight. All such factors, which, in the open literature, have been rarely analysed, may influence the flow response to change completely the aero-acoustic characteristics of the weapon bay.

The scope of this work was then to explore some problematics present in the design of modern weapon bays, such the effects of introducing a store inside the cavity, or chevrons for RCS reduction at bay's leading and trailing edges, with the latter tested both in an isolated cavity, surrounded by a flat plate, and in an "installed" cavity, where the bay was placed in a combat airframe. This also determined the decision to analyse cavity's aero-acoustic properties of the combination airframe/cavity at different airframe's angle of attack, being an effect, whilst never explored in open literature, important when considering the envelope in which a weapon bay usually operates.

3 METHODOLOGY

The experiments can be divided in two main groups, which are CFD numerical simulation and wind tunnel testing. While CFD is capable of analysing virtually every kind of geometrical/environmental combinations, wind tunnel analysis is confined to the utilisation of scaled models in only a limited number of boundary settings. Nevertheless, the wind tunnel recreates the real flow features while CFD models it, especially the most critical part, the turbulence phenomenon. Hence, CFD is subjected to errors in the reproduction of the flow characteristics that gives an uncertainty in the results obtained.

This study aimed to test the effects of geometry features on cavities generated when the bay is intended to be installed on stealth aircraft (chevrons at the cavity's leading and trailing edges as well as store presence). It was then decided to implement a double approach to these analyses. Wind tunnel campaigns were used as the standard analysis tool, to determine changes in the aero-acoustic field, whenever a new feature was introduced into the weapon bay. Numerical simulations were applied whenever the limits of the transonic wind tunnel were reached, which for this study consisted in the exploration of chevrons and airframe angle of attack variation effects with the cavity installed in a combat airframe. The following chapter will describe the methodologies and the apparatus utilised.

It was not decided to perform simulations at wind tunnel conditions because it was out of the scope of this research. The aim was to measure the changes introduced by geometry modifications of various level of complexity and not to make a comparison experimental and numerical data. So CFD was used as a tool to analyse configurations beyond wind tunnel capabilities.

3.1 WIND TUNNEL EXPERIMENTS

Experiments were performed in the closed circuit, ejector-driven, transonic wind tunnel, located at the Defence Academy of the UK, Shrivenham (Figure 3.1). The tunnel has a working section 500 mm long, 206 mm high and 228 mm wide (Figure 3.2). The air supply is provided by a Compair© L110-10 compressor, dried and stored in a 34 m^3 reservoir. With a maximum pressure of 6.89 bar, is possible to operate the tunnel for about 8 seconds, at a working section Mach number of 0.86. The wind tunnel Mach number is controlled, via a feedback mechanism, with a flap located at the air inlet main control valve.

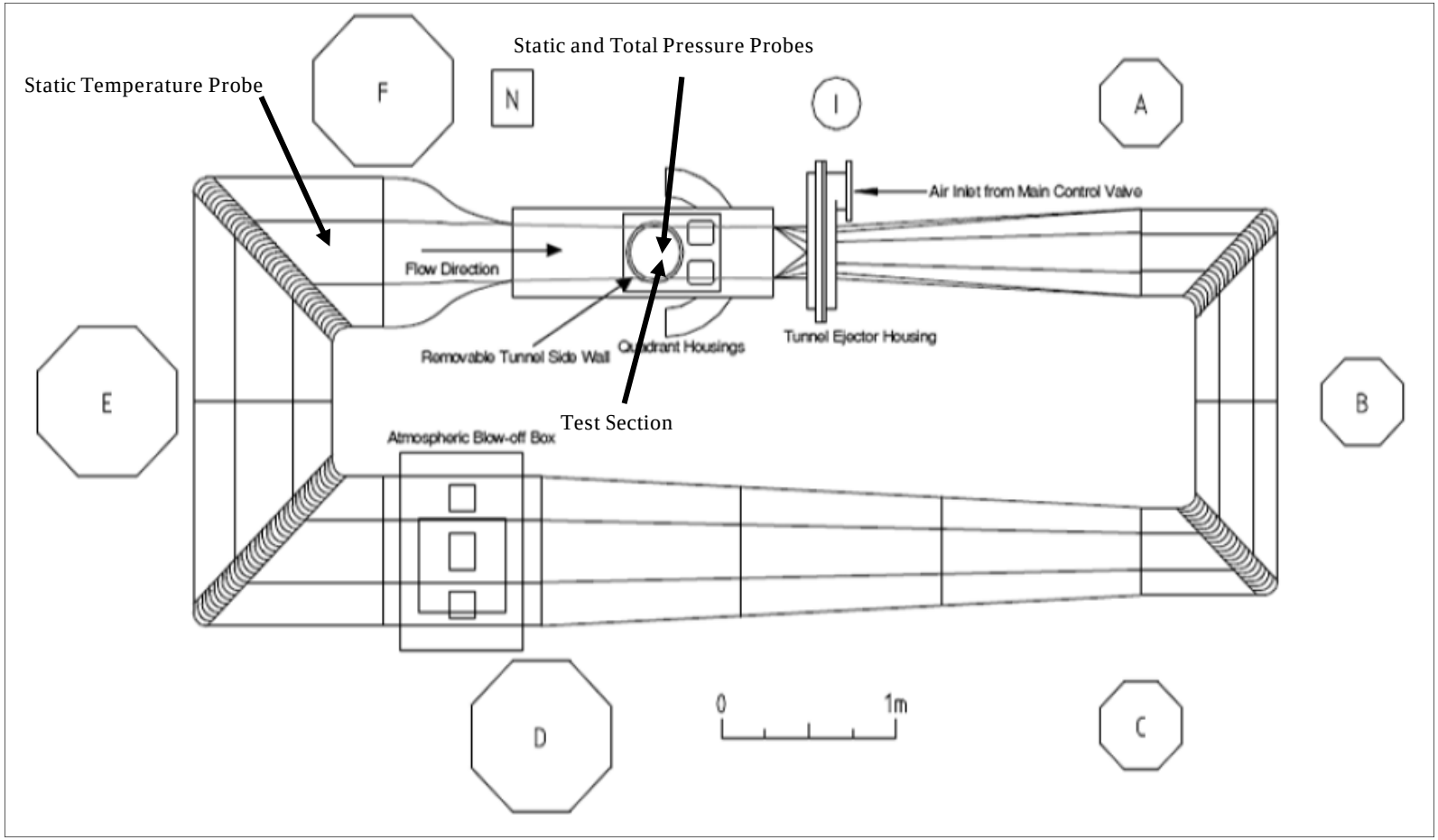

Figure 3.1. Shrivenham transonic wind tunnel schematics. *Free-stream quantities probes indicated by arrows.*

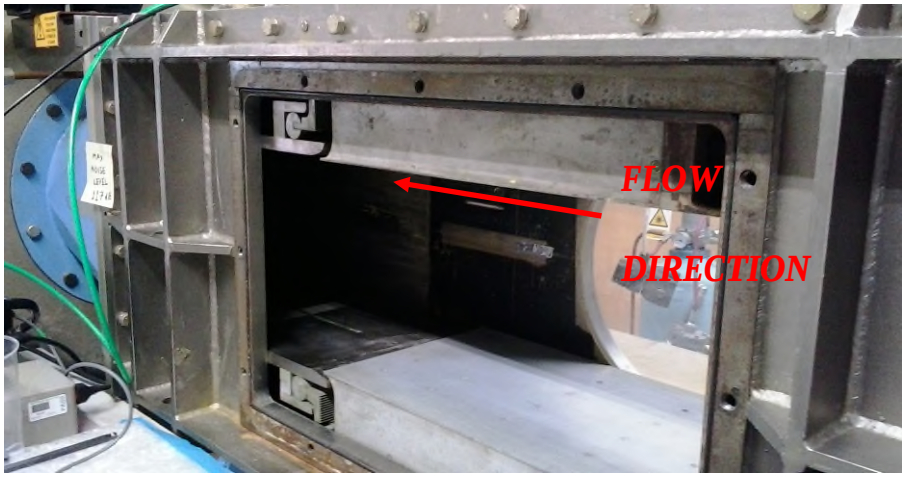

Figure 3.2 - Wind tunnel test section with side door removed.

Although all these Mach numbers are theoretically obtainable, when the cavity was installed the maximum Mach number attainable was 0.81 due to an unstart problem caused by reflected sound waves and the blockage factor. At this regime, the Reynolds number per unit length was equal to 13.9e+6 (see Table 3.3 for the freestream atmosphere values attained in this study).

3.1.1 TEST RIG

The cavity was obtained from a rectangular cut-out on a side of the wind tunnel test section, flush with the wall.

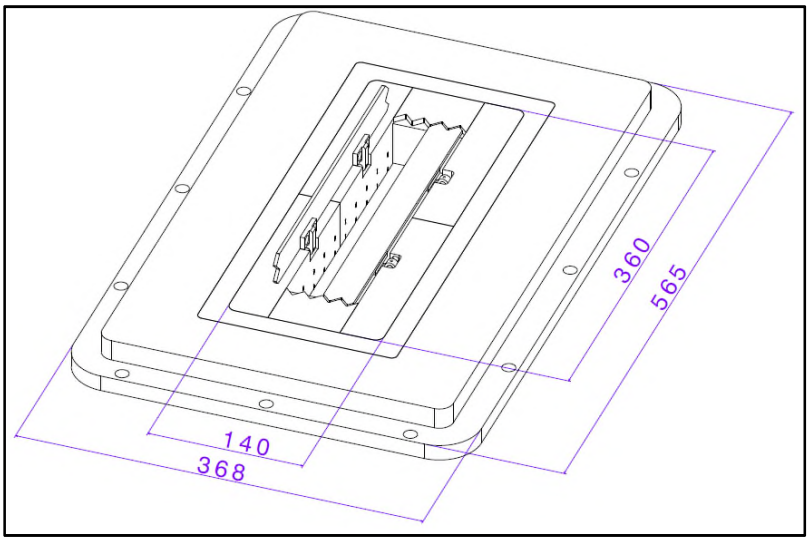

Figure 3.3 - Rig global layout with cavity and doors installed. *The cavity is depicted with one door open and one door closed. Dimensions are in millimetres.*

Such an arrangement, while imposing a fixed and non-variable boundary layer thickness at the bay leading edge, offered better performance regarding mass flow blockage issues and structural vibrations than a sting-mounted geometry. The overall rig assembly (Figure 3.3) was connected to the sidewall of the wind tunnel test section via a bolted connector. All the components of the assembly had a groove, on the leeward side, which housed a rubber seal in order to make the structure leak proof. The structure was built in aluminium alloy to reduce the weight to a minimum.

3.1.2 GEOMETRY DESCRIPTION

The cavity model used was based on the well-known Boeing M219-type, which is a rectangular cavity with a length-to-depth ratio of 5 and width-to-depth ratio of 1, and has been extensively used as a standard bench test for analyses on transonic cavity flows (see for example Lawson & Barakos (2011), Lawson & Barakos (2009), and Chaplin & Birch (2012)).

To make such a geometry capable to house a 500 lb class store[3] it was necessary to stretch the cavity in the transverse and longitudinal dimensions. A variant of the standard M219 cavity geometry called M219-Mod000 (see Figure 3.5), whose details are summarised in Table 3.1, was then introduced. The derived cavity, compared to the M219 model, was slightly longer and wider.

Table 3.1 – M219-Mod000 cavity geometry parameters.

DATA	VALUE
Cavity Length (L) [mm]	262.0
Cavity Depth (D) [mm]	46.0
Cavity Width (W) [mm]	65.0
Cavity W/D Ratio	1.41
Cavity L/D Ratio	5.69

The cavity assembly (Figure 3.4) was composed of six wall-blocks (four that constituted the sides of the bay and two that formed the front and rear walls) and a baseplate.

All the components were assembled with detachable bolts to make it possible to test different geometries. The leading and trailing edge blocks where constructed separately to

[3] Such cavity was specifically designed to accommodate a GBU-39 JDAM bomb.

the sidewalls to enable the possibility to test different transverse edge geometries without having to disassemble the whole cavity block.

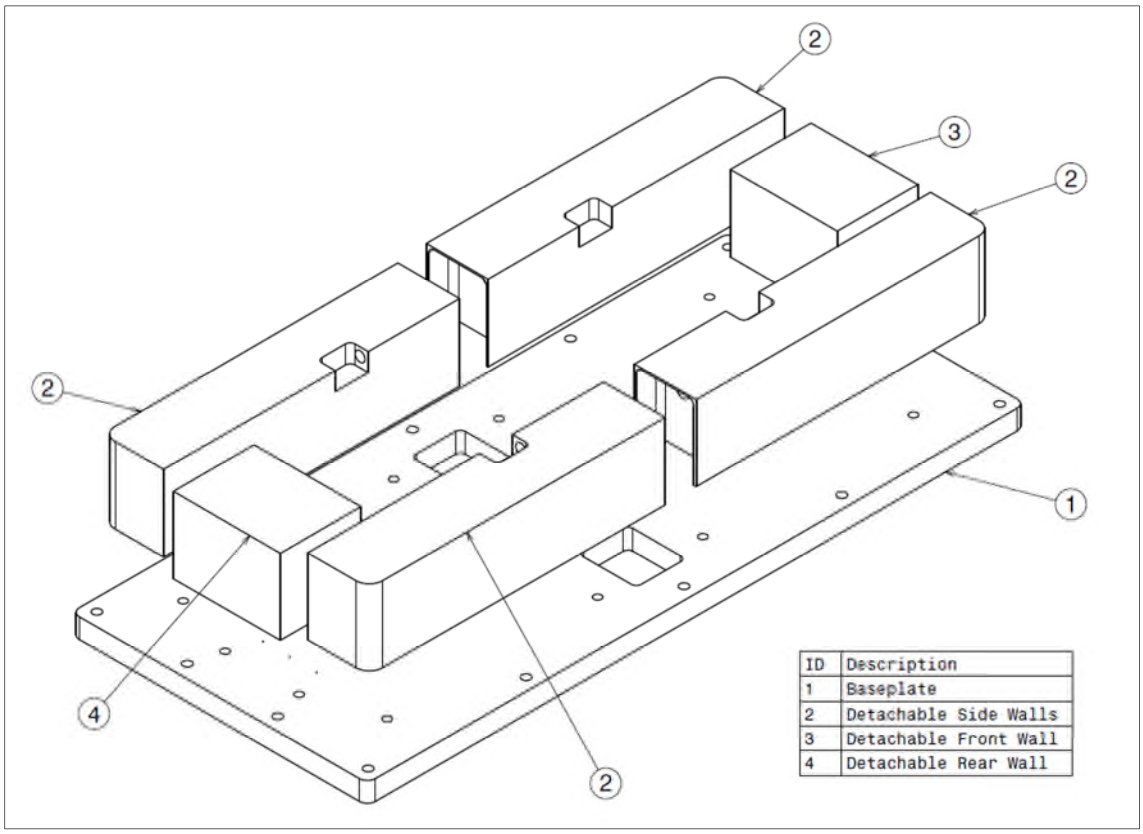

Figure 3.4 - Cavity assembly.

Table 3.2 - Rakes coordinate for wind tunnel experiments.

Name	***x*[mm]**	***y*[mm]**	***z*[mm]**	***x/L***	***2y/W***	***z/D***
Bay Origin	0.0	0.0	0.0	0.0	0.0	0.0
Rake 1L	26.20 52.40 78.60	-32.5	46.00	0.1 0.2 0.3	-0.5	1.0
Rake 1C	104.80 131.00 157.20	0.00		0.4 0.5 0.6	0.0	
Rake 1R	183.40 209.60 235.80	32.5		0.7 0.8 0.9	0.5	

The bay origin was placed in the cavity leading edge at the symmetry plane. The *x*-axis was then oriented towards the flow direction. The *z*-axis was positive towards the cavity floor, and the *y*-axis completed the reference frame to make it right handed (see Figure 3.5).

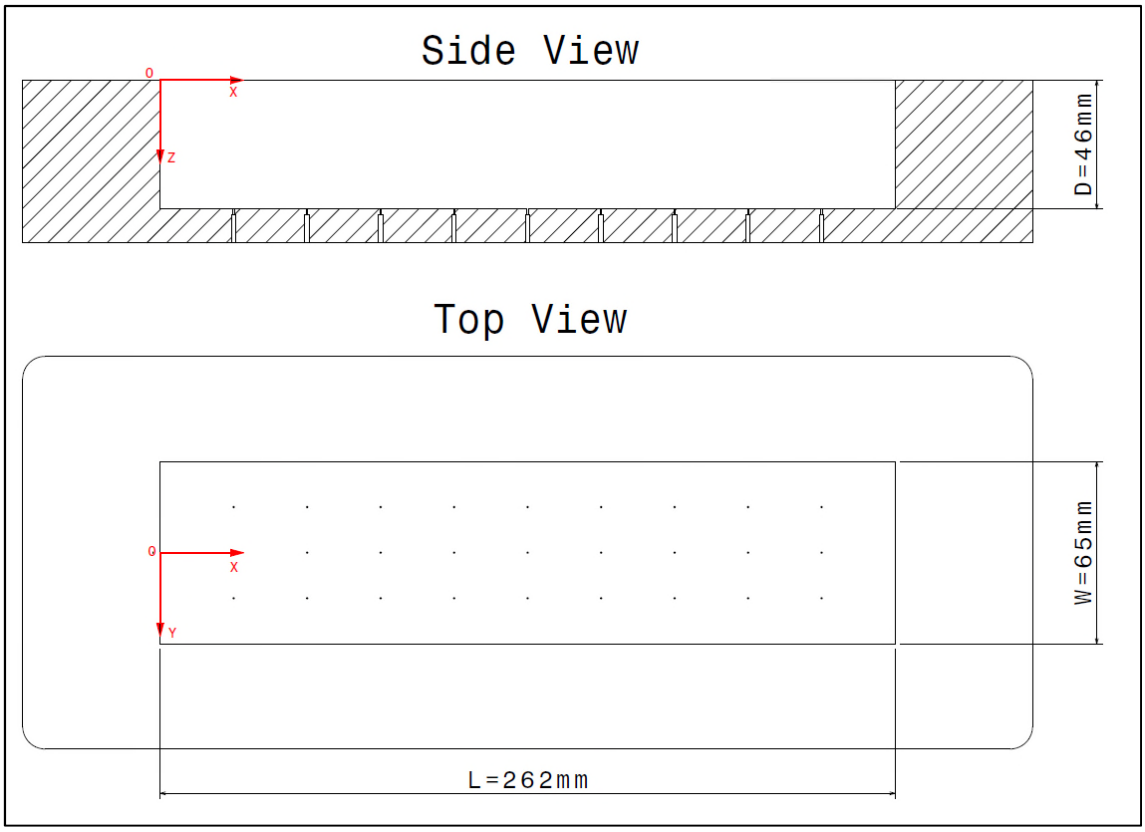

Figure 3.5 - Cavity scheme.

The cavity, apart from the leading and trailing edge geometries, was equipped with further details to increase the realism of the model. At each sidewall a door was installed, which either could be held fixed or made to move during the experiments. This capability was obtained by a simple rotation along an axis that did, however, require the presence of a small gap between the door and the surface surrounding the cavity. Inside the bay it was possible to mount a store. Finally, the cavity was able to accommodate collars, spanning the full depth and width of the bay. The adoption of the collars was developed as an innovative solution to overcome the adverse effects of transonic cavities. This approach had potential advantages over methods that involve external spoilers, deflectors, or blowing in that no actuation is required. Moreover, this configuration could reveal to be superior regarding the impact on airframe drag since, unlike spoilers, the collars do not extend in to the undisturbed flow.

LEADING AND TRAILING EDGE GEOMETRIES

Three leading and trailing edge geometries were developed and tested in this study (Figure 3.6). The reference configuration called type “A” (or Mod000) had the standard straight edge, usually utilised in cavity flow. While this was the basic shape used to derive

the main effects whenever a new detail was added, it suffered from the fact that with this configuration the doors could not be closed. From this geometry two additional models were developed. The first one, referred to as type “B” (or Mod001), incorporated the installation of a 45 degree saw-tooth pattern and a step, whose height was set equal to 5 mm to enable the closure of the doors. The second derived geometry, called type “C” (or Mod002) was directly derived from type “B”, but in this case the entire front and rear wall of the cavity was saw-toothed. This geometry could also accommodate the doors in a closed position.

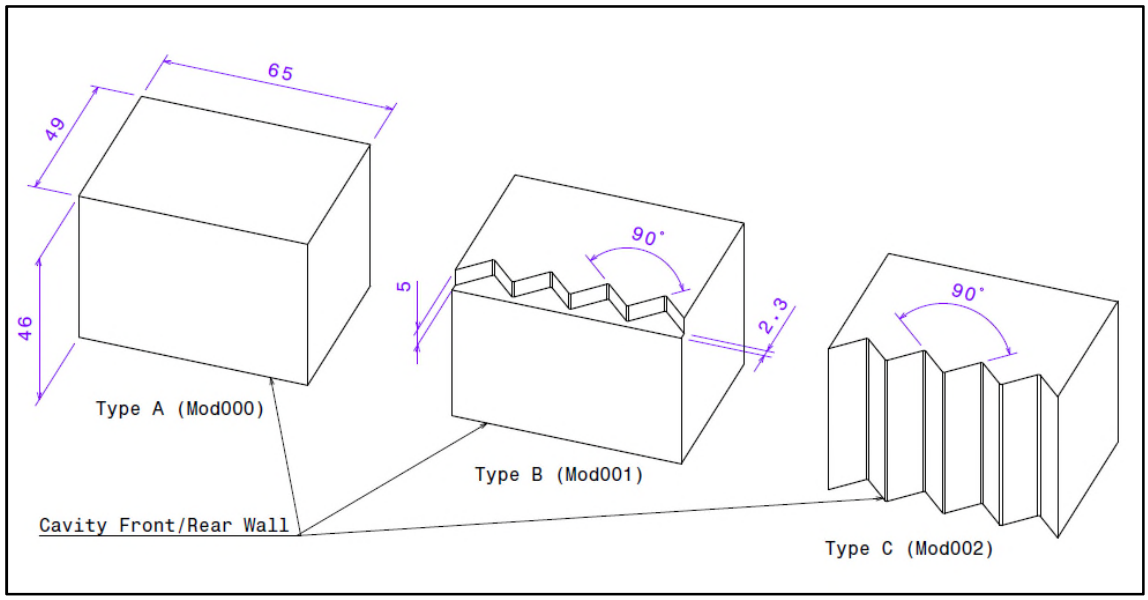

Figure 3.6 - Leading and trailing edge typologies used for wind tunnel experiments.

Dimensions in millimetres. See also APPENDIX A. for additional details of chevrons dimensioning.

Type “B” and “C” geometries were developed considering typical RCS reduction features installed on stealth aircraft weapons bays, and their analysis was directed to understand what effects such details may introduce on the aero-acoustics of the reference cavity model.

CAVITY DOORS

The cavity model comprised two controllable bay doors with 45 degree saw-toothed leading and trailing edges (see Figure 3.3). The aperture of the doors could vary between 0 degrees (doors closed) to 120 degrees (doors opened).

STORE AND COLLARS

To further represent a typical combat aircraft's cavity geometry, it was possible to install, inside the cavity, a simplified model of a GBU-39 JDAM (without fins), fixed to the rear wall with a sting (see Figure 3.7).

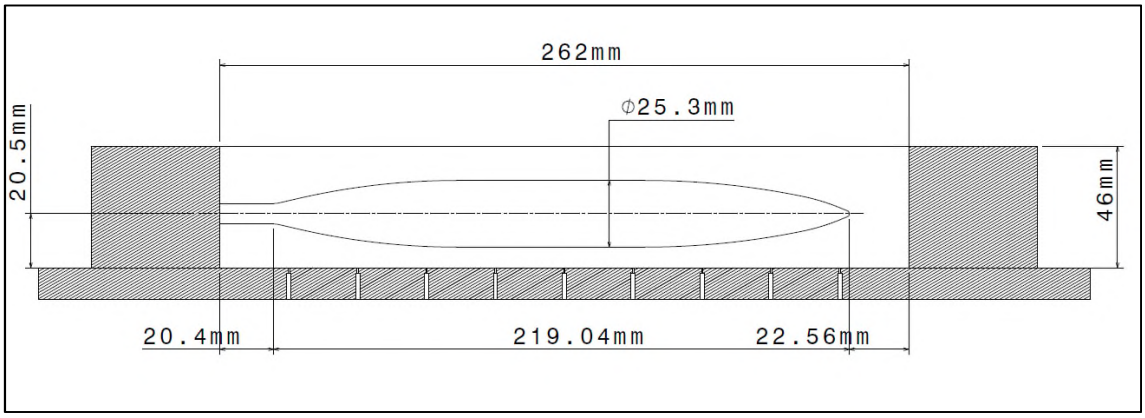

Figure 3.7 - Scheme of store installation inside cavity. *The store longitudinal axis coincides with cavity x-z plane of symmetry.*

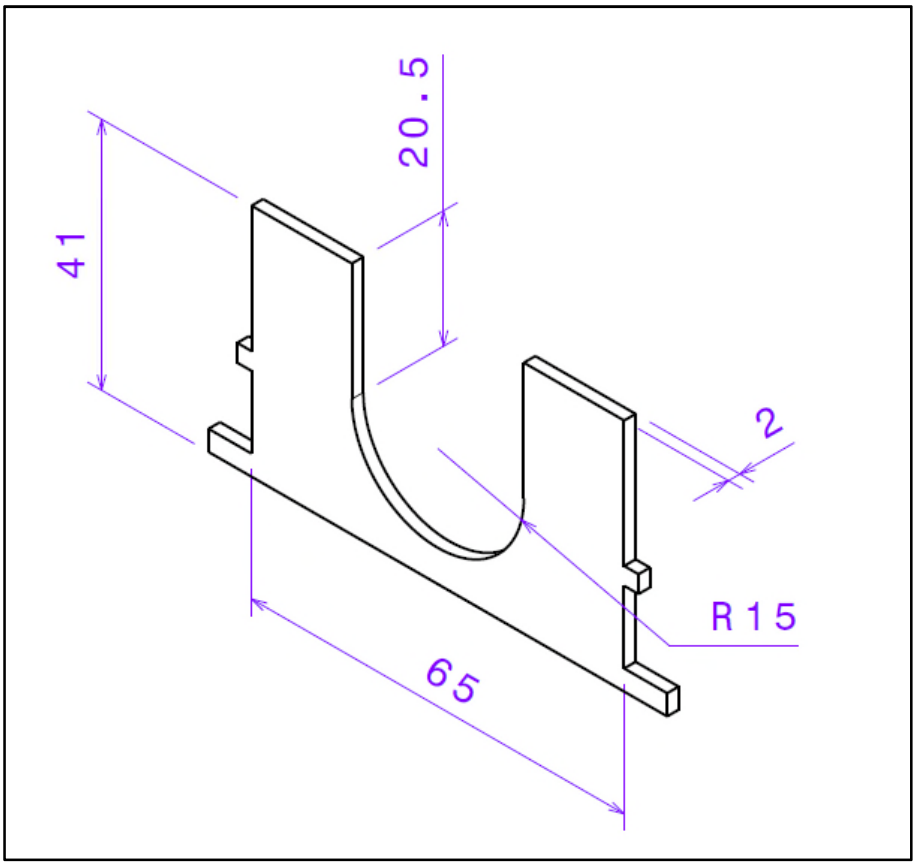

Figure 3.8 - Collar model used for wind tunnel experiments. *Dimensions are in millimetres.*

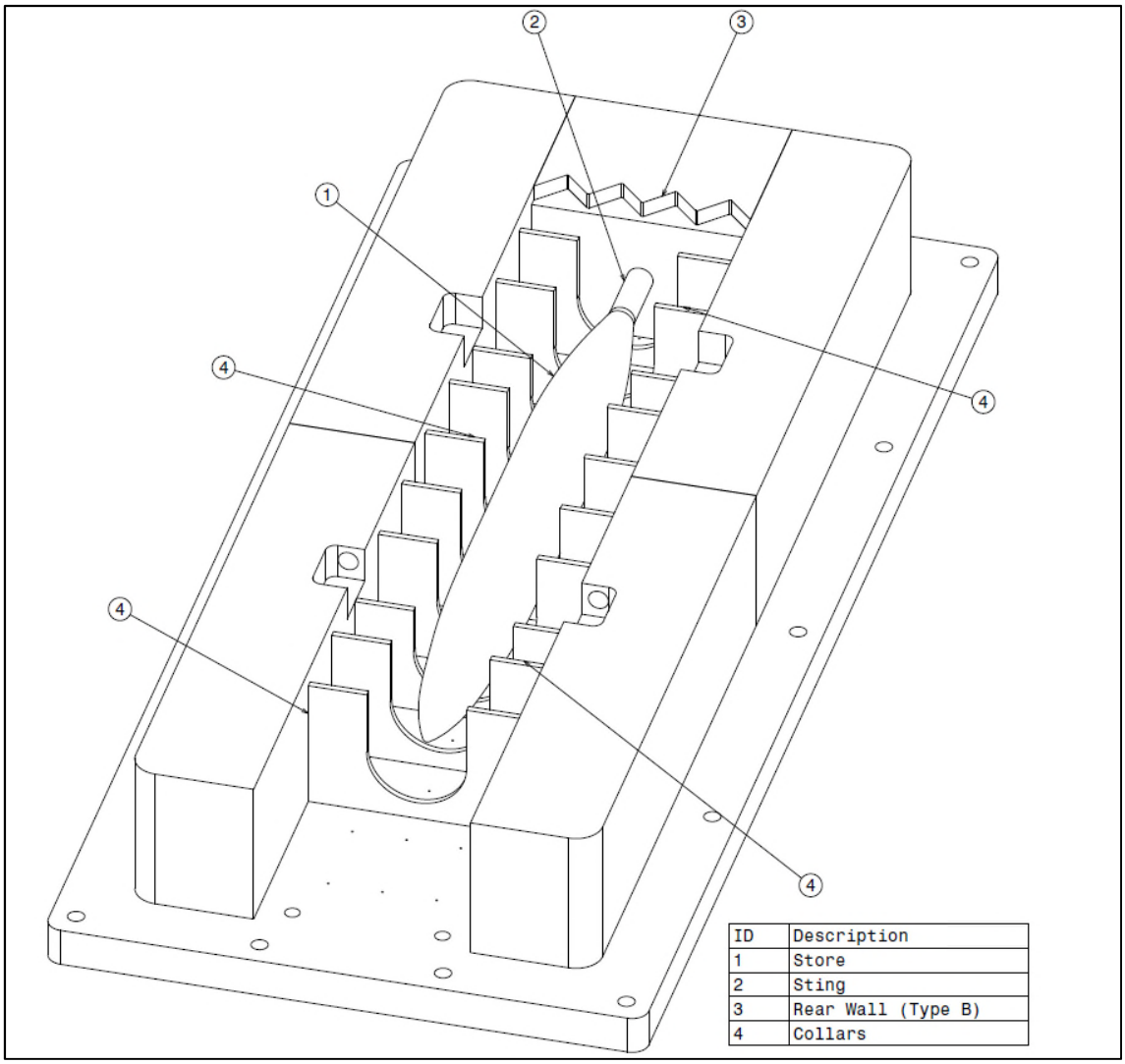

Figure 3.9 - Collars and store installation inside the cavity. *Front transverse wall block removed for ease of visualisation.*

Inside the cavity, it was also possible to install transverse collars (Figure 3.8). Such a geometry feature was developed as a passive flow control technique. Its origin lies in previous work, where, attempts to isolate the effects of a structural rib on cavity flow (Knowles, et al. (2015, 30-31 of March & 1 of April)), showed that a such a structure, if properly sized and located, could have beneficial effects on the levels of unsteadiness in the flow.

Collars of height equal to the full depth of the cavity and a cut-out to accommodate the store model were produced. They could be placed at positions corresponding to 5%, 15%, 25%, 35%, 45%, 55%, 65%, 75%, 85%, and 95% of cavity length (Figure 3.9). The

positions were chosen not to interfere with the location of pressure tappings. Finally, collars had tabs on each side, which were located in slots in the cavity sidewalls.

3.1.3 ENVIRONMENTAL SET-UP

The typical flow conditions for this study are summarised in Table 3.3. Here, Δ_{Dev} and σ_{Dev} indicate respectively the absolute maximum and the root-mean-square deviations from the reference value encountered in all the runs executed. The maximum deviation was 2% (though usually much less), while the repeatability of the results (i.e. the maximum deviation between any given pair of runs performed) was below 1%, for pressure coefficient and OASPL, and less than 2% for the frequency spectra.

Table 3.3 - Typical run condition.

QUANTITY	VALUE	Δ_{Dev}	σ_{Dev}	UNITS
M_∞	0.81	0.011	0.007	-
q_∞	32.0	0.517	0.300	kPa
p_0	102.8	0.746	0.529	kPa
p_∞	65.7	1.208	0.655	kPa
T_∞	258.7	3.020	2.000	K

The Reynolds number based on cavity length was equal to 4.07e+06. Finally, the incoming boundary layer to the cavity was fully turbulent with a thickness of 8.8 millimetres (Thangamani, et al. (2013)).

3.1.4 INSTRUMENTATION

The analogue pressure signals where collected by a ZOC22B (Scanivalve®) electronic pressure scanning module, capable of accepting 32 individual pressure sensors. The module maximum certified scan rate is 20 kHz well within experiment requirements. Total and static pressure was measured using a Furness Controls© FCO14 micro manometer while a K-type thermocouple was used for the measurement of the freestream temperature (see Figure 3.1 for ambient probes position in the wind tunnel). Only one port per run could be monitored. Data was sampled at 20 kHz for a total sample duration of 6.5536 seconds, or 131072 samples. Data was also filtered, during the acquisition phase, to remove aliasing effects, with a Bessel-type filter of 2nd order, with a cut-off frequency of 10 kHz, a passband ripple of ±1.5 dB at the cut frequency, and an attenuation slope of 40 dB per frequency decade.

Due to space constrains, the pressure transducers had to be connected to the pressure tappings via vinyl tubing. Such a configuration is prone to distortion in the measured

signals, since the vinyl tube has a frequency response correlated to its length and diameter. To overcome the problem a correction curve was generated measuring the distortion in the phase and amplitude introduced by the tubing. Using a sinusoidal sound generator connected to an amplifier, constant frequency and amplitude waves were generated by a speaker in a truncated-cone-shaped cavity. At the top of this cone were two ports, one that brought the pressure signal to the ZOC block utilising a vinyl tube of the same length of the ones used in the experiments; the other port was directly connected to a Kulite® MIC-190M-LT microphone.

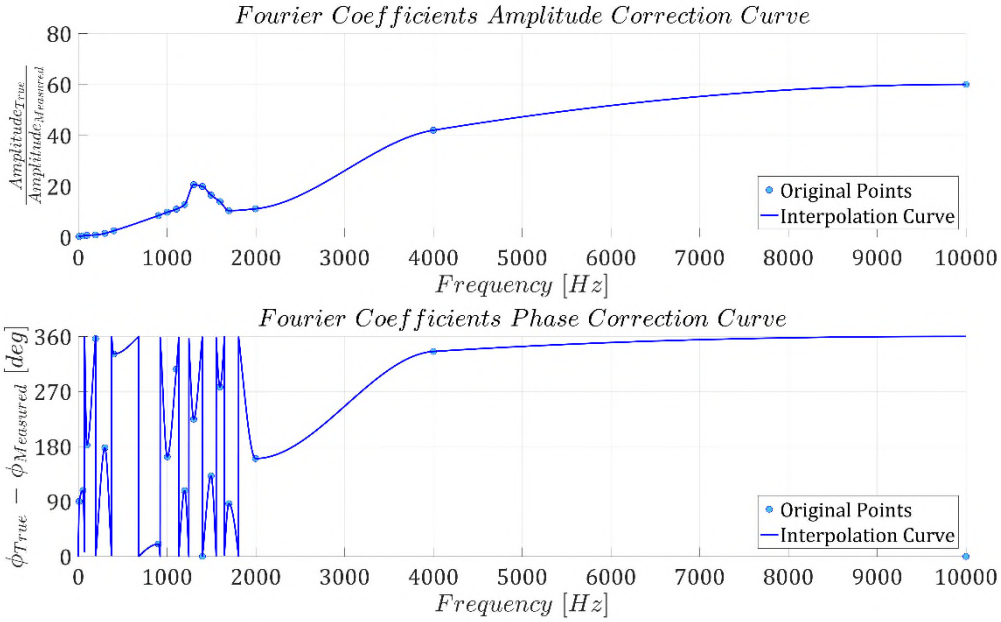

Figure 3.10 - Amplitude and phase correction curves trend with frequency.

The two signals were then FFT processed, and the phase and amplitude response compared. By varying the frequency of the wave generated it was possible to derive the frequency and phase distortion of the true signal introduced by the tubing and hence to obtain the correction curves., which were calculated, at each frequency tested, as amplitude ratio between distorted and true signal, and phase difference between distorted and true signal (see Figure 3.10). The final curves were obtained interpolating the results obtained at the test points.

Once these curves were known, it was possible to correct signals, recorded during wind tunnel experiments, in a post-processing phase. A typical pressure signal was FFT processed and its module and phase for each frequency bin was obtained. Subsequently amplitude and phase correction curves where applied for each frequency bin. Finally the

inverse FFT of the corrected coefficients resulted in the original signal corrected for the vinyl tubes distortion effects. An example of the correction effects is show Figure 3.11, where the SPL of a pressure signal corrected and non-corrected are compared.

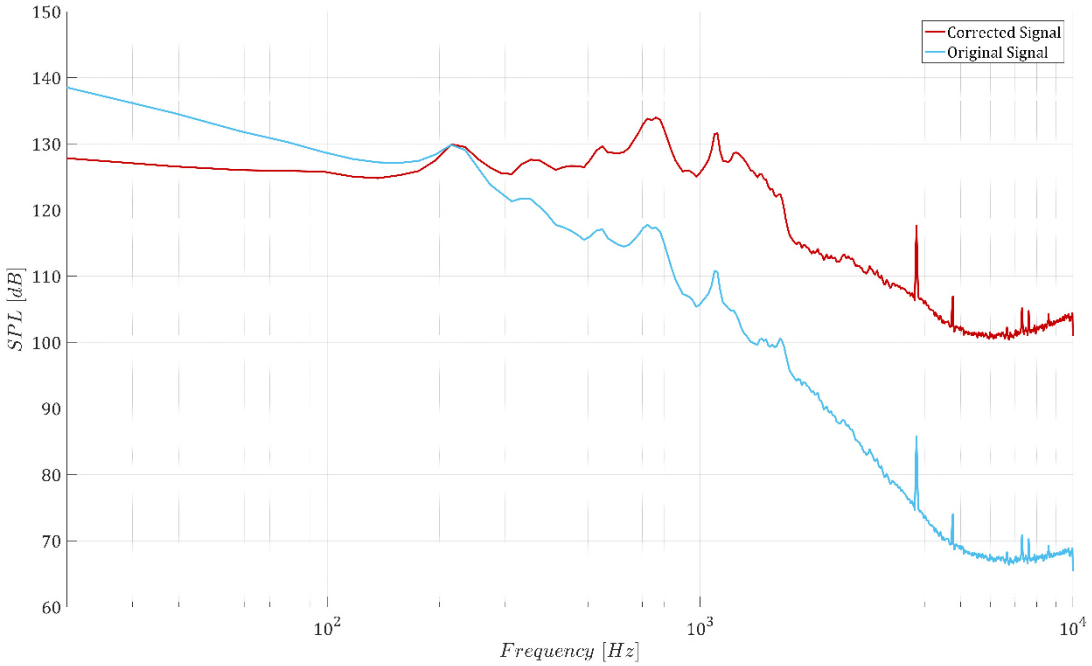

Figure 3.11 - Correction curve effects on SPL of a general pressure signal.

It is possible to see that vinyl tubes' distortion effects, which consisted in the attenuation of the signal power, were particularly strong at high frequencies (> 4000 Hz), where differences in excess of 30 dB were observed between the original and the corrected signal's spectrum. Distortion effects were lower at lower frequencies (>200 Hz, <4000 Hz), where, nevertheless the difference between the two spectra was around 10 dB. Finally, at extremely low frequencies (<200 Hz), the trend was reversed, with the tubes introducing an amplification of the pressure signal usually in the order of 2 dB at 100 Hz, and 10 dB at 20 Hz.

3.1.5 TEST CASE MATRIX

The versatility of the wind tunnel enabled the testing of more configurations with respect to the CFD simulations, and 24 different experiments were performed (see Table 3.4). Runs from 1 to 6 were devoted to analysing the different effects of leading and trailing

edge geometries (AA, BB, and CC) and the door opening angle (90 and 120 degrees[4]). Subsequently the effect of store presence was studied (runs from 7 to 12, see Figure 3.7 for installation details). While the cavity AA-type with 90 degree door opening angle was considered the reference configuration, 12 wind tunnel runs were performed to determine which derived geometry, BB or CC, had the better performance.

The subsequent 12 runs were dedicated to the analysis of collar effects with and without the store installed in the cavity.

In a previous study, Knowles, et al. (2017, 27-28-29 of March) demonstrated that installing 5 straight collars, at 25%, 33%, 50%, 67%, and 75% of cavity length considerably improved the aero-acoustic performance of the bay, suppressing all tones and reducing the OASPL levels by 10 dB. Following these results, it was decided to test all three types of cavity geometry with collars installed at all locations, naming this arrangement “Version 0”. Runs from 13 to 18 were devoted to explore the effects of these new arrangements in the flow. It was decided to analyse just one door-opening angle (90 degrees), since the previous campaign (runs from 1 to 12) indicated that such an opening angle was superior, in performance, with respect to the 120 degree case.

Once the properties of the cavity geometries with all collars installed was defined, a final campaign was launched to find a configuration with fewer collars but with similar performance to Version 0 (runs from 19 to 24). Three new collar arrangements were then developed and tested: Version 1 (collars at 15%, 35%, 55%, 75%, and 95% of cavity length), Version 2 (collars at 5%, 25%, 45%, 65%, and 85% of cavity length), and Version 3 (collars at 5%, 15%, 45%, 55%, 85%, and 95% of cavity length). The technical scheme of the cavity in all 4 collar layouts are summarised in Figure 3.12. All these versions were tested with the cavity type AA both with and without store installed.

[4] These two values were considered representative of typical weapons bay employment in current stealth aircraft.

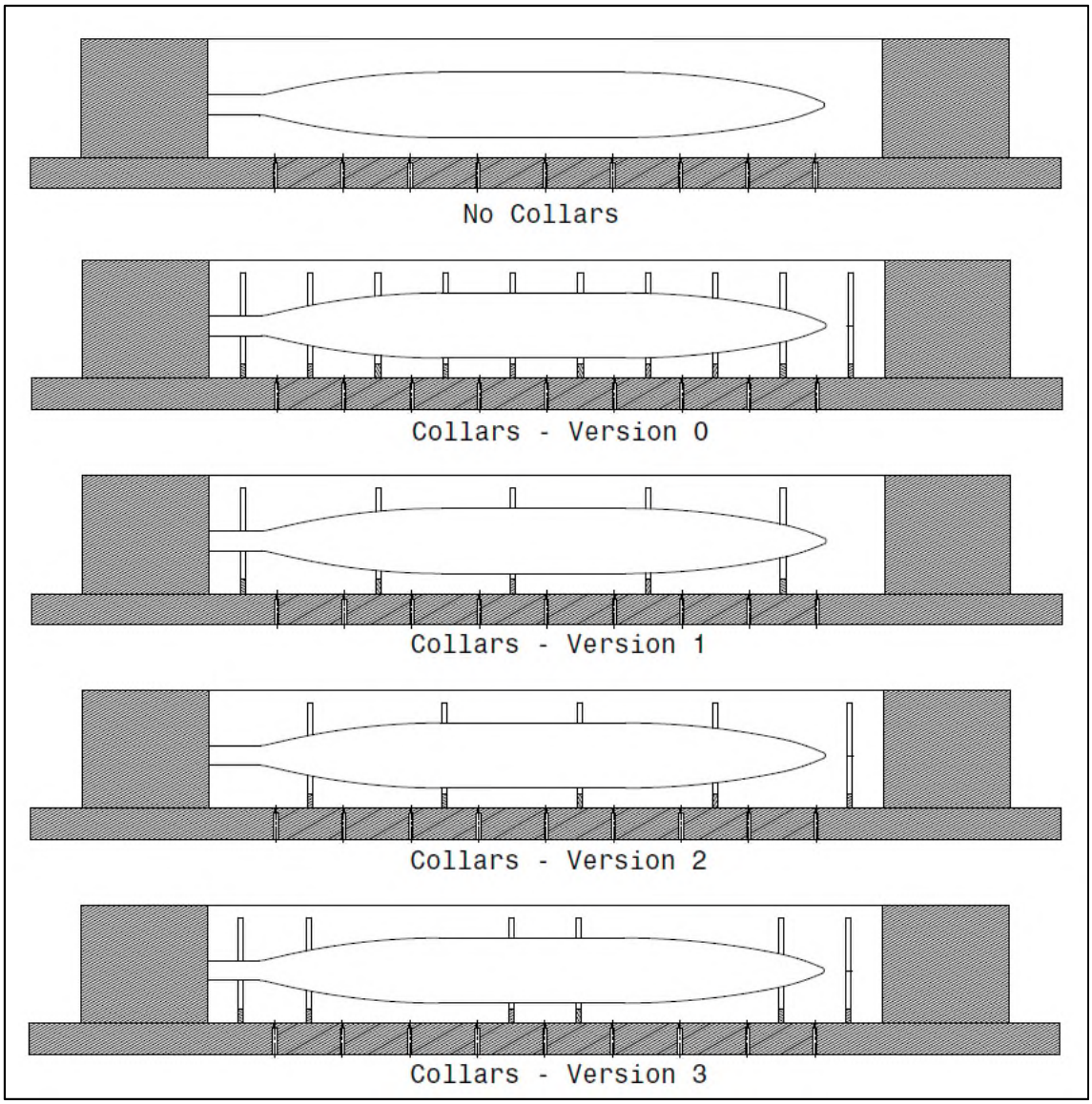

Figure 3.12 - Cavity scheme with store and collar versions installation details.

Table 3.4 - Wind tunnel experiments test matrix.

ID	CAVITY[5]	COLLAR POSITION[6]										STORE	DOORS ANGLE [deg][7]
		5%	15%	25%	35%	45%	55%	65%	75%	85%	95%		
1	AA												90
2	BB												90
3	CC												90
4	AA												120
5	BB												120
6	CC												120
7	AA											✓	90
8	BB											✓	90
9	CC											✓	90
10	AA											✓	120
11	BB											✓	120
12	CC											✓	120
13	AA	✓	✓	✓	✓	✓	✓	✓	✓	✓	✓	✓	90
14	AA	✓	✓	✓	✓	✓	✓	✓	✓	✓	✓		90
15	BB	✓	✓	✓	✓	✓	✓	✓	✓	✓	✓	✓	90
16	BB	✓	✓	✓	✓	✓	✓	✓	✓	✓	✓		90
17	CC	✓	✓	✓	✓	✓	✓	✓	✓	✓	✓	✓	90

[5] Leading and trailing edge topology of the cavity. See paragraph 3.1 for an accurate description. The double letter code indicates the topology of the leading and trailing edge of the cavity. A is the straight one, B is the indented edge with step and C is the full saw-toothed wall. Hence, for example, the configuration cavity AA is a configuration with straight leading and trailing edges.
[6] Presence of the collar at the indicated station, expressed in percent of cavity length.
[7] Door opening angle.

ID	CAVITY	COLLARS POSITION										STORE	DOORS ANGLE [deg]
		5%	15%	25%	35%	45%	55%	65%	75%	85%	95%		
18	CC	✓	✓	✓	✓	✓	✓	✓	✓	✓	✓		90
19	AA		✓		✓		✓		✓		✓	✓	90
20	AA		✓		✓		✓		✓		✓		90
21	AA	✓		✓		✓		✓		✓		✓	90
22	AA	✓		✓		✓		✓		✓			90
23	AA	✓	✓			✓	✓			✓	✓	✓	90
24	AA	✓	✓			✓	✓			✓	✓		90

3.2 CFD

The greater part of data resulting from cavity flow research has been produced from wind tunnel testing. More recently with the advent of high performance computers and new turbulence models, the computational contribution to the research on cavity flows has risen continuously. Apart from the capability to analyse any kind of configuration in any kind of environment, CFD offers other advantages with respect to wind tunnel testing. One of the main problem that afflicts wind tunnel measurements is that unsteady data gained from transducers have high temporal resolution, but low spatial resolution. On the other hand, more recent and expensive methods, such as particle image velocimetry or laser Doppler anemometry, tend to have high spatial resolution but low temporal resolution. The advantage of CFD is that it has the capability to deliver high levels of both spatial and temporal resolution.

Previous studies on cavity flows have shown good results using the DES[8] (Detached Eddy Simulation) turbulence modelling strategy (see for example Lawson & Barakos (2011)). This model, and its derivatives, has been found suitable for the engineering resolution of this kind of unsteady flow as shown by Menter (2012). Hence, it was decided to use the DES turbulence model in all CFD simulation of this work.

All the simulations were performed using the commercial software ANSYS FLUENT©15.0 as the solver and ANSYS ICEM©15.0 as the mesh builder.

3.2.1 GEOMETRY DESCRIPTION

The Boeing/AFRL 1303 model, used in this work, is a generic UCAV with a blended wing body (BWB) layout, an overall length of 10 m, and an overall span of 16.5 m. The w-shaped planform has a leading edge sweep of 47 degrees. The airframe is completed by the installation of two Boeing/M219 type weapon bays. The global layout is depicted in Figure 3.13. The aircraft is a transonic bomber drone for the air-to-ground mission, capable of delivering two standard class 500 lbs bombs on target. Instead of mounting a single weapon bay in the belly, it is configured with two separate bays on opposite sides. Since this UCAV model has been specifically designed for CFD and wind tunnel testing, air intakes and engine exhausts have been removed from the geometry in order to make it simpler. The M219 weapon bay is a rectangular cavity with length-to-depth ratio of 5 and

[8] The DES turbulence model was first introduced by Spalart, et al. (1997).

width-to-depth ratio of 1 and has been extensively used as a standard benchmark test for analyses on transonic cavity flows. Nevertheless, its installation in the airframe of the UCAV1303 requires some geometry modifications. The belly of the aircraft is not flat but has a mean slope, from centreline towards the wingtip, of 3.6 degrees. Moreover, to accommodate a 500 lb class bomb it has also been necessary to stretch the cavity in the transverse and longitudinal dimensions. In a similar way as previously done in the wind tunnel experiment, a variant of the standard M219 cavity geometry called M219-Mod000, whose details are summarised in Table 3.5, was then introduced.

Figure 3.13 - UCAV1303/M219 configuration.

The derived cavity, compared to the M219 model, is slightly longer and wider. Leading and trailing edges were no longer horizontal but inherited the slope of the airframe belly. Finally, the cavity floor remained unchanged and flat.

Table 3.5 - M219-Mod000 cavity geometry parameters[9].

DATA	VALUE
Cavity Length (L) [mm]	2830.0
Cavity Depth (D) [mm]	500.0
Cavity Width (W) [mm]	700.0
Cavity W/D Ratio	1.4
Cavity L/D Ratio	5.66

[9] These values, compared to the wind tunnel geometry, are correlated by a scale factor of 10.8:1. Such a relationship was taken from the UCAV1303 layout description of Chaplin & Birch (2012).

The bay was accompanied by two doors, with leading and trailing edge profiles double-saw-toothed at an angle of 45 degrees, for RCS reduction requirements. In this study, the doors were held fixed at an open position of 90 degrees with a small gap between the door and the airframe surface. No hinges were included for sake of simplicity. The derived CFD model was further simplified. In fact, in order to reduce the computational cost, the left bay was removed. The reference axis system (right-handed) used, with its origin at the UCAV nose symmetry plane, is positive oriented with the X-axis pointing downstream and the Z-axis pointing upwards (Figure 3.14).

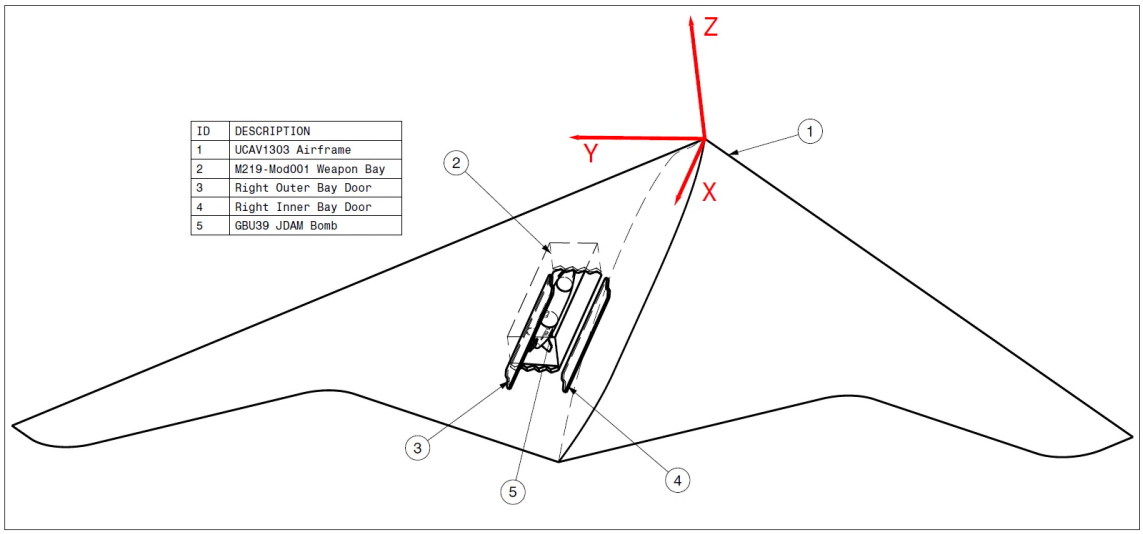

Figure 3.14 - CFD model used in computation.

The far field, used for computation, with the form of an ellipsoid, centred at the origin, had the semi-axis in the X/Y/Z directions respectively of 25*L*, 10*L* and 10*L*. These dimensions were taken from other similar studies (Lawson & Barakos, 2010) hence, having already been proven for their validity, no sensitivity study was conducted.

From the basic geometry (straight cavity edges Figure 3.15a) two additional edge configurations were developed. The first one, referred to as type “B” (or Mod001), incorporated the installation of a saw-tooth pattern and a step (Figure 3.15b). This new feature was developed to permit the accommodation of the bay doors in a closed position. The step height was arbitrary set equal to 55 mm. The second derived geometry, type “C” (or Mod002) was directly derived from type “B”, but in this case the entire front and rear wall of the cavity was saw-toothed (Figure 3.15c).

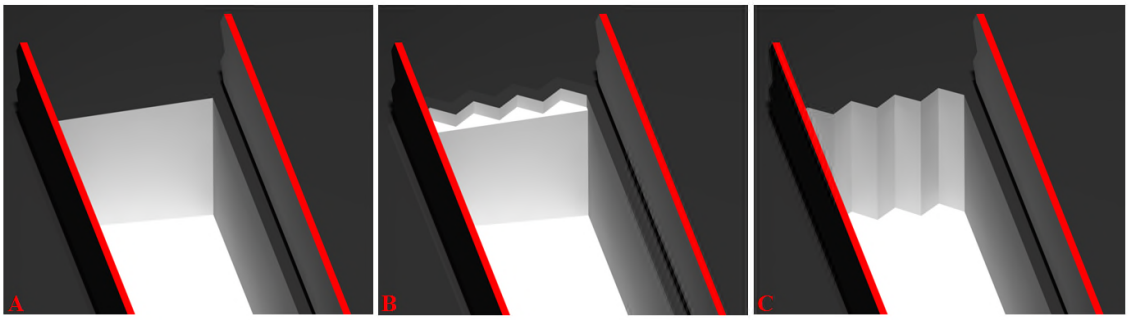

Figure 3.15 - Views of the leading edge of the three different models[10].

In all three cases, the geometry mounted the same bay doors at 90 degrees open. For the sake of simplicity, only the same leading and trailing edge configurations were tested, for three different geometries to be analysed with the CFD simulations.

For post-processing procedures, 54 probes, capable of monitoring pressure and velocity components, were placed in the cavity (see Figure 3.16). They were divided into six longitudinal rakes described in Table 3.6 (Note: x/L equal to 1 indicates the cavity rear face, $2y/W$ equal to 1 indicates the side wall towards the aircraft right wingtip and z/D equal to 1 indicates the cavity floor). Data was sampled at 10 kHz. Subsequently all time-histories were time-moving averaged with a rectangular window of 10 samples and 50% overlap to shield data from any aliasing effect that could have been introduced in the computation.

Table 3.6 - Rakes coordinate for CFD analyses.

NAME	x [mm]	y [mm]	z [mm]	x/L	$2y/W$	z/D
Bay Origin	3450.0	1150.0	-350.0	0.0	+0.0	0.0
Rake 1L	3733.0	800.0	150.0	0.1	-0.5	1.0
Rake 1C	4016.0	1150.0		0.2	+0.0	
Rake 1R	4299.0	1500.0		0.3	+0.5	
Rake 0L	4582.0	800.0	-350.0	0.4	-0.5	0.0
Rake 0C	4865.0	1150.0		0.5	+0.0	
Rake 0R	5148.0	1500.0		0.6	+0.5	
	5431.0			0.7		
	5714.0			0.8		
	5997.0			0.9		

[10] Note: these 3 cavity geometries were all tested in wind tunnels experiments, but installed on a flat plate.

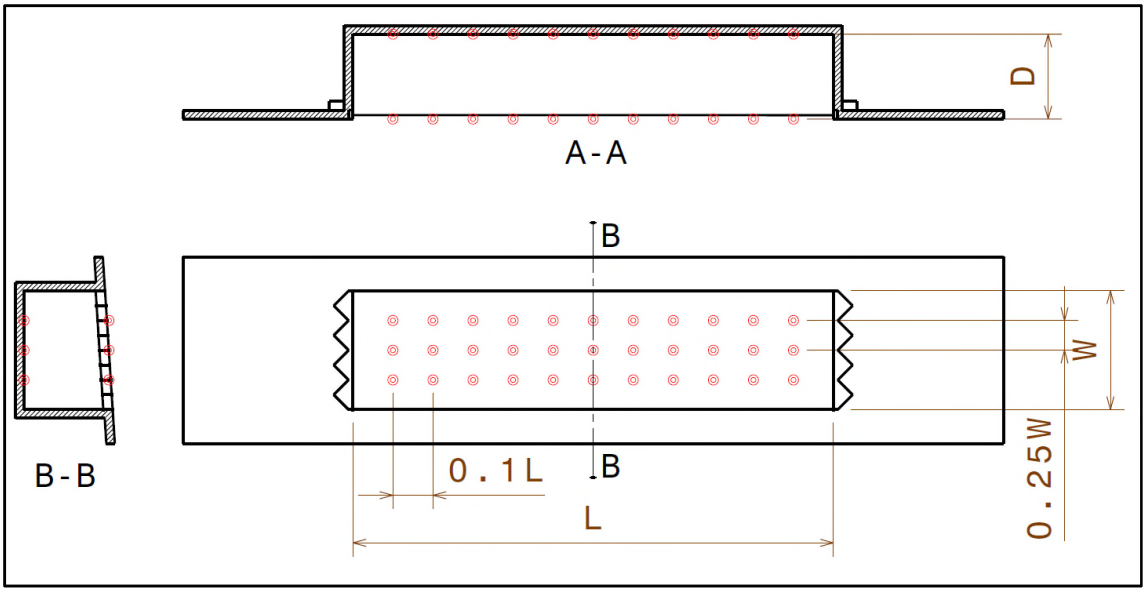

Figure 3.16 - CFD probes position (red dots). *Cavity type BB.*

3.2.2 COMPUTATIONAL METHODS

Detached eddy simulation is a turbulence model that blends RANS (Reynolds Averaged Navier-Stokes) modelling and LES (Large Eddy Simulation) modelling in an automatic way. The boundary, or grey area as defined in Spalart (2001), between the two formulations, in many cases is not well defined and it is strongly dependant on the quality of the mesh. A true grid convergence is never obtained since the finer the grid, the more scales are resolved and the more the simulation approaches the limit of LES. Hence, the decision as to which part of the flow turbulence to resolve and model is left to the user by the fact that DES adapts itself to the mesh given. Regarding the cavity flow problem, the aim is to have DES modelling in the whole shear layer to resolve eddies responsible for the aero-acoustics phenomena. Nevertheless, as shown in Thangamani et al. (2014), it is of paramount importance to correctly estimate the boundary layer status at the leading edge of the bay. Therefore, its history, i.e. the travel length before the bay edge, has to be adequately meshed in order for the RANS model to resolve it. Due to the complex geometry of the problem, it was decided to use an unstructured tetrahedral type mesh, with a prism layer wrapping the viscous surfaces, for accurate boundary layer resolution. The critical area was identified in the shear layer, detaching from the cavity leading edge, and the flow inside the bay. For an accurate shear layer modelling with DES, Menter (2012) suggests a mesh spacing of at least 1/5 of the local layer thickness, 1/20 being the optimal value. In this study, a value of 1/15 was considered a good compromise between computational cost and the quality of the result. Regarding the prism layer, enveloping all

viscous surfaces, Spalart (2001) suggests an expansion ratio of 1.3 starting from a y^+ value of 0.5 (also indicated by Wilcox (2006)), and to interrupt the layer growth when reaching a vertical dimension equal to half the value of the local boundary layer thickness. Viscous surfaces where enveloped with variable-height prims layers, comprising 29 levels. Following these indications a mesh of approximately 24e+6 elements was constructed for each case, of which 10e+6 was inside the cavity.

The simulations were performed choosing flight conditions representing a typical combat situation, i.e. a cruise Mach number of 0.85 and an altitude of 9144 m (30'000 feet) in ISA (International Standard Atmosphere)[11]. All other settings are listed in Table 3.7.

Table 3.7 - CFD simulations reference environmental conditions.

QUANTITY	VALUE	UNITS
H	9144.0	m
M_∞	0.85	$-$
U_∞	257.7	m/s
α	0.0	deg
β	0.0	deg
ρ_∞	0.459	kg/m^3
p_∞	30147	Pa
T_∞	228.77	K
ν_∞	3.241e-05	m^2/s
μ_∞	1.488e-05	kg/ms
a_∞	303.18	m/s
k_∞	90.0	m^2/s^2
Re_∞	2.225e+07	$-$
ω_∞	12.0	$1/s$

As may be observed, for the CFD simulations the Reynolds number, based on cavity length, differed from the one obtained in the wind tunnel experiments (2.225e+07 for the former against 4.7e+06 for the latter). Nevertheless, as stated previously, the aim was not to directly compare experimental and numerical data, hence the difference in Reynolds numbers was not considered determinant for completing the aim of this study. Moreover, due the different geometry surrounding each cavity (a flat plate in the experiments and an

[11] Even if these values were different from the conditions used in the wind tunnel experiments, they were chosen to represent a typical real-life situation in which the aircraft may operate. Also, the aim of this study was not to compare wind tunnel and CFD experiments but to understand the effects of geometry variations, hence the difference between the freestream values was not considered to be significant.

airframe in the numerical simulations) the status of the boundary layer at cavity the leading edge was already so different as to place any comparison out of scope.

The far-field turbulent kinetic energy was estimated with the general formula:

$$k_\infty = 1.5\left(U_\infty \cdot \frac{I}{100}\right)^2 \quad \textbf{(3-1)}$$

Here I is the turbulence intensity (in percent). A value of 3% was used in order to ensure the proper development of turbulent structures. The value was chosen not because it represented typical turbulence levels at 30'000 feet, which are usually zero but, as indicated in Menter (2012), to ensure the proper activation of the LES part of the DES turbulence model during the simulation. In fact, placing a zero-initial value for the turbulence intensity can cause the unnatural phenomenon, in which the solution does not activate the LES part of the model and remain stuck in a fully RANS condition (as indicated in Menter (2012)).

The specific dissipation rate was instead calculated with the following formula:

$$\omega_\infty = \frac{0.09^{0.75} \cdot k^{1.5}}{l_{ref} \cdot k} \quad \textbf{(3-2)}$$

Here l_{ref} was set equal to 0.1415 m, or half the size of the estimated boundary layer thickness at the cavity's leading edge, which is usually a zero-order method to estimate the size of the eddies inside a wall bounded flow (Davidson, 2004). Equation (3-1) and Equation (3-2) are general formulas for estimation of turbulent quantities in CFD computations involving objects in free air-stream (Spalart & Rumsey, 2007).

The unsteady simulations were performed using the IDDES – kω SST turbulence model (Shur, Spalart, Strelets, & Travin, 2008). The air was treated as an ideal compressible gas using Sutherland's law for viscosity modelling. Non-viscous fluxes were resolved using 3rd order schemes, viscous ones with a 2nd order, while gradients were evaluated using the least square method. The time marching scheme was an implicit second order dual type with five inner sub-iterations. The choice of the time step was to ensure a CFL number, Equation (3-3), around unity in all the elements (Menter, 2012).

$$CFL = \frac{dt \cdot U_{ref}}{dx} \quad \textbf{(3-3)}$$

Setting the free-stream velocity as U_{ref} and placing dx as the minimum mesh spacing encountered in grid requirements, i.e. the spacing of the shear layer at the cavity leading edge, a dt value equal to 1.0x10^{-5} s was adopted.

Unsteady simulations were started from a partially converged RANS solution, to reduce the start-up time. Finally, to resolve all the main modes expected in the problems the requirement of simulation duration of at least 30 cycles (Menter, 2012) of the frequencies of interest was observed. In this case, the aim was to resolve the physical problem up to the lowest Rossiter-Heller mode, estimated to be equal to 23 Hz using the Rossiter-Heller theory (Equation (2-3)), and hence the minimum total simulation duration requirement was 1.3 s. All the simulations where run for 220000 iterations, or 2.2 seconds.

To determine the convergence, in a procedure similar to the one adopted by Chaplin & Birch (2012), the trend of velocity component fluctuations inside the shear layer (probe at x/L = 0.8, 2y/W = 0.0, z/D = 0.0) was monitored. This, as shown in Figure 3.17, indicated that the solution was clear of the unphysical start-up transient after 20000 iterations (or 0.2 seconds).

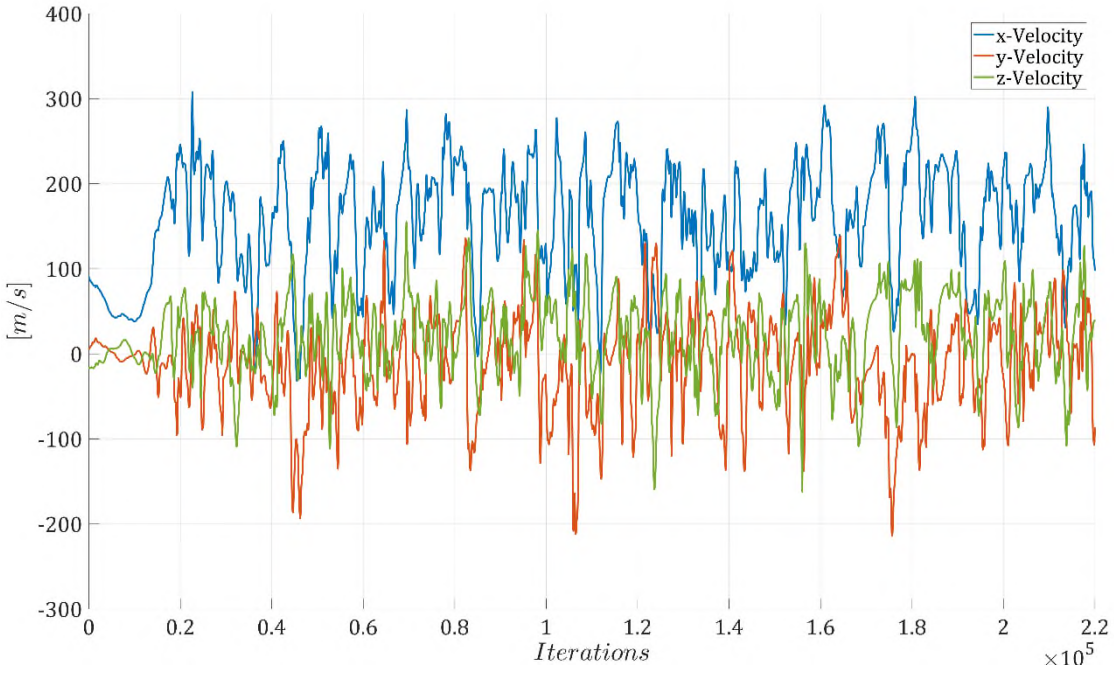

Figure 3.17 - Velocity component trends with iterations for CFD simulation of cavity type AA at zero angle of attack. *Data refers to a probe immersed in the shear layer (x/L = 0.8, 2y/W = 0.0, z/D = 0.0).*

3.2.3 TEST CASE MATRIX

Computational procedures to test geometry and environmental conditions that could not be tested in the wind tunnel. Hence, CFD simulations involved a complete aircraft model with the cavity installed. The first three cases tested (run ID 1, 5, and 6), were devoted to exploring the leading and trailing edge geometry (types AA, BB, and CC) effects. In such cases, bay doors were always opened at 90 degrees. Subsequently, the effect of angle of attack variation was explored, using the reference geometry AA (or the case with straight leading and trailing edges, run ID 2, 3, and 4) still mounted on the UCAV1303 airframe. Table 3.8 summarises all the simulations performed.

Table 3.8 - CFD simulations test matrix.

ID	CAVITY	DOOR ANGLE [deg]	ANGLE OF ATTACK [deg]
1	AA	90.0	0.0
2			3.0
3			4.5
4			6.0
5	BB	90.0	0.0
6	CC	90.0	0.0

3.3 POST-PROCESSING TECHNIQUES

The post processing activity focused on the analysis of the recorded signals. Usually frequency domain and time-frequency domain analyses are conducted in order to discern and synthetize the organised flow component from the random component. Flow visualisation, however, is an activity that is performed in parallel and is coupled with signal analysis, with the aim of providing visual information on particular flow features that could help to better understand the flow physics. However, in this case it was only possible to adopt it with the CFD simulation due to the absence of any appropriate visualisation capabilities in Shrivenham's wind tunnel.

3.3.1 DATA ANALYSIS PROCEDURES – SENSOR' SIGNALS

The analysis of a signal with the power spectrum alone cannot provide evidence of any time-localized feature since only frequency information can be extracted. In the standard power spectrum estimation (Fourier transform), the process under analysis is defined as a superimposition of statistically uncorrelated harmonic components. The distribution of power among these frequency components gives the power spectrum or power spectral density (PSD) of the process. As such, phase relations between frequency components are suppressed. This approach, in signal post-processing is also referred as "linear analysis"[12] and/or spectral analysis of first order. A common way to recover the phase information of the signal is the utilisation of time-frequency domain analysis, which enables to monitor the spectral content of the signal during its temporal evolution. Nevertheless, in some applications, to obtain further details of the underlying physics, it is necessary to look beyond the power spectrum to account as well the phase correlations and the interactions of the various harmonics which define a signal. Higher order spectral analysis (HOSA, defined also spectral analysis of order greater than one and/or "non-linear" spectral analysis) do contain such information. In general, there are two motivations behind the use of HOSA; to reconstruct the phase as well as the magnitude response of the signal and to detect and characterize nonlinearities[13] in the data.

[12] In this case, the term "linear" refers that all the components present in the spectrum are statistically uncorrelated and not dependent from each other behaviour.
[13]Nonlinearities in a signal indicate that the harmonics present in the spectrum are statistically correlated and their behaviour influence each other's.

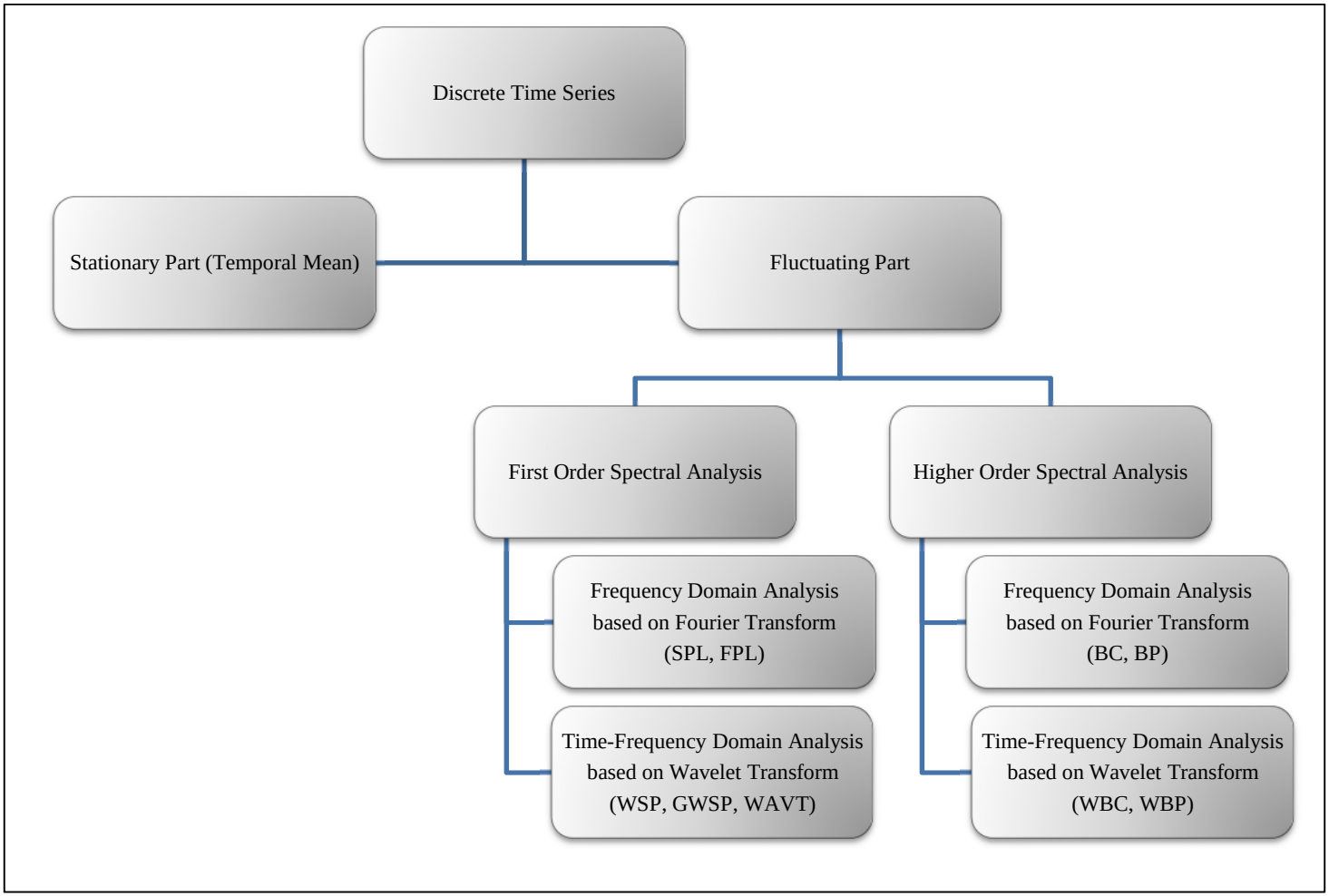

Figure 3.18 - JFTFA process identification.

Since these particular features are important to understanding the nature of cavity flows, it was decided to adopt a particular analysis process called Joint Frequency and Time-Frequency Analysis (JFTFA). Its application to a discrete time series is shown in Figure 3.18. In the first step the signal is divided into its stationary part (i.e. the mean) and the fluctuating part. The fluctuating part is then processed to extract both "linear" (1st order spectral analysis in frequency and time-frequency domain) and "non-linear" information from the fluctuating component of a signal. With the former approach basic information such as dominant tones (frequency domain analysis) and particular features such as mode switching and/or intermittency (time-frequency domain analysis) are extracted. With high order spectral analysis (performed in frequency and time-frequency domains) the statistically correlated harmonics of the signal are extracted and the level of interaction between them analysed.

FREQUENCY DOMAIN ANALYSIS

Given a discrete-finite time series of the form x_n with $n = 1,2,\dots N$, sampled at a time step dt, the discrete Fourier transform is defined as:

$$\hat{X}_k = \sum_{j=1}^{N} x_j \cdot e^{-\frac{2\pi k j \cdot i}{N}} \qquad \textbf{(3-4)}^{14}$$

Following this, the one sided power spectral density (PSD) is defined as:

$$PSD(k) = \frac{2}{F_s \cdot N} \cdot \hat{X}_k \cdot \hat{X}_k^* \qquad k = 1,2 \dots \dots \frac{N}{2} + 1 \qquad \textbf{(3-5)}$$

The associated frequency vector is then defined as:

$$f = \left(0,1,2 \dots \cdot \frac{N}{2}\right) \cdot \frac{F_s}{2 \cdot N} \qquad \textbf{(3-6)}$$

The common practice for a long time-series is to divide it into a defined number, M, of shorter overlapping elements, calculate the PSD for each segment, and then take the average. This is done to reduce the variance of the estimation, which is proportional to $1/M$. In this study, the analysed time series were each divided into blocks with 50% overlap and with a number of samples equal to the ratio F_s/F_r. A Hanning window was

[14] In this study, when segments were not power of 2, were zero-padded.

then applied to each block to reduce leakage effects. Finally, the PSD of the original signal was calculated by averaging the PSD of each block.

In order to discriminate between nonlinearly coupled waves and the spontaneously excited independent waves in a time series it is necessary to adopt high-order (or non-linear) spectral analysis. Quadratic non-linearity implies that for a triad of frequencies f_1, f_2, and f_3, with corresponding phases ϕ_1, ϕ_2, and ϕ_3, the following equations are satisfied:

$$f_1 + f_2 = f_3 \tag{3-7}$$

$$\phi_1 + \phi_2 = \phi_3 + \vartheta \tag{3-8}$$

Here ϑ is a constant phase angle. Equation (3-7) is the necessary condition for frequency coupling while Equation (3-8) is mandatory for phase coupling. More specifically, non-linearity is quantified using a quantity called *bi-coherence* (BC) which is a direct derivation from the bi-spectrum (BS), defined also as the double Fourier transform of the third order moment, or more generally the third order cumulant:

$$BS(f_1, f_2) = \langle \hat{X}(f_1) \cdot \hat{X}(f_2) \cdot \hat{X}^*(f_3) \rangle \tag{3-9}$$

If the bi-spectrum is normalised, the bi-coherence spectrum (BC) is obtained:

$$BC(f_1, f_2) = \sqrt{\frac{|BS(f_1, f_2)|^2}{\langle \left| \hat{X}(f_1) \cdot \hat{X}(f_2) \right|^2 \rangle \cdot \langle \left| \hat{X}(f_3) \right|^2 \rangle}} \tag{3-10}$$

The bi-coherence is bounded between 0 and 1 by the Schwarz inequality. According to Kim & Powers (1979) the squared value of the bi-coherence, $BC^2(f_1, f_2)$, can be interpreted as the fraction of power at f_3 due to the quadratic phase coupling among f_1, f_2, and f_3. Phase information and cycle geometry can instead be obtained by the bi-phase (BP), expressed as

$$BP(f_1, f_2) = atan\left(\frac{imag\{BS(f_1, f_2)\}}{real\{BS(f_1, f_2)\}}\right) = \phi_1 + \phi_2 - \phi_3 = \vartheta \tag{3-11}$$

Maccarone (2013) noted that this quantity must be defined in the full 2π cycle so that no information is lost within the signal. Moreover, he showed that the bi-phase is also an indicator of the cycle geometry. The real component of the bi-spectrum describes the

extent to which the time series is skewed (i.e. the distribution of the peaks around the mean value), while the imaginary component describes the extent to which the time series is symmetric in terms of time in a statistical sense. Therefore, a null bi-phase (the imaginary part of the bi-spectrum null with the real part of the bi-spectrum positive) will indicate a skewed non-linear-generated wave that will spend most of its time below the mean value with high peaks towards the positive regions. The reverse is true for a bi-phase of 180 degrees, indicating negative skewness. The other relevant values of BP are ±90 degrees. In this case, the wave will have a symmetric probability distribution around the mean value, but will be asymmetric along the time evolution. An example of this case is a saw-tooth time series. A 90 degree bi-phase saw-tooth wave will express a time series with linear rising but rapid falling, while a bi-phase of 270 degrees will represent the opposite pattern, with a rapid rise followed by a linear falling. In both cases, however, the skewness of the resultant wave will be null.

TIME-FREQUENCY DOMAIN ANALYSIS

A Fourier transform is a tool for finding the frequencies present in a signal, but it is unable to calculate the exact time at which a particular spectral component is present. Moreover, its accuracy relies on long time series (compared to the time scales of the problem) that are not always available. In addition, frequency domain analysis is valid only if the signal under consideration is statistically stationary. However, in many instances this does not represent the reality of the situation, so it is preferable to analyse a signal in the time-frequency domain. The simplest technique is to use the short time Fourier transform (STFT). This technique, used to determine the sinusoidal frequency and phase content of local sections of a signal as it evolves in time, is based upon a procedure that divides the time series into shorter overlapping segments of equal length, considered statistically stationary. At each of these segments, the Fourier transform is applied in order to obtain the spectrum of each and hence a time-frequency picture of the signal (or map). Naming $\widehat{SX}(k,n)$ the value of the transform at a frequency, k, and time index, n, it is possible to write:

$$\widehat{SX}(k,n) = \frac{1}{N} \cdot \sum_{j=1}^{N} x_j \cdot w_p(j-n) \cdot e^{-\frac{2\pi k j \cdot i}{N}} \qquad \textbf{(3-12)}$$

Equation (3-12) is identical to Equation (3-4) apart from the term w_p, which is called the "*window of the transform*" and is used to divide the original series into shorter segments of

width p (the derivation of the power spectral density is analogous to the Fourier transform, i.e. by substituting $\hat{X}_k$ with $\widehat{SX}$ in Equation (3-5)). In this study, a Hanning window with 50% overlapping segments was used. The characteristic of the STFT is that it is capable of identifying possible statistical non-stationary phenomena affecting the original time series. The apparent advantage of the STFT often disappears due to what is sometimes referred to as the *problem of time-frequency resolution*. The *Gabor-Heisenberg Indetermination Principle* (Equation (3-13)) states that it is impossible to know exactly what spectral components are present in a signal at a given time t.

$$\Delta t \cdot \Delta f \geq K \tag{3-13}$$

The quantity K is a constant that usually depends on the window function used in the time-frequency transform. It is then possible only to know the time intervals in which a certain band of frequencies is present. In a Fourier transform, the problem of frequency resolution is not present because ideally all the existing frequencies are present, while no information is known regarding the resolution in time. However, the windowing in the STFT imposes a resolution in time (the width of the windows) which implies a maximum available frequency resolution. This evolves into two antithetical situations. If high resolution in frequency is required (small Δf used) the resolution in time is sacrificed (big Δt used). Conversely, if high resolution in time is required (small Δt used) the resolution in frequency is sacrificed (big Δf used). So the choice of the window becomes of great importance and it is dependent on the particular problem being studied. This problem is resolved by the wavelet transform, in which the dimension of the window varies for every spectral component, i.e. it changes when moving from low frequencies to higher ones. A wavelet is a function, real or complex, $\psi(\eta)$ with a zero mean localized in both time and frequency (Farge, 1992). The wavelet transform can be both discrete (with only an orthogonal basis necessary) and continuous (both non-orthogonal and orthogonal required). In this study, a Morlet wavelet was used, consisting of a plane wave modulated by a Gaussian:

$$\psi_0(\eta) = \pi^{-1/4} \cdot e^{i\omega_0\eta} \cdot e^{-\eta/2} \tag{3-14}$$

The Morlet is a complex, non-orthogonal wavelet basis with ω_0 being the non-dimensional central frequency, set here at 6, which is a standard value appropriate to this study (Farge, 1992). The continuous wavelet transform of a discrete time series x_n is defined as the convolution of x_n with a scaled and translated version of $\psi_0(\eta)$:

$$w(s,n) = \sum_{j=1}^{N} x_j \cdot \psi^* \left(\frac{(j-n) \cdot dt}{s} \right) \quad \textbf{(3-15)}$$

As before, dt is the time step of the time series. Equation (3-15) indicates that "varying the wavelet scale, s, and translating along localized time index, n, a picture can be constructed showing both the amplitude of any features versus scales and how this amplitude varies with time" (Torrence & Compo, 1998). The subscript 0 in the mother wavelet has been dropped to indicate that, before applying the transform, the function $\psi_0(\eta)$ has been normalised. This is an expedient to ensure that the derived wavelet at each scale has unit energy and hence that the wavelet transform is weighted only by the amplitude of x_j. The discrete Fourier transform (DFT) of $\psi_0(\eta)$ is indicated by $\hat{\psi}_0(s\omega_k)$, with the angular frequency ω_k defined as:

$$\omega_k = \begin{cases} +\dfrac{2\pi k}{Ndt} : & k \leq N/2 \\ -\dfrac{2\pi k}{Ndt} : & k > N/2 \end{cases} \quad \textbf{(3-16)}$$

It is then possible to define the normalisation, in the frequency space, as:

$$\hat{\psi}(s\omega_k) = \left(\frac{2\pi s}{dt} \right)^{1/2} \cdot \hat{\psi}_0(s\omega_k) \quad \textbf{(3-17)}$$

With this normalisation, it is ensured that, at each scale, the following relation holds:

$$\sum_{k=1}^{N} \left| \hat{\psi}(s\omega_k) \right|^2 = N \quad \textbf{(3-18)}$$

As stated by Torrence & Compo (1998), the wavelet transform can be approximated by the inverse Fourier transform of the product of the DFT of the time series ($\hat{X}_k$, see Equation (3-4)) and the complex conjugate of $\hat{\psi}(s\omega_k)$. The final equation then becomes:

$$W(s,n) = \sum_{k=1}^{N} \hat{X}_k \cdot \hat{\psi}^*(s\omega_k) \cdot e^{i \cdot \omega_k n dt} \quad \textbf{(3-19)}$$

The scales, s, of the Morlet wavelet transform, are correlated with the frequencies in which the signal is decomposed by the following equation

$$^1/_f = \frac{4\pi}{\omega_0 + \sqrt{2 + \omega_0^2}} \cdot s \qquad \textbf{(3-20)}$$

Here again, ω_0 is the central frequency of the mother wavelet. For a non-orthogonal wavelet, such as the Morlet one, the set of scales used is discrete (Farge, 1992). A suitable procedure for the choice of the exact set of scales to represent accurately the problem has been developed in Torrence & Compo (1998). They wrote the scales as a fractional power of 2:

$$s_j = s_0 \cdot 2^{j \cdot dj} \quad j = 0,1,\dots,J \qquad \textbf{(3-21)}$$

The variable s_0 is the smallest resolvable scale (and hence according to Equation (3-20) the highest resolved frequency). According to the Nyquist rule, s_0 should be chosen such that the corresponding frequency is equal to $1/(2dt)$; this was implemented for this study. The parameter dj commands the spacing between the scales (its inverse determines the number of frequency points per octave). A standard value for the Morlet wavelet is 0.5. Smaller values give finer resolution in the frequency domain. In this study dj was set equal to 0.05, it being an optimum compromise between frequency and time resolution (Torrence & Compo, 1998). Finally, the total number of scales, or J, is determined by the following equation:

$$J = \frac{1}{dj} \cdot \log_2\left(\frac{Ndt}{s_0}\right) \qquad \textbf{(3-22)}$$

Once the transform is applied, it is possible to reconstruct the original time series using either deconvolution or the inverse filter. From Farge (1992), the inverse wavelet transform is obtained:

$$x_n = \frac{dj \cdot dt^{1/2}}{C_\delta \cdot \psi_0(0)} \cdot \sum_{j=0}^{J} \frac{real\{W(s_j, n)\}}{s_j^{1/2}} \qquad \textbf{(3-23)}$$

The factor $\psi_0(0)$ removes the energy scaling, while $s_j^{1/2}$ converts the wavelet transform to an energy density. C_δ is the reconstruction factor, and is a constant for each wavelet function. Note that if the original time series was complex the $real\{\ \}$ operator should have been replaced by the $imag\{\ \}$ operator. It can also be shown (Torrence & Compo, 1998) that the total energy of the signal is conserved under the wavelet transform, and the equivalent Parseval's theorem for wavelet analysis is:

$$\sigma^2 = \frac{dj \cdot dt}{C_\delta \cdot N} \cdot \sum_{n=1}^{N} \sum_{j=0}^{J} \frac{W(s_j, n) \cdot W^*(s_j, n)}{s_j} \quad \textbf{(3-24)}$$

Once the transform has been calculated, it is possible to define the wavelet power spectrum (WPS) as:

$$WPS(s, n) = W(s, n) \cdot W(s, n)^* \quad \textbf{(3-25)}$$

The WPS is a map that, at each time index, n, and scale, s, associates a real value that expresses the intensity of the signal at that particular time ($t = (n-1) \cdot dt$) at that particular frequency (Equation (3-20)).

If a vertical slice through a wavelet plot is a measure of the local spectrum, then the time-averaged wavelet power spectrum ($\overline{W}^2(s)$) over a certain period is defined as:

$$\overline{W}^2(s) = \frac{1}{n_2 - n_1 + 1} \cdot \sum_{n=n_1}^{n_2} W(s, n) \cdot W^*(s, n) \quad \textbf{(3-26)}$$

Following this definition, averaging over all the length of the signal, the global wavelet spectrum, or $GWS(s)$, is obtained:

$$GWS(s) = \frac{1}{N} \cdot \sum_{n=1}^{N} W(s, n) \cdot W^*(s, n) \quad \textbf{(3-27)}$$

However, as stated in Maraun & Kurths (2004), with the adopted normalisation of Equation (3-17), while a flat noise spectrum is preserved, sine waves of equal amplitude exhibit different integrated powers, proportional to their oscillation scale, leading to possible misinterpretations of the results. This issue can be resolved by normalising the wavelet power spectrum by the factor s/dt. The new obtained value is such that waves of equal amplitude present themselves with peaks of the same amplitude in the wavelet map, making it much easier to inspect the time-frequency spectrum. It is possible to observe that this normalisation is also present in Equation (3-24) (Parseval's theorem for wavelets) and recovers the effects introduced by Equation (3-17). It is then possible to introduce the wavelet spectral power ($WSP(s, n)$) coupling Equation (3-24) and Equation (3-25) , expressed in decibels, as:

$$WSP(s,n) = 10 \cdot \log_{10} \frac{WPS(s,n)}{\kappa^2} \cdot \frac{dt}{s} \quad \textbf{(3-28)}$$

Here κ is a normalisation constant, which enables the WPS non-dimensional to be derived. In this study, for pressure signals, κ was set equal to $2x10^{-5}$ Pa, the threshold of human hearing. For all other signals, it assumed the dummy value of 1. The factor dt/s enables comparisons of similar amplitude peaks localised at different scales. When the definition of WSP is coupled with Equation (3-27), and the summation is extended over all the signal length, it is possible to define the global wavelet spectral power ($GWSP(s)$) as:

$$GWSP(s) = 10 \cdot \log_{10} \frac{GWS(s)}{\kappa^2} \cdot \frac{dt}{s} \quad \textbf{(3-29)}$$

As Equation (3-26) expresses the averaging in time of the wavelet coefficients, the average in scales can be expressed similarly, i.e. the scale averaged wavelet power ($\overline{W}^2(n)$) over a certain scale interval:

$$\overline{W}^2(n) = \frac{dj \cdot dt}{C_\delta} \cdot \sum_{j=s_1}^{s_2} \frac{W(s_j,n) \cdot W^*(s_j,n)}{s_j} \quad \textbf{(3-30)}$$

This quantity is a new time-series expressing the average variance in a certain scale's band identified by the limits s_1 and s_2. If the summation is then extended to the whole domain, the result will be the trend of the energy of the signal (and hence of the variance) varying with time.

It is convenient to divide this quantity by the signal variance and then to express everything in decibel units. In this way, positive values will express periods where the local signal power is above the signal's variance, while for negative values the opposite will be true. The wavelet averaged variance trend ($WAVT(n)$) is then defined as:

$$WAVT(n) = 10 \cdot \log_{10} \left(\frac{dj \cdot dt}{C_\delta \cdot \sigma^2} \cdot \sum_{j=0}^{J} \frac{W(s_j,n) \cdot W^*(s_j,n)}{s_j} \right) \quad \textbf{(3-31)}$$

Using the wavelet transform, it is also possible to correlate signals in the time-frequency domain. Given two time series x_n and y_n with wavelet transforms $W_x(s,n)$ and $W_y(s,n)$ the wavelet cross spectrum $W_{xy}(s,n)$ is then defined as:

$$W_{xy}(s,n) = W_x(s,n) \cdot W_y^*(s,n) \quad \textbf{(3-32)}$$

This quantity defines areas with high common power. However, it is more convenient to use the coherence and phase of the signals instead of the net common power. This then introduces the wavelet local correlation coefficient $WLCC_{xy}(s,n)$ and the wavelet local correlation phase $WLCP_{xy}(s,n)$ as:

$$WLCC_{xy}(s,n) = \frac{\left|S\left(W_{xy}(s,n) \cdot s^{-1}\right)\right|^2}{S(|W_x(s,n)|^2 \cdot s^{-1}) \cdot S\left(\left|W_y(s,n)\right|^2 \cdot s^{-1}\right)} \quad \textbf{(3-33)}$$

$$WLCP_{xy}(s,n) = atan\left(\frac{imag\left\{S\left(W_{xy}(s,n) \cdot s^{-1}\right)\right\}}{real\left\{S\left(W_{xy}(s,n) \cdot s^{-1}\right)\right\}}\right) \quad \textbf{(3-34)}$$

Here $S(\,)$ is a smoothing operator in time and scale, i.e. $S\big(W(s,n)\big) = S_{scale}\left(S_{time}\big(W(s,n)\big)\right)$, as defined in Grinsted, et al. (2004). For the Morlet wavelet, the combined operators are respectively:

$$S_{time}\big(W(s,n)\big)|_s = \left(W(s,n) \cdot c_1^{\frac{-(n \cdot dt)^2}{2s^2}}\right)|_s \quad \textbf{(3-35)}$$

$$S_{scale}\big(W(s,n)\big)|_n = \big(W(s,n) \cdot c_2 \prod(0.6s)\big)|_n \quad \textbf{(3-36)}$$

Here c_1 and c_2 are normalization constants determined numerically and $\prod$ is the rectangular function. $WLCC_{xy}(s,n)$ and $WLCP_{xy}(s,n)$, which respectively spans from 0 to 1 (non-dimensional), and from $-\pi$ to π radians, represent the normalised covariance and the absolute phase between the two signals.

The wavelet and Fourier transform bi-spectrum, bi-coherence and bi-phase can all be defined in similar ways, and interpretation is the same. The difference is that the former quantities can be defined over a sub-domain of the temporal length of the signal in order to analyse particular moments where statistically non-stationary behaviour is expected. The wavelet bi-spectrum, between two time indices n_1 and n_2, with $N_s = (n_2 - n_1 + 1)$, and using Equation (3-20) to change scale with frequency, is defined as:

$$WBS(s_1,s_2) = \frac{1}{N_s} \cdot \sum_{n=n_1}^{n_2} W(s_1,n) \cdot W(s_2,n) \cdot W^*(s_3,n) \quad \textbf{(3-37)}$$

$$\frac{1}{s_3} = \frac{1}{s_1} + \frac{1}{s_2} \tag{3-38}$$

The bi-phase is then defined as:

$$WBP(s_1, s_2) = atan\left(\frac{imag\{WBS(s_1, s_2)\}}{real\{WBS(s_1, s_2)\}}\right) \tag{3-39}$$

The wavelet bi-coherence is finally expressed as:

$$WBC(s_1, s_2) = \sqrt{\frac{|WBS(s_1, s_2)|^2}{\frac{1}{N_s}\sum_{n=n_1}^{n_2}|W(s_1, n) \cdot W(s_2, n)|^2 \cdot \frac{1}{N_s}\sum_{n=n_1}^{n_2}|W(s_3, n)|^2}} \tag{3-40}$$

As in the case of the bi-coherence, the wavelet bi-coherence is an indicator of phase coupling between the triad of waves defined by the scales s_1, s_2 and s_3 (see Equation (3-38)). The interpretation of these new higher order statistical quantities is the same as in frequency domain analysis. The difference is that, in this case, they are all based on a time-frequency domain transform of the signal, and hence they are able to capture any particular time localised features (given an appropriate choice of the interval N_s) that otherwise could be hidden, by taking into consideration the whole length of the time series.

When examining waves, whose behaviour is not statistically stationary it is useful to introduce a further quantity, called the *index of persistence*, or simply *persistence* (PR) which expresses the percentage of the signal time length in which a given frequency band is active, i.e. has enough power to be considered a feature of the flow and not simply just background noise. It is possible to then write:

$$PR|_{s1}^{s2} = \sum_{n=1}^{N}\sum_{j=s1}^{s2}\frac{A(s, n)}{n \cdot j} \cdot 100 \tag{3-41}$$

Here $A(s, n)$ is the "activity map", i.e. a map equal to 1 whenever the local wavelet power spectrum is above a reference value and 0 otherwise.

$$A(s,n) = \begin{cases} 1 & : \quad \dfrac{WPS(s,n)}{\sigma^2} \geq \dfrac{1}{2} P_s \cdot \chi_2^2(p) \\ 0 & : \quad \dfrac{WPS(s,n)}{\sigma^2} < \dfrac{1}{2} P_s \cdot \chi_2^2(p) \end{cases} \tag{3-42}$$

Here χ_2^2 is the chi-square function with 2 degrees of freedom, p is the desired confidence level, set equal to 95% in this study, and P_s is a background red-noise spectrum, built using autocorrelation coefficients of the original time series[15].

Equation (3-41) is then bounded between 0% (no time-activity) and 100% (full-time activity) and is particularly useful to investigate how much a wave is effectively active during the time-window analysed. Finally, the PR index, even if originally defined with wavelet transform map, can be calculated, using every other time-frequency domain transform with its associated activity map.

PRESSURE DATA ANALYSIS

In the analysis of pressure signals, it is useful to define the Sound Pressure Levels (SPL) and the Overall Sound Pressure Level (OASPL), calculated using Equations (3-43) and (3-44). These quantities are all expressed in decibel units.

$$SPL(f) = 10\, log_{10}\left(\frac{PSD_{p_f}(f) \cdot \Delta f_{ref}}{p^2_{reference}}\right) \tag{3-43}$$

$$OASPL = 20\, log_{10}\left(\frac{\sigma_p}{p_{reference}}\right) \tag{3-44}$$

Here $p_{reference}$ is the minimum audible pressure, equal to 2x10^{-5} Pa, which is defined as the threshold of human hearing, and Δf_{ref} is a reference frequency posed equal to 1Hz, which is used to make this new quantity non-dimensional (PSD units are, for pressure signals, Pa^2/Hz). The PSD may be obtained from Equations (3-5) and (3-12). In case it is necessary to compare pressure signals obtained at different freestream conditions, it is convenient to use another non-dimensionalisation procedure, based on the freestream dynamic pressure instead of $p_{reference}$. Fluctuating pressure level (FPL) and overall fluctuating pressure level (OAFPL) are then defined as:

[15] For a detailed discussion on the derivation of such a background spectrum, see the error estimation section for wavelet analysis.

$$FPL(f) = 10\,log_{10}\left(\frac{PSD_{p_f}(f)\cdot\Delta f_{ref}}{q_\infty^2}\right) \quad \textbf{(3-45)}$$

$$OAFPL = 20\,log_{10}\left(\frac{\sigma_p}{q_\infty}\right) \quad \textbf{(3-46)}$$

Here q_∞ is the free-stream dynamic pressure. Finally, for the analysis of pressure gradients in the cavity floor the mean pressure coefficient was defined as:

$$\overline{C_p} = \langle\frac{2}{\gamma\cdot M_\infty}\cdot\left[\frac{p}{p_\infty}-1\right]\rangle \quad \textbf{(3-47)}$$

Here the overbar indicates that the quantity has been time-averaged.

3.3.2 DATA ANALYSIS PROCEDURES – FLOW VISUALISATION

Flow visualisation is used to determine any correlation between fluid structures present in the cavity, and the results obtained by signal analysis. In the current study three techniques have been used to analyse the geometrical arrangement of eddies inside the cavity. As stated earlier, this was only possible in CFD post-processing since no flow visualization techniques were available in the wind tunnel facility. The first methodology used was the iso-surface of Q-criterion, known also as the second invariant of the velocity gradient tensor $(\bar{\bar{A}})$, defined as:

$$Q = 0.5\cdot(\Omega^2 - S^2) \quad \textbf{(3-48)}$$

$$\Omega_{ij} = \frac{1}{2}\left(\frac{\partial U_i}{\partial x_j} - \frac{\partial U_j}{\partial x_i}\right) \quad \textbf{(3-49)}$$

$$S_{ij} = \frac{1}{2}\left(\frac{\partial U_i}{\partial x_j} + \frac{\partial U_j}{\partial x_i}\right) \quad \textbf{(3-50)}$$

$$A_{ij} = \frac{\partial U_i}{\partial x_j} = S_{ij} + \Omega_{ij} \quad \textbf{(3-51)}$$

This eddies' method of visualisation is directly derived from the analysis of an iso-surface of constant vorticity. In this case, however, rotational motion $(\bar{\bar{\Omega}})$ is separated from the shear layer motion $(\bar{\bar{S}})$, to avoid displaying the latter. Obviously, since it is a variable,

which depends on an unsteady velocity field, it will itself be unsteady. According to the value of Q chosen, it is possible to visualise both small and big eddies in the flow. Since this study is interested in the analysis of the global fluid structure inside the cavity, only iso-surfaces of $Q = 100 \cdot L^2/U_\infty^2$ were displayed (with L equal to the cavity length), as suggested in Menter (2012). The second visualisation technique used was the visualisation of the modulus of the gradient of the density[16] defined as:

$$\left|\overrightarrow{\nabla\rho}\right| = \sqrt{\left(\frac{\partial\rho}{\partial x}\right)^2 + \left(\frac{\partial\rho}{\partial y}\right)^2 + \left(\frac{\partial\rho}{\partial z}\right)^2} \qquad \textbf{(3-52)}$$

Since the flow is compressible in nature, this quantity will enhance the visualisation of the shear layer structure and also any shock waves, if present. Finally, in order to visualise the velocity and vorticity vector fields inside the cavity, a technique *called line-integral convolution* (LIC) was used. LIC is a visualisation technique first introduced by Cabral & Leedom (1993). The algorithm processes vector fields to produce a high-density streamline plot illustrating the features of the flow. The rationale behind this procedure is that the local behaviour of a vector field can be approximated by computing a local streamline starting from a point of the domain and moving out in both negative and positive directions. The advantage of this technique, with respect to a simple streamline visualisation, is that the details are dependant only on the original mesh resolution and not on the seeding points used for integration, as would be the case for streamline algorithms.

The basic process begins by combining a vector field, defined on a rectangular grid (Figure 3.19b), with an input image of the same resolution as the grid (Figure 3.19a). Each pixel therefore corresponds to one cell of the vector grid. At the first cell, a streamline of a given length is integrated forward and backward using the vector field. The corresponding pixel in the output image is then assigned the mean intensity of the pixels lying under that streamline and the process is repeated at the next pixel / cell. As the calculation progresses, pixels on the same streamline are assigned similar intensities, resulting in the filtering, or smearing, of the input image along the streamlines of the vector field. The result obtained is shown in Figure 3.19c. The selection of white-noise input image is preferred as it results in an output image dominated by the vector data.

[16] This technique of flow visualisation is also commonly known as the Schlieren visualisation technique.

To improve the quality of the image, the process outlined by Okada and Kao (1996) is then applied. Using a constant vector field, the first LIC pass is performed with a white noise input image. Subsequent passes use the output of the previous pass as their input. Additionally, the output of the second pass is sharpened to enhance the edges of the streamlines and then equalised to improve the overall contrast, prior to its use in the final pass.

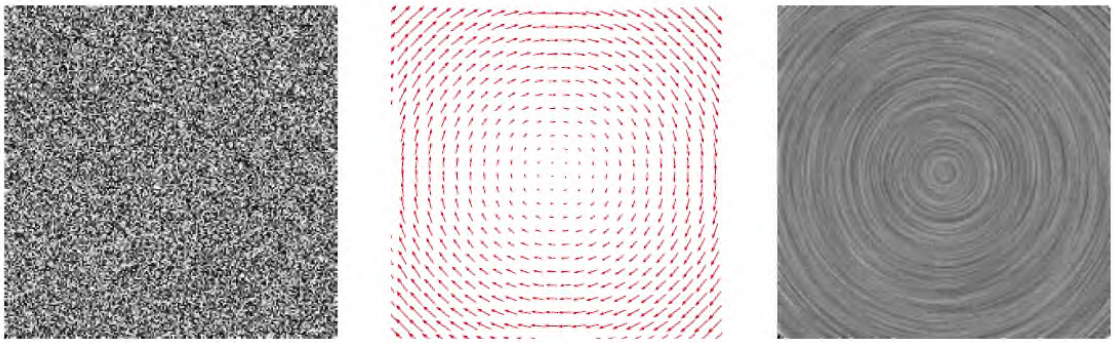

Figure 3.19 - LIC input/output procedure.

Finally, a procedure using neighbour interpolation (as suggested by Stallin & Hege (1995)), de-couples the resolutions of the input vector field and the output image. This allows the generation of high-resolution pictures, reducing the sampling requirement of the original data, since the interpolation increases the number of points (i.e. pixels) from which the picture is formed respect to the original sampled data.

3.4 ERROR ANALYSIS

Uncertainties (or errors) in the experimental results can be divided into systematic errors (ϵ_s) and random errors (ϵ_r). The systematic error in experimental observations can be introduced by instrument reading errors as well as by inaccuracies of the experiment to re-create the real flow situation. Random errors are caused by unknown and unpredictable changes in the experiment. These changes may occur in the measuring instruments as well as in the environmental conditions. This error, which can be quantified by applying statistical analysis, is usually reduced as the number of measurement samples of the experiment are increased.

Numerical simulation measurements are also affected by random errors. Furthermore, CFD is affected by the discretisation error (ϵ_d), which is the effect of resolving the flow equations in time and space at a discretised point instead of considering the flow as a continuum.

The following section will describe the approach used in this study to quantify the various type of errors.

3.4.1 RANDOM ERRORS

The quantification of the random errors, which are dependent on the numerical quantity of the observations in an experiment/simulation, can be performed using statistical analysis. This had a different approach according to the quantity under consideration.

For the estimation of the random error effects on mean values the approach previously derived by Bruun (1996) was used. Given a measurement of N samples, the relative error of the calculated mean of a generic signal x with respect to the true value can be estimated using the following formula:

$$\epsilon = \frac{\mu_x^{Calculated}}{\mu_x^{True}} = z_{score} \cdot \frac{1}{\sqrt{N'}} \cdot \frac{\sigma_x^{Calculated}}{\mu_x^{Calculated}} \quad \textbf{(3-53)}$$

In this equation z_{score}, indicates how many standard deviations are necessary for a Gaussian distribution of mean zero and unity standard deviation, in order to obtain a desired confidence level. N' is the corrected number of samples. According to Dawdy & Matalas (1964), the number of independent observations is fewer than N because, if the time series is auto-correlated, each observation is not separated from the information in

other observations. Given a discrete-finite time series of the form x_n with $n = 1,2,\dots N$, the auto-correlation coefficient, at a time lag k, is defined as:

$$r_k = \frac{c_k}{c_{k=0}} \tag{3-54}$$

Where c_k is defined as:

$$c_k = \frac{1}{N-1} \cdot \sum_{n=1}^{N-k} (x_n - \bar{x}) \cdot (x_{n+k} - \bar{x}) \tag{3-55}$$

It is then possible to define the corrected number of samples as:

$$N' = N \cdot \frac{1 - r_1}{1 + r_1} \tag{3-56}$$

Here r_1 is the lag-1 auto-correlation coefficient.

In the estimation of the random error effects on power spectral density measurements, the procedure described in Newland (1993) was used. For a given confidence level p, it is possible to define the following relation:

$$\frac{PSD_{Calculated}}{PSD_{True}} \in \left[\chi_k^2(1-p), \chi_k^2(p)\right] \cdot \frac{1}{k} \tag{3-57}$$

Here p expresses the desired confidence level, while χ_k^2 is the chi-square probability density function of k degrees of freedom[17], a number that can be estimated using the following relation:

$$k = 2B_eT \tag{3-58}$$

B_e is the bandwidth of the window used to calculate the Fourier spectrum while T is the temporal length of the signal. In wind tunnel experiments, the equivalent 2σ offset (i.e. a confidence level of 95%, using a frequency resolution of 20 Hz, was equal to -0.39 dB to +0.39 dB, relative to the calculated value, while for CFD simulations, due to the samples being shorter and the frequency resolution of 2 Hz, the 2σ offset on PSD was of -1.91 dB to +2.57 dB.

[17] The chi-squared distribution with k degrees of freedom is the distribution of a sum of the squares of k independent standard normal random variables.

Since the spectral analysis was characterised by the distinction of energy peaks from the background signal noise, it was also decided to introduce a confidence level curve, capable of separating the true signal features from random, non-significant events. This necessitated the introduction of an appropriate background spectrum model. It was assumed that different realisations of the analysed process would have been randomly distributed about this mean or expected background, and the actual spectrum could be compared against this random distribution. For turbulence phenomena, like those characterising cavity flows, an appropriate background spectrum is the "red noise" (increasing power with decreasing frequency). This assumption can be easily validated by the fact that the energy cascade spectrum of turbulence, passed the peak localised value at the largest scales (low frequencies), continually decreasing towards the Kolmogorov microscales (high frequencies) (Davidson (2004)). Moreover, spectra of cavity flows from wind tunnel experiments (see for example Chaplin & Birch (2012)) showed that the general trend of the power content of the background noise is to decrease with increasing frequencies. A simple model for red noise is the univariate autoregressive process, that proposed by Gilman et al. (1963). This has, after normalisation, the following power spectrum:

$$P_k = \frac{1-\alpha^2}{1+\alpha^2-2\alpha\cdot\cos(2\pi k/N)} \tag{3-59}$$

$$\alpha = \frac{r_1+\sqrt{r_2}}{2} \tag{3-60}$$

Here k $(= 0,1,\ldots..N/2)$, while r_1 and r_2 are the lag-1 and lag-2 autocorrelation coefficients of the original time series calculated from Equation (3-54). Note that setting α equal to 0, the power spectrum of a Gaussian white noise is obtained. Once obtained, the expression for the background noise spectrum, as described in Equation (3-61), was used to separate the true features from the spectrum.

$$\frac{PSD}{\sigma^2} \geq \frac{1}{2}P_k\cdot\chi_2^2(p) \tag{3-61}$$

Here χ_2^2 is the chi-square function with 2 degrees of freedom, while p is the confidence level.

In time-frequency analysis, it is not possible to define an equivalent of equation (3-57), since this formula is modelled by assuming as true properties the characteristic of a signal

in which temporal length is infinite. However, by definition, wavelet analysis is oriented to the determination of the temporal nature of a signal, which will be destroyed in a passage to infinite length. The random errors effect on wavelet analysis was then quantified using the procedure indicated in Torrence & Compo (1998), based on the definition of Equation (3-61). A threshold value was calculated using the expression of the right hand side of Equation (3-62) choosing a confidence level p (usually of 95%, for red-noise based processes (Torrence & Compo, 1998)). Subsequently, the wavelet spectral power was compared to this threshold value; if less, the "null hypothesis" was accepted, that is the wavelet power value was only caused by randomness. Otherwise, the "null hypothesis" was rejected with a confidence level of p.

$$\frac{|W(s,n)|^2}{\sigma^2} \geq \frac{1}{2} P_k \cdot \chi_2^2(p) \qquad \textbf{(3-62)}$$

Unfortunately, an equivalent theoretical expression for a reference background spectrum was not available for all the JFTFA quantities. Bi-coherence, wavelet bi-coherence and wavelet coherence therefore had to be based upon a different strategy. It was decided to adopt Monte-Carlo methods for the determination of proper background noise. The standard procedure was the generation of 1000 surrogate datasets of red-noise that were then passed on to the routine that calculated the quantity under consideration (bi-coherence, bi-phase...etc.). From the obtained ensemble, the $P = 100(1 - \alpha_p)$ percentile was computed, where P represented the threshold above which the bi-coherence value was considered a true feature and not rejected, and α_p the statistical significance. The value obtained was then used as the threshold, above which the feature under examination was considered true.

3.4.2 SYSTEMATIC ERRORS

Experimental systematic errors are introduced by the inaccuracy of the instrumentation used, and the inaccuracy of the capability of the experimental set-up to recreate the reality of the flow phenomena under study.

In the former case, since all measurements of pressure were conducted using a Scanivalve® ZOC22B transducer (see Paragraph 3.1.4), it was possible to quantify the amount of systematic error due to instrumentation. According to the manufacturer specifications, at the operating pressure used in this study, the scanner introduced on the measured signal a maximum deviation of ±0.0008 times the value monitored. The other

instruments used in deriving flow properties (see Paragraph 3.1.4), i.e. the K-type thermocouple for static temperature measurements, and the Furness Controls© FCO14 micro manometer for static and dynamic pressure measurements, had a precision of ±0.0075 and ±0.0030 times the value monitored respectively.

Another source of systematic error, was the temporal variations of the freestream quantities during each wind tunnel run. The wind tunnel, which used a feedback system to control the flap valve during the blow-down phase, had a temporal response, and the flow properties varied in the test section during a typical run. A typical trend is shown in Figure 3.20. As shown, freestream static temperature, static pressure, and dynamic pressure assumed variation always below 0.02 times relative to the mean temporal value. This, on its own implicated that the Mach number, oscillated around the mean value of 0.81 by ± 2%.

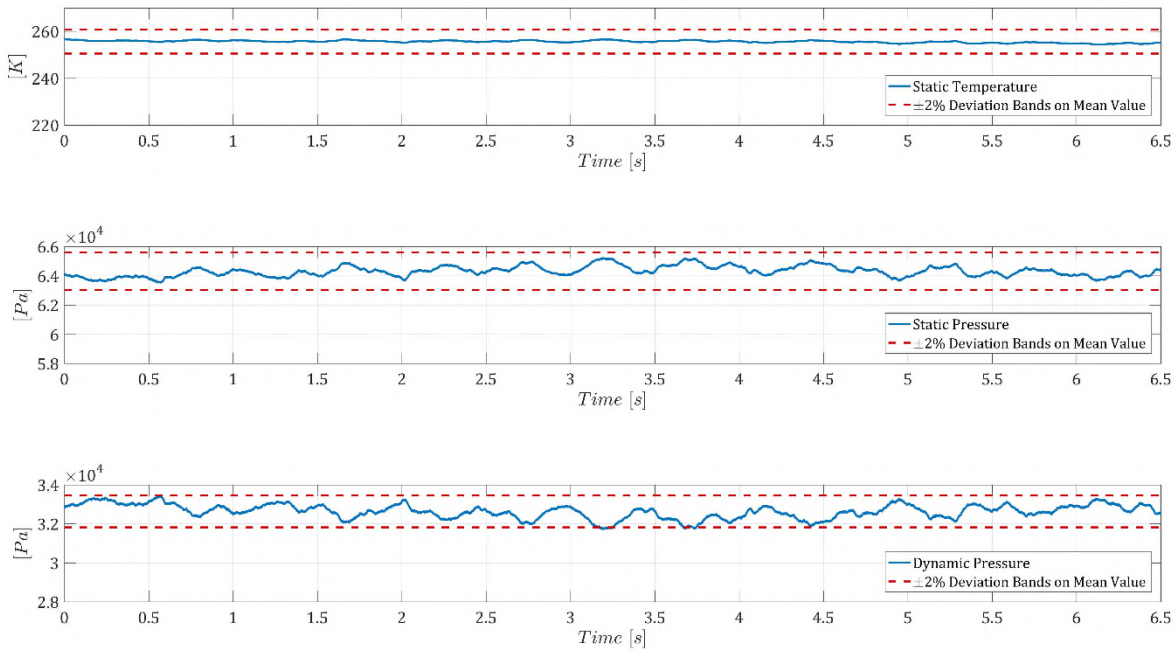

Figure 3.20. Free-stream static temperature, static pressure, and dynamic pressure temporal trend during a wind tunnel run. *Red dash lines indicate 2% bands deviation on mean value. This data was taken from the run of type AA cavity with doors opened at 90 degrees.*

Data from literature (Tracy & Plentovich, 1997) indicated that variations on the freestream quantities by this level of percentage, did not affected the spectral properties of the cavities. On the other side, it was decided to take into accounts these differences on environmental conditions between each experiment, so spectra and root mean square

fluctuations were compared using respectively FPL and OAFPL quantities (see Equations (3-45) and (3-46)). These on their own were calculated by using for each run the temporal mean of the dynamic pressure value. This enabled comparisons between different runs, thus reducing the influence of the variations on the environmental quantities.

3.4.3 DISCRETISATION ERROR

CFD simulations are influenced by round-off errors, dissipation of momentum fluxes induced by the numerical schemes, and especially turbulence modelling. Whenever DES modelling is used, a true mesh convergence is difficult to obtain because the more the grid is refined the more the eddy structures, characterising the flow, are resolved, up to the limit of LES modelling. Nevertheless, a validation of the mesh and the computational procedures was deemed necessary. No data was available for a full-scale configuration, however, the study of Chaplin & Birch (2012), consisting of both wind tunnel experiments and CFD simulations, was made available in the form of a complete dataset of information regarding a scaled UCAV1303/M219 geometry.

The validation process required the development of a wind-tunnel-size scale model, and the geometry described in Paragraph 2.1.1 was scaled by a factor of 1:10.8 (the scale factor was taken from Chaplin & Birch (2012) – Note that in the reference study and this study the Reynolds number based on cavity length was respectively equal to 5.12e+06 and 5.37e+06). An iterative procedure was used, whereby grids were constructed using the procedures described in Paragraph 2.1.2. After each computation, data was compared with the results obtained by Chaplin & Birch (2012) and errors in the peak values and location of the resonant mode were calculated. Each successive grid, in an iterative procedure, was constructed starting from the previous one, by adapting the mesh to the flow structure, in order to optimise the spatial organization of the elements. The iterations were stopped when the maximum computational limits of Cranfield University's HPC system were reached[18].

The comparison of the results obtained with the final grid with the data taken from Chaplin & Birch (2012) is shown in Table 3.9 and

[18] According to the FLUENT® user guide, for simulations involving 256 CPU cores (which was the maximum quota available per person at the Astral system); this limit is fixed around a mesh of 25e+6 elements.

Table 3.10. Although the errors were high, the situation was considered satisfactory for the overall aim of this study. In fact, the CFD simulations were aimed at exploring the effects of geometrical changes, and not to determine the exact performance of a given configuration. Therefore, as long as the procedures of mesh-building and case settings were held constant for all cases, and hence the error obtained was always similar, comparisons could be made with good confidence. A further refinement of the grid was not felt necessary because other parameters would have influenced the results. In fact, the Chaplin & Birch (2012) cavity dimensions were slightly different to those used in this simulation (L/D of 5.4 against L/D of 5.66), as well as the doors' installation (the presence of a gap between the door and the airframe surface and their relative distance with respect to the cavity's centreline). Particular attention was directed towards the three principal modes characterising the spectra of the pressure signals in the front and rear walls of the cavity. From

Table 3.10, it is possible to see how the error in prediction of the power levels of each mode was low for M1 and M2, with a value of 2%, while for M3 the percentage error was higher with a value of 7%.

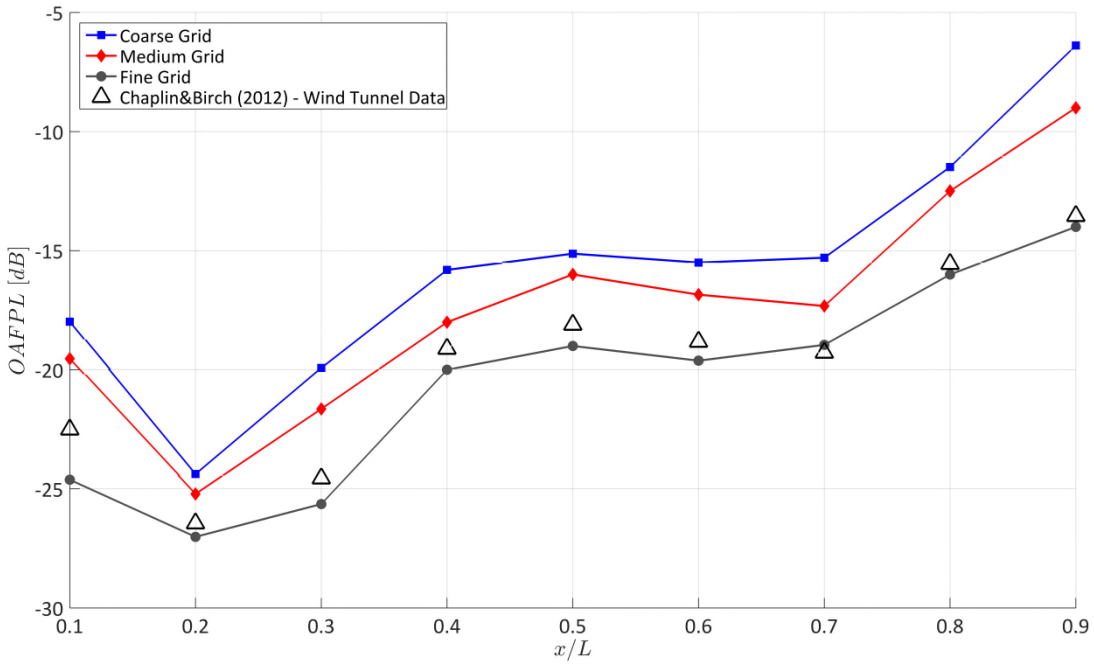

Figure 3.21 - Effect of grid resolution on the OAFPL value on cavity floor. *"Fine Grid" is the final grid obtained after the interruption of the mesh adaptation process.*

Table 3.9 - Comparison of the main resonance modes with data taken from Chaplin & Birch (2012).

Location	Mode	Current Study		Chaplin & Birch (2012) Wind Tunnel		Chaplin & Birch (2012) CFD	
		St	SPL [dB]	St	SPL [dB]	St	SPL [dB]
Front Wall	1st	0.2769	137	0.3505	137	0.3487	134
	2nd	0.6417	150	0.7722	150	0.7704	149
	3rd	1.0225	135	1.1675	127	1.1793	126
Rear Wall	1st	0.2769	146	0.3606	149	0.3779	145
	2nd	0.6417	158	0.7731	160	0.7722	156
	3rd	1.0225	144	1.2076	139	1.2761	138

Table 3.10 - Percentage error on the main resonance modes compared with data taken from Chaplin & Birch (2012).

Location	Mode	Error on Wind Tunnel[19]		Error on CFD[20]	
		% St	% dB	% St	% dB
Front Wall	1st	-20.0	+0.0	-20.5	+2.2
	2nd	-16.9	+0.0	-16.7	+0.6
	3rd	-12.4	+6.3	-13.2	+7.1
Rear Wall	1st	-23.2	-2.0	-26.7	+0.6
	2nd	-16.9	-1.2	-16.9	+1.2
	3rd	-15.3	+3.5	-15.3	+4.3

A poorer match was obtained regarding the Strouhal numbers at which each mode was located. In this case, M1 was located with a gross 20% error, M2 with 17%, and M3 with 15%[21]. Finally, agreement was much better for the OAFPL along the cavity floors. In this case, the maximum deviation registered between the final mesh configuration and the Chaplin & Birch (2012) data was always below ±3.5 dB (see Figure 3.21). Although the errors were appreciable, the precision obtained was considered satisfactory for the aim of this study. In fact, the CFD simulations were performed to explore the effects of

[19] Percentage error between the current study and the wind tunnel results of Chaplin & Birch (Chaplin & Birch, 2012).
[20] Percentage error between the current study and the CFD results of Chaplin & Birch (Chaplin & Birch, 2012).
[21] A similar finding was obtained by Khanal (2010). Such error was attributed to the numerical dissipation, introduced on the flow oscillations, by the discretization algorithm, used by the solver (a 3rd order scheme), of the momentum equations. He demonstrated that, with a proper upgrade of the discretization scheme, from the 3rd to the 4th order, it was possible to reduce considerably the error on the location of the Rossiter-Heller tones on the Strouhal axis.

geometrical changes and not to determine the exact performances of a given configuration. Therefore, as long as the procedures used for mesh-building and case settings were held constant for all cases, and hence the errors obtained were always similar, comparisons could be made with good confidence. Further refinement of the grid was therefore not considered necessary. Indeed, the Chaplin & Birch (2012) cavity dimensions were slightly different to those used in this simulation (L/D of 5.4 versus L/D of 5.66), as well as differences in the doors' installation (the presence of a gap between the door and the airframe surface and their relative distance with respect to the cavity's centreline).

4 GEOMETRY EFFECTS - WIND TUNNEL EXPERIMENTS

The trend in military airframe design has placed a great emphasis in the reduction of the radar cross section for improved survivability in a modern battlespace. Aerodynamic design, including weapons bays, has adapted to comply with stealth features for radar echo reduction. Therefore, serration of cavity leading and trailing edges is a common and necessary feature, which has not been studied in detail in the open literature. Hence, this chapter will be devoted to study the effect that is introduced when a standard cavity is modified to adopt a saw-tooth scheme at its front and rear edges. As described in paragraphs 3.2.1 and 3.1.2, two serrated-type configurations were derived from the reference one. The effect of the door opening angle was investigated as well, with two configurations tested, one at 90 degrees opening and the other at 120 degrees.

Pressure time-histories of 2^{17} samples which, recorded at F_s equal to 20 kHz, and constituting time histories of 6.5536 s in length, were collected during wind tunnel runs. The approach of triple decomposition (Hussain, 1986) was used to analyse the results, whereby the flow was divided into a time-mean part (mean flow analysis) and unsteady part (non-stationary flow analysis), with the unsteady part further divided into a coherent component (the Rossiter-Heller modes) and an incoherent component (broadband noise due to general turbulence).

Since, as summarised in Table 3.3, it was not possible to repeat the exact identical freestream conditions for each experiment it was decided to utilise FPL and OAFPL quantities to present the results instead of SPL and OASPL to enable a direct comparison of cavity aero-acoustic properties even if the environmental conditions are not the same.

Finally, the reference configuration was defined as the AA cavity type (straight leading and trailing edges) with doors open at 90 degrees.

4.1 MEAN FLOW ANALYSIS

The longitudinal $\bar{C}_p$ of the reference configuration (Figure 4.1) had a trend which assumed characteristics of both an open-type and a transitional-open type cavity (Tracy & Plentovich (1993)). In fact the mean-pressure-coefficient curve, while having a concave-convex shape, typical of transitional-type flows, always assumed positive values typical of closed-type flows. Such a characteristic, taking as a reference the flow schematics described by Tracy & Plentovich (1993), suggested the presence inside the cavity of a

main clockwise vortex, approximately centred at cavity station x/L = 0.5 (which indeed corresponded to the $\bar{C}_p$ curve inflection point), accompanied by two smaller eddies, located beneath the principal one and placed in the front and rear part of the cavity. In agreement with Tracy & Plentovich's (1993) classification, the front vortex was characterised by a counter-clockwise rotation, explaining the positive values of the mean-pressure coefficient in this area, while the rear vortex assumed a clockwise sense of rotation.

The $\bar{C}_p$ curve started with a value of 0.040 at x/L = 0.1 and dropped to reach an absolute minimum of 0.035 at x/L = 0.4. Coefficient values, from this station on, began to rise, reaching the absolute maximum of 0.14 at x/L = 0.8. The final value, at the cavity's rearmost station, was 0.115.

The introduction of BB and CC type geometries altered the mean pressure coefficient trend along the cavity floor. The BB type, maintained the same curve structure whilst increasing the longitudinal gradient. In this case the minimum and maximum $\bar{C}_p$ values were respectively 0.030 and 0.155. The inflection point was still at x/L = 0.5. If the CC geometry type was instead introduced, the curve underwent further changes. First, the minimum and maximum $\bar{C}_p$ values were very different from the reference case, with the former now assuming a value of 0.100 and the latter to 0.220. Secondly, the minima point was no longer located at x/L = 0.4, but was shifted to x/L = 0.3. Longitudinal positions of inflection and maximum points remained unchanged.

The changes introduced by the derived configurations could be correlated by a different displacement of the secondary vortices inside the cavity. Lower $\bar{C}_p$ values at the front of the bay indicated a rearrangement of the counter-clockwise vortex, with a displacement of its centre with respect to the position assumed in the reference configuration. Additionally the greater value of the longitudinal gradient of the $\bar{C}_p$ curve indicated that a change in the intensity of the main and rear clockwise vortices had occurred.

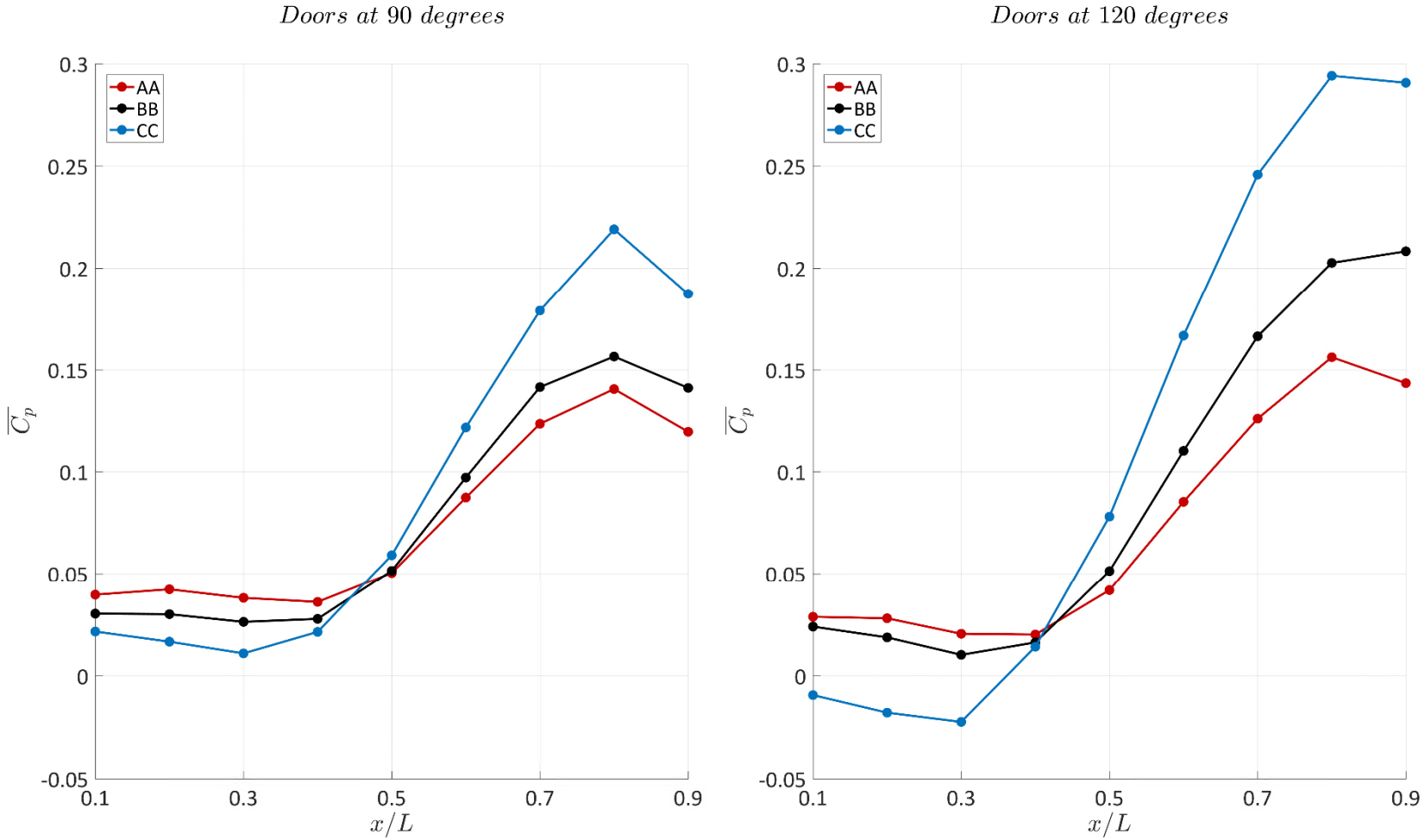

Figure 4.1 - Geometry effects on mean pressure coefficient. *Data refers to central rake.*

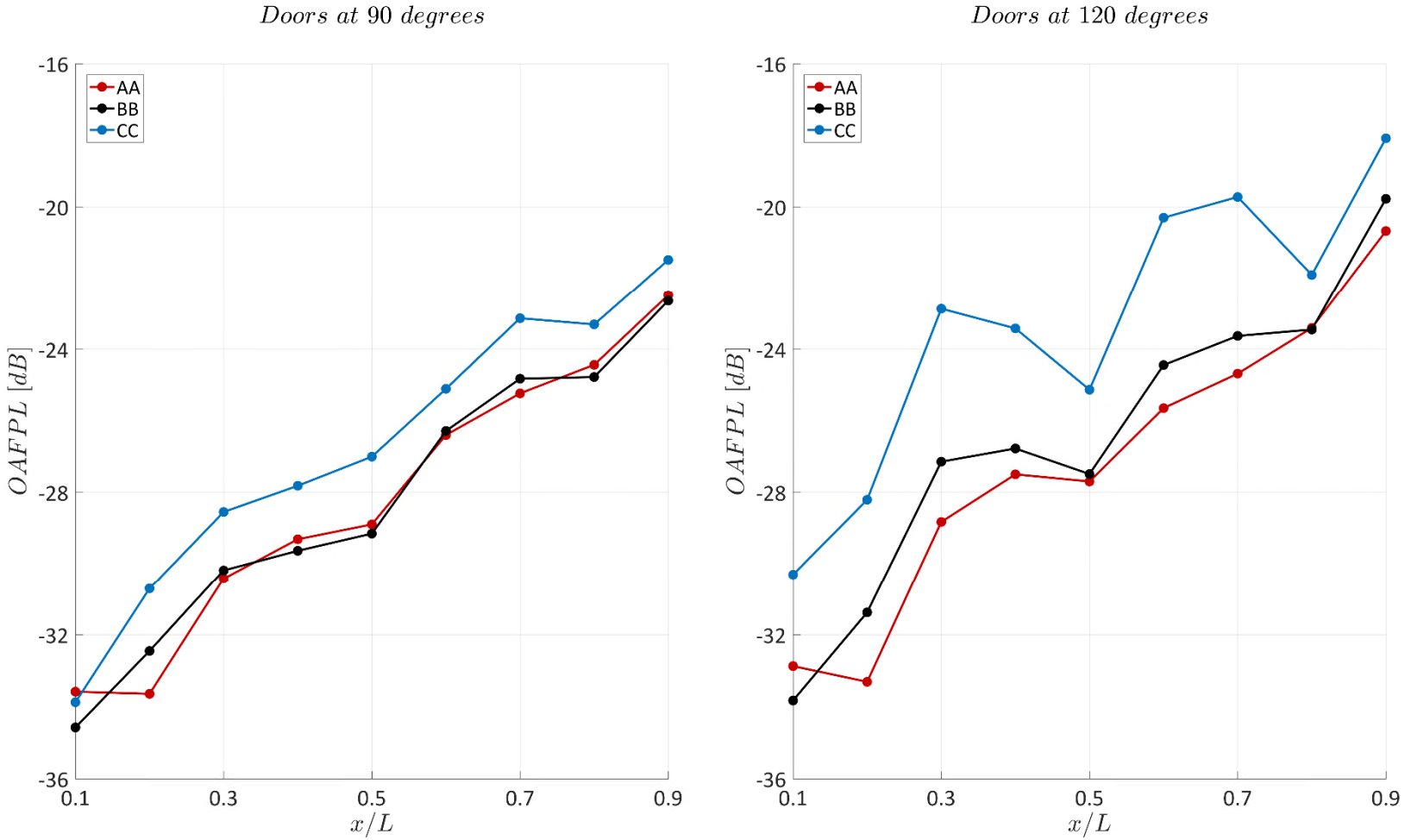

Figure 4.2 - Geometry effects on OAFPL. *Data refers to central rake.*

These changes may have been prompted by the different status of vorticity injected into the shear layer due to the indentation profile present in configuration BB and CC[22]. Nevertheless, since no flow visualisation was possible at this stage, additional explanation on flow changes could not be given.

When the door position was changed from 90 degrees to 120 degrees open, the effect, for all configurations, was an increase of the longitudinal gradient of the mean-pressure coefficient curves. The AA type cavity saw its minimum $\bar{C}_p$ drop to 0.020 and its maximum rise to 0.160. The BB type cavity also had a similar change, with a minimum value of 0.01 and a maximum of 0.205. The longitudinal position also changed, from x/L = 0.8 in the 90 degree door configuration, to x/L = 0.9 in the 120 degree configuration. Finally, geometry CC underwent the most significant changes. The mean pressure coefficient assumed negative values up to x/L = 0.4, with the minimum of -0.025 located at x/L = 0.3. The subsequent rise in pressure was the greatest between all the tested cases, with a peak value of 0.295 obtained at x/L = 0.8.

Similar conclusions were derived in the analysis of the OAFPL charts (Figure 4.2). The reference configuration curve has a triple "V" shape, with levels ranging from -33.5 dB at the front most station to -22.5 dB at the rear most station. Configuration BB values were nearly the same as AA ones, with the only difference that, in the former case, the curve, starting from x/L = 0.1, had a positive gradient up to x/L = 0.4, a negative gradient between x/L = 0.4 and x/L = 0.5, and a positive gradient for the rest of the cavity. The latter instead, presented a negative gradient from x/L = 0.1 to x/L = 0.2, while for the rest of cavity's length an OAFPL curve with positive gradient was observed. Configuration CC has the same shape as the BB geometry; however, the whole curve was translated upwards by 1 dB. Again, the opening of doors at 120 degrees augmented the pressure load at all stations, with the overall maximum values, at x/L = 0.9, rising to -20.5 dB, -19.7 dB, and -18.0 dB respectively for the AA, BB, and CC geometry configurations. Additionally, the CC cavity assumed a much more pronounced double-"V"-shape[23] with respect to the 90 degrees doors case. Again, the change of the curves with different geometry configurations was attributed to a different displacement of the three-vortex system inside the cavity.

The outcome obtained when the door position effects were tested was not in line with expectations. As demonstrated in previous studies (Murray & Jansen, 2012), the introduction of

[22] Such hypothised changes were subsequently confirmed by CFD analysis which made possible a direct visulalisation of the velocity vector field (see Paragraph 5.1).
[23] Such double-V shape is considered due to the presence in the curve of two local minima (x/L = 0.5 and x/L = 0.8), excluding the absolute minimum at x/L = 0.1.

doors usually causes a deterioration of the aero-acoustic characteristics (i.e. an increase of the overall power of the pressure fluctuations). It was expected that a door opening angle of 120 degrees would have offered better performance with respect to the 90 degree door configuration, in which the flow was constrained more by the doors. Nevertheless, OAFPL analysis demonstrated the opposite and better performance was obtained by opening the doors at 90 degrees. The reason of such an outcome could be explained by looking to a section view of the cavity with the different door configurations (Figure 4.3). When the doors assumed a 90 degree opening angle there was a gap between the wall and the doors themselves. Air could spill inside the cavity through the aperture, which had a beneficial effect, reducing the constraint on the flow. Such an aperture did not exist when the doors were open at 120 degrees, because they were in direct contact with the wall, obstructing the lateral spillage of air, and placing the cavity in a worse condition.

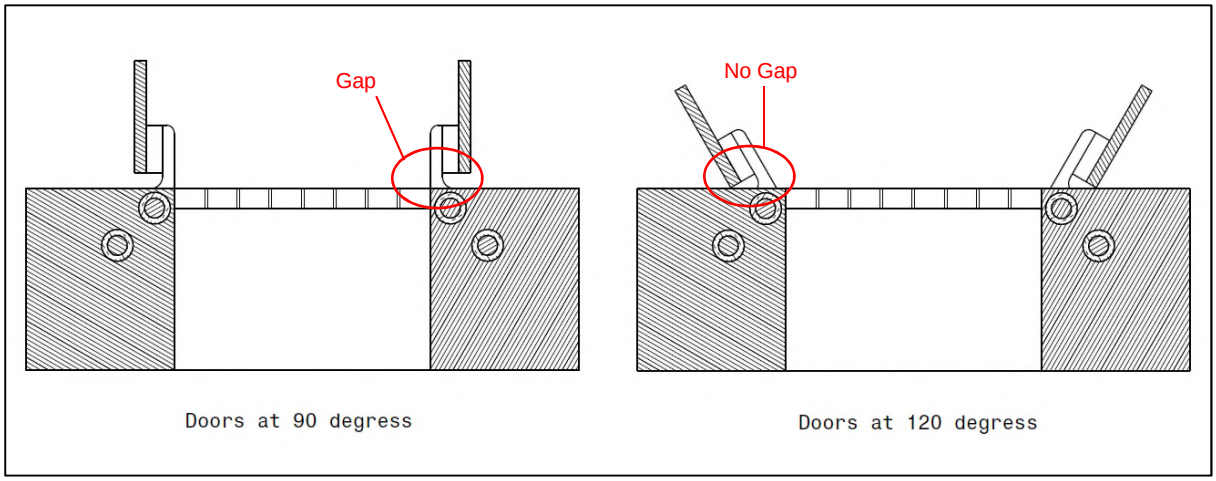

Figure 4.3 - Cross section view of cavity with doors open at 90 and 120 degrees. *The section is a cut in the cavity YZ plane, looking downstream.*

4.2 NON-STATIONARY FLOW ANALYSIS

Non-stationary flow analysis concentrated on the pressure histories recorded at station x/L = 0.9 which, as indicated in the OAFPL plots (Figure 4.2), had the highest OAFPL. The FPL analysis of the reference configuration (Figure 4.4) identified four Rossiter-Heller modes: M1 (St = 0.227, FPL = -53.13 dB), M2 (St = 0.7895, FPL = -49.09 dB), M3 (St = 1.1540, FPL = -51.49 dB), and M4 (St = 1.296, FPL = -54.40 dB). Their values were close to the theoretically-predicted values, with the second mode, M2 being the dominant tone. It was also observed that lower frequency (St<0.08) spectra amplitudes were less for doors at 90 degrees compared to 120 degrees. While the exact origin of this phenomenon was unknown, it was assumed to be correlated to the different mass flow blockage that the two doors position induced on the tunnel.

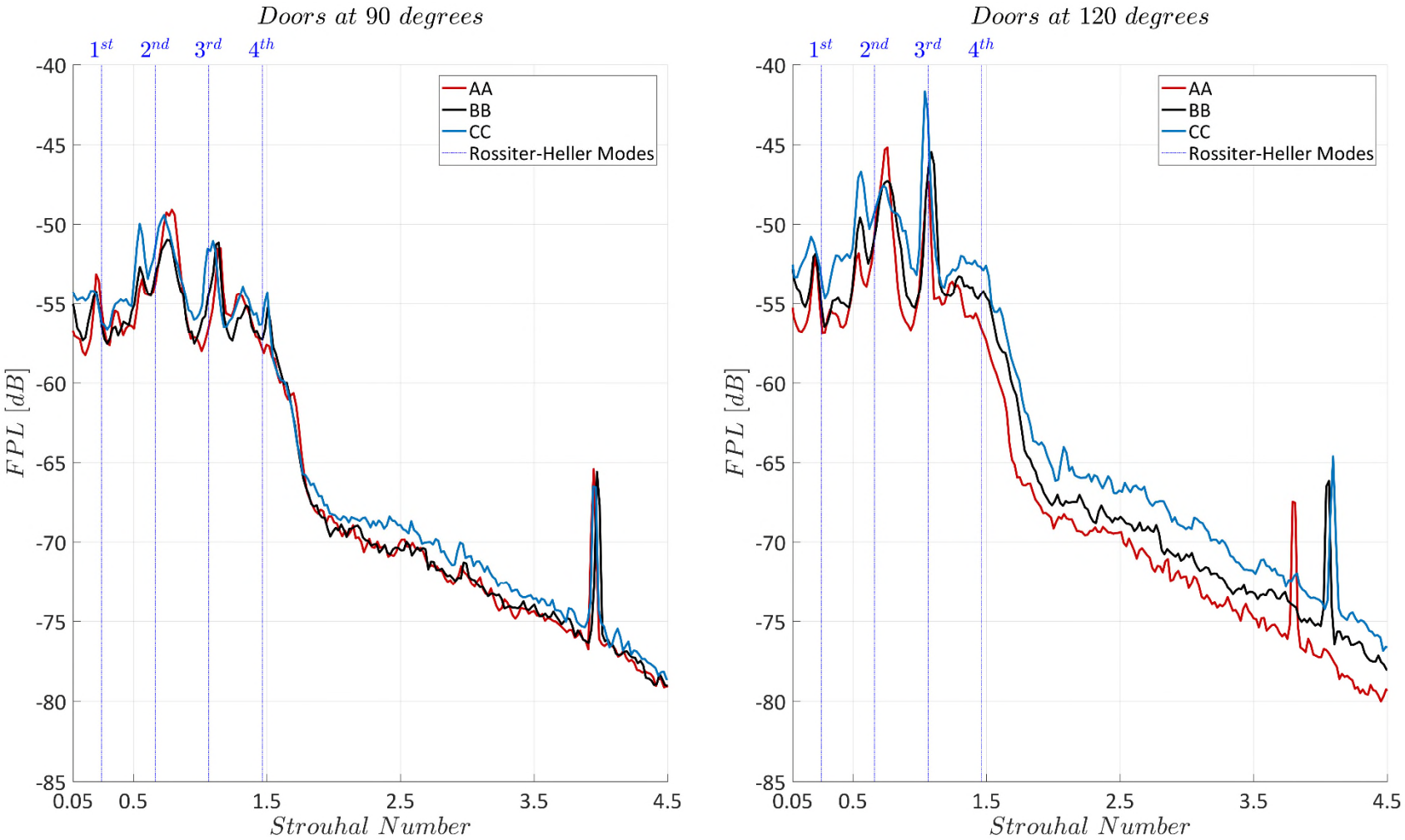

Figure 4.4 - Geometry effects on FPL. *Data refers to pressure probe located at x/L = 0.9, 2y/W = 0.0, z/D = 1.0.*

Analysing the power spectrum of the freestream Mach number, it was observed that the tunnel test-section velocity oscillated, within the limits described in paragraph 3.4.2, more with doors at 120 degrees than doors at 90 degrees, behaviour which was assumed to be responsible for the difference in spectral response of the two door configurations at such low Strouhal number.

No qualitative spectra change was observed between doors at 90 and 120 degrees, indicating that a similar fluid resonant mechanism developed in both door opening positions. The differences observed were only quantitative with doors at 120 degrees experiencing higher FPL values for the resonant tones.

In the Fourier spectrum it was also possible to observe additional peaks with the most prominent being the one located at a Strouhal number of 3.9480 and a FPL value of -65.42. Such a mode was unexpected. The theoretical formula (Equation (2-3)), indicated it as a 10^{th} Rossiter-Heller tone, however, it was considered unlikely that such a wave should be associated with the typical longitudinal flow phenomenon. The corresponding wavelength was 89.27 mm, a value slightly greater than the cavity width. It was then hypothesised that such a mode was a transverse oscillatory phenomenon, occurring in the shear layer, and favoured by the restraining presence of the doors. Following this hypothesis, the tone was labelled Mt. The theory was subsequently confirmed by CFD computations, which permitted the visualisation of the wave in transverse oscillations of the shear layer (see the discussion in Paragraph 5.2).

The adoption of configuration BB introduced little variation. The Strouhal numbers corresponding to the tones was unchanged. The main difference was registered for M2, which experienced a decrease of 2 dB with respect to the reference case. The major changes were instead observed with the CC-type geometry. In this case, a new peak, named Sb, located at a Strouhal number of 0.5488 and with a FPL value of -49.97 dB, appeared in conjunction with M2. To have a better view on this particular mode it was decided to apply the JFTFA technique to the pressure signal. Figure 4.6b reports the result of the STFT analysis (or spectrogram)[24]. The time-frequency map is accompanied by the standard Fourier spectrum (Figure 4.6.a) for ease of interpretation. All four Rossiter-Heller tones, identified from the frequency domain analysis, had their equivalent in the spectrogram map. The main feature observed was the intermittency of every resonant tone. The PR index (see Equation (3-41)) for each mode was respectively:

[24] Repeat run analysis indicated that the temporal evolution of the signal was influenced by the initial conditions of the test and data acquisition. Nevertheless, features like mode switching and amplitude modulation always occurred in the signal. Hence the aim of this temporal analysis was to get additional information on what triggered these non-stochastic phenomena.

44.56% for M1, 95.81% for M2, 97.06% for M3, 96.92% for M4, 83.24% for Mt, and 89.90% for Sb. Analysing the map, it was decided to zoom in on the temporal plane and pass the extracted interval to wavelet analysis. Such a procedure unveiled the temporal trend of the modes whilst not losing resolution on frequency. The chosen interval, from 1.4 to 1.6 seconds, was selected because, during this time, M2 and Sb reached their maximum peak power. This could be evidenced by analysing the band-integrated SPL quantity (BISPL), defined as:

$$BISPL(n) = 10 \cdot log_{10}\left(\frac{\frac{2}{F_s \cdot N} \cdot \frac{1}{(k_2 - k_1)} \cdot \sum_{k=k_1}^{k_2} \widehat{SX}(k,n) \cdot \widehat{SX}^*(k,n)}{p^2_{reference}}\right) \quad \textbf{(4-1)}$$

Here $\widehat{SX}(k,n)$ is the STFT of the signal calculated using Eq.(3-12). This quantity enables the monitoring of the temporal trend of the SPL contained in a determined Strouhal (frequency) band. As shown in Figure 4.5 the BISPL values of M2 and Sb reached an absolute maximum in the interval chosen for the analysis.

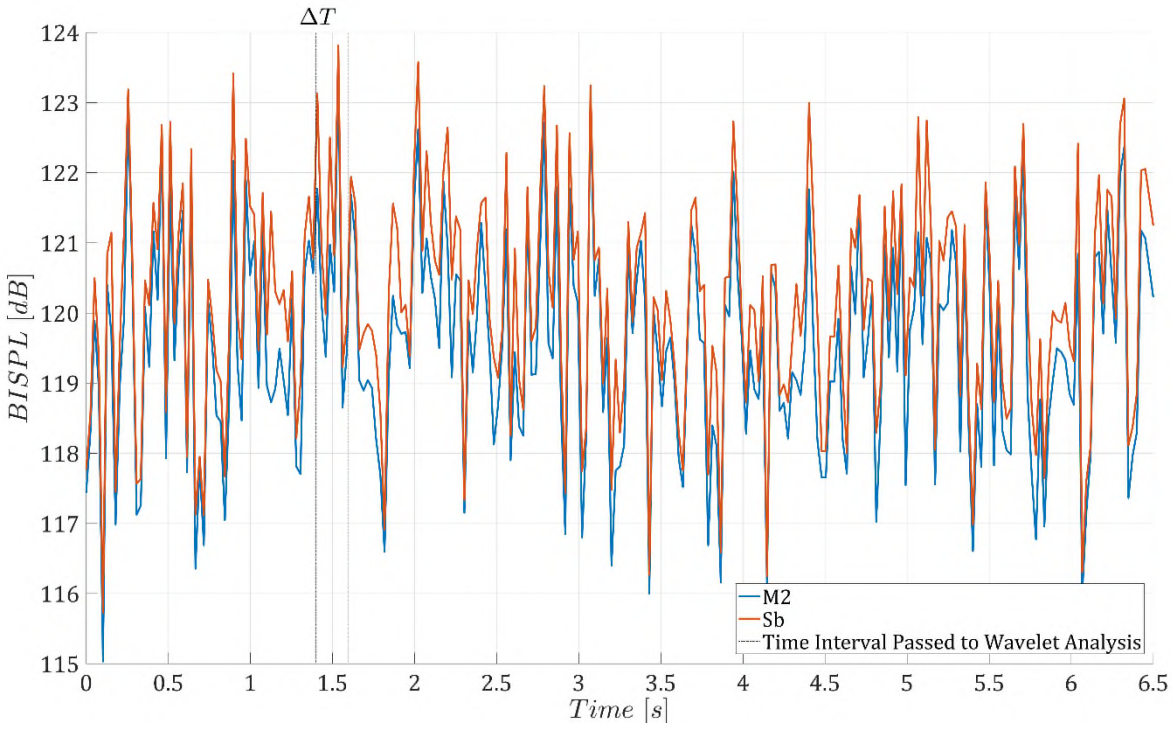

Figure 4.5 - BISPL trend for M2 and Sb. *Data refers to configuration CC, doors at 90 degrees.*

The result of the wavelet analysis of this interval is shown in Figure 4.7, which is divided into 4 parts. Figure 4.7a shows the standard FPL curve, derived from the Fourier transform of the signal.

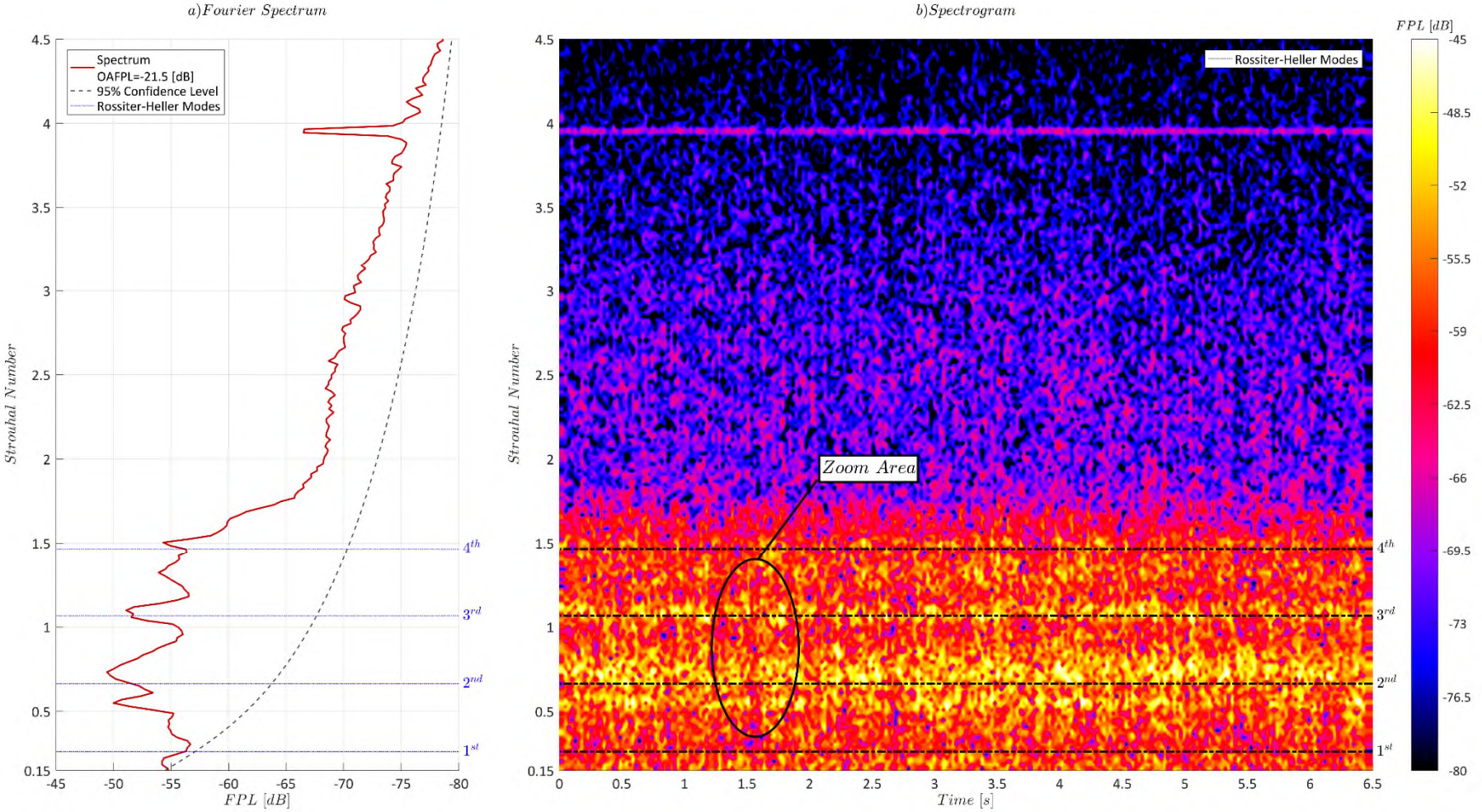

Figure 4.6 - STFT analysis of pressure signal at x/L = 0.9, $2y/W$ = 0.0, z/D = 1.0. *Data refers to configuration CC, doors at 90 degrees. The ellipse indicates the significant temporal event around which the wavelet analysis was performed.*

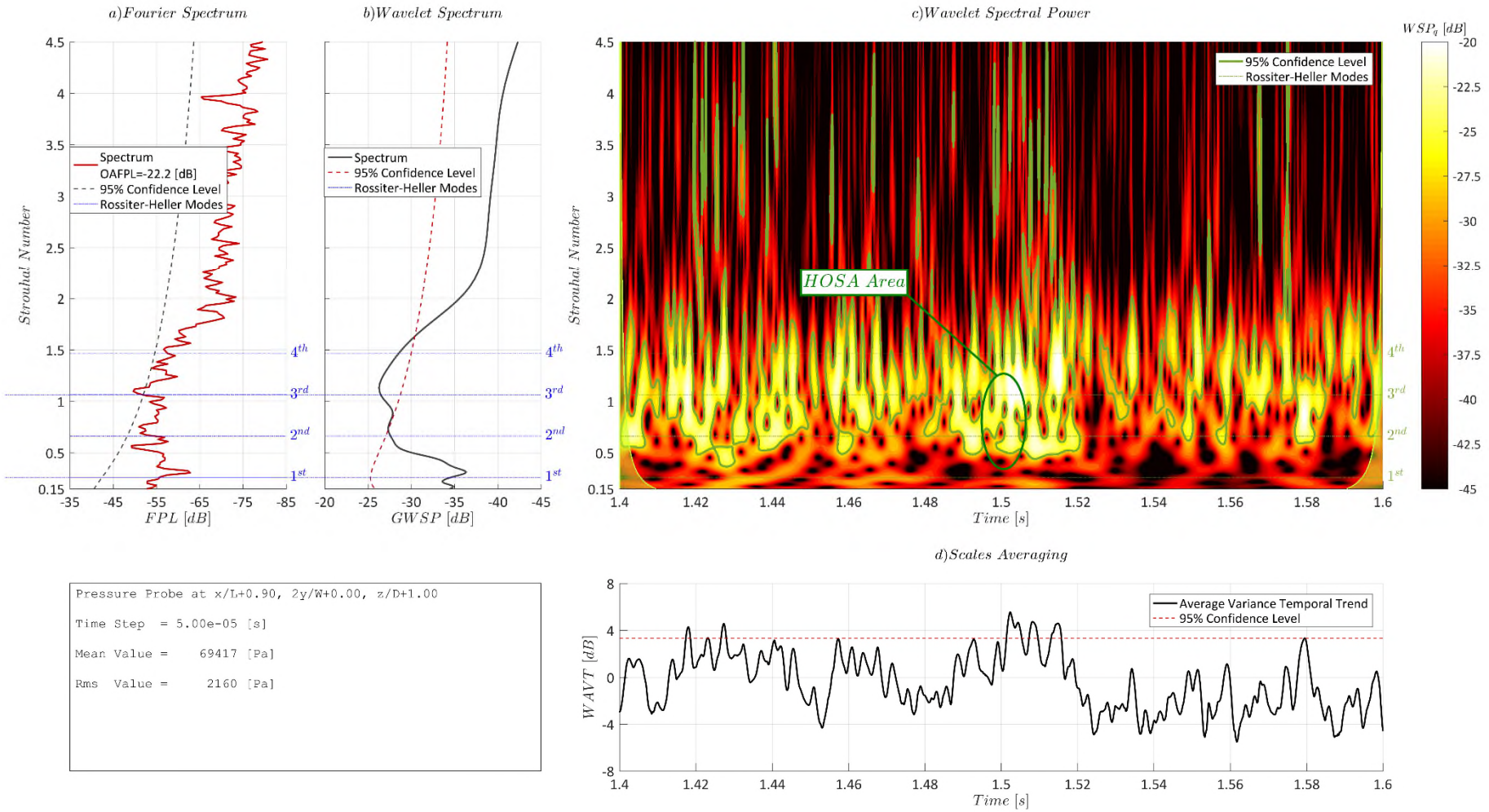

Figure 4.7 - Wavelet analysis of pressure signal at x/L = 0.9, $2y/W$ = 0.0, z/D = 1.0. *Data refers to configuration CC, doors at 90 degrees, time interval from 1.4 to 1.6 seconds. The ellipse indicates the significant temporal event around which the wavelet bi-coherence analysis was performed.*

Figure 4.7b instead represents the WSP quantity. In both plots, the 95% confidence level[25] threshold is shown. Peaks above this curve have a 5% possibility to be a false feature of the flow and 95% possibility to be a true feature. Finally, lines indicating the location of the theoretical value of the Rossiter-Heller tones were added. Figure 4.7c shows the time-frequency map obtained by the wavelet analysis of the signal. Confidence level thresholds are drawn as green contour lines. The map also reports the cone-of-influence (green-shaded areas at the edges), which regroups all the points influenced by the finite nature of the signal (also referred to as the signal truncation transform error). The map colour reflects, at each point, the WSP quantity allocated at that particular time, in that particular frequency. Finally, Figure 4.7d represents the wavelet scale averaged power, or WAVT. Figure 4.7a (Fourier spectrum), confirmed the existence of all the tones, even if, considering such a short-duration time interval, only M3 acquired enough power to cross the confidence level threshold. In the GWSP plot, only M2 and M3 had enough power to be considered true features (Figure 4.7b). Curiously, Mt and M4 appeared only in the wavelet map (Figure 4.7c), while M1, was never able to cross the confidence level due to its low temporal intermittence (see Figure 4.7b[26]). Sb and M2 continued to co-exist, with the former having a minor persistence with respect to the latter (22.29% for Sb and 34.56% for M2) as in the STFT analysis.

In order to understand if Sb was a proper tone or the effect of non-linear interactions, it was decided to utilise HOSA methodologies, applying the wavelet bi-coherence transform (WBC). A time interval from 1.50 to 1.51 seconds was chosen to perform the summation in time using Equation (3-40). In such a temporal frame, both M2 and Sb had high energy levels and the signal expressed the maximum value of WAVT. Figure 4.8 shows the results obtained. This figure represents all the possible combinations of the Strouhal vector, spanning from 0.0 to St_N[27]. The coordinates of each point in the (St_I, St_J) plane establish, with their algebraic sum, a triad of Strouhal numbers whose squared bi-coherence value is expressed at that precise location. The symmetrical nature of the transform properties (Kim & Powers, 1979) enable it to be applied only inside the triangle defined by the coordinates [0 0; $St_N/2$ $St_N/2$; St_N 0] (Note that Figure 4.8 shows a zoom on the left side of the validity domain for ease of visualization). The squared bi-coherence varies from 0.0 to 1.0 whereby 0.0 denotes a complete absence of coupling while

[25] The value of 95% (equivalent to 2 standard deviations), was chosen since it is common in the literature (see Torrence & Compo (1998)) to use such a number when dealing with non-stationary wavelet analysis of time series.
[26] M1 has a cycle of on-off activity with a period of 0.4 seconds, a value bigger than the interval used for wavelet analysis. Hence, the latter classified it as an ordered phenomenon (i.e. a wave) but with insufficient power to be considered a true feature of the flow.
[27] Note that St_N is the equivalent Strouhal number of the Nyquist frequency value.

1.0 indicates that the three Strouhal numbers are 100% power coupled, i.e. the power content of one of them is completely induced by the non-linear interaction of the other two. Since the energy transfer process has no sign in the supporting mathematical formula, there is no way of telling whether the energy is passed through a sum- $(St_K = St_I + St_J)$ or difference- $(St_I = St_K - St_J \ , \ St_J = St_K - St_I)$ type process. Thus, the sum-type process shown in the figure does not imply anything regarding the direction of the energy flow. The wavelet bi-phase is instead indicated by arrows, with 0 degrees pointing right, 90 degrees pointing up, 180 degrees pointing left, and 270 degrees pointing down.

In the WBC map an area of high squared bi-coherence, with values exceeding 0.90 and bi-phase 0.0, was distinguished. This zone of the plot identified a triplet composed by Sb, and the first and second sub-harmonics of M2, implying that the additional mode was a tone prompted by the non-linear interactions between M2's sub-harmonics, and generated by the quadratic interaction of the second Rossiter-Heller tone with itself.

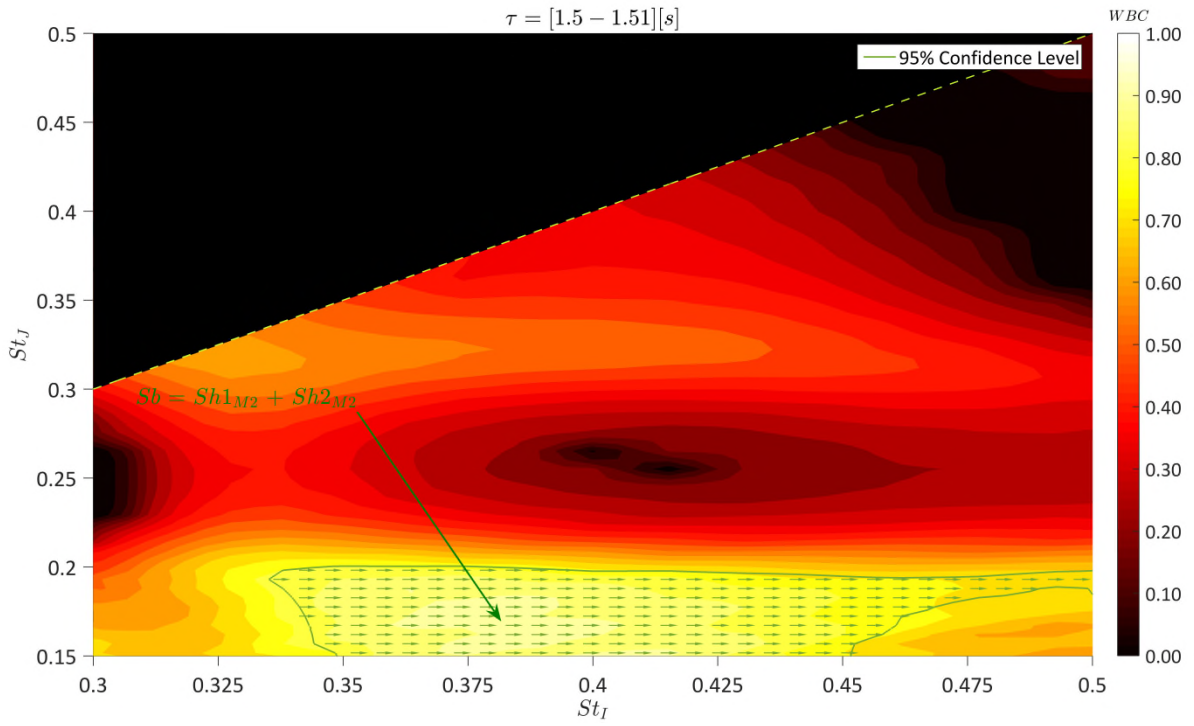

Figure 4.8 - Wavelet bi-coherence analysis for pressure signal at x/L = 0.9, $2y/W$ = 0.0, z/D = 1.0. *The time interval of integration is from 1.50 to 1.51 seconds. Arrows indicate wavelet bi-phase. Data refers to configuration CC, doors at 90 degrees.*

The non-linear generation of sub-harmonics in acoustic systems was described by Yen (1971) as a process occurring whenever the medium is prone to non-linear behaviour. Perturbations generating the wave must be of extremely high amplitude, physical obstacles must be present to confine the energy spreading, and the waves must exhibit an unstable behaviour. All these

conditions were easily met by the cavity operating in a transonic environment, justifying the generation of sub-harmonics of M2.

When doors were kept open at the larger angle of 120 degrees, the situation deteriorated for all cavity configurations (Figure 4.4). All tones increased their power, as well as the broadband noise. The reference geometry AA experienced a 5 dB FPL increase of the main modes M2 and M3, while Mt changed its Strouhal number from 3.948 to 3.792. Finally, M4 was hidden by noise and was no longer distinguishable as an individual tone. In configurations BB and CC, there was a change also in the structure, since the new door-opening angle resulted in M3 being the strongest tone instead of M2 as was shown in the 90 degrees case. Moreover, the CC-type cavity experienced a 13 dB increase in M3 power, and presented the curious case in which Sb had a FPL higher than its progenitor M2. Such a rearrangement of the spectrum structure was a direct consequence of the effect of the leading and trailing edge geometry indentations on the shear layer[28].

In order to understand better the fluid-resonant behaviour occurring within the cavity, the stream wise variation in FPL associated with each tone was plotted. Figure 4.9 reassumes the power's trend along the central rake for M1, M2, M3, M4, Mt, and Sb. In general, M1, M2, and M3 followed the theoretical rule of Tracy & Plentovich (1997), in which it is stated that the trend of the tones peaks along the cavity length assumes the shape of a curve with a number of minima equal to the mode number. M1 had a single "V" trend with local minima located around the centre of the cavity and this shape did not vary with the adoption of different geometries. Such an outcome was expected; since M1's wavelength is bigger than the cavity length, local details played no influence on this mode. M2 had a double "V" shape, with minima located at x/L = 0.2 and x/L = 0.7. The doors opening at 120 degrees slightly changed the position of the second minima point, moving it forward to x/L = 0.6. M3's theoretical triple "V" shape was barely recognisable, since the most forward-located minimum point, usually placed between x/L = 0.1 and x/L = 0.3, did not appear in all configurations. The other two minima points were less influenced by geometry and tended to maintain their reference positions at x/L = 0.5 and x/L = 0.8. M4 did present a multiple minima behaviour; nevertheless, its trend did not exhibit a proper regularity expressed by the theoretical rule. Of particular interest was the trend of Sb which exactly matched the one of M2, confirming its origin derived in the HOSA analysis. Mt on its own revealed that its nature was not the one of a Rossiter-Heller-like mode. The assumed flat

[28] With the subsequent CFD simulations, it was possible to visualise the vorticity and its relative change according to the cavity's geometry. See the discussion in Paragraph 5.2.

behaviour across the whole cavity length indicated a local phenomenon not triggered by a standard longitudinal resonance mechanism.

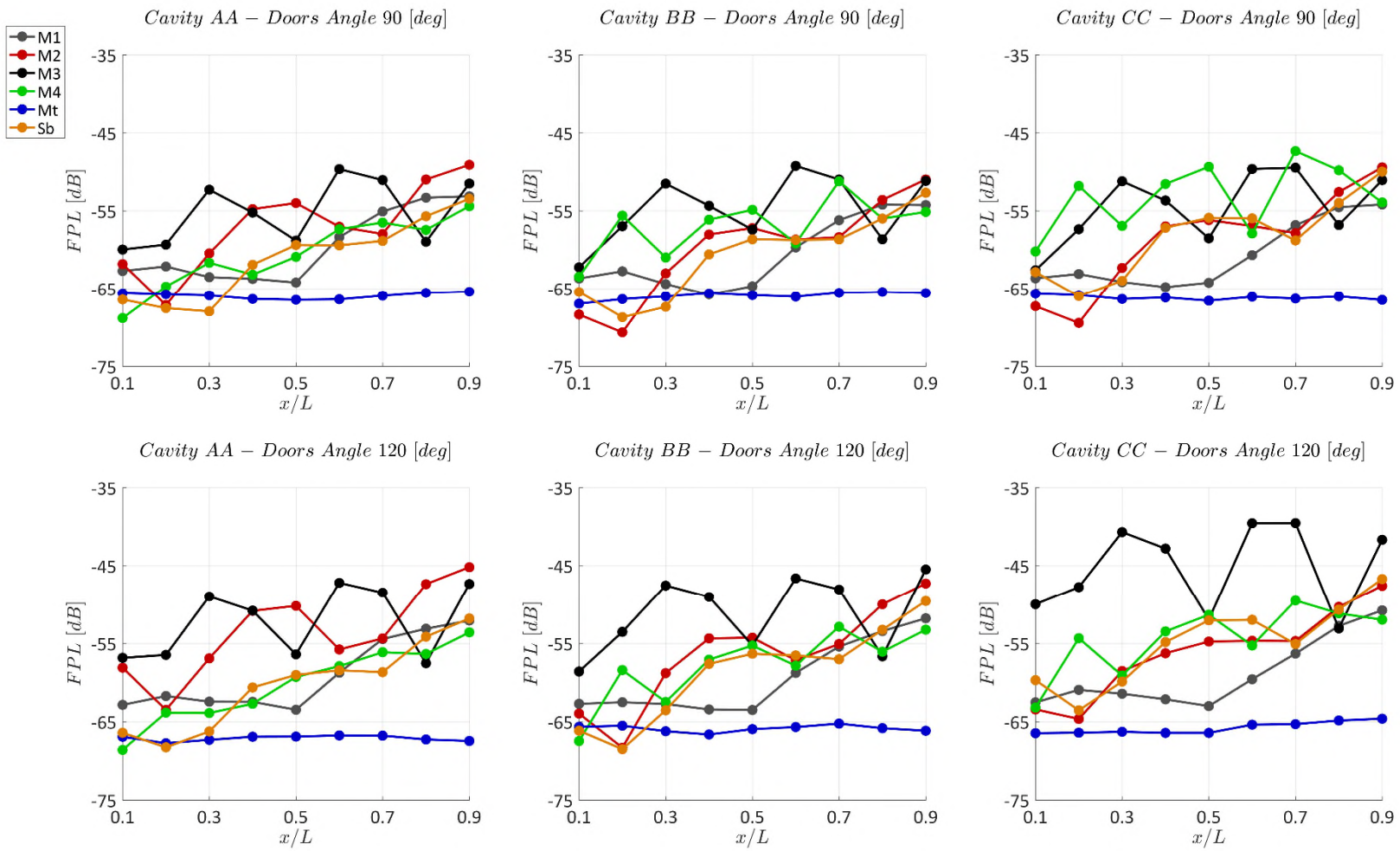

Figure 4.9 - Mode shape comparison along cavity centreline.

4.3 CHAPTER CONCLUSIONS

The wind tunnel analysis of the indentations and door-opening angle effects on an M219-derived cavity demonstrated that these two geometrical features influenced the aero-acoustic response of the cavity, both quantitatively and qualitatively. The reference case AA, had the typical behaviour of a transitional-type cavity. The mean pressure coefficient curve, along the cavity length, had a concave-convex shape, with values always positive. The OAFPL longitudinal trend was characterised by a triple "V" shape, with the maximum value attained at the cavity's rear face. The introduction of the geometries with indentations (BB and CC cavity types) did not alter the behaviour of the mean flow properties, but only affected the overall values. The $\bar{C}_p$ curves experienced an increase of the longitudinal gradient, with configuration CC having the highest effects. OAFPL curves were instead similar for configuration AA and BB, while in configuration CC, at all longitudinal stations an increase of 1 dB respect to the reference geometry was observed. Changing the door-opening angle had more profound effects. Again, while the general shape of the curves, of the mean flow properties, remained unchanged, the absolute values were affected. Contrary to what was expected, a door angle of 120 degrees increased the longitudinal pressure gradient and increased the OAFPL values no matter which cavity geometry was tested. The cause was found to be due to the gap between the doors and the surface surrounding the cavity. Such a gap was open with the doors at 90 degrees and closed with the doors at 120 degrees. Closing the gap obstructed the spillage of air through it, which had detrimental effects on the overall aero-acoustic properties of the cavity.

Non-stationary flow analysis identified the presence of four Rossiter-Heller tones, M1, M2, M3, and M4, with Strouhal values close to the theoretically-predicted ones. An additional resonant peak, called Mt, was registered in all configurations. While its Strouhal value might have characterised it as a 10th Rossiter-Heller mode, its power trend at different cavity longitudinal stations did not present variations. This induced the hypothesis that such a mode was not a Rossiter-Heller type tone but rather a local phenomenon, probably correlated with the transverse dimension of the cavity. The introduction of the BB geometry did not influence in any appreciable way the shape of the spectrum. Conversely, the CC configuration, introduced an additional tone. JFTFA indicated that this mode, labelled Sb, was the product of the non-linear interaction of the first and second sub-harmonics of M2.

The change of door angle to 120 degrees, in accordance, with the OAFPL analysis results, elevated the power response in all spectra. Particularly profound changes were encountered in the CC configuration, where M3 experienced an abrupt rise of 10 dB and became the dominant mode, while Sb acquired more power than its progenitor M2.

Finally, the time-frequency maps indicated that all modes assumed an intermittent behaviour during the temporal evolution of the signal. These “on/off” cycles were quite regular and their periods varied from mode to mode.

Table 4.1 - Summary of the main modes for all geometry configurations. *All data refers to the analysis of pressure signals recorded at station x/L 0.9, 2y/W 0.0, z/D 1.0. See Figure 4.10 for scatter plot representation.*

GEOMETRY	DOORS ANGLE [deg]	MODE ID	St	FPL [dB]	OAFPL [dB]
AA	90.0	M1	0.2227	-53.13	-22.48
		M2	0.7895	-49.09	
		M3	1.1540	-51.49	
		M4	1.2960	-54.40	
		Mt	3.9480	-65.42	
BB	90.0	M1	0.2240	-54.25	-22.63
		M2	0.7739	-51.01	
		M3	1.1410	-51.15	
		M4	1.5070	-55.27	
		Mt	3.9710	-65.59	
CC	90.0	M1	0.1829	-24.19	-21.48
		M2	0.7317	-49.42	
		M3	1.0980	-51.05	
		M4	1.5040	-54.30	
		Mt	3.9430	-66.50	
AA	120.0	M1	0.2139	-52.08	-20.67
		M2	0.7585	-45.19	
		M3	1.0700	-47.34	
		Mt	3.7920	-67.46	
BB	120.0	M1	0.2258	-51.80	-19.77
		M2	0.7596	-47.29	
		M3	1.0880	-45.48	
		Mt	4.0650	-66.16	
CC	120.0	M1	0.1871	-50.78	-18.08
		M2	0.7276	-47.58	
		M3	1.0390	-41.68	
		Mt	4.0960	-64.62	

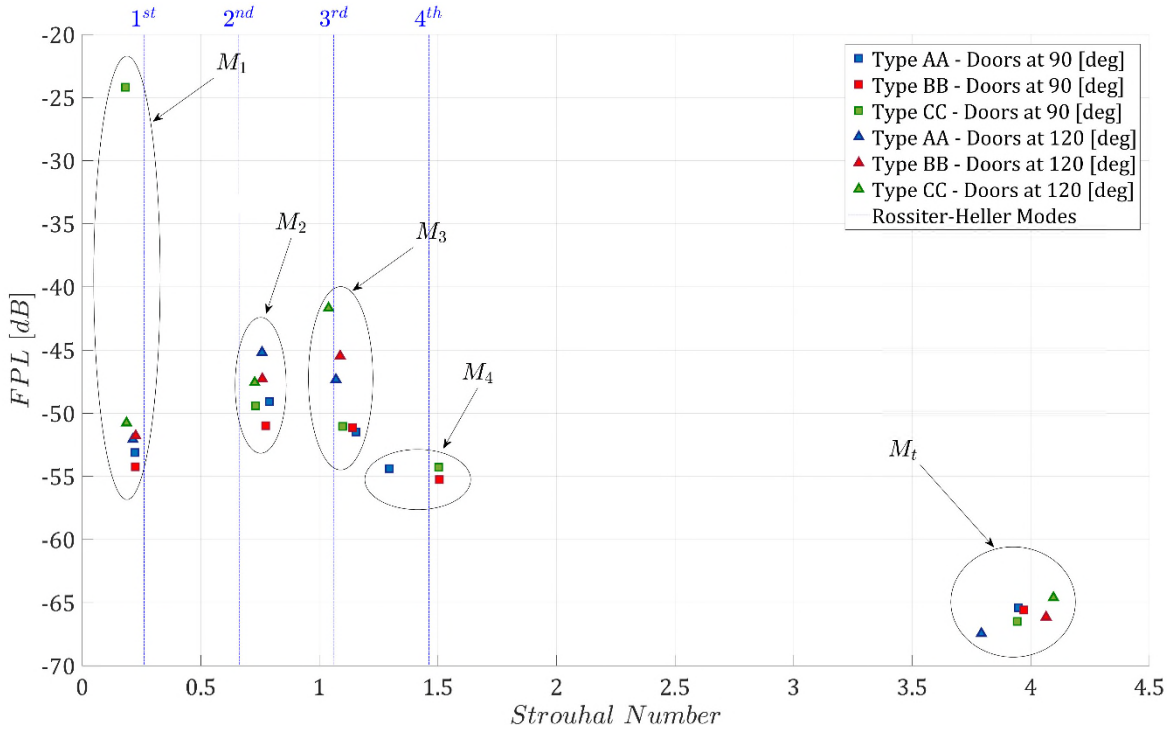

Figure 4.10 - Summary of the main modes for all geometry configurations. *All data refers to the analysis of pressure signals recorded at station x/L 0.9, 2y/W 0.0, z/D 1.0.*

5 GEOMETRY EFFECTS - CFD SIMULATIONS

All the CFD simulations had a duration of 2 seconds, excluding the initial set-up time. In all cases, angles of attack and sideslip were null. Being a time-consuming procedure (each case required a total wall-clock time of approximately 40 days, using 256 cores @ 2.1 GHz), it was decided to analyse only three configurations (cavity types AA, BB, and CC) installed on a UCAV airframe, with doors positioned at 90 degrees opening.

Again, the approach of triple decomposition (Hussain, 1986) was used to analyse the results. Mean pressure, mean velocity, and OASPL quantities were investigated and analysed to address mean flow properties, while the non-stationary part of the analysis used the Fourier, wavelet, and HOSA procedures.

Finally, the short temporal length of the signal histories, typical of these CFD simulations (usually in the order of a thousand samples) were also a good benchmark to demonstrate the strength of the double frequency domain/time-frequency domain capabilities of the JFTFA technique.

5.1 MEAN FLOW ANALYSIS

The longitudinal mean pressure coefficient (Figure 5.1) had the typical trend of a transitional-open type cavity, with a shallow negative gradient up to x/L = 0.4, in which the $\bar{C}_p$ always assumed negative values, ranging from -0.22 to -0.25, followed by an increase towards positive values, in which the curve changed from concave to convex and where the longitudinal gradient became positive. The effects of leading and trailing edge saw-tooth modifications were essentially minimal. Results indicated that the mean pressure coefficient was much more dependent on general parameters like cavity L/D, rather than to geometric details in which the derived geometries differed with respect to the reference one. The shape and the values measured for the mean pressure coefficient were not in accordance with the reference wind tunnel study of Tracy & Plentovich (1993) and a marked difference between the wind tunnel and CFD curves was observed. The cavities were expected to have an open-type mean flow structure, with positive pressure coefficients. The discrepancy was attributed to the influence of the UCAV's lower surface pressure gradient and, as shown in Figure 5.1, such behaviour had already been observed by Lawson & Barakos (2010) in their CFD analysis of a UCAV1303/M219 configuration scaled to wind tunnel dimensions. The deviation between the $\bar{C}_p$ curves observed in the experiments and the ones obtained in the CFD simulations could be explained by the fact that, in the latter case, since the cavity was installed in an UCAV airframe, it would have been subjected to induced pressure gradients. Such gradients, when applied to a low-speed flow, like

the one inside a cavity, could have been capable to influence the arrangement of the mean-velocity vortex structures hence altering the mean pressure coefficient values at bay's floor. Furthermore, CFD analysis suggested that, being the $\bar{C}_p$ values inferior respect to wind tunnel experiments, a higher mean velocity was encountered through the cavity. Again this phenomenon could have been induced by pressure gradients present in the UCAV's belly.

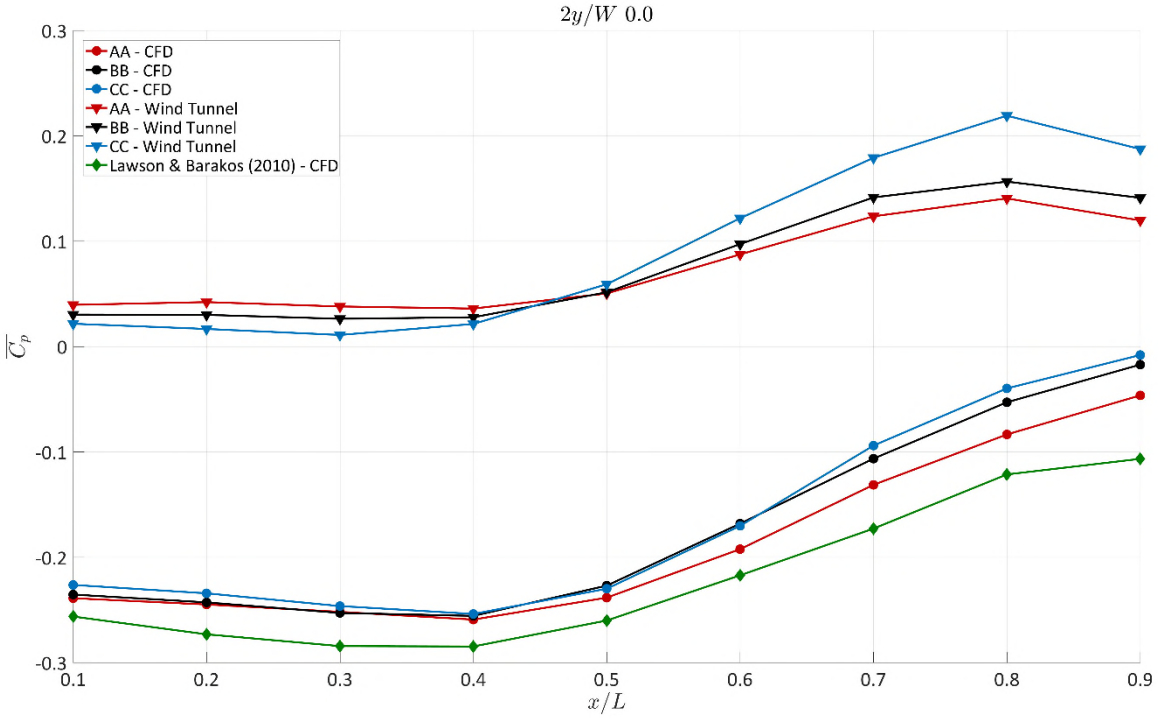

Figure 5.1 - Geometry effects on mean pressure coefficient and comparison with wind tunnel experiments. *Data refers to central rake.*

The analysis of the mean velocity vector in the symmetry plane of configuration AA (Figure 5.2) indicated a three-vortex arrangement usually not present in cavities with *L/D* ratios between 5 and 6. The usual single low-speed vortex, typical of open-type cavities, did not appear and the overall fluid arrangement was influenced by the drop, towards the cavity floor, of the shear layer. Such a drop increased the intensity of the main clockwise vortex (Figure 5.2; arrow 2), which was responsible for the generation of a secondary counter-clockwise vortex (Figure 5.2; arrow 1). This, in turn, induced the negative pressure coefficient in the front part of the cavity. A third clockwise vortex was also present in the rear part of the cavity (Figure 5.2; arrow 3).

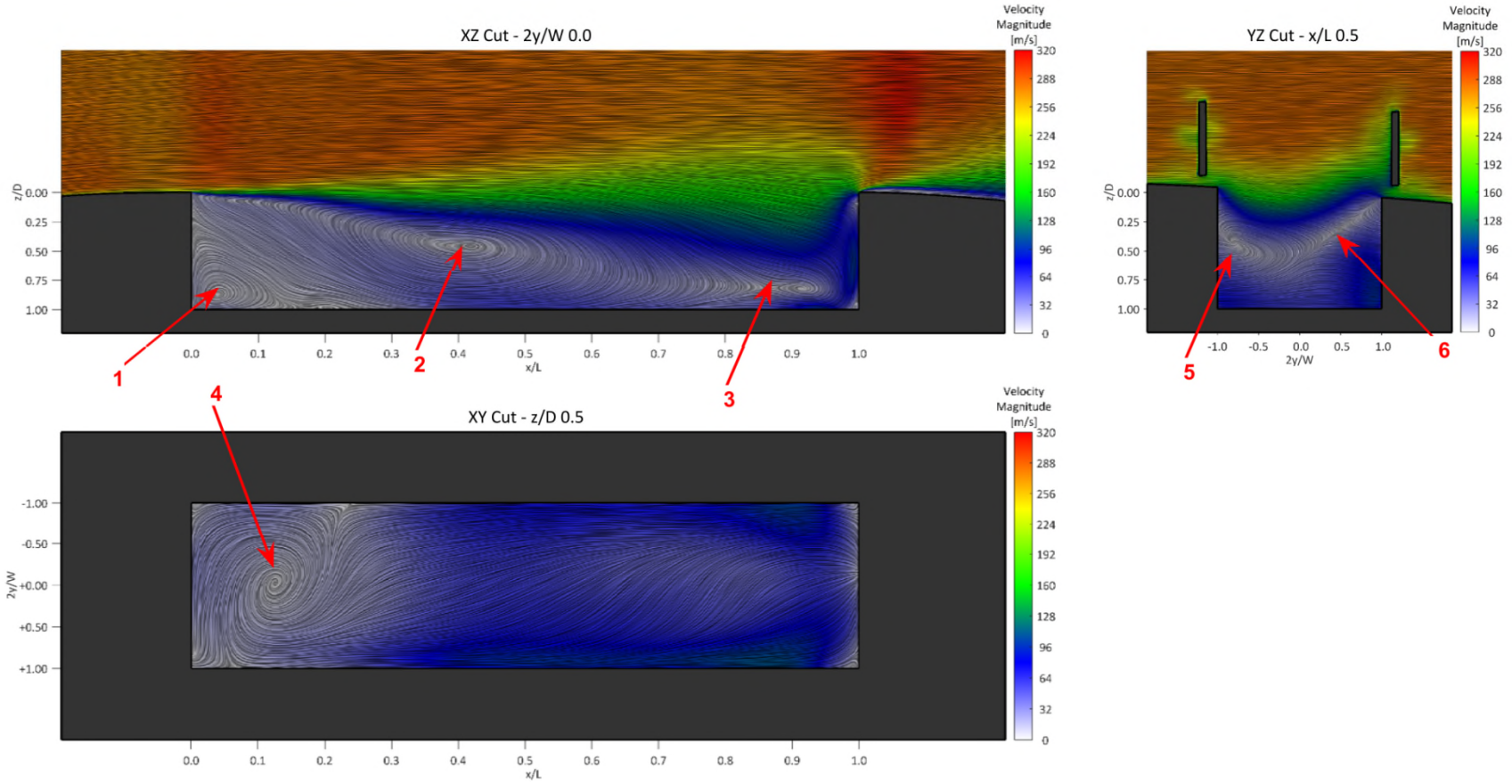

Figure 5.2 - LIC visualisation of the mean velocity vector field coloured by velocity magnitude. *The figure shows cuts at three different planes for configuration AA. The flow is from left to right in the x-y and x-z planes, and out of the page in the y-z plane. The numbered arrows indicate flow features discussed in the text.*

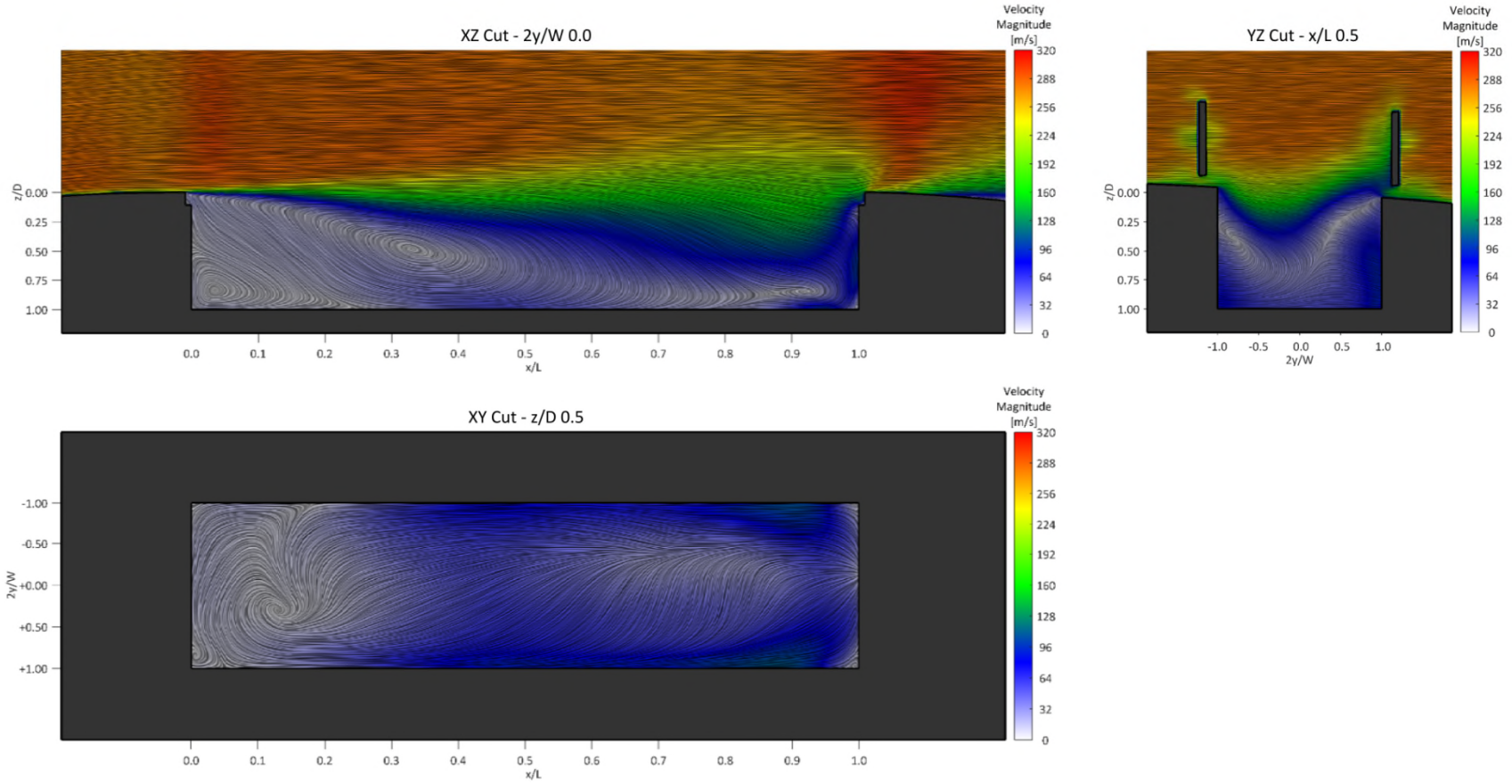

Figure 5.3 - LIC visualisation of the mean velocity vector field coloured by velocity magnitude. *The figure shows cuts at three different planes for configuration BB. The flow is from left to right in the x-y and x-z planes, and out of the page in the y-z plane.*

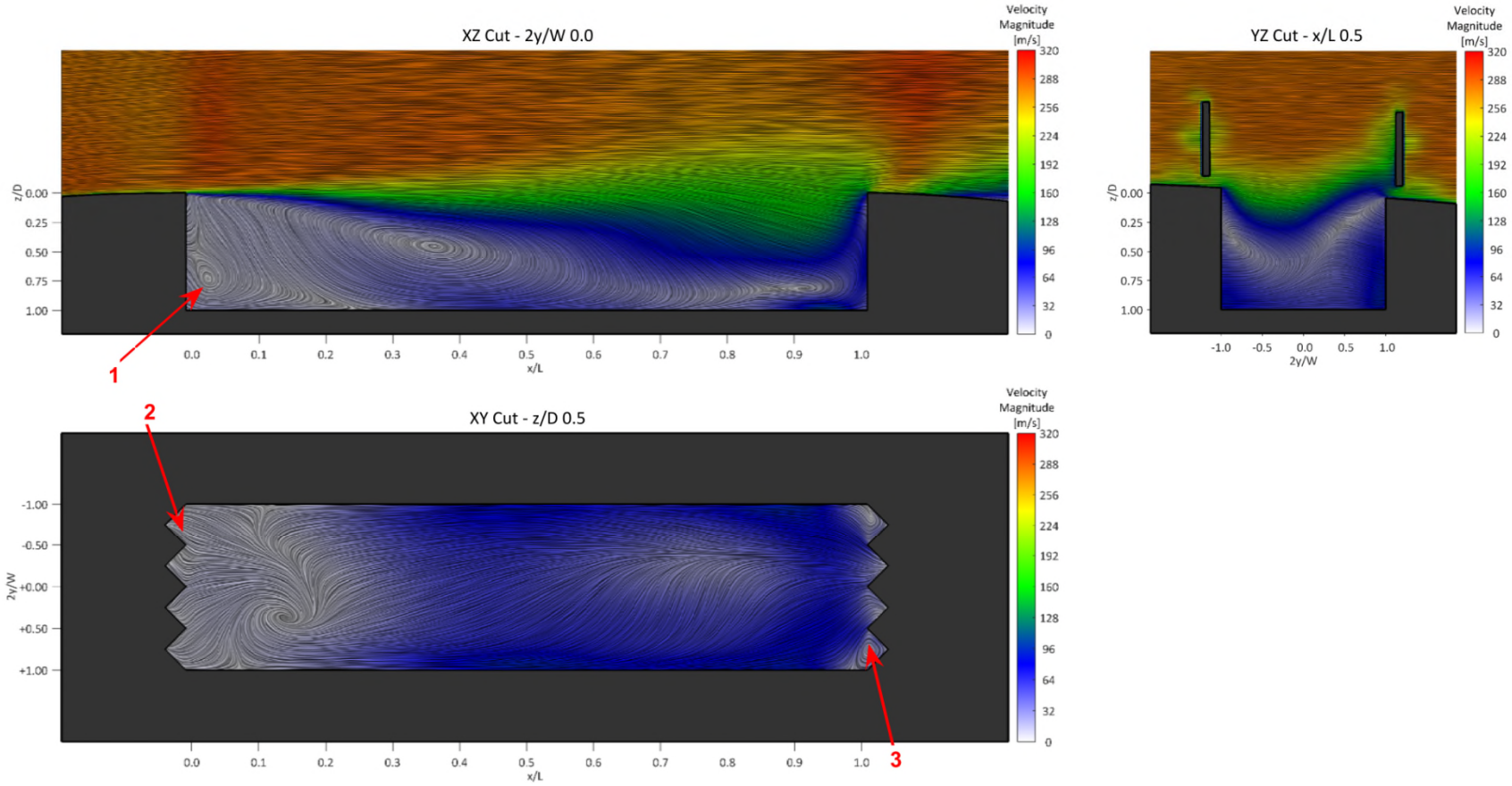

Figure 5.4 - LIC visualisation of the mean velocity vector field coloured by velocity magnitude. *The figure shows cuts at three different planes for configuration CC. The flow is from left to right in the x-y and x-z planes, and out of the page in the y-z plane.*

The situation in the *x-y* plane, at $z/D = 0.5$, indicated no relevant structures beyond $x/L = 0.3$. Only a small tendency of the flow to drift towards the left side[29] of the cavity was observed, indicating minimal lateral asymmetry in the mean flow[30]. In the front part of the cavity a large vortex was present, with its centre located at $x/L = 0.12$ and $2y/W = 0.00$ (Figure 5.2; arrow 4). Finally, a *y-z* orientated cut, at $x/L = 0.5$ indicated a crossflow induced by the UCAV's sloping lower surface. The shift of the focus point towards the left side of the cavity (Figure 5.2; arrow 5) indicated the presence of a longitudinal axis vortex, while the locus of separation[31] on the right side (Figure 5.2; arrow 6) delineated the areas of the downstream shear-layer-induced flow to the upstream reversed flow inside the cavity. The overall picture indicated that, beyond $x/L = 0.5$, the flow rotated clockwise from the main eddy (Figure 5.2; arrow 2), and was tilted around the *z*-axis in the right side of the cavity, while it remained unchanged in the left side of the cavity, as shown in the *x-y* plane. Analysing the mean surface streamlines and the mean pressure coefficient in front of the cavity (see Figure 5.5) it was observed that there was no particular bending of the streamlines incoming to cavity leading edge, nor there was a pronounced pressure difference between cavity's side edges. This left the only source of asymmetry to be localised in the different height of the left and right walls, which apparently was enough to influence the low speed flow inside the cavity.

The effects of configuration BB were almost null (Figure 5.3). The only observed difference was in *the x-y* cut view, where the forward vertical-axis vortex, had a position slightly shifted towards the right side of the cavity with respect to case AA. Configuration CC displayed changes related to the saw-toothed geometry of the front and rear walls. The small vortex in the front of the cavity was located slightly upward from the floor with respect to the other two geometries (Figure 5.4; arrow 1). This positional change was correlated to the added space around the eddy offered by the front wall's indentations (Figure 5.4; label 2). In comparison to the flat wall cases, here the geometry offered less resistance to the upward movement of the vortex, naturally induced by the main clockwise eddy. The indentations also created small recirculation areas at the rear wall (Figure 5.4; arrow 3). However, apart from these slight changes, the overall configuration remained unchanged, suggesting again that the time-averaged properties of the cavity were much more influenced by overall dimensions (L/D, W/D) than the local geometry's details.

---

[29] Left and right side of the cavity are respectively the side towards the UCAV's plane of symmetry ($2y/W = -1.0$), and the side towards UCAV's right wingtip ($2y/W = +1.0$).

[30] Similar behaviour was observed by Khanal (2010) in his CFD studies on a cavity of L/D = 4.0 and W/D = 1.0 at transonic regime.

[31] For a detailed discussion on the classification of singularities in a vortex field, see Peake & Tobak (1980).

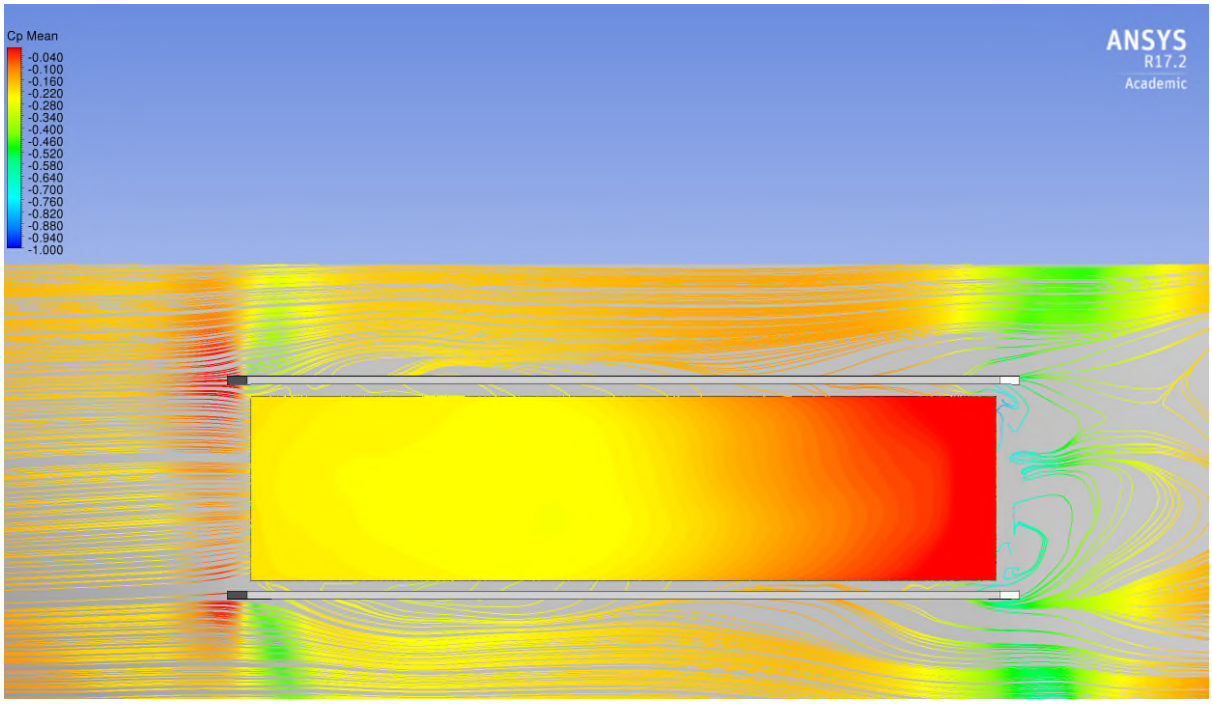

Figure 5.5 - Mean surface streamlines coloured by $\overline{C}_p$, and contours of $\overline{C}_p$ on cavity's floor. *View from above. Flow from left to right. Configuration AA.*

Similar observations could be made using streamline visualisation. As shown in Figure 5.6, for configuration AA the main clockwise vortex occupied the major part of the cavity (arrow 1). The other two subsidiary vortices (arrow 2 and arrow 3) were secondary eddies induced by the primary one.

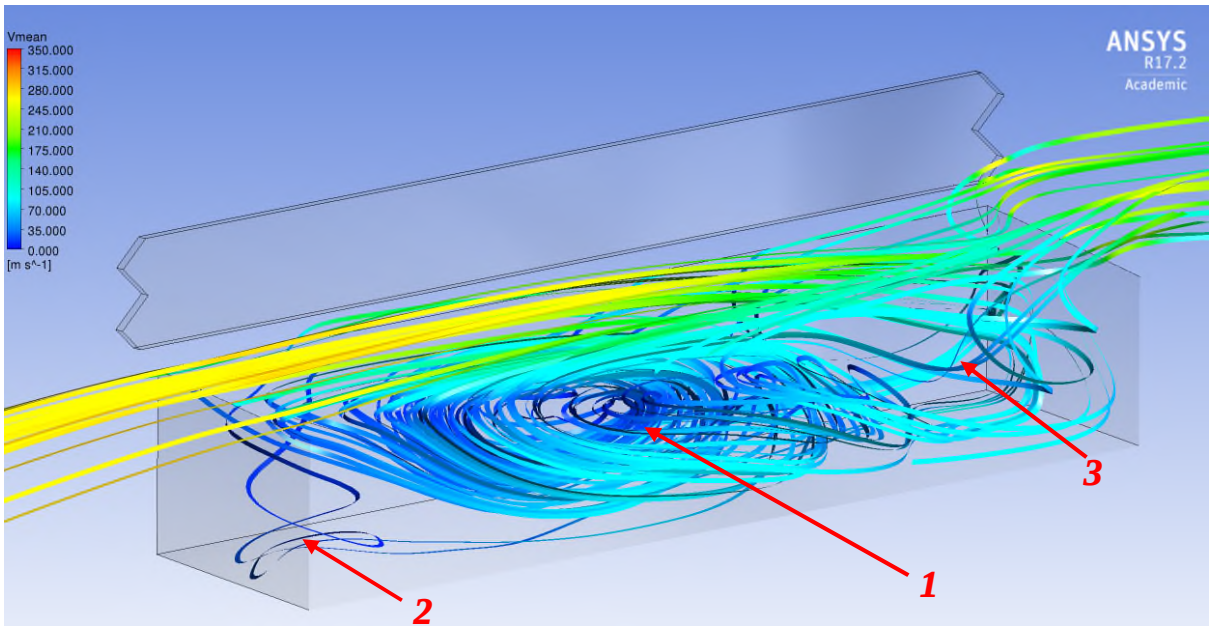

Figure 5.6 - Streamlines (coloured by velocity magnitude) of the mean velocity vector field. *Configuration AA. Flow from left to right. Side of the cavity removed for ease of visualisation.*

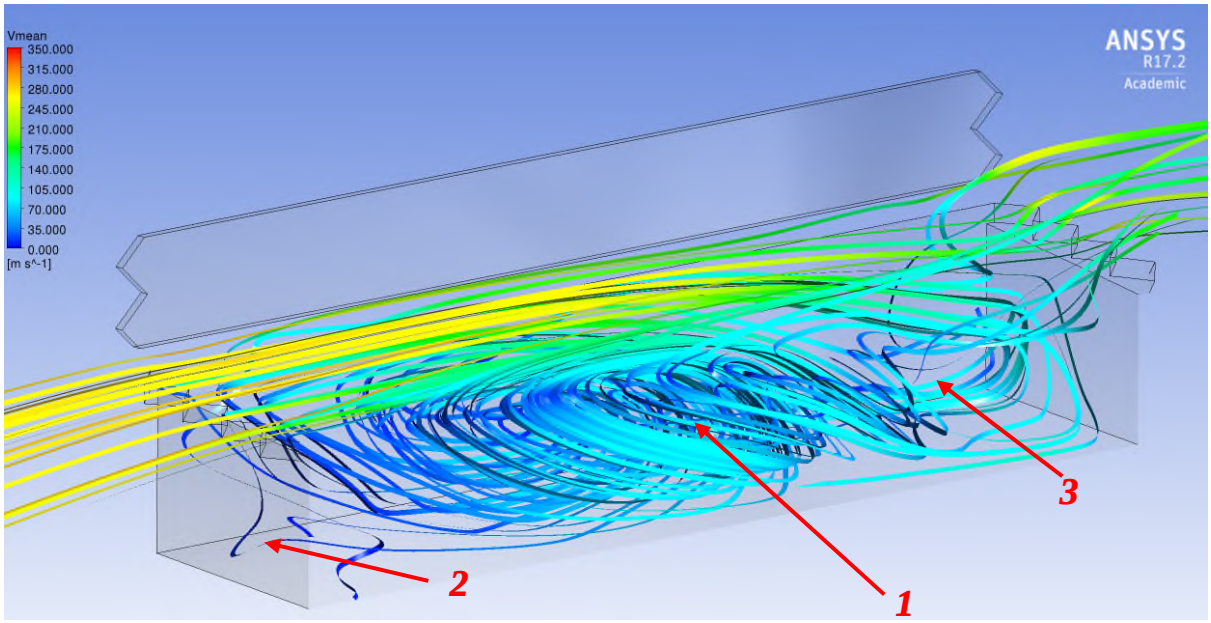

Figure 5.7 - Streamlines (coloured by velocity magnitude) of the mean velocity vector field. *Configuration BB. Flow from left to right. Side of the cavity removed for ease of visualisation.*

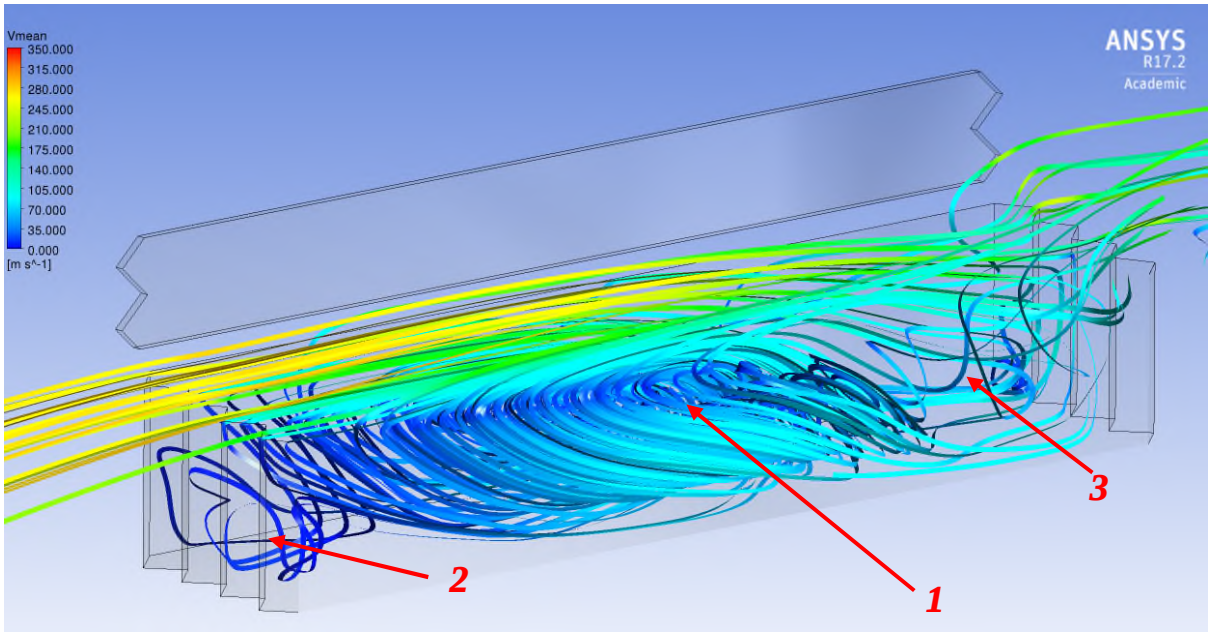

Figure 5.8 - Streamlines (coloured by velocity magnitude) of the mean velocity vector field. *Configuration CC. Flow from left to right. Side of the cavity removed for ease of visualisation.*

Comparing Figure 5.6 with Figure 5.7 (cavity type BB) and Figure 5.8 (cavity type CC) showed how the different geometries slightly modified the spatial organisation of the main eddy (arrows 1) but produced a different arrangement of the secondary (arrows 2) and tertiary (arrow 3) eddies, explaining the differences observed in the LIC plots. The main consequence of geometry modification was that it affected the local path of the streamlines inside the cavity but did not change the overall structure of the mean velocity vector field which was still

represented by a main clockwise vortex and secondary recirculation regions between the former and the cavity front and rear walls.

Similar conclusions were derived in the analysis of the OASPL charts (Figure 5.9). Each configuration showed minimal difference between the central and lateral rakes and the effect of changing the cavity leading and trailing edge shapes introduced minimal variations. The typical OASPL curve assumed a concave-convex-concave form, with inflection points located between x/L = 0.2 and x/L = 0.3, and at x/L = 0.6, that in the mean velocity vector field corresponded respectively to the point of separation generated by the main vortex and the front wall vortex, and to the starting point of the shear layer drop inside the cavity. The front wall noise level attained values around 153.1 dB that decreased to 151.5 dB at x/L = 0.2. Moving downstream, a rise in the noise level was observed that brought the OASPL to a local maximum value of 158.5 dB, attained at x/L = 0.6. In the rear part of the cavity, the curve re-assumed the original concave shape, that ended with an overall maximum value, at x/L = 0.9, of 162.1 dB. Configurations BB and CC showed a similar trend, presenting variations, with respect to the reference geometry, below ±1 dB.

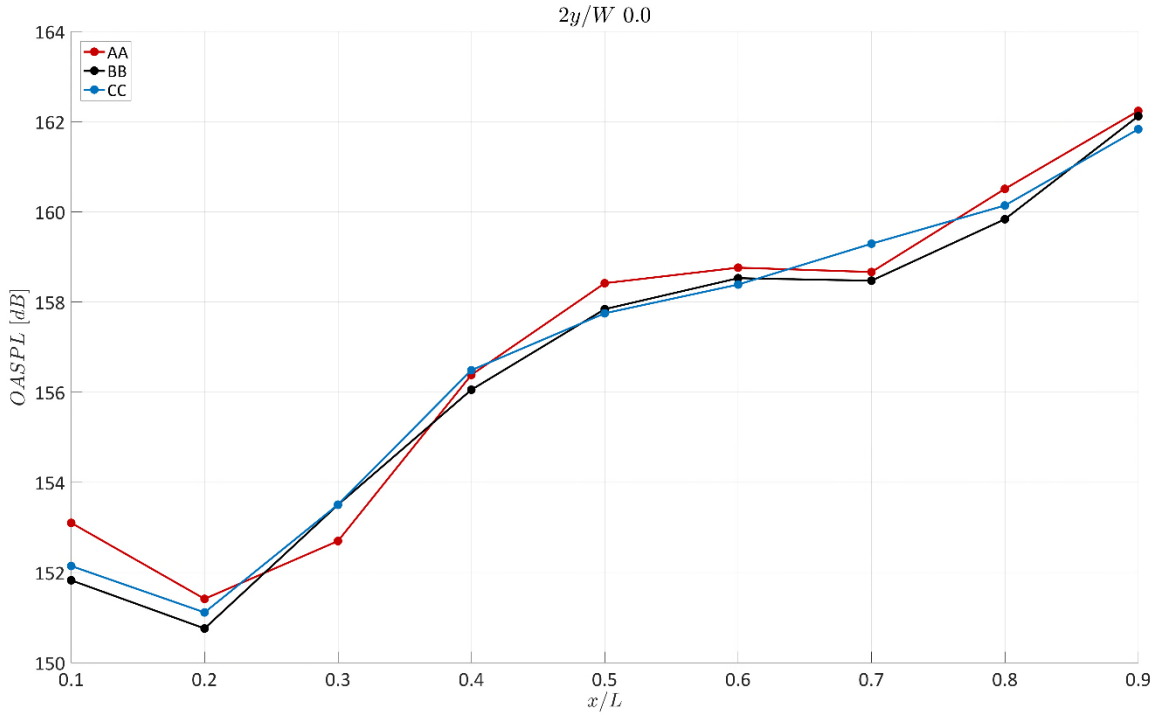

Figure 5.9 - Geometry effects on OASPL. *Data refers to central rake.*

5.2 NON-STATIONARY FLOW ANALYSIS

Nonstationary flow analysis was centred on the JFTFA technique, focusing particularly on the rearmost station of the cavity (x/L = 0.9), being the cavity's area with higher pressure fluctuations, as demonstrated by the OASPL curves. The resonant modes were compared with the theoretically-predicted values of the Rossiter-Heller equation (Equation (2-3)). The results for the reference configuration are reported in Figure 5.10. Here the Fourier analysis (Figure 5.10.a) indicated three main Rossiter-Heller modes, with their peaks close to the theory-predicted value, M1 (St 0.2574, SPL 144.6 dB), M2 (St 0.6434, SPL 150.5 dB) and M3 (St 0.9866, SPL 136.2). An additional peak was also present at a Strouhal number close to the theoretically-predicted 4th resonant mode; however, its value was beneath the confidence level threshold and could not be considered, in this case, a true feature of the flow. Looking at the time-averaged wavelet spectrum plot (Figure 5.10.b), indicated that only M2 crossed the 95% confidence level boundary, and be considered as a true tone in the frequency domain.

This discrepancy was addressed by the analysis of the time-frequency domain map (Figure 5.10.c). Here it was possible to observe that all modes had an intermittent nature, i.e. they were not active for the whole time length of the signal. Using the persistence index formula (Equation (3-41)), the PR indices calculated were, respectively, 3.87% for M1, 28.33% for M2, and 1.51% for M3. Such low PR values for M1 and M3 was the reason for the difference between the Fourier and the wavelet time-averaged spectra. Nevertheless, it was possible to determine that the nature of the pressure fluctuations, apart from the most powerful and regular M2, were time-localised events with no particular regularity in time. From the scales-averaged plot (Figure 5.10.d), the intermittency of the overall signal was monitored. Here peaks above the confidence level threshold were coincident with time windows in which a particular phenomenon occurred, that is the simultaneous presence in the spectrum of two of the main modes (i.e. M2 and M1, or M2 and M3).

Of particular relevance was the presence of an additional tone not correlated with the Rossiter-Heller modes (see text-arrows labelled Mt in Figure 5.10.a, Figure 5.10.b, and Figure 5.10.c). This aspect was already known from the wind tunnel experiments (see Paragraph 4.2).

In the Fourier plot (Figure 5.10.a), Mt was located at a Strouhal number of 3.324 with a power level of 136.5 dB. In the wavelet analysis, this mode was spread over a wide Strouhal band, ranging from 3.0 to 4.5 (Figure 5.10.c).

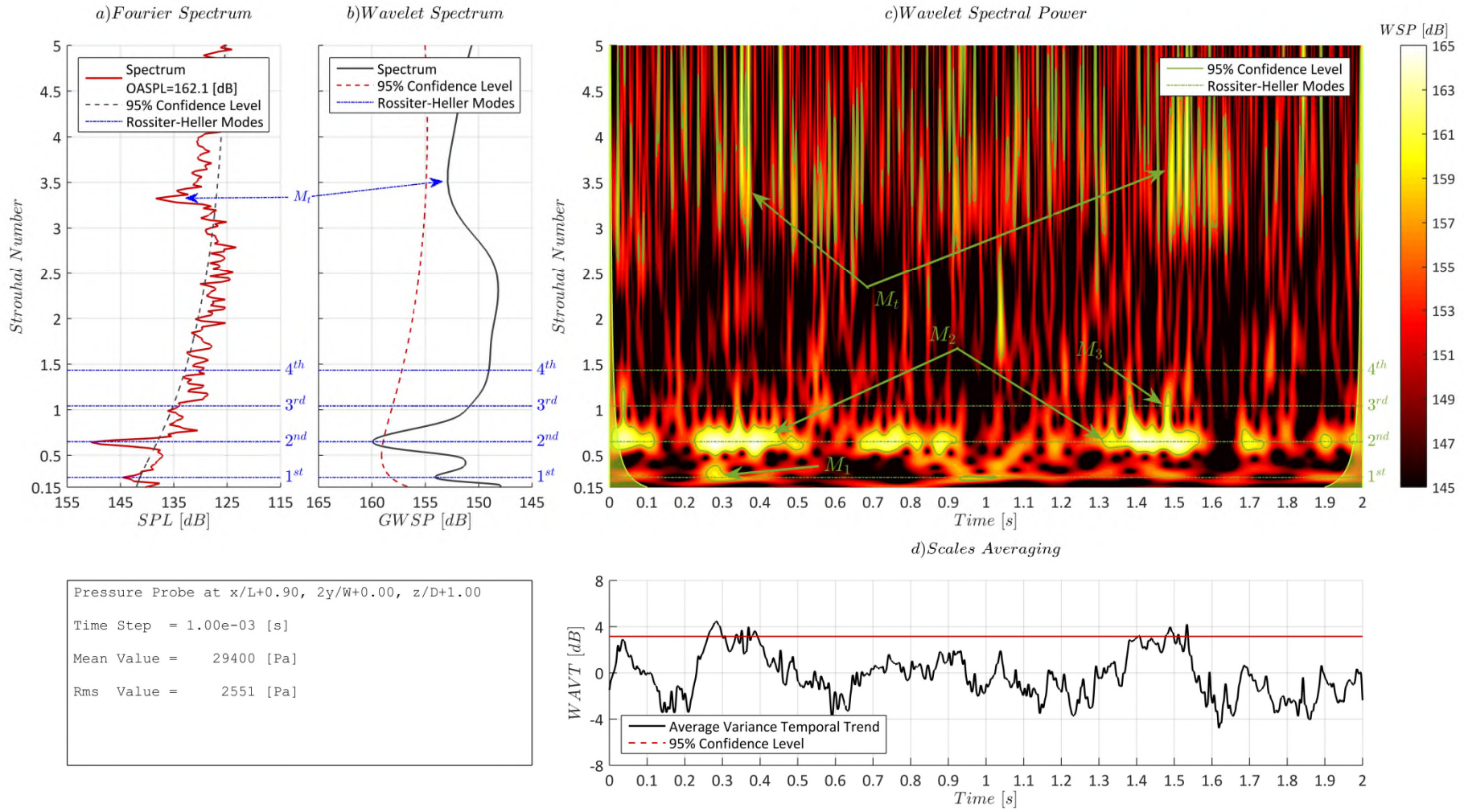

Figure 5.10 - Wavelet analysis of pressure signal at x/L = 0.9, $2y/W$ = 0.0, z/D = 1.0. *Data refers to configuration AA.*

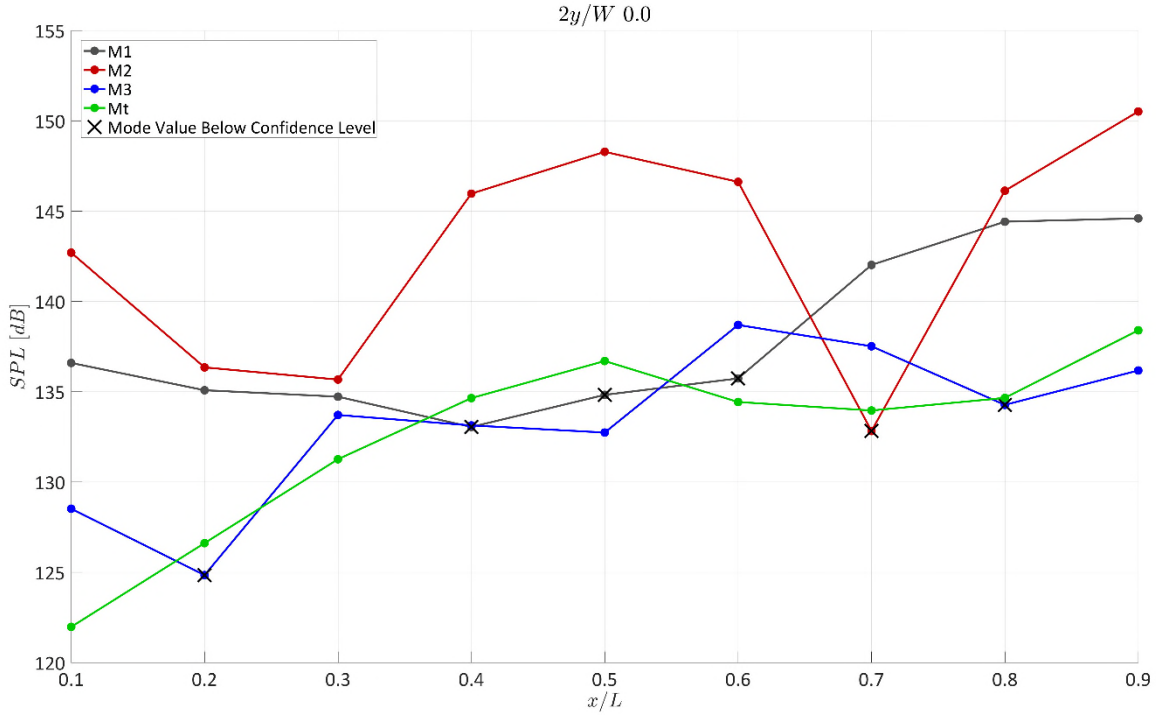

Figure 5.11 – Comparison of the mode shape along the cavity centreline. *Data refers to configuration AA. Cross marks indicate the station in which the SPL value was below the 95% confidence level threshold.*

The characteristic footprint of the Mt mode, in the time-frequency space, was the occurrence of bursts of energy localised in time but diffused in frequency, probably suggesting the presence of frequency modulation characteristics. The tone PR index was high, 17.39%, confirming that the true essence of this phenomenon was to be a resonating mode. This dictated the necessity for a better characterisation of the nature of the tones encountered in the time-frequency analysis.

The distribution of the mode power and Strouhal number along the cavity centreline were then analysed, obtaining the results depicted in Figure 5.11 and Figure 5.12 . Figure 5.11 shows the power's trend along the central rake for modes M1, M2, M3, and Mt. The black cross mark indicates a station where the local SPL value was below the confidence level threshold, hence the peak could not be considered as a true feature of the spectrum. M1, M2, and M3 assumed the longitudinal trend described by Tracy & Plentovich (1993), in which the curve, along the cavity's length, is characterised by a number of minima points equivalent to the mode number. Furthermore, the stations at which the modes' power was below the confidence level threshold corresponded to minima points. This supported the hypothesis that M1, M2, and M3, were Rossiter-Heller tones with a strong intermittent behaviour. A different situation was encountered for Mt.

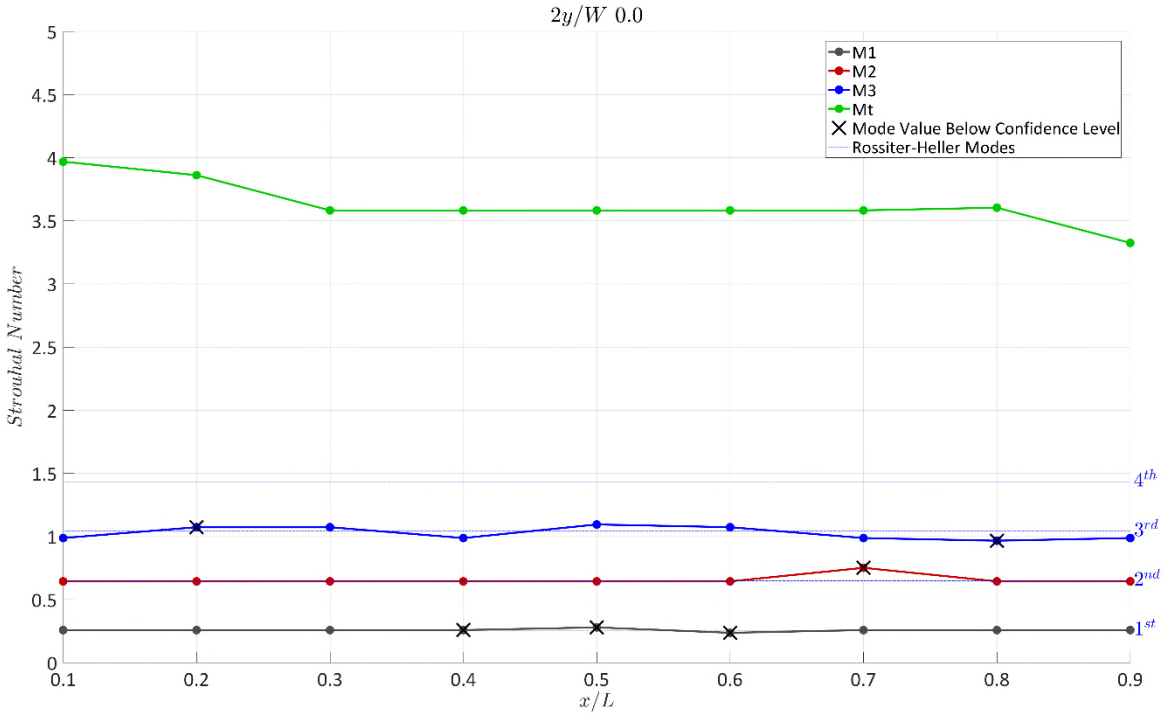

Figure 5.12 - Location of the Rossier-Heller modes in the Strouhal axis along the cavity centreline. *Data refers to configuration AA. Cross marks indicates station in which the SPL value was below the 95% confidence level threshold.*

This tone did not follow the Tracy & Plentovich (1993) rule. Moreover, the Strouhal number corresponding to the tone, contrary to all other modes, increased in the front part of the cavity and decreased in the rear (see Figure 5.12). This additional outcome strongly supported the hypothesis that the mechanism generating mode Mt was different with respect to the standard Rossiter-Heller mechanism.

An additional analysis was conducted on the spatial arrangement of the waves[32]. Pressure signals on the cavity floor at stations x/L = 0.1 and x/L = 0.9, on the centreline rake, were correlated via wavelet analysis, and the WLCC and WLCP trends over time for M1, and M2 were extracted and analysed. The same procedure was applied for pressure signals at stations x/L = 0.2 for the left and right rakes.

[32] The spatial arrangement of a wave describes the direction of propagation with respect to the cavity geometry, i.e. longitudinally, transverse, and vertically.

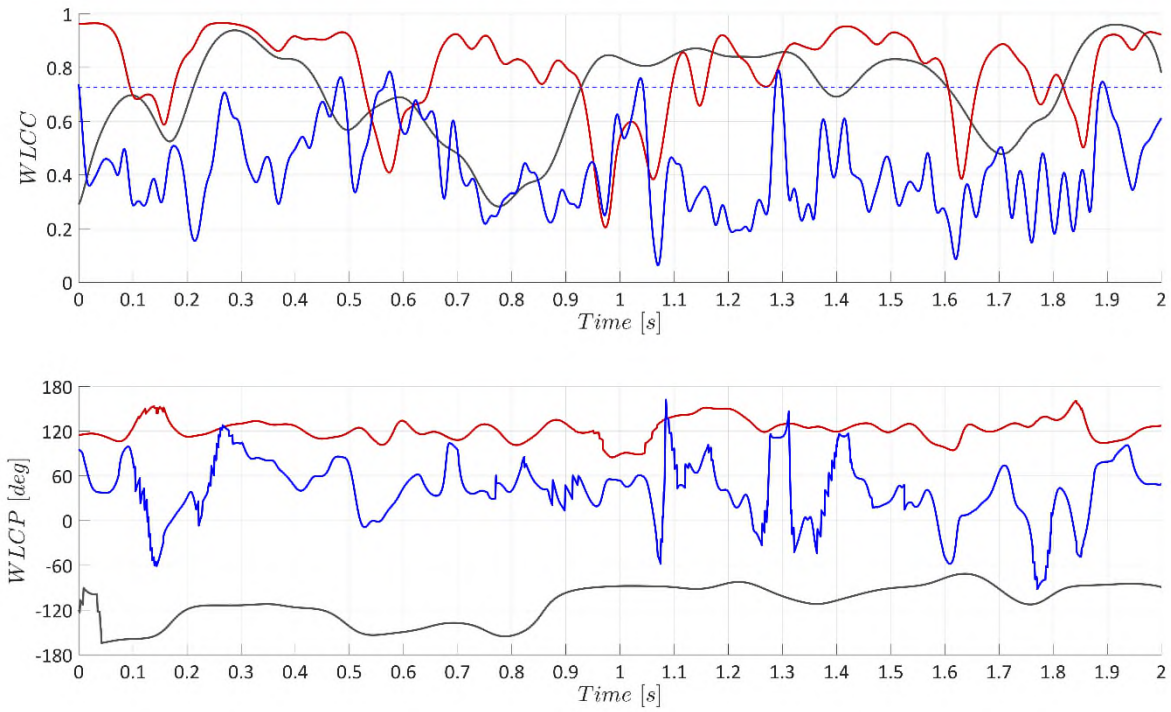

Figure 5.13 - WLCC and WLCP trends for M1, M2, and M3. Wavelet correlation analysis between pressure signal at x/L = 0.1, $2y/W$ = 0.0, z/D = 1.0 and pressure signal at x/L = 0.9, $2y/W$ = 0.0, z/D = 1.0. *Data refers to configuration AA.*

This scheme allowed the determination of which tone was eventually a longitudinal standing wave (correlation of points at the same transverse stations but different longitudinal stations, or simply longitudinal correlation), and which was a transverse wave (correlation of points at different transverse stations but the same longitudinal stations, or simply transverse correlation). Longitudinal correlation for M1, M2, and M3 (Figure 5.13) indicated that for these tones, whenever the WLCC value was above the confidence threshold, a slightly oscillatory phase around a constant non-zero value occurred. Coherence was high, always above 0.8, however, the intermittency of the signals influenced the results, avoiding the retention of a constant phase angle for long periods. M3's WLCC, due to the mode's low PR value, was valid only for short time periods; nevertheless, in these intervals the WLCP phase curve had points of local maxima/minima, and hence a phase derivative with respect to time equal to zero. This fact, albeit not regular as in the M1 and M2 case, indicated that, in such time intervals, M3 phase had the tendency to settle on a constant value, even if never reaching such characteristic. All these findings were a clear indicator that all three modes, whenever active, assumed the behaviour of longitudinal standing waves.

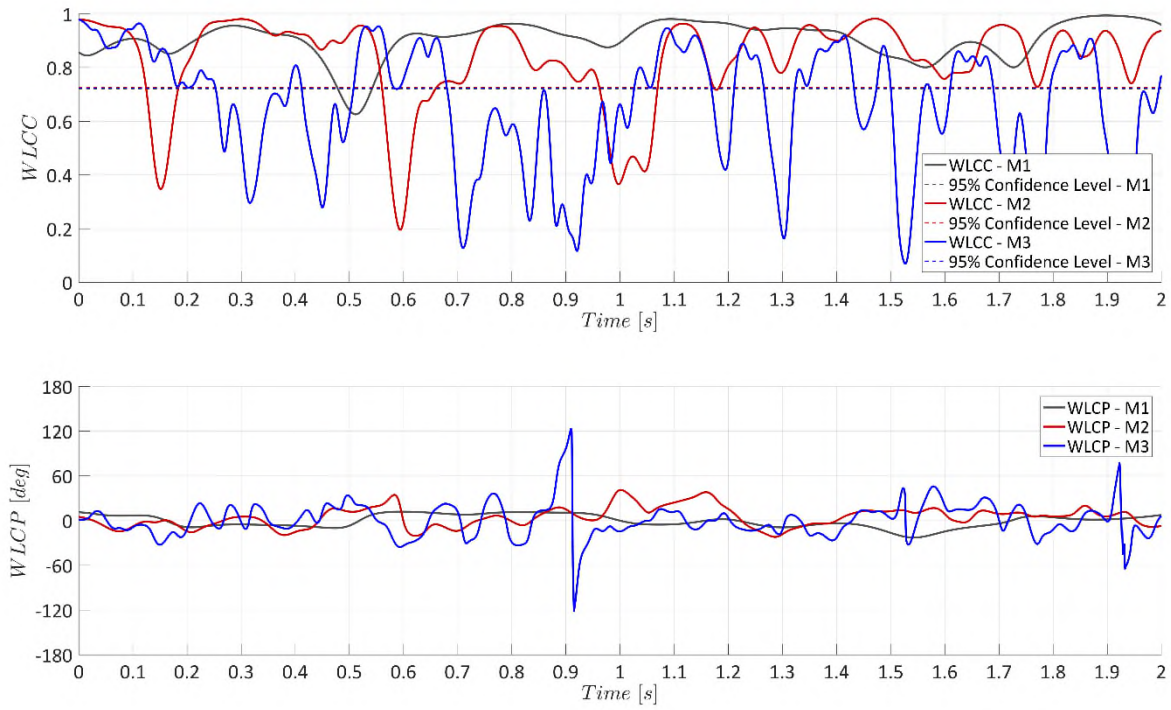

Figure 5.14 - WLCC and WLCP trends for modes M1, M2, and M3. Wavelet correlation analysis between the pressure signals at x/L = 0.2, $2y/W$ = -0.5, z/D = 1.0 and at x/L = 0.2, $2y/W$ = +0.5, z/D = 1.0. *Data refers to configuration AA.*

The transverse correlation at x/L = 0.2 (Figure 5.14) still indicated high levels of coherence, with values usually between 0.9 and 1.00. The WLCP value, for all three modes, was always close to zero indicating that the two points under consideration experienced no relative phase delays at the passage of the wave front, again confirming that effectively M1, M2, and M3 were longitudinal standing modes with little or no transverse variations. By comparison, the situation for Mt was completely different. Neither the longitudinal nor the transverse correlations indicated any kind of correlation indicating that this mode was not a Rossiter-Heller like one. The origin of Mt was surmised to be a localised phenomenon, still caused by oscillations of the shear layer, but of a different nature than the feedback mechanism described by Rossiter. A time-spatial wavelet analysis[33] of the Strouhal band of each mode confirmed this intrinsic difference in nature (Figure 5.15). The pattern of M1 and M2 had a periodicity in both time and space. M3, even if absent in a good part of the signal, maintained a regular pattern whenever active. By contrast the temporal periodicity of Mt was nearly absent and the spatial signature, whenever the mode was active, changed in the time history.

[33] This analysis is based on monitoring, via wavelet transform, the trend of a particular Strouhal band during time at different locations.

With the help of the Schlieren visualisation technique (based on density gradient) nine time frames of the CFD data were produced and compared[34]. The aim was to understand the behaviour of the shear layer and discover the origin of Mt. Figure 5.16 and Figure 5.17 were developed by monitoring the temporal trend in the symmetry plane and in a transverse plane located at x/L = 0.2. These pictures where complemented by the trend of the velocity vector components with time (Figure 5.18) measured at three different points immersed in the shear layer (x/L = 0.2, 2y/W=-0.5, z/D = 0.0; x/L = 0.2, 2y/W = 0.0, z/D = 0.0; x/L = 0.2, 2y/W = +0.5, z/D = 0.0). From the analysis of Figure 5.16 it was possible to fix the beginning of the oscillation of the shear layer at a position around x/L = 0.2, from where the flow underwent a perturbative motion via turbulence burst. The time-dependent passage of a rolling vortex from station x/L = 0.2 was reflected in strong oscillation of the horizontal x-velocity component (Figure 5.18 Upper), which underwent variations from a minimum of 100 m/s to a maximum of 250 m/s. Furthermore, even if the three monitored points were placed at the same longitudinal station, the oscillations of x-velocities had different trends in time, underlying the presence of a transverse fluctuation along the cavity YZ plane. The analysis of the frames, displaying the same time history evolution, in the transverse plane at x/L = 0.2 (Figure 5.17), revealed the occurrence of random oscillation of shear layer position in both the vertical (towards and away from the bay) and transverse (from side to side) directions. In this case peak and dips in the y-velocity and z-velocity components (Figure 5.18 Middle & Lower) showed the passage of eddies which moved from side to side in the cavity. Again the occurrence of different time histories moving from side to side of the cavity (i.e. from probe located at 2y/W = -0.5 to probe located at 2y/W = +0.5) indicated the presence of a fluctuating mechanism also in the transverse direction that made the shear layer, at this station, assume a structure not constant through the cavity span (see also Figure 5.25). Additionally, a time-varying flow in the gaps between the bay doors and the aircraft belly was identified. The motion inside this small aperture could have been the reason for the appearance of local perturbations in the pressure fluctuations globally named Mt. This transverse instability was also reflected in the mean flow asymmetries in the vector field obtained in Figure 5.2, and was particularly dominant in the first 20% of cavity length. In this area, in which the shear layer was not yet heavily perturbed, these transverse disturbances had a strong influence on the flow. In fact, Figure 5.11 indicated that in the front of the cavity the power expressed by Mt was comparable to the main Rossiter-Heller tones. Moving downstream, the burst of the free vorticity changed the situation, due to the increase in the power of the longitudinal modes.

[34] All the Schlieren pictures were generated by cutting the cavity with a plane and visualising the flow properties on this surface only.

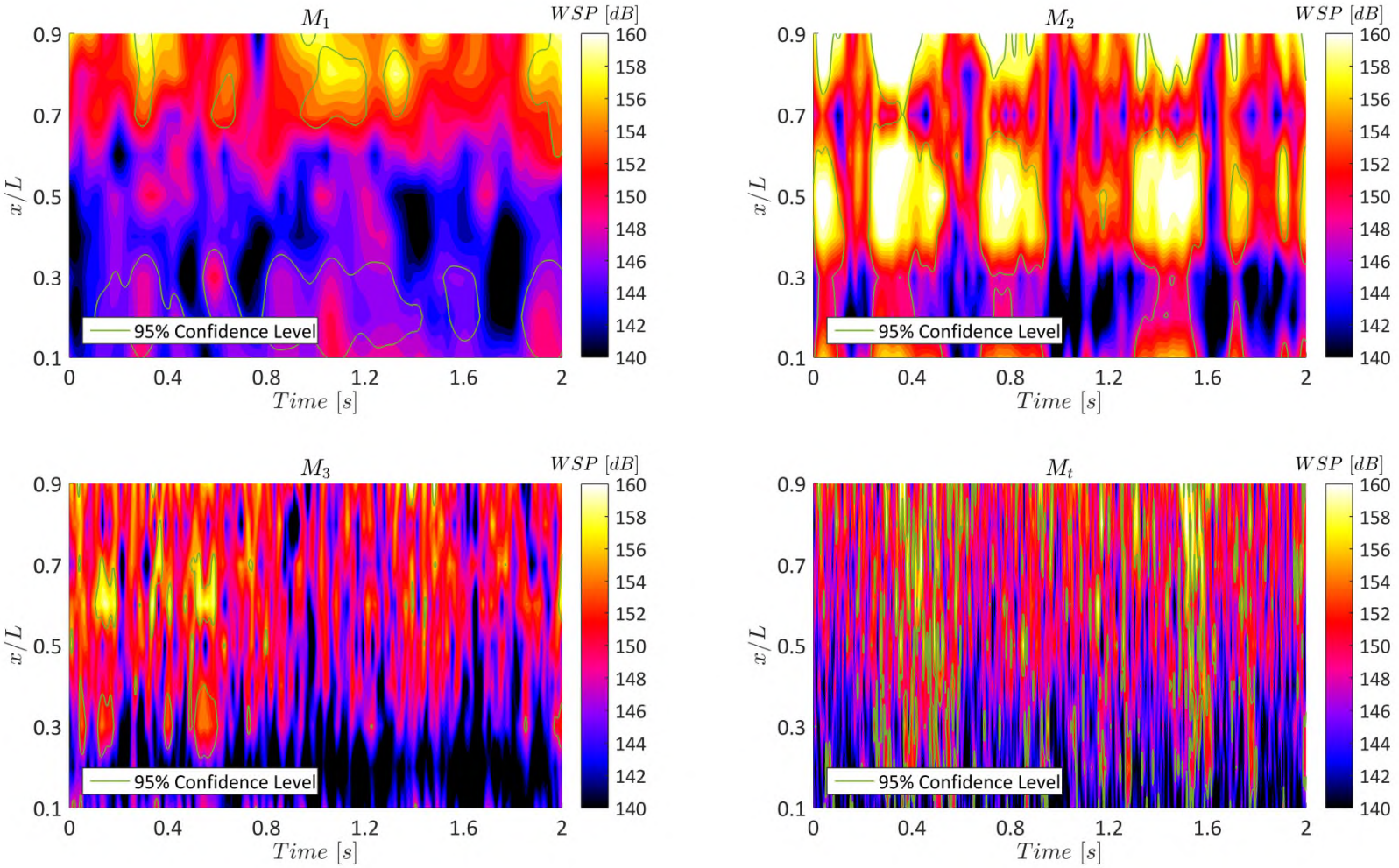

Figure 5.15 - Wavelet spatial-temporal analysis for the modes of pressure signals recorded at Rake 1C. *Data refers to configuration AA.*

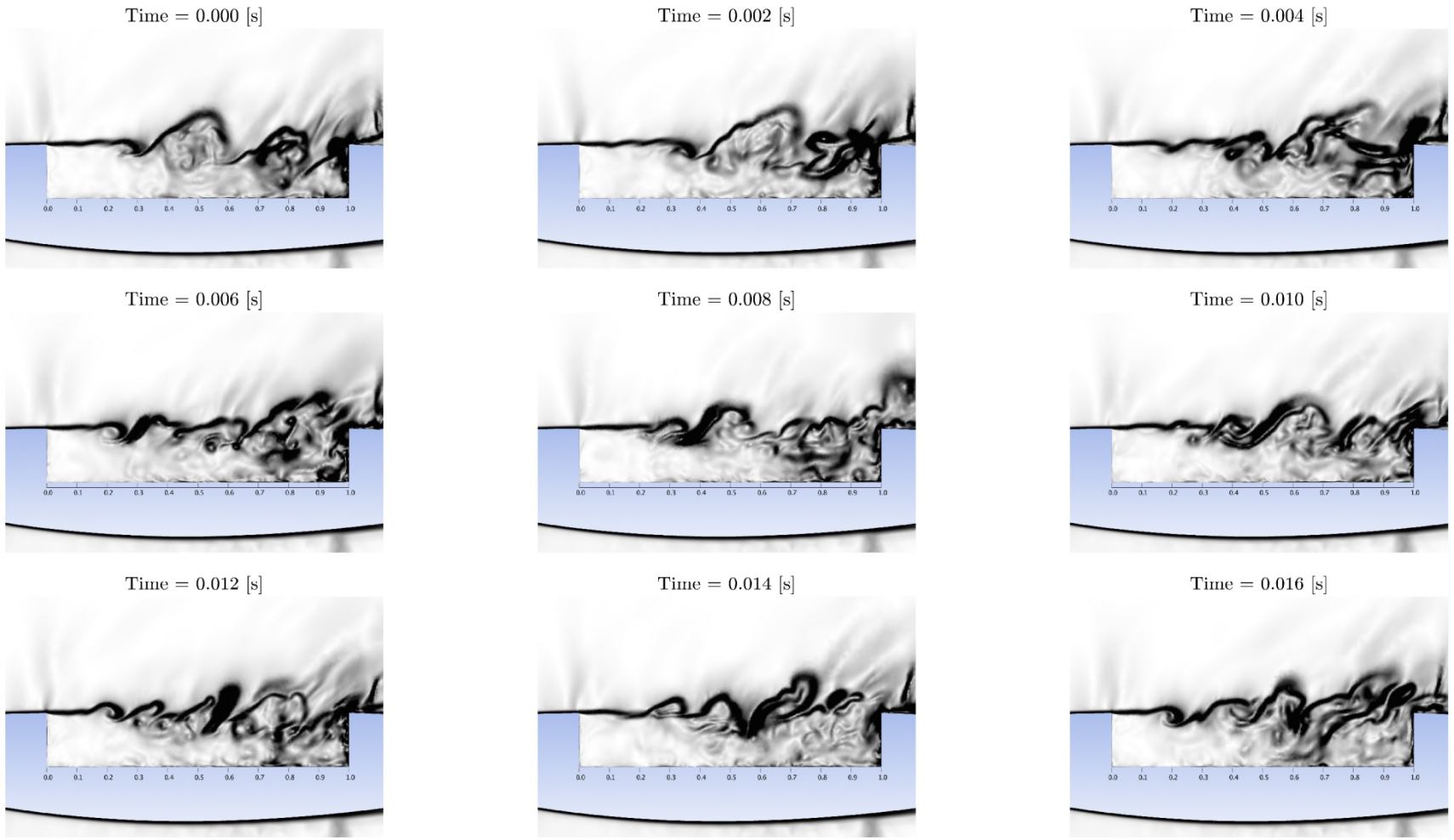

Figure 5.16 - Temporal Schlieren frames of cavity flow, planar slice at $2y/W = 0.0$. *Flow direction from left to right. Simulation time for the start of recording was t = 1.5 s (see Figure 5.10). Data refers to configuration AA.*

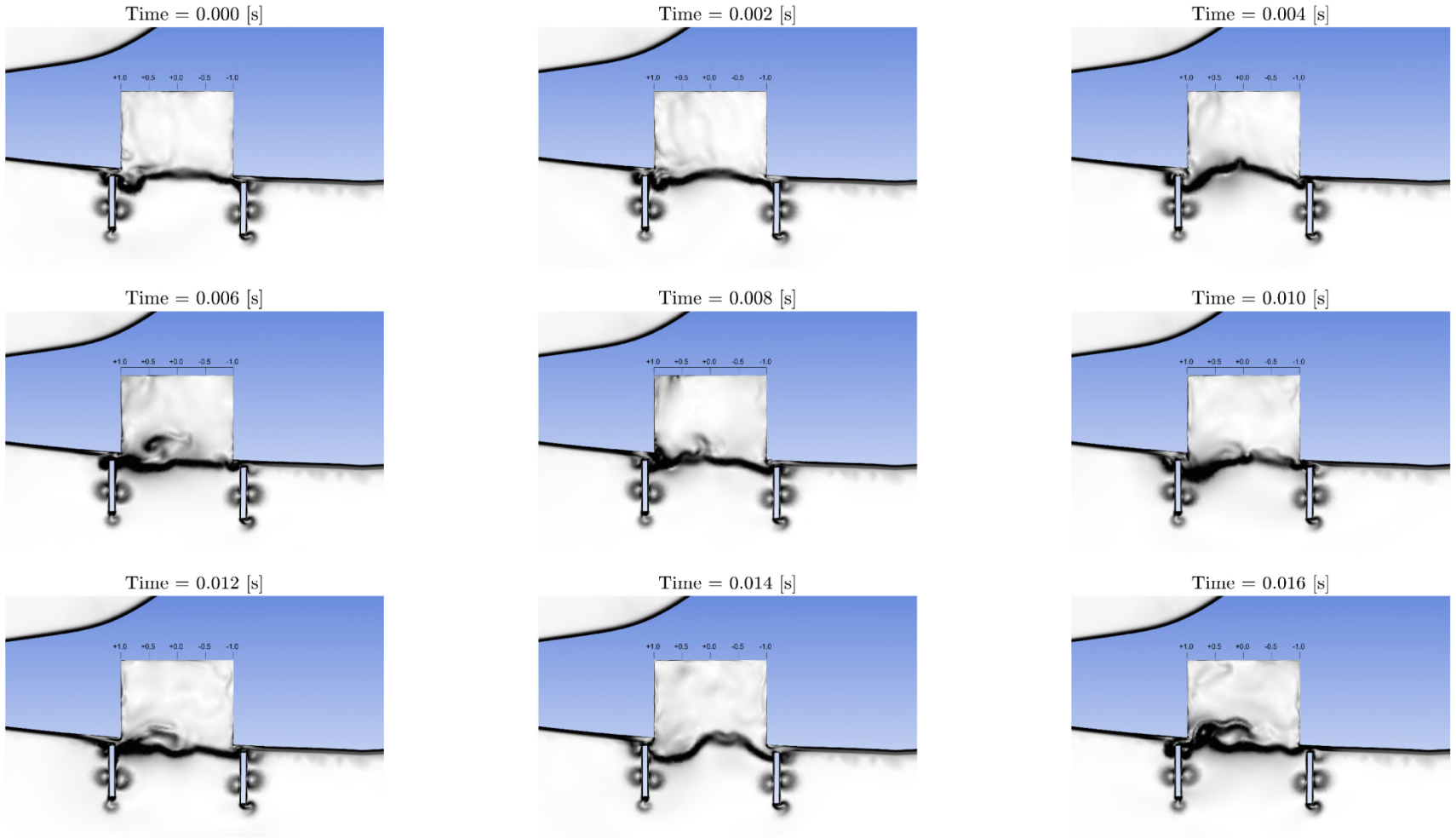

Figure 5.17 - Temporal Schlieren frames of cavity flow, planar slice at x/L = 0.2. *Flow direction towards the page. Simulation time for the start of recording was t = 1.5 s (see Figure 5.10). Data refers to configuration AA.*

The transverse mode, even if still present, was concealed by the increase in power of the Rossiter-Heller modes in the rear of the cavity. Nevertheless, Mt persisted as a localised phenomenon, possibly due to the strong difference between its wavelength and the ones of the Rossiter-Heller modes. Additionally, the source of the mechanism, probably originating in the flow moving through the gap between the doors and the aircraft, was kept alive by the fluctuating pressure field induced by the fluctuating shear layer bridging the leading and trailing edge of the cavity.

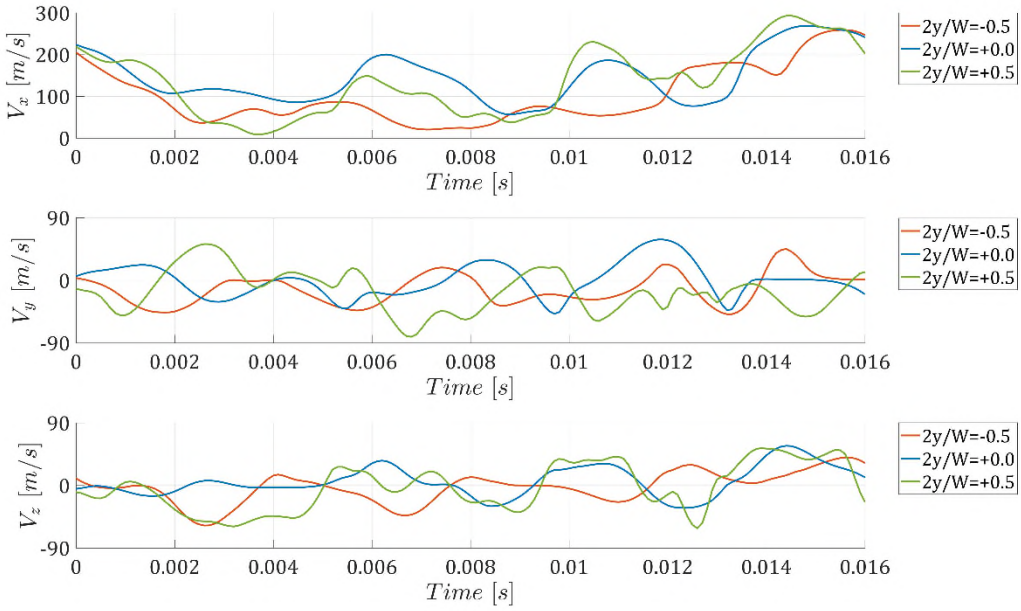

Figure 5.18 - Temporal evolution of the velocity vector components inside the shear layer across cavity span at x/L = 0.2 and z/D = 0.0. *Flow direction towards the page. Simulation time for the start of recording was t = 1.5 s (see Figure 5.10). Data refers to configuration AA. Note: z-direction positive inside the cavity.*

The association of Mt with a transverse instability of the shear layer could also explain the fact that, while in the experiments Mt's Strouhal number was about 4.0, in numerical simulations this value decreased to values close to 3.5. Such drop, might again been explained by local differences on cavity geometry between the experimental set-up (flat surface surrounding bay) and the numerical set up (aircraft belly with a sideward slope).

The adoption of geometry BB inside the cavity introduced peculiar differences. In this new configuration, together with M1, M2, M3, and Mt, two new modes appeared, M4 and M5 (Figure 5.19). M2 remained as the main mode, with a SPL equal to case AA (150.5 dB for case AA versus 150.4 dB for case BB) and a similar PR index (29.59% versus 28.33%). The situation for M1 was different, in which the persistence dropped to a mere 1.27%. Mt too experienced a PR reduction

from the previous 17.39% to 11.58%. This PR reduction was reflected also in the peaks' SPL values, which in the BB configuration, were reduced by 1.2 dB (M1) and 1.5 dB (Mt). A completely different trend was observed for M3. This mode increased its SPL value by 2.9 dB and, moreover, boosted the PR index from 1.51%, in the reference geometry, to 4.70%.

The Fourier spectrum (Figure 5.19.a) indicated the additional presence of M4 (St = 1.373, SPL = 137.4 dB) and M5 (St = 1.737, SPL = 135.3). The tones had, respectively, PR values of 2.60% and 1.65%, which was greater than M1. Wavelet analysis (Figure 5.19.c) identified tones M4 and M5 as significant events, localised in short time intervals, hence having the structure of bursts of energy. Apart from M2, all other tones had the same such characteristic. Nevertheless, time-spatial wavelet analysis still confirmed M1, M2, M3, M4 and M5 as real Rossiter-Heller-like modes. As shown in Figure 5.20, for each of these modes, it was possible to recognise a periodic pattern during the temporal evolution of the simulation. Tones M4 and M5 appeared to lie at the boundary between organised wave patterns and broadband noise. They displayed quasi-regular on/off trends at x/L = 0.5 and 0.7 (M4), and at x/L = 0.3 (M5). Mt confirmed its particular nature. Its temporal periodicity was again nearly absent and the spatial signature, whenever the mode was active, changed in the time history, indicating a localised phenomenon not comparable with the nature of standing waves typical of Rossiter-Heller modes. A feature that could be identified by the analysis of the GWSP (Figure 5.19.b) was that the peak of energy associated with M1 was located at a Strouhal number of 0.3149 compared to 0.2601 for case AA. Additionally, as already stated, its PR index was more typical of noise than an organised wave. Nevertheless, both Fourier and wavelet spectra indicated that, although below the confidence level threshold, at this Strouhal number organised wave behaviour was attained. Such an atypical phenomenon was clarified by applying the wavelet bi-coherence transform (WBC).

At the time intervals of interest (0.19 to 0.25 seconds), the summation in time of Equation (3-40), showed in Figure 5.19.b, that M2 and M3 co-existed. In this time interval, M1 did not cross the confidence level threshold; nonetheless, an elevated accumulation of energy at the corresponding Strouhal number was present. Figure 5.21 shows the results obtained in the WBC analysis of this time interval.

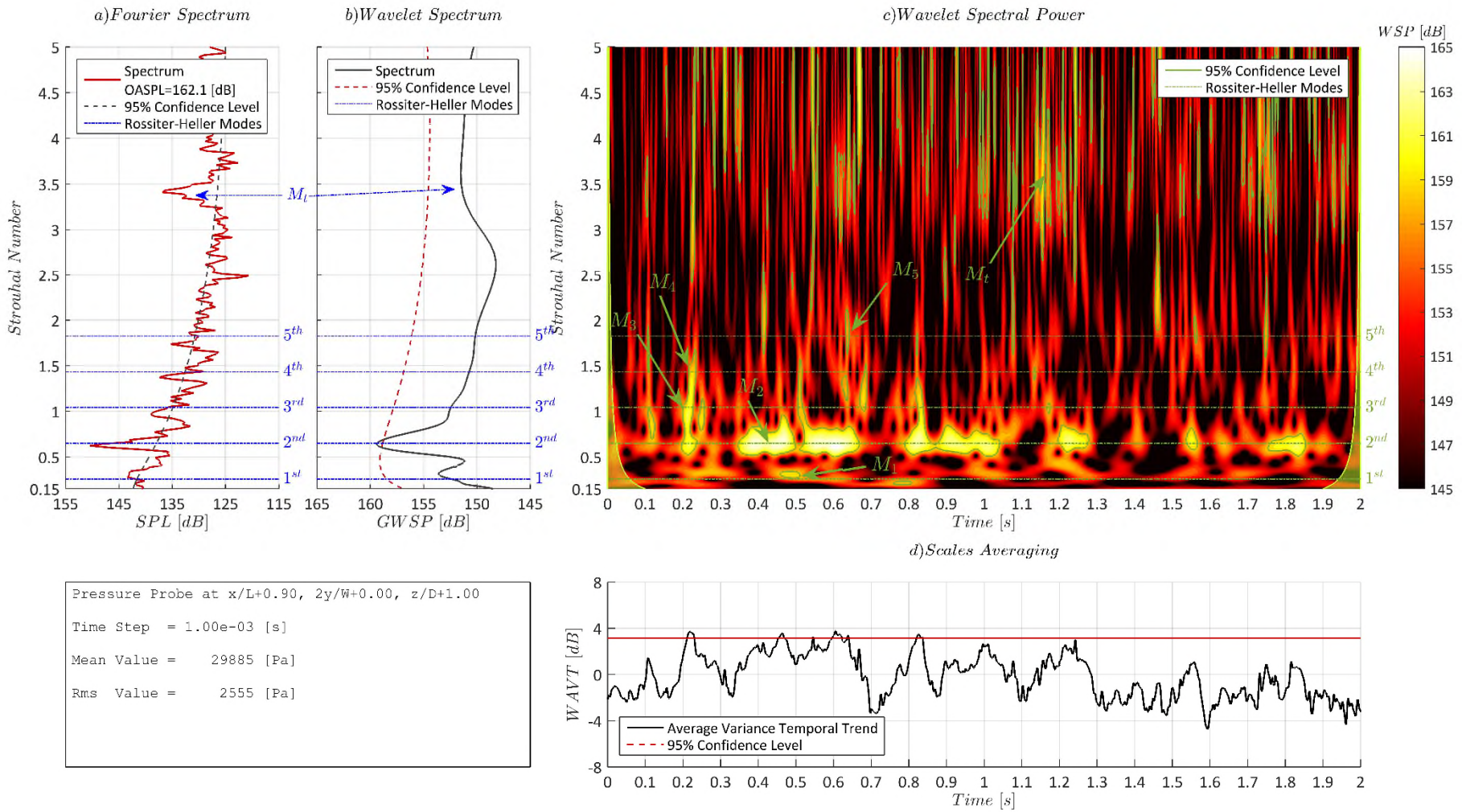

Figure 5.19 - Wavelet analysis of the pressure signal at x/L = 0.9, $2y/W$ = 0.0, z/D = 1.0. *Data refers to configuration BB.*

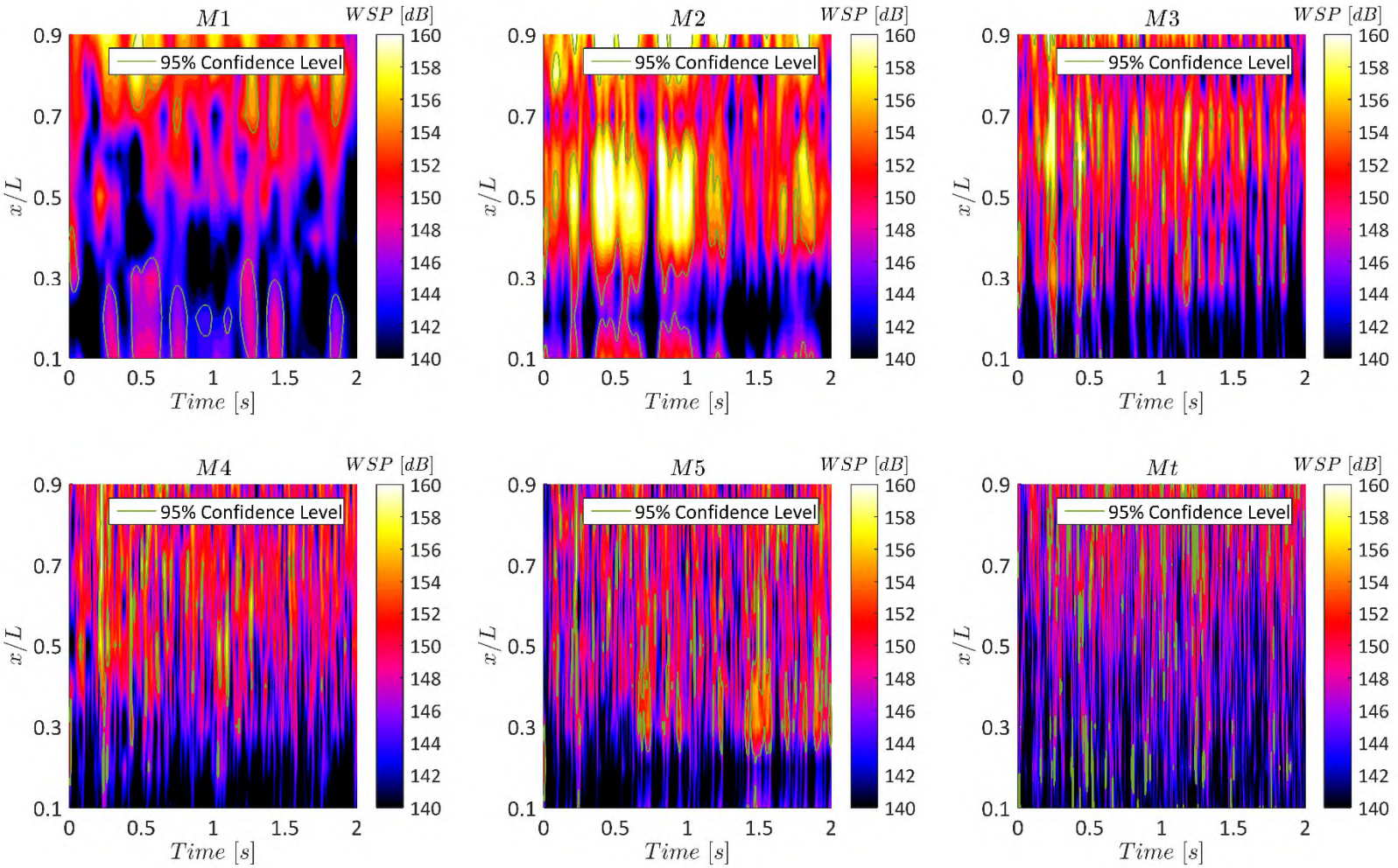

Figure 5.20 - Wavelet spatial-temporal analysis for the modes of pressure signals recorded at Rake 1C. *Data refers to configuration BB.*

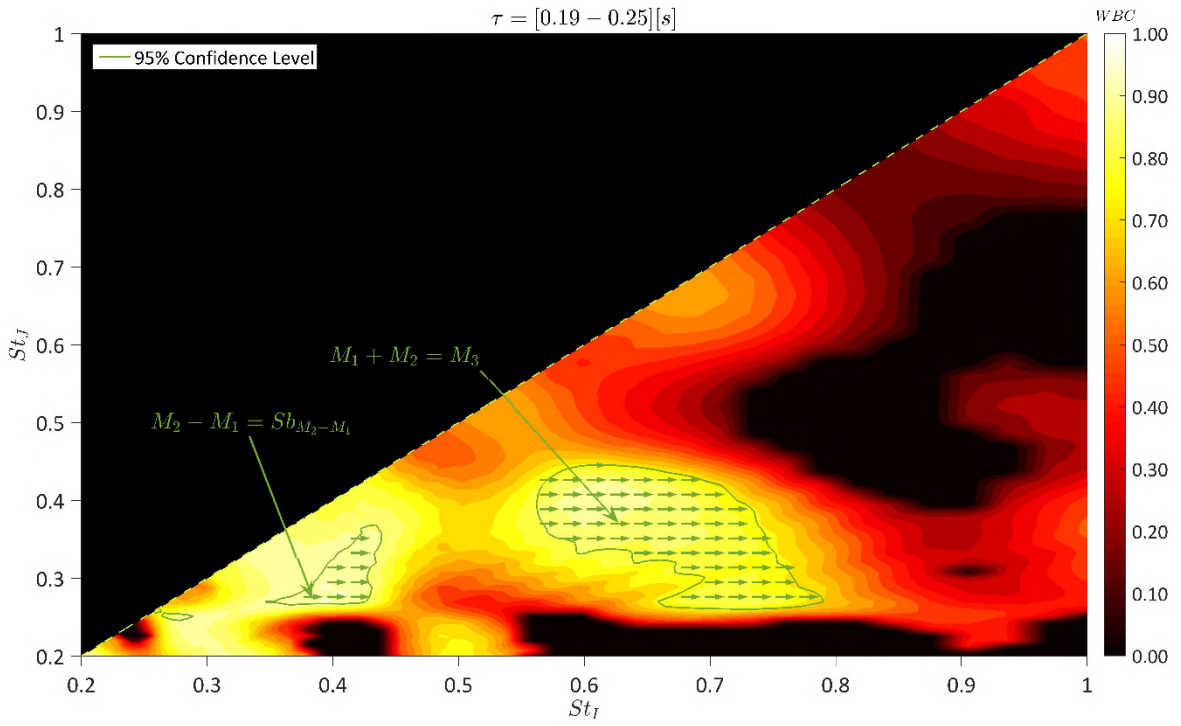

Figure 5.21 - Wavelet bi-coherence analysis for the pressure signal at x/L = 0.9, $2y/W$ = 0.0, z/D = 1.0. *The time interval of integration is from 0.19 to 0.25 seconds (see Figure 5.19). Arrows indicate wavelet bi-phase. Data refers to configuration BB.*

The outcome of the non-linear analysis indicated two areas of high bi-coherence. The first interaction involved M1, M2 and M3. As indicated, the squared bi-coherence was in excess of 0.95 attesting a full exchange of energy between the tones. Additionally, the bi-phase for the coupled triad was zero, providing evidence that the three modes, during their dynamics, were all in phase. Comparing this result with the wavelet map of Figure 5.19.b, it was observed that, while in the latter M1 was not present, the WBC analysis shows M1 as a participant in a process involving elevated exchange of energies between waves. Nevertheless, in Figure 5.21 it was possible to observe that, at the Strouhal number of M1 WSP values were high, denoting a probable energy dump mechanism from M3 and M2 towards M1 which, however, was not enough to acquire a SNR typical of a resonant mode.

The other interaction highlighted in Figure 5.21 involved the triad M2, M1 and their algebraic difference, called Sb_{M2-M1}. Similarly, in this case, the squared bi-coherence was nearly 1.0 and the bi-phase was equal to zero. Such a new mode had to be considered a non-linear-generated sub-harmonic from the coupling of M1 and M2, and was of a second-generation type, i.e. it derived from another existing non-linear interaction. The final picture involved a cascade mechanism (Figure 5.22), in which M3 and M2 interacted to dump energy on a wave at a Strouhal number

corresponding to M1. Such a wave was involved in another non-linear interaction with M2 to generate an additional wave, Sb_{M2-M1}, forming a final four-coupled wave system.

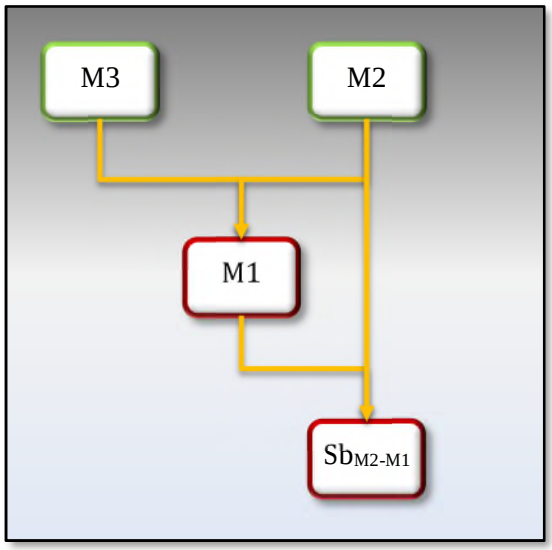

Figure 5.22 – Cascade of non-linear interaction of M2 and M3 derived from WBC analysis of the pressure signal at x/L = 0.9, $2y/W$ = 0.0, z/D = 1.0. *The time interval of integration is between 0.19 to 0.25 seconds.*

Such a structure, however, had to have an unstable nature, since its duration seemed to be limited to the time interval analysed. Moreover, the derived waves, M1 and Sb_{M2-M1}, failed to emerge from the background noise and appear as proper tones, which would be expected if this kind of phenomenon had a stable nature. M2, whose wavelength at these environmental conditions was around twice the cavity's length, was prone to instability due to its bigger dimension with respect to the bay's size. While in configuration AA this translated in an intermittent behaviour, in configuration BB, where the persistence was reduced[35], this triggered the non-linear interactions. This difference, as well as the overall changes that the saw-tooth leading edge and step geometry introduced could be explained by the effect of the saw-tooth profiles on the behaviour of the detached shear layer. In comparison to the straight leading edge case of geometry AA, the indentations of configuration BB had the peculiarity of splitting and tilting the vorticity, so from a transverse axis unique vortex, the shear layer was split into a large number of smaller eddies with tilted axes[36] This transformation from a big eddy to several

[35] The reduction of persistence could be associated with an increase of instability of the mode that "experienced greater difficulty" in being present in the spectrum.

[36] A straight leading-edge cavity prompts the detachment of an eddy structure principally oriented with the transverse axis (see Figure 5.25) and of length comparable with bay width. The introduction of chevrons changes the situation. The large eddy is replaced by smaller structures, which at the detachment

smaller dimensional structures decreased the coherence of the wave pattern, introducing a smearing effect, which was reflected in the pressure footprint of the modes. This aspect was also confirmed by the analysis of the signal energy temporal trend (Figure 5.19d) that, in comparison to case AA had a less pronounced peak (usually attributed to coherent signals) and a more uniform trend with time (more typical of noise and small coherent eddies).

The last cavity geometry analysed (CC) presented, for the pressure signal at x/L = 0.9, a picture similar to configuration BB. JFTFA identified five Rossiter-Heller-like modes (Figure 5.23), M1, M2, M3, M4, and M5. The main difference was represented by the characteristics of M1. Fourier analysis (Figure 5.23.a) placed this tone at a Strouhal number of 0.2548 instead of 0.3149 as was the case for cavity BB. Additionally, the SPL increased by 3 dB to 146.4 dB. From the wavelet analysis (Figure 5.23.c), it was possible to see that such a tone changed also its temporal characteristics, increasing the PR index up to 7.24%, the highest value for M1 of the three cavity types. M2, whilst still the strongest mode, saw a decrease in its power and persistence, with a SPL value of 148.7 dB and a PR value of 18.29%. A similar decrease in power and persistence was also registered for the minor modes, M3 (St = 0.9223, SPL = 138.6 dB, PR = 1.63%), M4 (St = 1.3300, SPL = 134.5 dB, PR = 0.59%), and M5 (St = 1.6940, SPL = 134.9 dB, PR = 1.45%). The striking difference between this cavity configuration, and cases AA and BB, was the new nature of Mt. Global wavelet analysis (Figure 5.23.b) indicated an accumulation of power at higher Strouhal numbers and in this band wavelet analysis (Figure 5.23.c) assumed an almost regular trend in the occurrence of the bursts of energy as the signal evolved during time. However, in the Fourier spectrum (Figure 5.23.a) no particular corresponding peak was evident. Moreover, the wavelet barycentre for such a mode, as shown in the GWSP plot of Figure 5.23.b, was located at a Strouhal number of 4.167, a value much higher than cases AA and BB. The wavelet time-spatial analysis (Figure 5.24) confirmed the previous temporal-spatial arrangements for all the tones. M1, M2, and M3 were true Rossiter-Heller modes, with particularly high power corresponding approximately to the outcome of the analysis of Figure 5.11, with a single “V”-like trend along the cavity length for M1, a double “V” trend for M2, and a triple “V” trend for M3. Wavelet analysis identified their intermittent characteristic with time. Stations at which M4 and M5 had a quasi-temporal periodicity could also be identified. M4 had a more temporal-regular behaviour in the rear part of the cavity, while M5 assumed a regular temporal pattern at x/L = 0.3 and x/L = 0.8. Mt instead was confirmed to be a localised phenomenon instead of a standing wave.

---

point are aligned with the serrating edge of the cavity that immediately evolves into intertwined systems of small pockets of vorticity (see Figure 5.26).

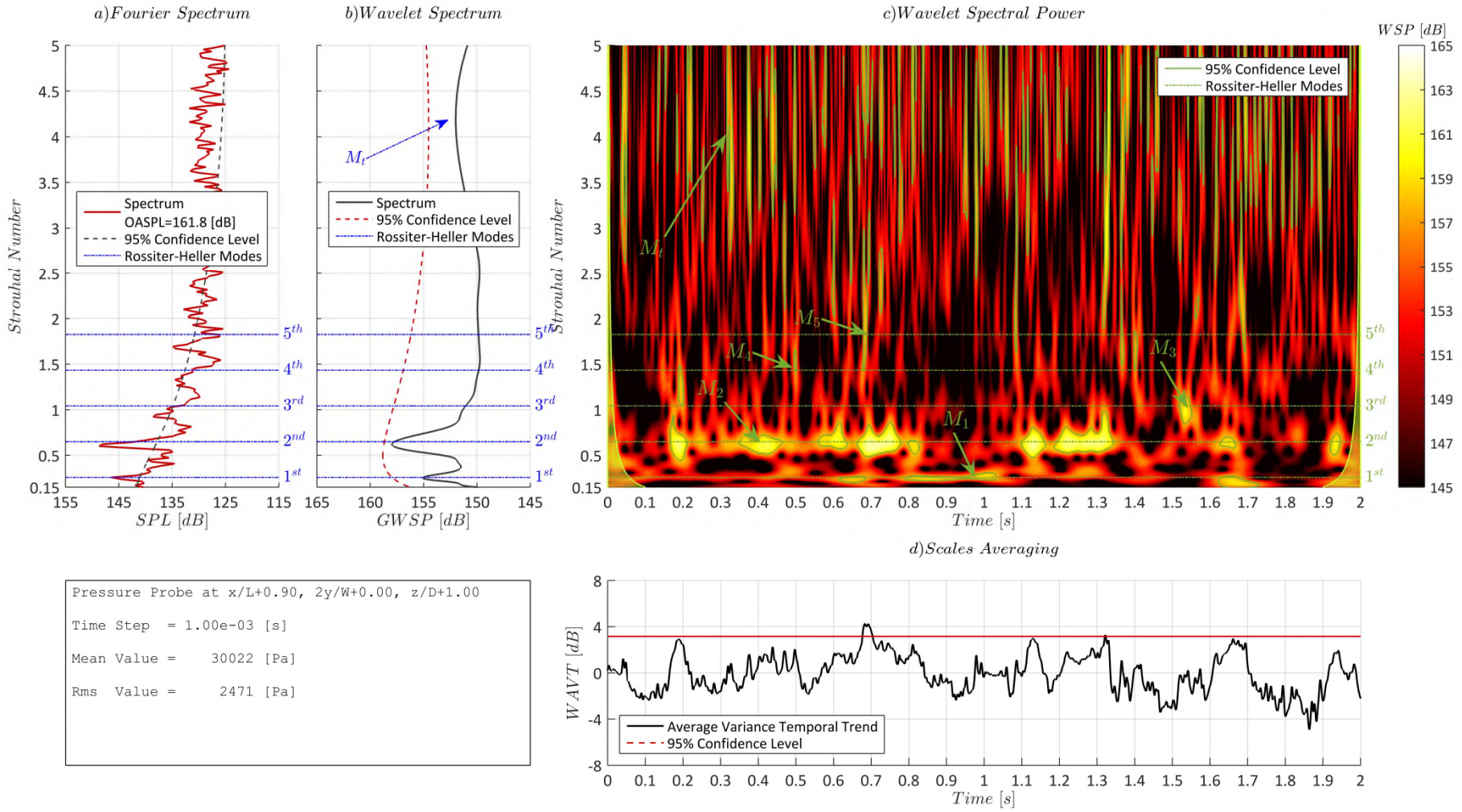

Figure 5.23 - Wavelet analysis of the pressure signal at x/L = 0.9, $2y/W$ = 0.0, z/D = 1.0. *Data refers to configuration CC.*

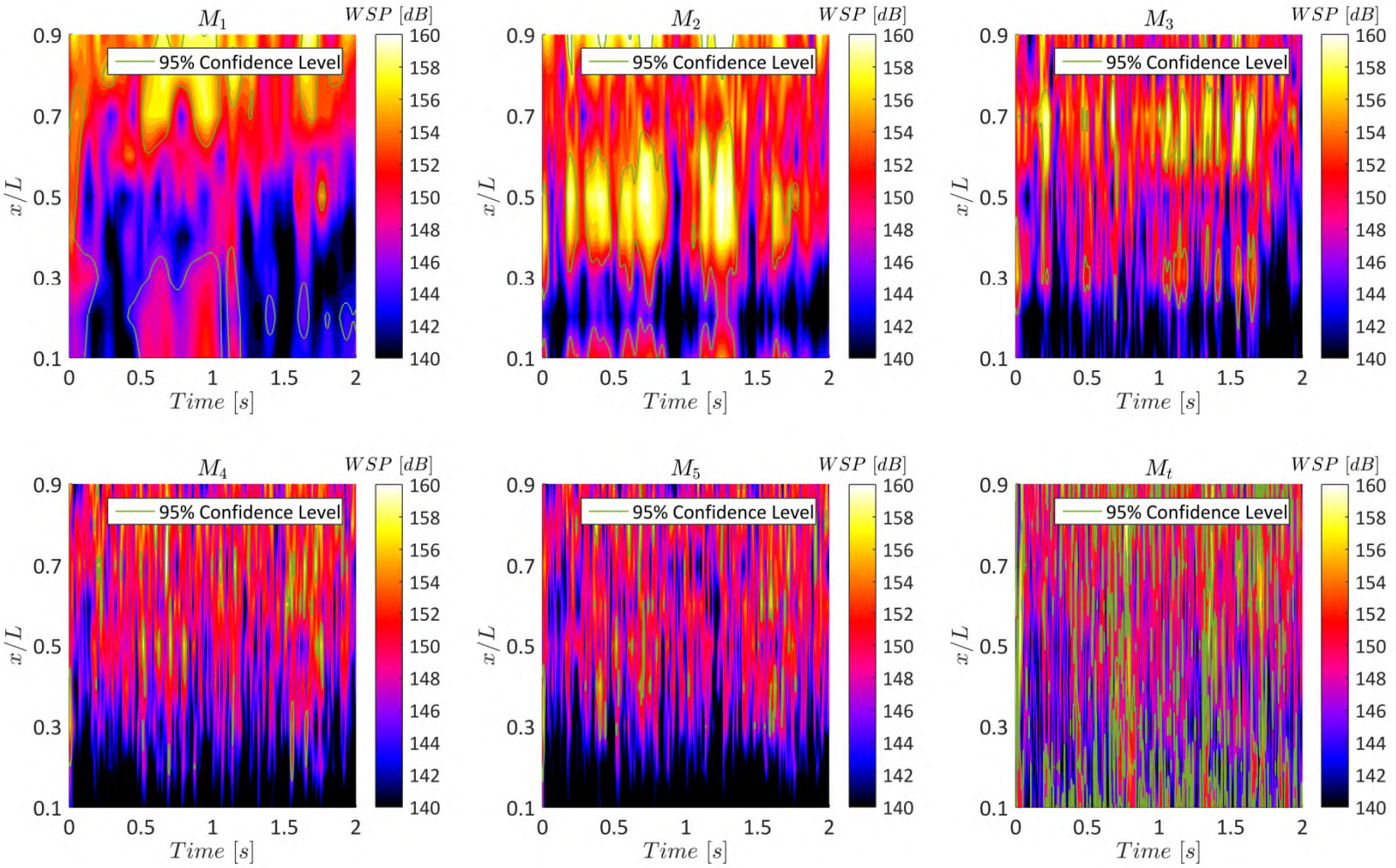

Figure 5.24 - Wavelet spatial-temporal analysis for the modes of pressure signals recorded at Rake 1C. *Data refers to configuration CC.*

Additional insight into the dynamics of the flow was obtained by analysing snapshots of iso-surfaces of the Q-criterion. For each configuration, a time was chosen at which the WAVT of the pressure signal (measured at x/L = 0.9, $2y/W$ = 0.0, z/D = 0.0) had a local maximum and M2, which in all three cases was the dominant tone, had a local peak. This ensured that the analysis was conducted at a time of high flow activity. The corresponding times were t = 0.4 s for configuration AA, t = 0.6 s for configuration BB, and t = 0.7 s for configuration CC.

The reference configuration AA (Figure 5.25) was characterised by alternate detachment of transverse-axis vortices at the leading edge. These structures, moving downstream, experienced tilt and shear motions that changed their shape, fragmenting the original arrangements into smaller eddies. Upon impact with the cavity's trailing edge the original structure was replaced by sparse vortices and a great number of smaller elements of vorticity, which according to Hussain (1986) are a generator of acoustic noise during their decay and tendency to return to isotropy. The fact that the detachment of the shear layer at the leading edge formed a distorted dominant vorticity structures was correlated to the transverse oscillation of the shear layer (evidenced on Schieleren analysis, Figure 5.17). Such aspect impeded a simultaneous roll-up, along the transverse direction of the cavity, of the detached shear layer, forming the distorted structures shown in Figure 5.25.

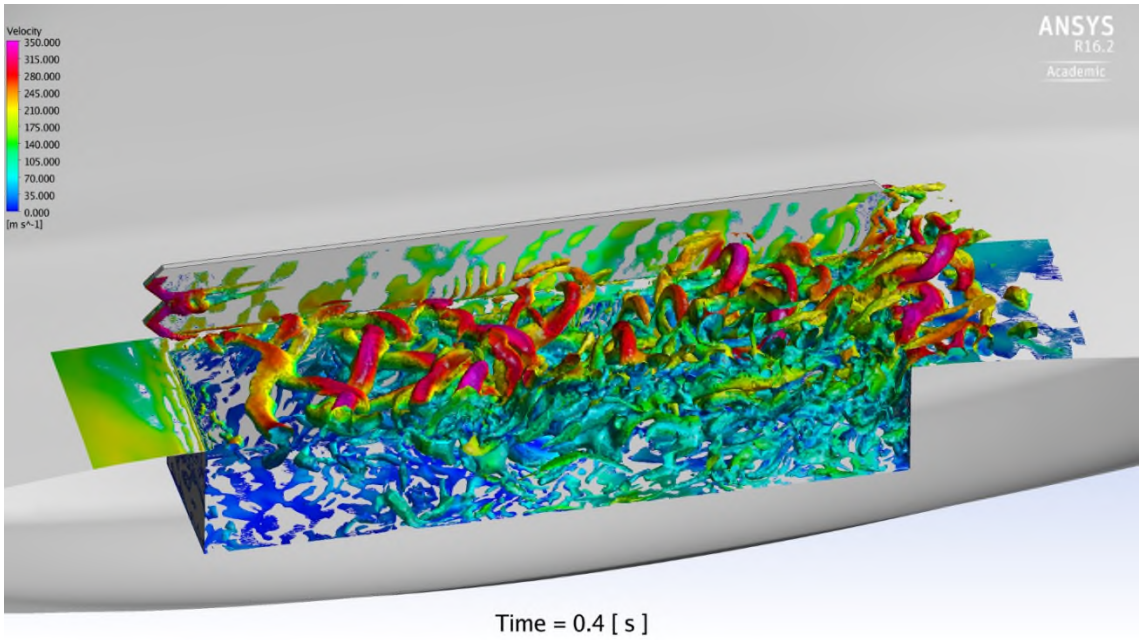

Figure 5.25 - Iso-surface of $Q = 100 \cdot L^2/U_\infty^2$. *Configuration AA. Flow from left to right. Snapshots were taken at times at which the pressure signal (measured at x/L = 0.9, 2y/W = 0.0, z/D = 1.0) had peaks in both the WAVT and M2 histories.*

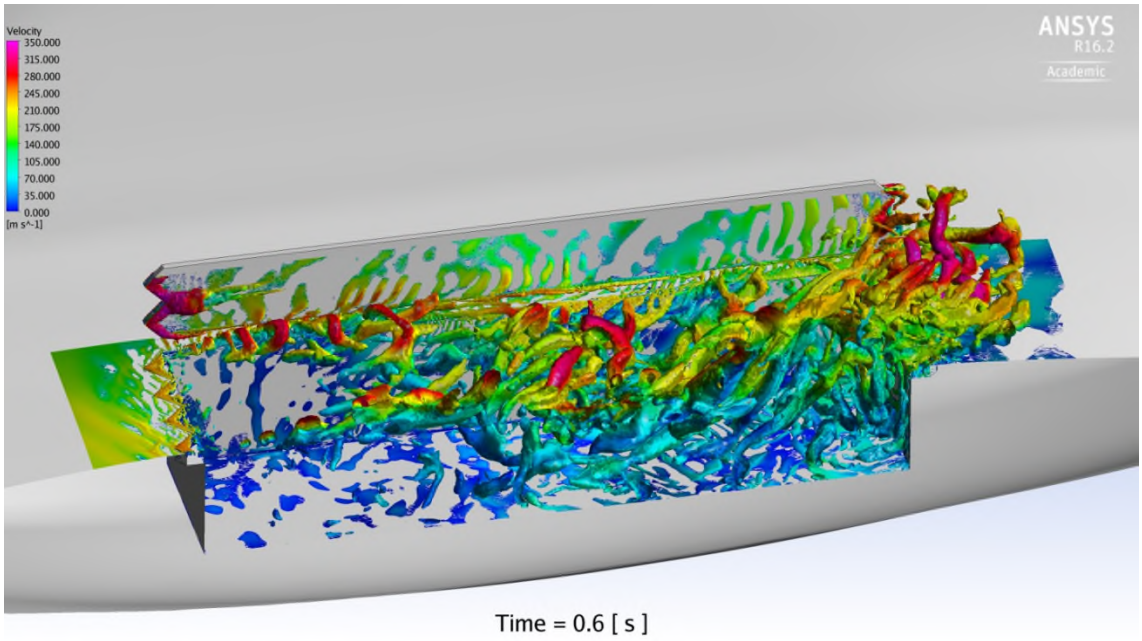

Figure 5.26 - Iso-surface of $Q = 100 \cdot L^2/U_\infty^2$. *Configuration BB. Flow from left to right. Snapshots were taken at times at which the pressure signal (measured at x/L = 0.9, 2y/W = 0.0, z/D = 1.0) had peaks in both the WAVT and M2 histories.*

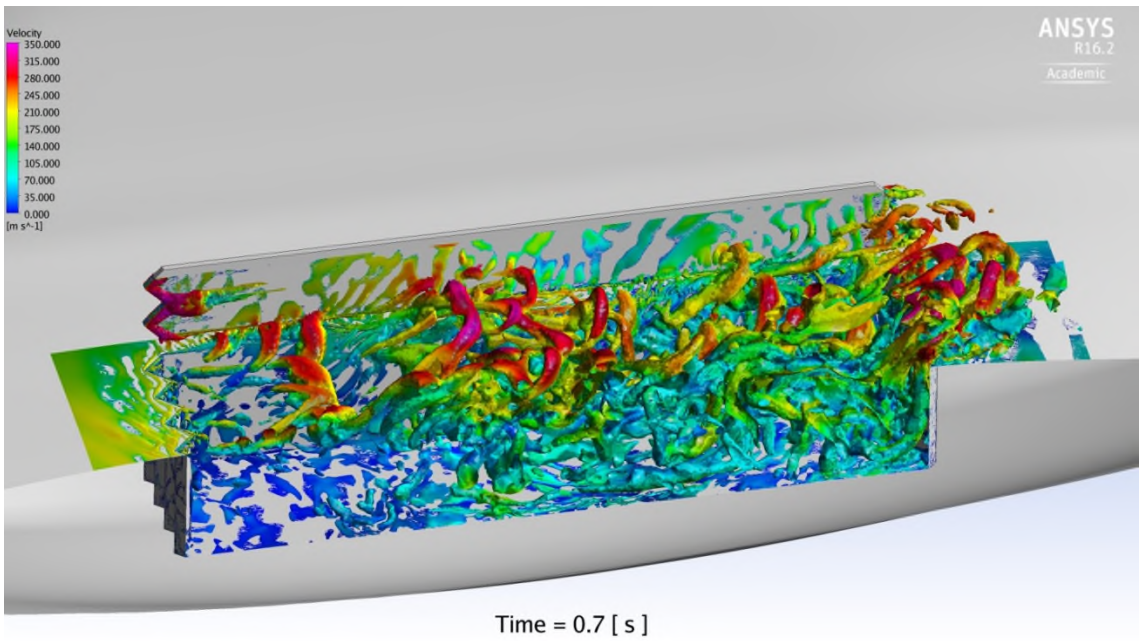

Figure 5.27 - Iso-surface of $Q = 100 \cdot L^2/U_\infty^2$. *Configuration CC. Flow from left to right. Snapshots were taken at times at which the pressure signal (measured at x/L = 0.9, 2y/W = 0.0, z/D = 1.0) had peaks in both the WAVT and M2 histories.*

The situation for cavity BB was completely different. The transverse eddies, characterising case AA, were replaced by different structures, independent from one another, due to the effect of the saw-tooth pattern leading edge (Figure 5.26). At each sawtooth indentation, a pair of small vortices were detached. In addition, the greater part of the central area of the leading edge was occupied by flow experiencing high shear stress[37], favouring the ejection of smaller structures. The splitting of vorticity induced by the geometry of the leading edge prompted an immediate passage to disordered flow structures. This increased randomness in the structure of the shear layer accounted for the different behaviour of the modes inside this type of cavity. Configuration CC had a similar vertical structure to BB (Figure 5.27), however, a difference was recorded in the shear layer's detachment zone that was occupied by sparse longitudinal axis structures, absent in case BB. Their formation was allowed by the absence of the step and the presence of the front wall's indentations. The trailing edge of configuration CC seemed also to offer the best performance, regarding noise behaviour, due to the flow structures that accumulated at the rear of the cavity. Here, in comparison to cases AA and BB, the eddies, instead of colliding with the flat wall and dissipating giving rise to strong sound waves, experienced a slight relief mechanism favoured by the saw-tooth geometry, that reduced the power released from the impact.

5.3 CHAPTER CONCLUSIONS

Installing the cavity models on the UCAV1303 airframe permitted an analysis the differences between the characteristics of a weapon bay geometry tested in an isolated environment, and the consequences derived by the influence of the aerodynamic field of the aircraft. Moreover, CFD simulations enabled the discovery of flow properties that it was not possible to analyse in wind tunnel experiments.

Mean flow analysis indicated that the cavity geometry (AA, BB, or CC type) had a small effect on the trend and the values of the mean pressure coefficient and OASPL curves. When the reference CFD bay geometry was analysed the main difference between it and the isolated case of the wind tunnel experiments was the presence of negative mean pressure coefficients in the front of the cavity. Nevertheless, the concave-convex mode

[37] Since Q-criterion separates areas dominated by rotation from areas dominated by shear, absence of surfaces in zones of the shear layer, when the visualisation is based on an iso-surface of Q-criterion, implies that those areas are dominated by shear.

shape remained the same. Additionally, the OASPL curved varied from the triple “V” shape of the isolated cavity, to the double “V” shape of the installed one.

The analysis of the mean velocity vector field indicated the presence of a three vortex structure, with a main clockwise eddy accompanied by two smaller ones. Slight asymmetries in the transverse direction were found, principally induced by the different height of the cavity sidewalls to comply with the airframe’s lower surface slope in that direction. The various leading and trailing edge geometries again, introduced only local variations in the structure of the flow, implying that the cavity was much more influenced by the surrounding environment, represented by the UCAV, than to local details.

Different trends were instead discovered in the non-stationary flow analysis. The reference configuration was characterised by the presence of two main Rossiter-Heller modes, M1 and M2. Additionally, M3 could be recognised in the wavelet map. Nevertheless, its persistence was so low that the Fourier analysis failed to address it as a true feature of the flow. An additional tone, Mt, already identified in the wind tunnel analysis (see Paragraph 4.2), was also present. Wavelet longitudinal correlations and wavelet spatial analysis characterised M1, M2, and M3 as longitudinal standing waves, whereas Mt had a local nature, which varied from station to station. The analysis of density-gradient pictures finally confirmed the nature of such a mode, which was generated by transverse oscillations of the shear layer, enhanced by the airflow inside the gap between the bay doors and UCAV lower surface. The introduction of sawtooth indentations in configuration BB changed the structure of the spectrum, with the addition of the fourth and fifth Rossiter-Heller tones. Such a difference was a direct consequence of the nature of the shear layer detaching from the cavity’s leading edge. Iso-surfaces of Q-criterion identified that, with respect to the transverse-axis, alternate-detachment of eddies from the saw-tooth leading-edge split and rearranged the vorticity into smaller structures, affecting the characteristics of the aero-acoustics of the system. This was also true for configuration CC. Nevertheless, it appeared that a completely indented wall further lowered the PR indices of all modes. Additionally Mt was so much affected that, whilst being represented as a continuous diffused burst of energy in the wavelet map, it was characterised as broadband noise in the Fourier analysis.

This CFD campaign demonstrated the differences between wind tunnel studies on isolated cavities, and the reality of installation on a weapon bay in an airframe. While mean flow

properties were less affected, the qualitative aspect of the non-stationary flow was profoundly changed.

This set of experiments also identified an aspect that is often not considered in experimental investigation. Wind tunnel analysis usually collects time histories equivalent to thousands of times the characteristic time of the cavity. In real cases, however, the nature of employment of weapon bays is such that the effective time of opening of the cavity is of the order of hundreds t_{Char}. As long as boundary conditions are kept constant, this factor affects only the level of random error of the experiments, which, is usually bigger for CFD than the wind tunnel, because in the former the number of samples collected is less with respect to the latter. However, if experiments and/or simulations are taken into consideration where the boundary conditions are no longer constant, the temporal scaling factors must be respected as well as the dimensional ones. For example, if it is intended to simulate a weapon bay door opening, care must be taken when using a scale model. If in the full-scale case the doors open in a frame equivalent to n-times t_{Char} the same value must be recreated whenever testing a scale model.

Table 5.1 - Summary of the main modes for all geometry configurations. *All data refers to the analysis of pressure signals recorded at station x/L 0.9, 2y/W 0.0, z/D 1.0. Doors angle 90 degrees. Incidence and sideslip null.*

GEOMETRY	MODE ID	St [FFT]	SPL [dB]	St [GWSP]	GWSP [dB]	PR %	OASPL [dB]
AA	M1	0.2574	144.6	0.2601	154.1	3.87	162.1
	M2	0.6434	150.5	0.6404	159.9	28.33	
	M3	0.9866	136.2	1.0400	150.8	1.51	
	Mt	3.3240	138.4	3.4990	152.9	17.39	
BB	M1	0.2788	143.4	0.3149	153.6	1.27	162.1
	M2	0.6220	150.4	0.6411	159.4	29.59	
	M3	0.9652	139.0	0.9649	152.7	4.70	
	M4	1.3730	137.4	1.3460	151.0	2.60	
	M5	1.7370	135.3	1.7140	150.3	1.65	
	Mt	3.4100	136.9	3.6200	151.5	11.58	
CC	M1	0.2574	146.4	0.2548	155.1	7.24	161.8
	M2	0.6006	148.7	0.6205	157.9	18.29	
	M3	0.9223	138.6	0.9285	151.6	1.63	
	M4	1.3300	134.5	1.2610	150.1	0.59	
	M5	1.6940	134.9	1.6440	149.8	1.45	
	Mt	-	-	4.1670	152.0	15.19	

6 ANGLE OF ATTACK EFFECTS

In combat-live situations, military aircraft may release a store at incidences other than zero implying that a weapon bay could experience an oncoming flow with a local angle of attack. Nevertheless, the standard approach, in public literature, to the analysis of cavity flows, even when installed in airframes, has always been to fix the angle of attack seen by the cavity to zero, in order to explore the effects of other parameters. It was decided, therefore, to investigate the effects of angle of attack to take a further step forward in bridging the knowledge gap between research models and real-life applications. The incidences analysed, in addition to the reference configuration at 0.0 degrees, were 3.0, 4.5, and 6.0 degrees. Such spacing was considered a good compromise between accuracy in the analysis of AOA effects and the length of time of the CFD simulation campaign. In this case it was not possible to have a double (experimental and computational) approach, hence, it was conducted only in CFD on the UCAV1303/M219-AA geometry (cavity with straight leading and trailing edges). The angle of attack of 4.5 degrees was investigated retrospectively due to the sudden change in flow properties that were discovered passing from an incidence of 3.0 to an incidence of 6.0 degrees. All runs were executed with bay doors at 90 degrees open and at the same flight conditions indicated in Table 3.7. As in the previous chapter, the results will be divided into mean flow analysis and non-stationary flow analysis.

6.1 MEAN FLOW ANALYSIS

The introduction of a positive incidence generated a vertical component of the freestream velocity, directed towards the cavity interior. It was expected that the mean qualities of the flow would be influenced by this angle of attack, and so it was confirmed. The analysis of the central longitudinal rake of the mean pressure coefficient indicated that the typical trend of transitional-open type cavity, described in Paragraph 5.1, was maintained. As shown in Figure 6.1 the effect of passing from 0.0 to 3.0 degrees and from 3.0 to 6.0 degrees of AOA was a shift of the curve towards higher $\bar{C}_p$ values, approximately 0.1 units every 3 degrees. An unexpected trend was encountered at 4.5 degrees AOA. Here, only stations up to x/L = 0.4 experienced the upward constant displacement, while for the rest of the bay, the pressure coefficient was nearly equal to the 3.0 degrees case. Such an out of line result indicated that inside the cavity some flow configuration change had occured. Analysis of the mean velocity vector field revealed a complex process of flow structures that changed every time the angle of attack was varied. As described in Paragraph 5.1, the

reference configuration at zero incidence was characterised in the XZ cut on the bay's symmetry plane by a main clockwise vortex centred at x/L = 0.4 and two secondary vortices close to the cavity floor; the front one, with a counter clockwise sense of rotation, while the back one with a clockwise trend. The first incidence step, from α = 0.0 degrees (Figure 6.2) to α = 3.0 degrees (Figure 6.3), showed a variation of this arrangement. At zero angle of attack the front part of the cavity, in the XY plane at z/D = 0.5, was dominated by a large clockwise vortex, centred approximately at x/L = 0.1. At this new incidence the flow had a significantly altered configuration.

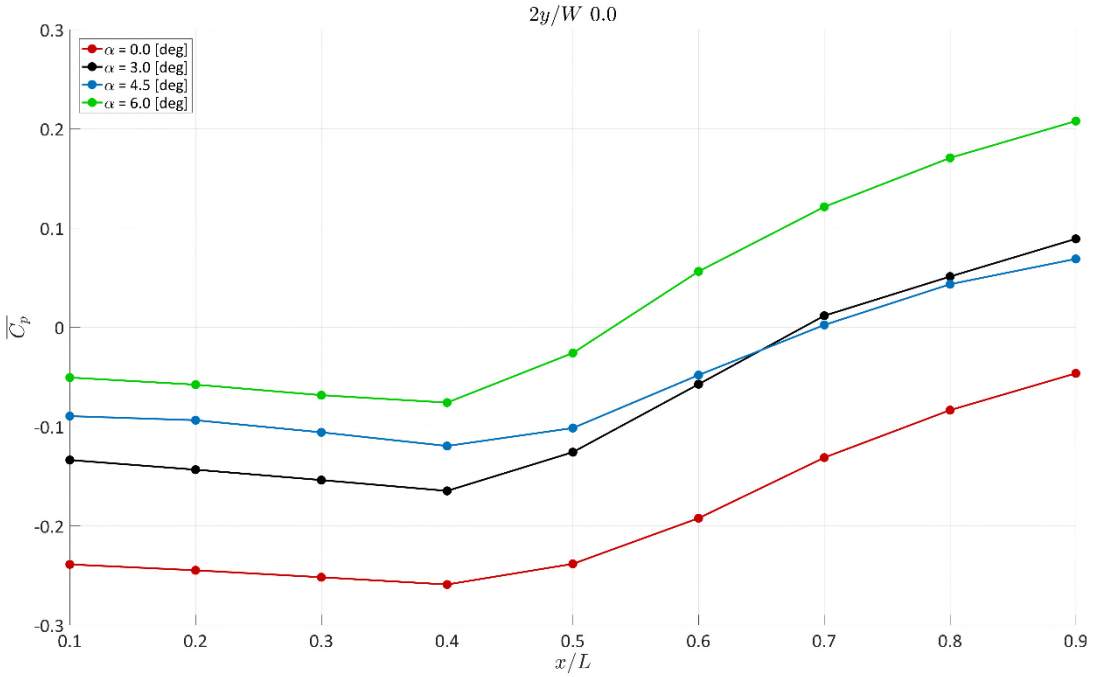

Figure 6.1 - Angle of attack effects on mean pressure coefficient. *Data refers to central rake.*

At 3.0 degrees AOA, a multiple eddy system replaced the previous single vortex in the XY plane, extending its topological influence up to x/L = 0.25 (in the reference case the main vortex occupied an area up to x/L = 0.2). The XZ cut also indicated a configuration change. The organised field present between the front and the main vortex, which characterised the reference configuration, was replaced by a different streamline pattern, with the addition of a further secondary vortex beneath the main one, placed around x/L = 0.25. From the XZ cut view, it was possible to see the effect of the vertical component of the freestream velocity, which enhanced the mass flow entrapment inside the cavity. The combination of these new fluid configurations caused the parallel displacement of the mean pressure coefficient curve as incidence was changed from zero degrees to 3.0

degrees. In the next angle of attack step (4.5 degrees, Figure 6.4), a new flow configuration was observed. From the XY cut view, it was noticed that the single vortex structure reappeared in the front of the cavity, but in this case with a counter clockwise orientation. This area of the bay changed configuration also in the XZ view with a strongly disorganised flow. Here it was also observed that the main clockwise vortex was smaller and moved towards the front of the cavity, probably due to the increased inward motion of the shear layer, which experienced a substantial drop towards the bay, nearly colliding with the floor around station x/L = 0.9. Such enhanced downward bending of the streamlines tilted the major axis of the main vortex downwards, bringing the floor in the rear part of the cavity closer to a higher speed flow, and helping to explain the behaviour of the mean pressure coefficient in this area. As shown in Figure 6.2 and Figure 6.3, the main vortex assumed an elliptical form, due to the combined action of stretching by the shear layer, and constraint by the cavity's floor. However, for both the reference case and the α = 3.0 degrees one, the ellipse's major axis was almost horizontal. In the α = 4.5 degrees case, the major axis was instead tilted downwards by approximately 30 degrees. The final angle of attack investigated, (6.0 degrees, Figure 6.5), maintained the main vortex major axis tilt and the centre of the eddy was moved rearwards up to station x/L = 0.3. The standard three-eddy structure in the XZ cut view, typical of the reference case, was restored, but the bay's front secondary vortex had a clockwise sign instead of counter clockwise. A strong asymmetry was registered in the front of the cavity, in the XY cut view, which did not affect in any way the mean pressure trend. A notable feature was encountered at the cavity trailing edge. At this point a large separation zone was formed dominated by the inward shear layer displacement, which moved the impact point at the bay's rear face deeper inside the cavity. Once impacted, the mass flow was directed outside of the cavity, separating at the sharp trailing edge and giving rise to a vortex. Such a separation, while probably existing in all other cases, was strongly pronounced at this incidence and of larger dimensions.

The OASPL curves (Figure 6.6) had a behaviour similar to the mean pressure coefficient. While the general shape was always similar to the reference one (concave-convex-concave form with inflection points located between x/L = 0.2 and x/L = 0.3, and at x/L = 0.6), the effect of the angle of attack variation was distinguished by an overall translation of the curve.

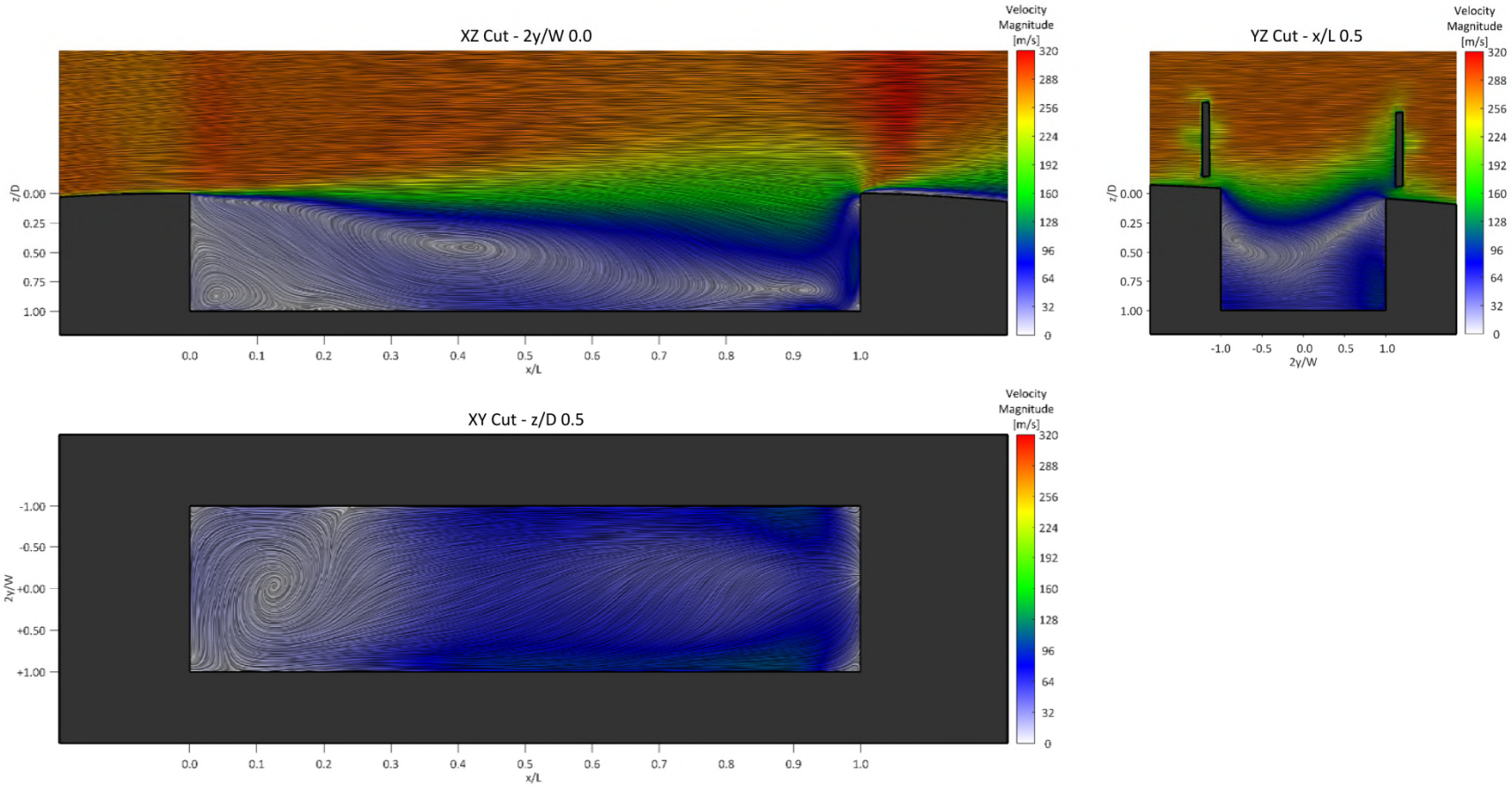

Figure 6.2 - LIC visualisation of the mean velocity vector field coloured by velocity magnitude. *The sketch shows cuts at three different planes for α = 0.0 degrees. Flow from left to right in the XY and XZ view, and out of the page in the YZ view.*

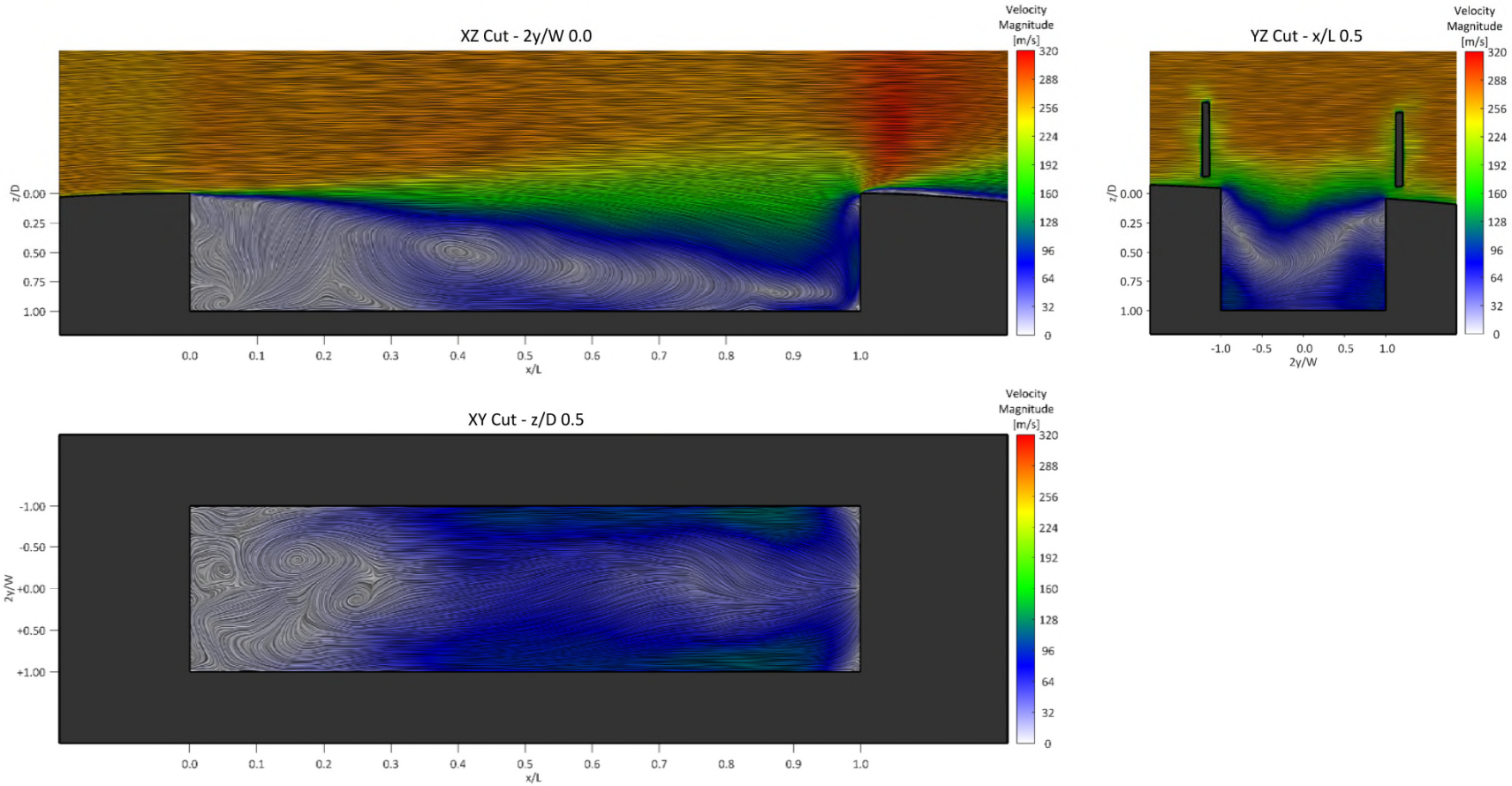

Figure 6.3 - LIC visualisation of the mean velocity vector field coloured by velocity magnitude. *The sketch shows cuts at three different planes for α = 3.0 degrees. Flow from left to right in the XY and XZ view, and out of the page in the YZ view.*

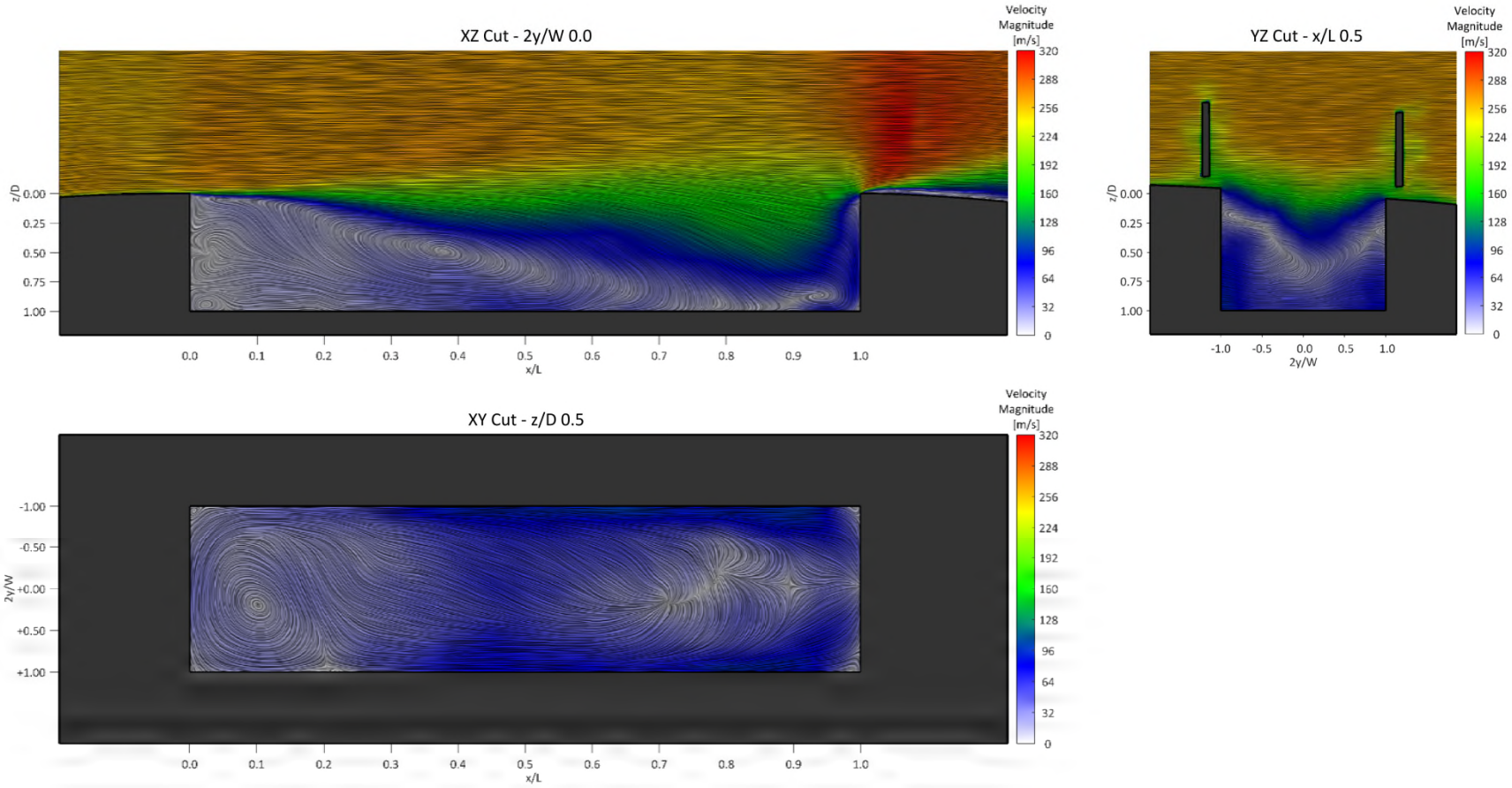

Figure 6.4 - LIC visualisation of the mean velocity vector field coloured by velocity magnitude. *The sketch shows cuts at three different planes for α = 4.5 degrees. Flow from left to right in the XY and XZ view, and out of the page in the YZ view.*

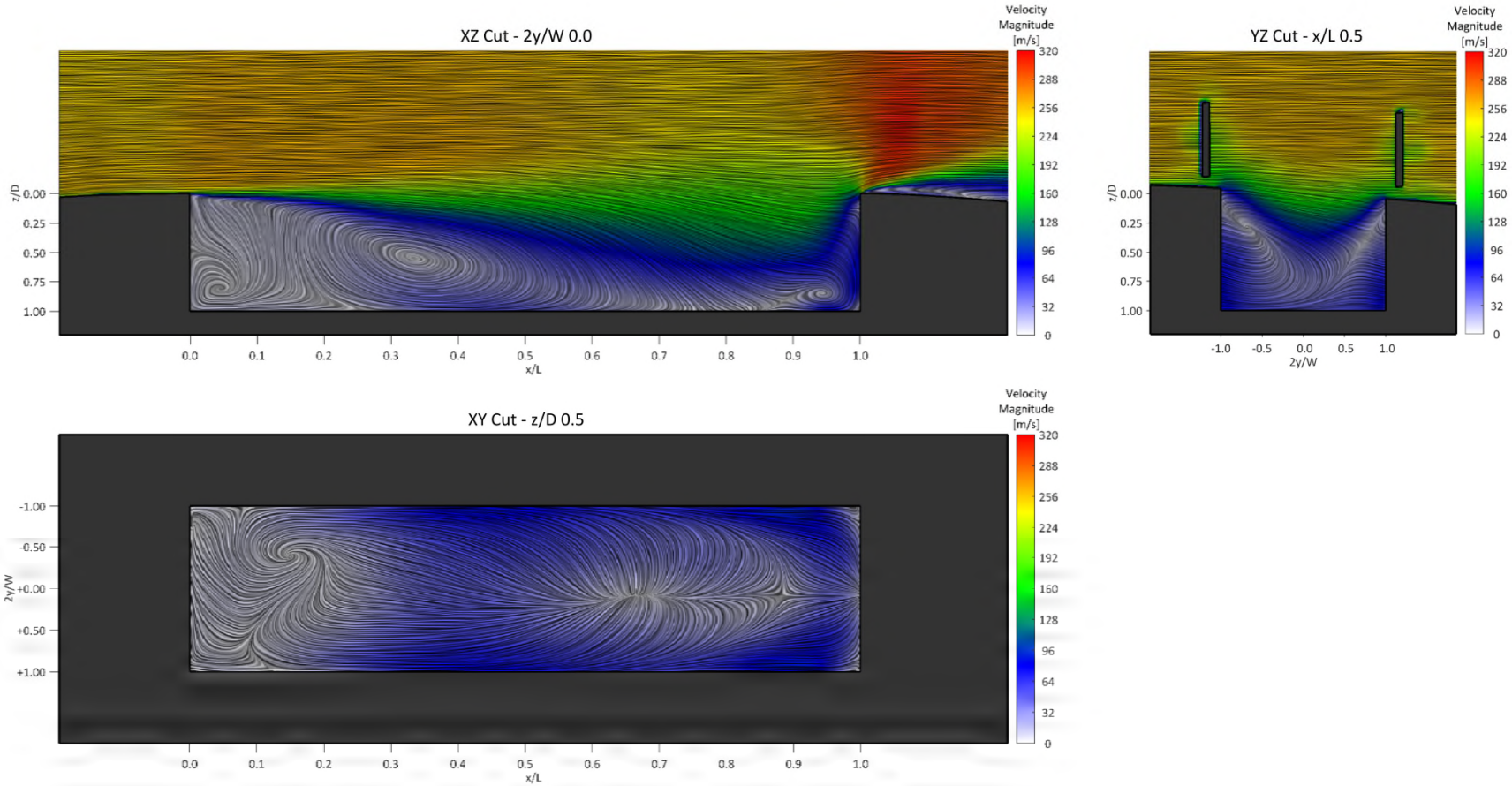

Figure 6.5 - LIC visualisation of the mean velocity vector field coloured by velocity magnitude. *The sketch shows cuts at three different planes for α=6.0 degrees. Flow from left to right in the XY and XZ view, and out of the page in the YZ view.*

Changing the incidence from 0.0 degrees to 3.0 degrees increased the OASPL by 1 dB at all stations. This observation correlated with the increase in freestream flow inside the cavity adding more energy to the pressure oscillations, however, from 3.0 degrees to 4.5 degrees of incidence this trend was reversed. In this case, the signal power was lowered by an average of 3 dB in the whole cavity, suggesting that the changing flow topology, recorded in the analysis of the mean vector field, altered the noise accumulation mechanism. The last incidence step, from 4.5 degrees to 6.0 degrees, restored the original trend and the OASPL curve was raised by 2 dB, returning to a noise level similar to the reference case.

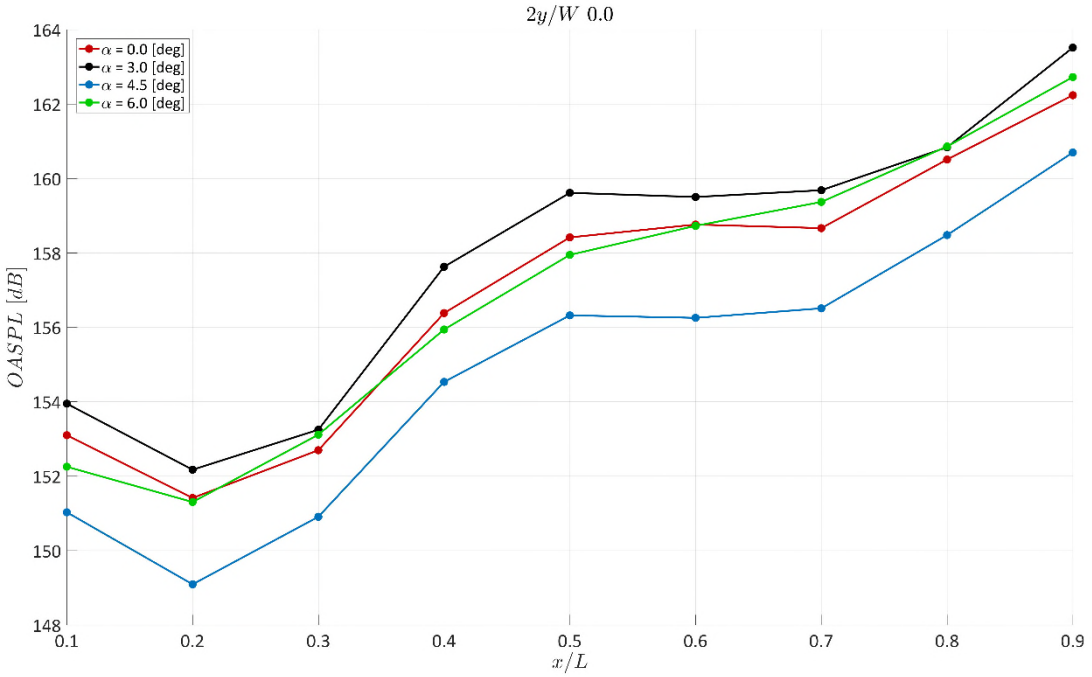

Figure 6.6 - Angle of attack effects on OASPL. *Data refers to central rake.*

From this analysis, it was clear that the cavity flow underwent a strong flow re-configuration between 3.0 and 6.0 degrees of incidence.

6.2 NON-STATIONARY FLOW ANALYSIS

The non-stationary study of the angle of attack effects concentrated on the JFTFA analysis of the pressure signals registered at station x/L = 0.9, $2y/W$ = 0.0, z/D = 1.0.

In the reference case (α = 0.0 degrees - Figure 6.8), it was found that the pressure signal was characterised by the presence of three Rossiter-Heller-like modes (labelled M1, M2, and M3) and an additional mode (labelled Mt), created by the combined effect of the presence of the bay doors and the flow in the gaps between them and the airframe lower

surface. All tones had a strong intermittent behaviour, experiencing short-time bursts of activity followed by longer times of absence. M2 was the strongest tone and had the highest PR index with respect to all the other resonant modes. Upon increasing the incidence to 3.0 degrees (Figure 6.9) the principal tones, M2 and M1, increased their power levels, by 2.5 dB and 3.6 dB respectively. Furthermore, while the PR index of M2 increased slightly from the 28.33% of the null incidence case to 33.03%, M1 saw a doubling of this quantity, from the previous 3.87% to 6.22%. Such a result indicated that the increased angle of attack reinforced the nature of the main resonant modes making also them less intermittent and more stable. Mt too slightly increased its power and persistence. The main change from the zero angle of attack case was the complete disappearance of M3. While the Fourier transform (Figure 6.9.a) indicated the presence of a small amplitude power peak, the wavelet analysis (Figure 6.9.b – t=1.85 s) indicated just one particular burst of energy crossing the confidence level boundary.

Analysing the wavelet time-spatial map (Figure 6.7) of the Strouhal band containing the zero incidence M3 tone, it was possible to observe only occasional medium-power events, between station x/L = 0.6 and x/L = 0.7. This may have been sufficient for a peak to appear in the Fourier analysis. Nevertheless, the signal to noise ratio was so low that the occasional energy burst observed would have been probably better defined as a random occurring event rather than an organised intermittent tone. It was decided, therefore, to categorise all the power content in this band as background noise instead of a Rossiter-Heller mode.

At α = 4.5 degrees (Figure 6.10), the overall configuration remained unchanged, with the presence of M1, M2 and Mt. However, in this case the power of the modes and the broadband noise was lower. Additionally, while the PR index of M1 remained unchanged, M2 saw a decrease, lowering its value to 25.30%. Mt also decreased its persistence, to a value of 16.71%. Such a weakening of the main mode could be the reason for the decrease of the characteristic OASPL curve at this incidence.

The reason for M2's sensitivity to incidence variation might have resided in its characteristics. Its wavelength was, in fact, slightly below twice the cavity length. This put the tone antinode point coinciding with the cavity trailing edge, making this mode strongly influenced by external variation of incidence. By comparison, M1's wavelength, approximately equal to five times the cavity's length, had a node and antinode far away from the bay's trailing edge and was less likely to be influenced by small angle of attack

variations. Mt too, being a mode not correlated with longitudinal variations of the velocity vector field, was less influenced to angle of attack variations than to M2.

As shown in the mean flow analysis, at α = 4.5 degrees, the shear layer trajectory deviated from the α = 0 case and tended to penetrate inside the cavity, affecting the energy accumulation mechanism of the pressure signal at the bay's rear face. The JFTFA of the highest incidence, α = 6.0 degrees (Figure 6.11), showed the appearance of an additional mode, M4, located at a Strouhal number of 1.265, and the restoration of M3. In this case, the power of the main tones (M1 and M2) were higher than at α = 4.5, and the SPL values were similar to the α = 0.0 degree case. The mode characteristics were respectively SPL = 146.5 dB and PR = 6.38% for M1, SPL = 147.9 dB and PR = 13.69% for M2, SPL = 139.4 dB and PR = 2.15 % for M3, SPL = 137.7 dB and PR = 1.04 % for M4, and SPL = 140.5 dB and PR = 25.43% for Mt. A feature identified from the wavelet time-frequency map (Figure 6.11.c), was the nature of M3 and M4, which appeared only in a time-localised frame of the signal, between t = 0.5 and t = 0.6 seconds. The remainder of the data did not present any particular energetic content in these two bands. Nevertheless, analysing the time-spatial map of the modes it was possible to determine that these were not a casual phenomenon occurring in the signal, as in the α = 3.0 degrees case, but true tones present in the flow. From Figure 6.12 it was possible to see how M3, between x/L = 0.5 and x/L = 0.7 had a strong signature in time. This corresponded to a cavity location in which M2 was absent, probably favouring the formation of M3. Similarly, M4, indicated a spatial arrangement that, even if more smeared with respect to M3, had a regularity typical of a resonant mode.

An additional insight into the dynamics of the flow was taken by analysing snapshots of iso-surfaces of Q-criterion (Figure 6.13). For each incidence, a time was chosen at which the WAVT of the pressure signal (measured at x/L = 0.9, $2y/W$ = 0.0, z/D = 0.0) had a local maximum. Distinguishable features could be located at both the cavity's leading and trailing edges. At the leading edge, the alternate vortex detachment scheme was well recognizable at all angles of attack, however, at an incidence of 6.0 degrees this scheme was altered and eddies had lower overall velocity. At the bay's rear face, the scheme always changed with incidence. At 0.0 degrees, this area was characterised by an entanglement of medium sized eddies with high-speed areas. At 3.0 degrees, the density of vortex filaments was reduced but the high velocity spot remained. Once 4.5 degrees of incidence was reached the filaments appeared smaller and with lower velocity, indicating a less-organised vortex flow, and explaining the lower pressure fluctuations characterising this case. At the final angle of attack, 6.0 degrees, the vortex field structure was resumed,

with high-speed spots and bigger filaments. Such changes indicated a correlation between vortex field dispersal and the characteristics of the pressure signal. The incremental change of angle of attack introduced a profound alteration of the characteristics of the entangled vortex filament scheme colliding with the rear of the cavity. Whenever, such filaments were smeared, dispersed, or had less energy, the noise generation mechanism was reduced. It seemed, in fact, that in cavity flow, noise generation was produced by the passage of vorticity from larger anisotropic structures (such organised vortex filaments), to smaller isotropic regions of vorticity (turbulence decay mechanism, see Hussain (1986)).

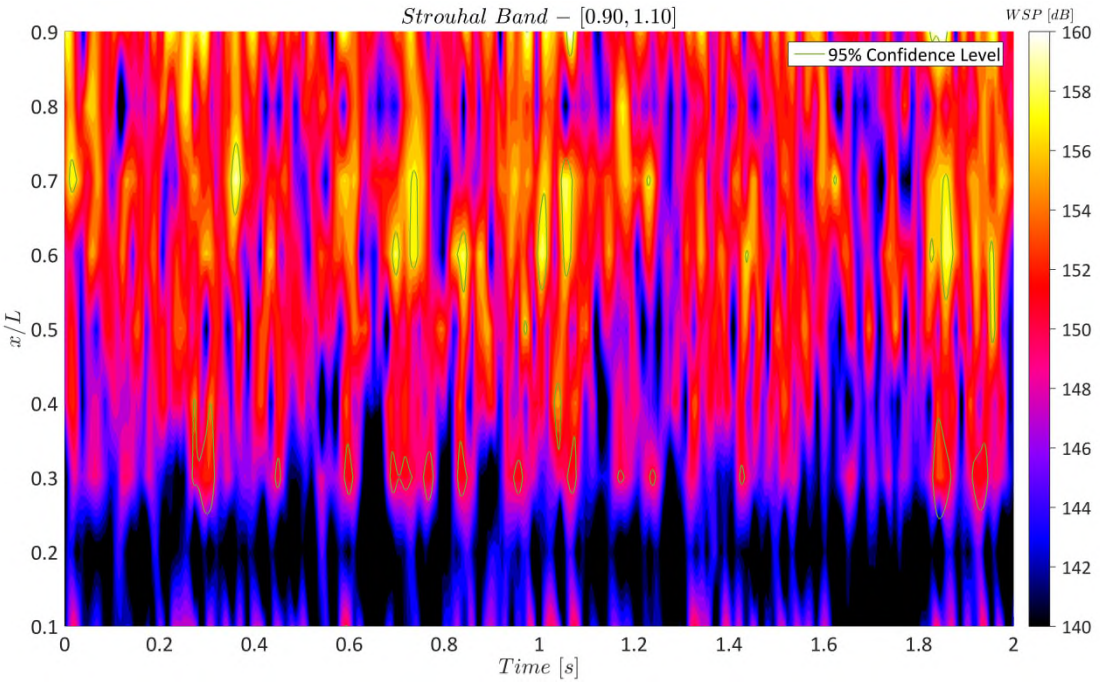

Figure 6.7 - Wavelet spatial-temporal analysis for the Strouhal band between 0.9 and 1.1 of pressure signals recorded at Rake 1C. *Data refers to* $\alpha = 3.0$ *degrees.*

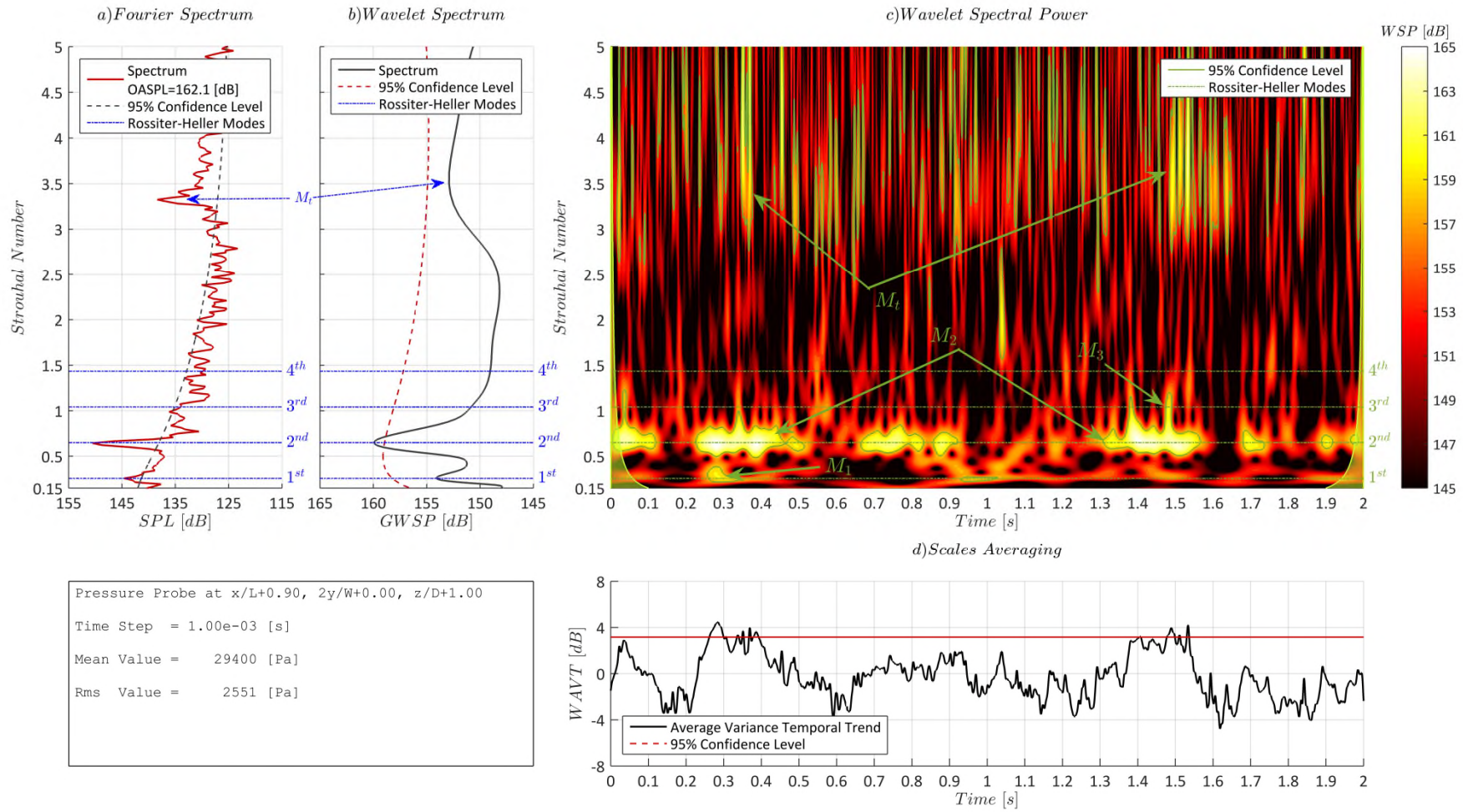

Figure 6.8 - Wavelet analysis of the pressure signal at $x/L = 0.9$, $2y/W = 0.0$, $z/D = 1.0$. *Data refers to* $\alpha = 0.0$ *degrees.*

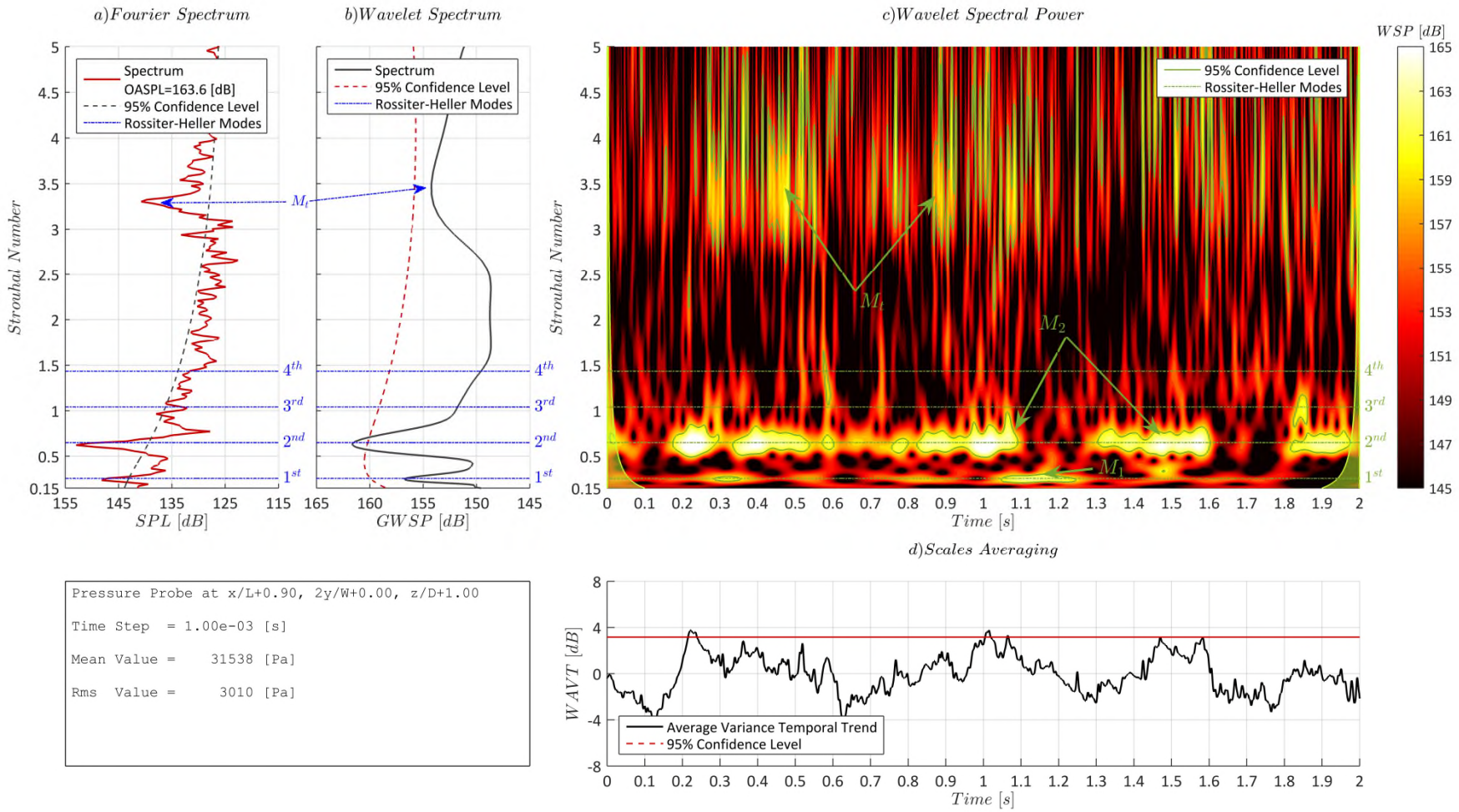

Figure 6.9 - Wavelet analysis of the pressure signal at $x/L = 0.9$, $2y/W = 0.0$, $z/D = 1.0$. *Data refers to* $\alpha = 3.0$ *degrees.*

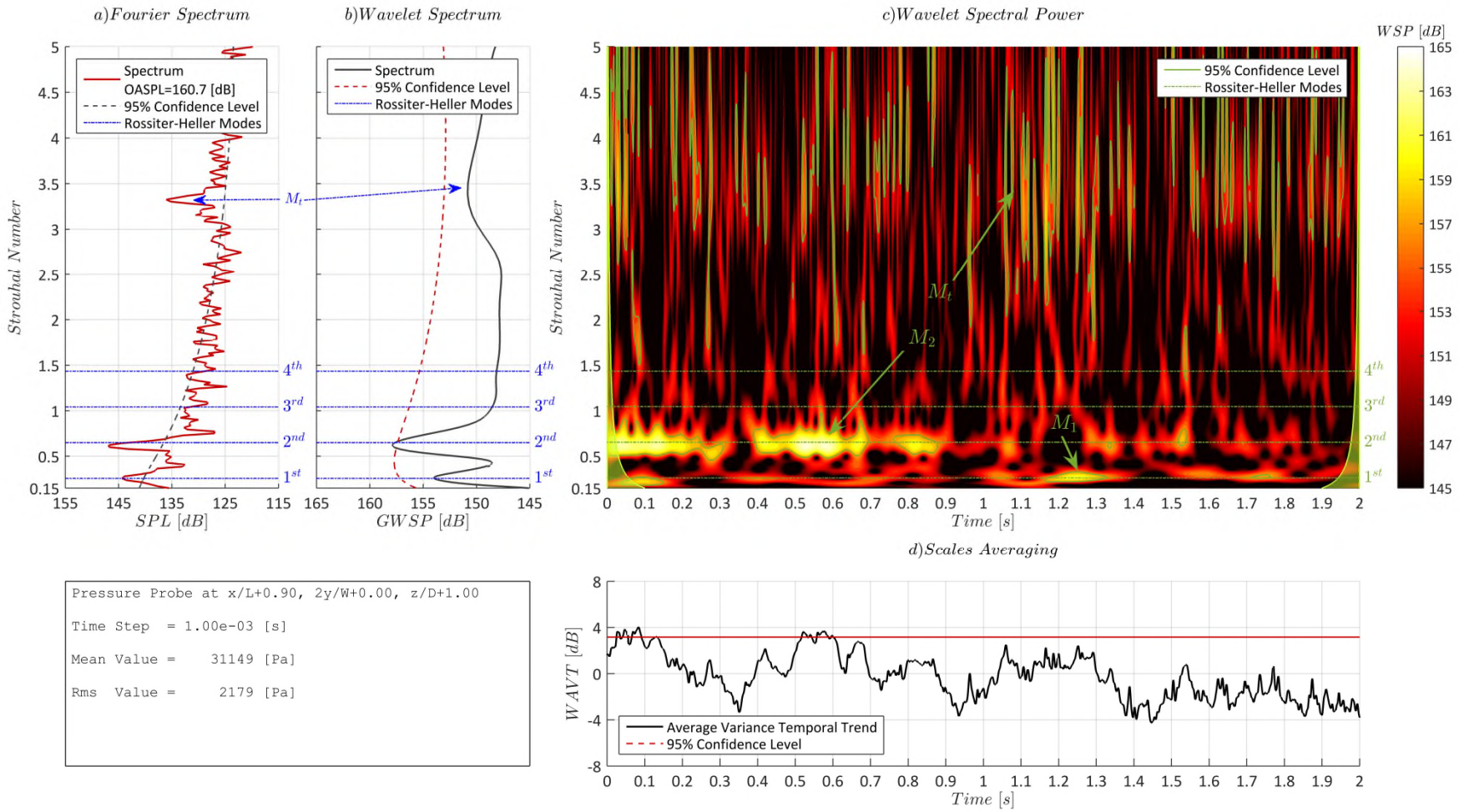

Figure 6.10 - Wavelet analysis of the pressure signal at $x/L = 0.9$, $2y/W = 0.0$, $z/D = 1.0$. *Data refers to* $\alpha = 4.5$ *degrees.*

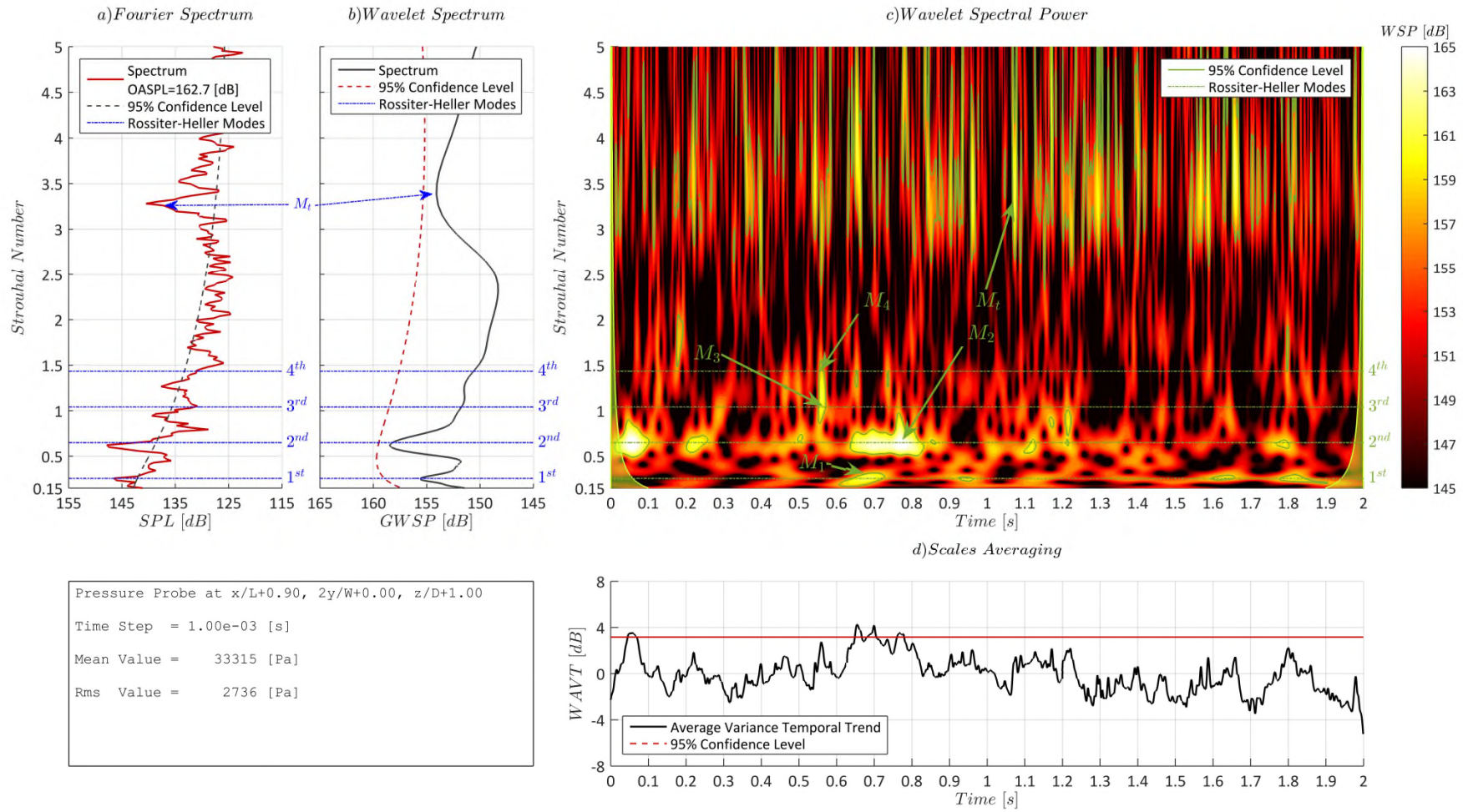

Figure 6.11 - Wavelet analysis of the pressure signal at $x/L = 0.9$, $2y/W = 0.0$, $z/D = 1.0$. *Data refers to* $\alpha = 6.0$ *degrees.*

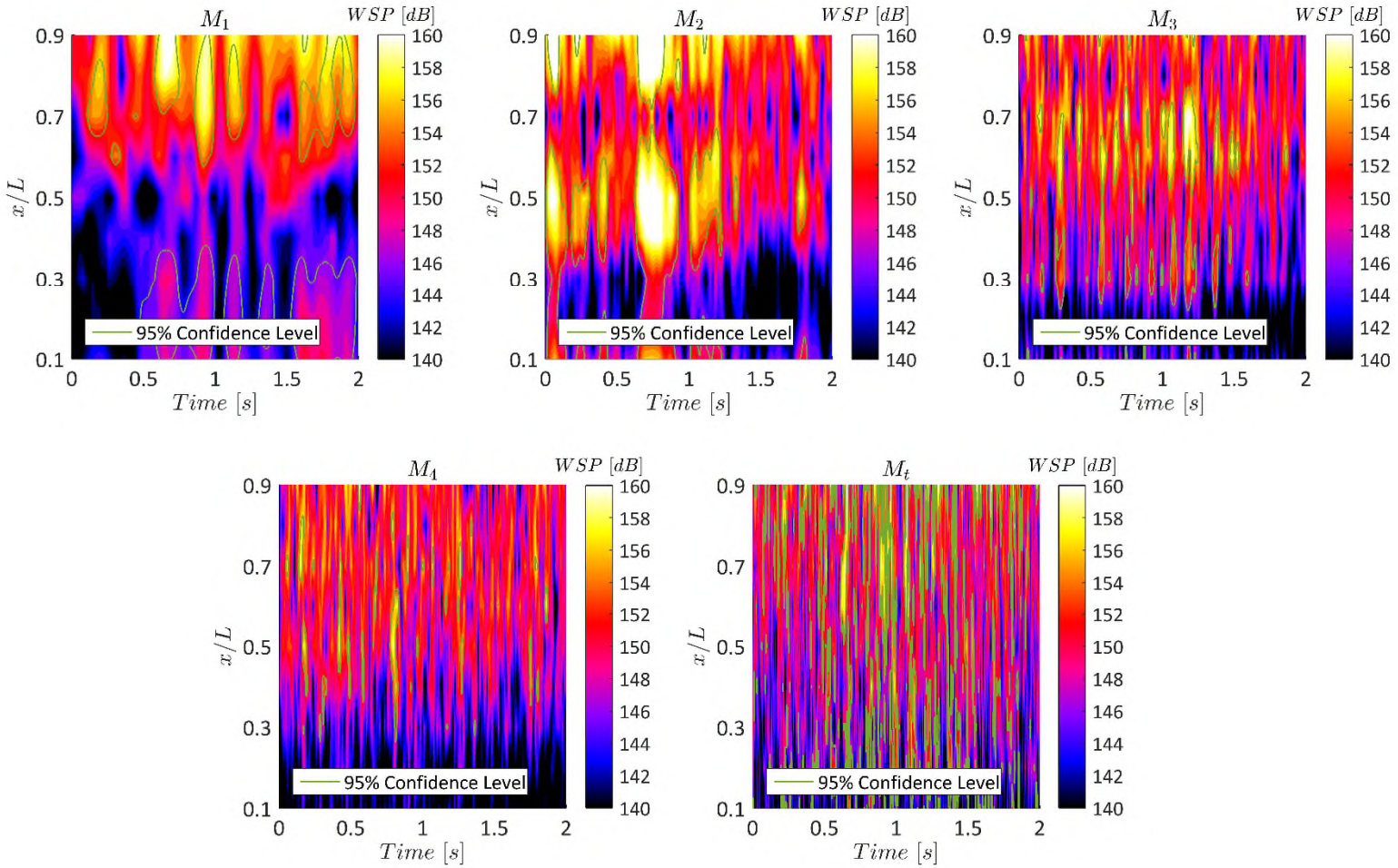

Figure 6.12 - Wavelet spatial-temporal analysis for the modes of the pressure signals recorded at Rake 1C. *Data refers to* $\alpha = 6.0$ *degrees.*

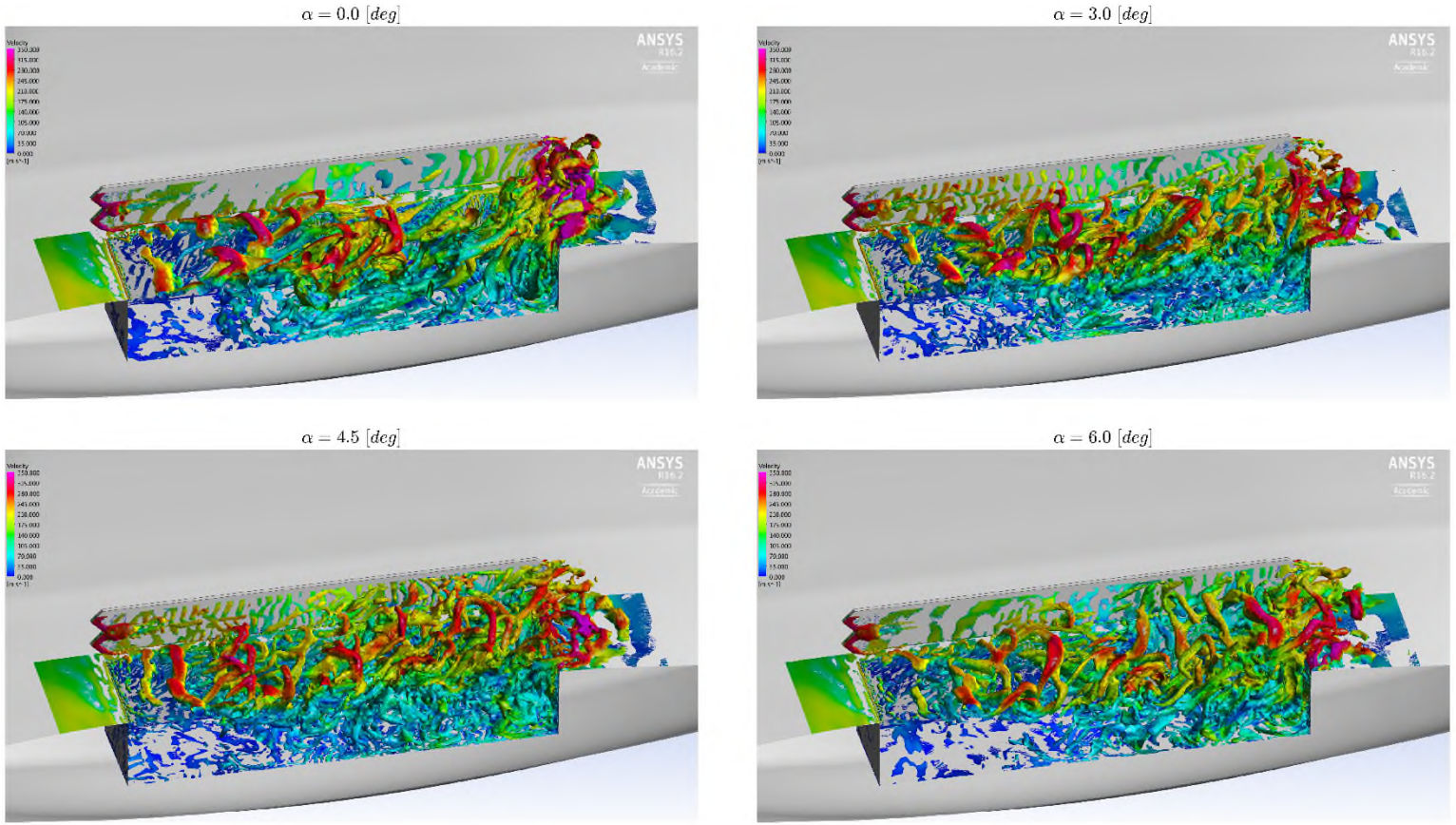

Figure 6.13 - Angle of attack effects on the Iso-surface of $Q = 100 \cdot L^2/U_\infty^2$. *Data is coloured by velocity magnitude (Min= 0.0 [m/s], Max=350.0 [m/s]. Flow from left to right. Snapshots were taken at times corresponding to the pressure signal's (measured at x/L = 0.9, 2y/W = 0.0, z/D = 1.0) local peaks of energy.*

6.3 CHAPTER CONCLUSIONS

Varying angle of attack was proven to influence all mean quantities measured. The mean pressure coefficient saw an overall increase whenever the incidence was increased, with a slope of 0.03 $\bar{C}_p$ units per degree. This result was correlated with the increased mass flow towards the cavity's floor increasing the vertical component of freestream velocity. A particular effect was observed at an incidence of 4.5 degrees, where only the front part of the cavity experienced the mean pressure coefficient rise, while the rear assumed a value equal to the 3.0 degree case. Such a phenomenon was justified by the flow configuration change that the mean velocity vector field experienced inside the bay. A noteworthy feature was that the main clockwise vortex that occupied the greater part of the cavity and had an elliptical shape, rotated its major axis by 30 degrees clockwise when passing from the 3.0 degree to the 4.5 degree case, maintaining this geometry at 6.0 degrees. Such a change was the main reason behind the critical incidence identified in the 4.5 degree case. OASPL was influenced by this phenomenon. While it increased its value at all stations if the incidence was raised from 0.0 to 3.0 degrees (the gradient was around 0.3 dB per degree), as soon as the critical angle of attack was reached, the overall curve dropped to noise levels 3 dB below the reference case. Once passed the critical point, the previous trend was resumed, with the gradient now assuming an approximate value of 1.3 dB increase per degree of angle of attack increase.

Non-stationary flow analysis also revealed a strong dependence on angle of attack variations. Increasing incidence in fact augmented all tones power and PR indices except for M3 that faded, being assimilated into the broadband noise. Such a trend continued up to an incidence of 4.5 degrees where, while the overall tone configuration was maintained, all the modes saw a decrease in their power and persistence, especially M2, which was strongly influenced by having an antinode coinciding with the cavity's trailing edge. Beyond this critical angle of attack, a new configuration was established, with the restoration of M3 and the appearance of a fourth Rossiter-Heller like tone. Additionally, the PR index of M2 dropped to values comparable with the other modes. Power values of the modes present assumed values below the 3.0 degree case but above those of the 0.0 degree case.

Such behaviour was correlated to the structure of the vortex filaments colliding with the cavity rear face. Whenever these eddies were smeared, dispersed or had lower speeds, due to angle of attack variations, the noise seemed to be reduced.

Table 6.1 - Summary of the main modes for all tested angles of attack. *All data refers to the analysis of pressure signals recorded at station x/L 0.9, 2y/W 0.0, z/D 1.0. Doors angle 90 degrees. Cavity type AA.*

ANGLE OF ATTACK [deg[	MODE ID	St [FFT]	SPL [dB]	St [GWSP]	GWSP [dB]	PR %	OASPL [dB]
0.0	M1	0.2574	144.6	0.2601	154.1	3.87	162.1
	M2	0.6434	150.5	0.6404	159.9	28.33	
	M3	0.9866	136.2	1.0400	150.8	1.51	
	Mt	3.3240	138.4	3.4990	152.9	17.39	
3.0	M1	0.2359	148.2	0.2506	156.7	6.22	163.6
	M2	0.6220	153.0	0.6315	161.6	33.03	
	Mt	3.3030	140.8	3.4800	154.2	21.84	
4.5	M1	0.2574	144.4	0.2628	153.9	6.64	160.7
	M2	0.6220	146.8	0.6214	157.8	25.30	
	Mt	3.3240	136.1	3.3890	150.8	16.71	
6.0	M1	0.2574	146.5	0.2527	155.6	6.38	162.7
	M2	0.6220	147.9	0.6203	157.4	13.69	
	M3	0.9437	139.4	0.9227	152.4	2.15	
	M4	1.2650	137.7	1.2330	151.5	1.04	
	Mt	3.2820	140.5	3.3880	154.1	25.43	

7 STORE AND COLLAR EFFECTS

The standard approach to study cavity flows is usually based on the analysis of simple rectangular shapes, adding systematically geometry details to close the gap between the model and the final configuration installed on the airframe. A lot of activity has been involved in the analysis of store effects inside a cavity, and some examples of store influence can be found in the open literature (see for example Lawson & Barakos (2012), Chaplin & Birch (2012), Khanal (2010)). Therefore, it was decided to perform a similar study to explore store effects on the wind tunnel cavity model studied in Chapter 1. A single, simplified representation of a GBU39 JDAM bomb, with fins removed for ease of manufacturing, was mounted centrally inside the cavity (Figure 7.1). The shape of the store was chosen to maintain a relationship with the original design of the M219-type cavity, which was designed to accommodate such ordnance. The store was tested with all leading and trailing edge geometry types (AA, BB, and CC), and the two door opening angles, 90 and 120 degrees, already studied in Chapter 1.

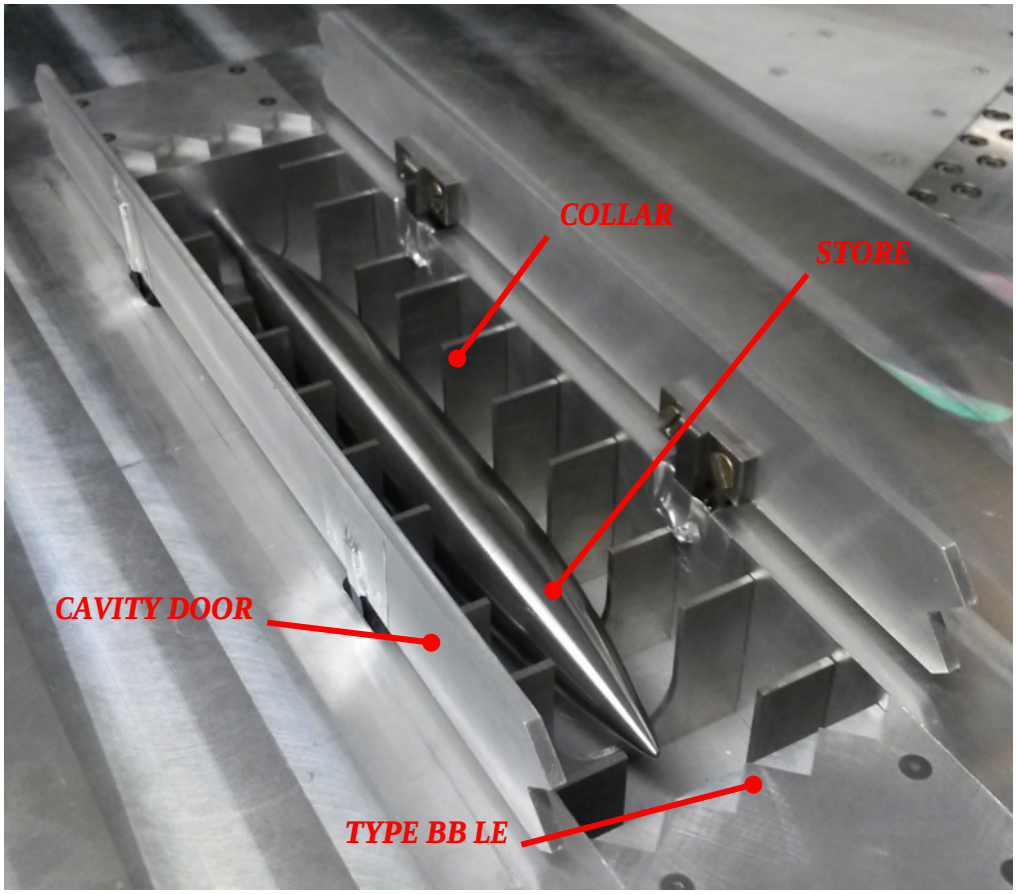

Figure 7.1 - Wind tunnel model of the cavity with store and collars installed. *In this image, the doors are shown in a 90 degree open position.*

Once the store effects campaign was completed, attention shifted towards the collars. Such a geometry feature was developed as a passive flow control technique. Its origin lies in previous work, where attempts to isolate the effects of a structural rib on cavity flow (Knowles, et al. (2015, 30-31 of March & 1 of April)), showed that such a structure, if properly sized and located, could have a beneficial effect on the levels of flow unsteadiness. Collars of height equal to the full depth of the cavity with a cut out to accommodate the store (Figure 7.1) were produced and placed at various positions to determine an optimum configuration. Since previous experiments demonstrated that the aero-acoustic properties of the cavity were superior with doors open at 90 degrees, the collars were tested in this configuration only.

7.1 STORE EFFECTS

The six cavity configurations studied in Chapter 1, (geometry AA, BB, and CC type with doors open at 90 and 120 degrees) underwent another analysis campaign to understand the flow changes when a store was installed inside the cavity.

7.1.1 MEAN FLOW ANALYSIS

A noteworthy result of this wind tunnel campaign was that, no matter which geometry the store was installed in, the outcome of the mean flow analysis was essentially the same. As shown in Figure 7.2, unlike the empty-cavity case the mean pressure coefficient, with the store installed, did not vary when the different combinations of leading and trailing edge geometries and door opening angles were tested. Such an outcome implied the existence of a sort of shielding mechanism induced by the store, which prevented geometry changes affecting the pressure footprint on the cavity's floor. The mean pressure coefficient curve shape was still concave-convex, with local minima, local maxima, and inflection points respectively located at x/L = 0.4, x/L = 0.6, and x/L = 0.8. In all configurations, coefficient values were always positive, ranging from 0.01 to 0.16. The only minor changes were observed when the cavity geometry passed from straight transverse edges (Type AA) to indented ones (Type BB and CC). In the latter cases, the absolute maximum $\bar{C}_p$ was 0.01 units higher than in the former case.

Similar results were obtained by analysing the OAFPL curves (see Figure 7.3). Again, the store introduced an apparent shielding/isolating effect, which lowered the OAFPL values and made them largely independent from the cavity geometry in which they were installed.

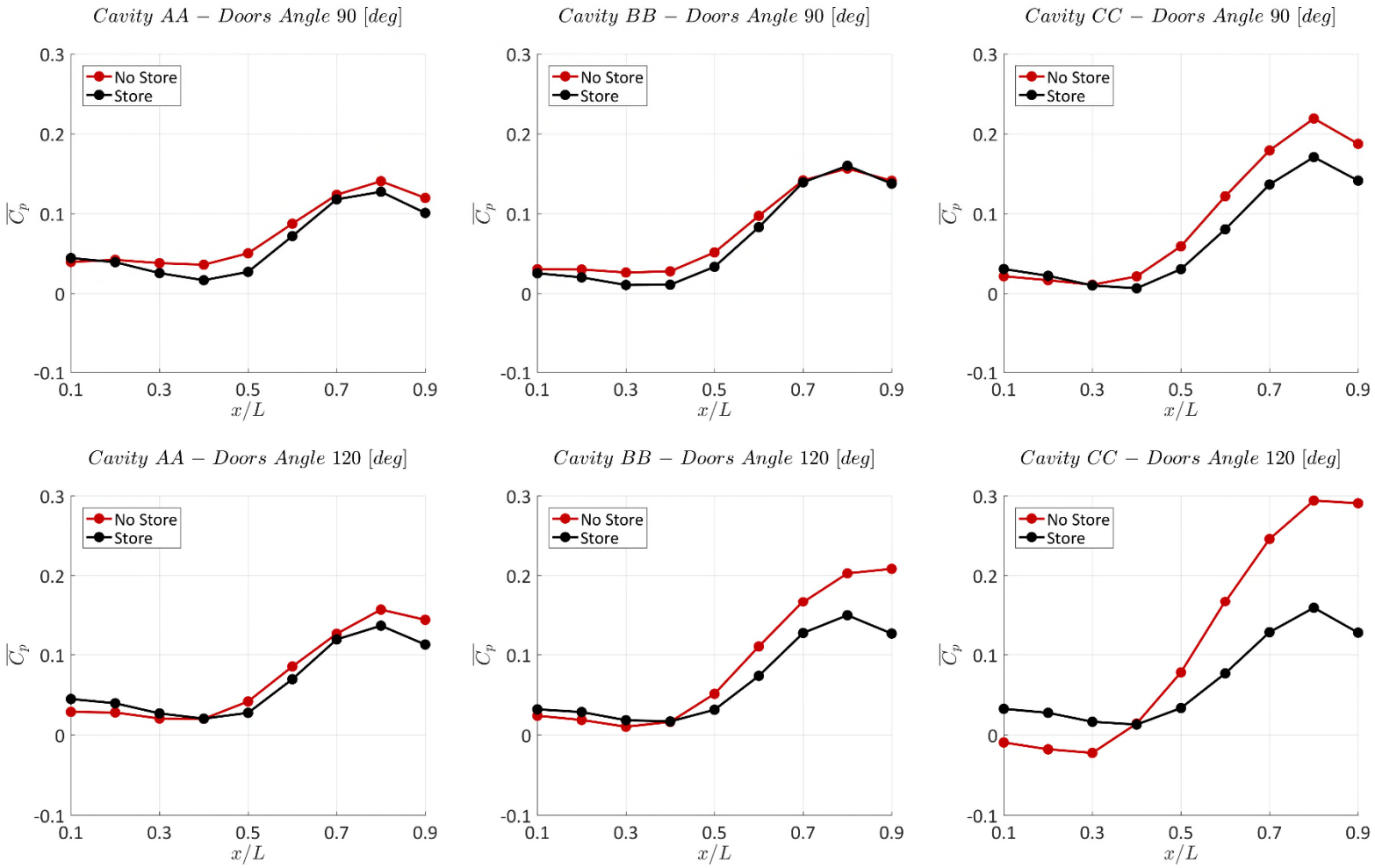

Figure 7.2 - Store effects on mean pressure coefficient. *Data refers to the central rake.*

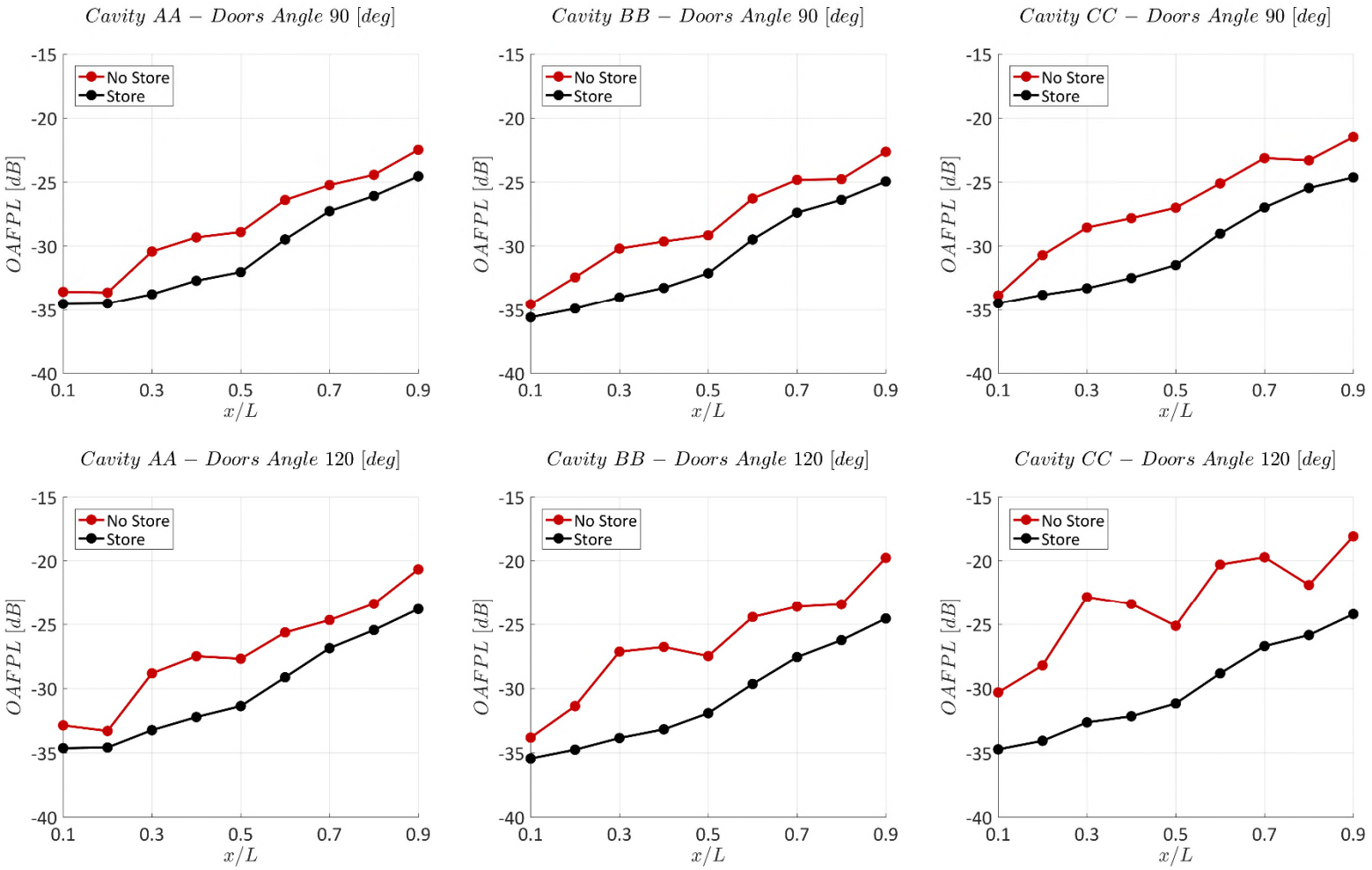

Figure 7.3 - Store effects on OAFPL. *Data refers to the central rake.*

The streamwise trend in OAFPL was significantly altered, becoming almost a linear increase in the OAFPL levels from the front to the rear of the cavity, with values ranging from -35 dB to -25 dB.

7.1.2 NON-STATIONARY FLOW ANALYSIS

The spectral analysis of the fluctuating part of the pressure signals indicated that the presence of the store had a beneficial effect on the aero-acoustic properties of the cavity (see Figure 7.4). In the reference configuration (Type AA - doors at 90 degrees opening), the main tones, M2 and M3, experienced a power decrease of 5 dB, while Mt dropped by 7 dB. Broadband noise was slightly reduced as well, but much less, of the order of 1 dB. A different trend was instead detected for M1. This mode gained 3 dB with respect to the non-store case.

Door-opening angle had no effect on the AA-type geometry, but influenced the derived geometries. Additionally, in contrast to the mean quantities, changing the leading and trailing edge geometry continued to influence the shape of the frequency spectrum of the pressure signal. The trend was similar, for all configurations, with all modes and broadband noise reduced in power, while M1 became the dominant tone. The introduction of the store was particularly effective in reducing the FPL magnitude in the BB- and CC-type cavities with the doors open at 120 degrees. Nevertheless, the performance achieved was not superior to their corresponding 90 degree door open equivalent. The suppression effect of the store was in line with the outcome of the OAFPL analysis and, in fact, its presence acted as an obstacle to the resonating mechanism, influencing all tones and the broadband noise as well.

Analysis of the longitudinal shape of M1 (i.e. the mode power at different longitudinal stations) indicated that the introduction of the store influenced its behaviour, which deviated from the theoretical rule of Tracy & Plentovich (1997). As shown in Figure 7.5, the characteristic “V” shape was replaced by a concave-convex structure with a minimum point located at x/L = 0.3, an inflection point located at x/L = 0.6, and a maximum point located at x/L = 0.9. For all geometries, independence was maintained from the door-opening angle. Cavity configuration (type AA, BB, and CC) altered the general distribution of this tone, although the result affected the quantitative values rather than the overall shape.

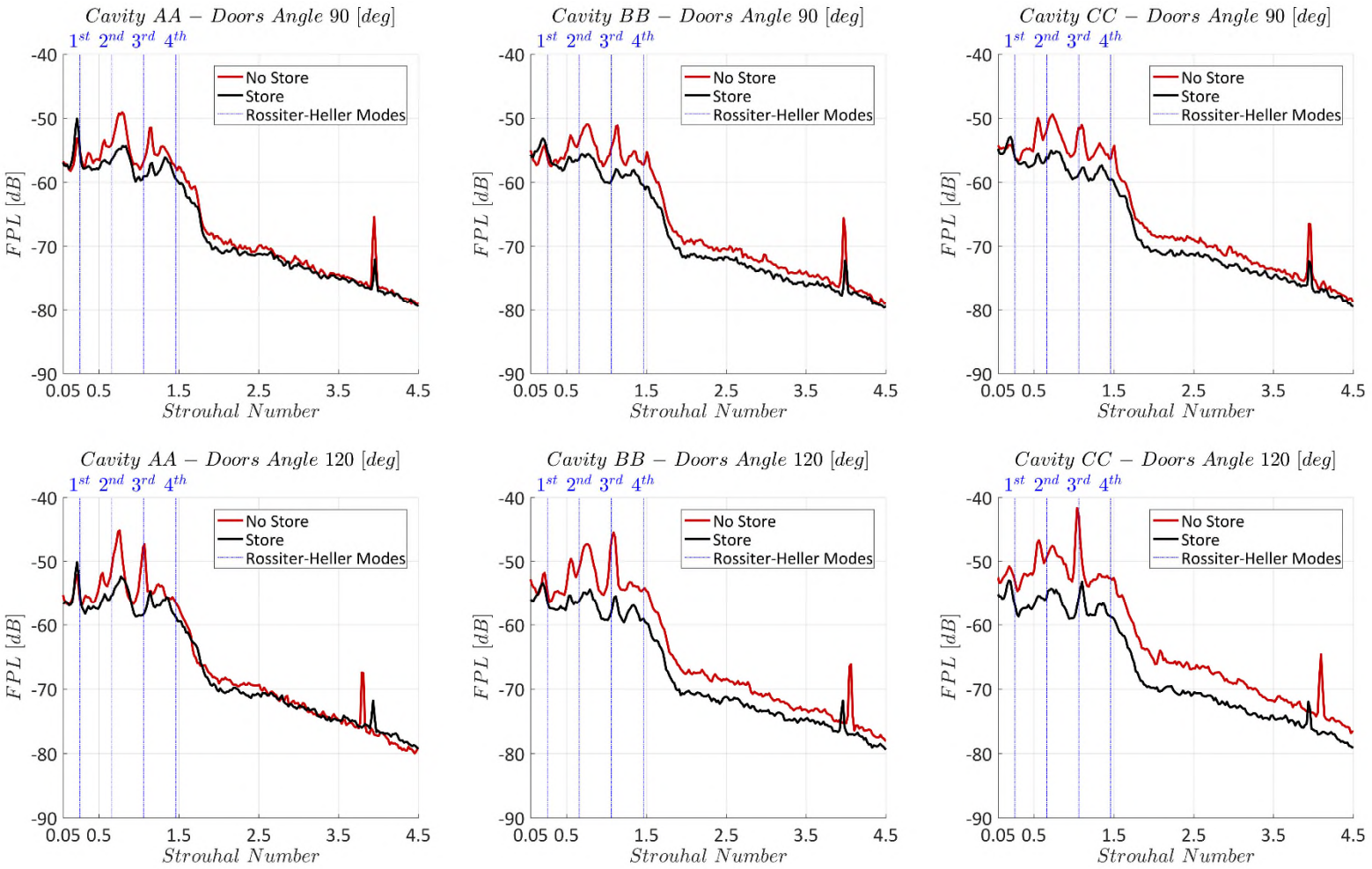

Figure 7.4 - Store effects on FPL. *Data refers to the pressure probe located at x/L = 0.9, 2y/W = 0.0, z/D = 1.0*

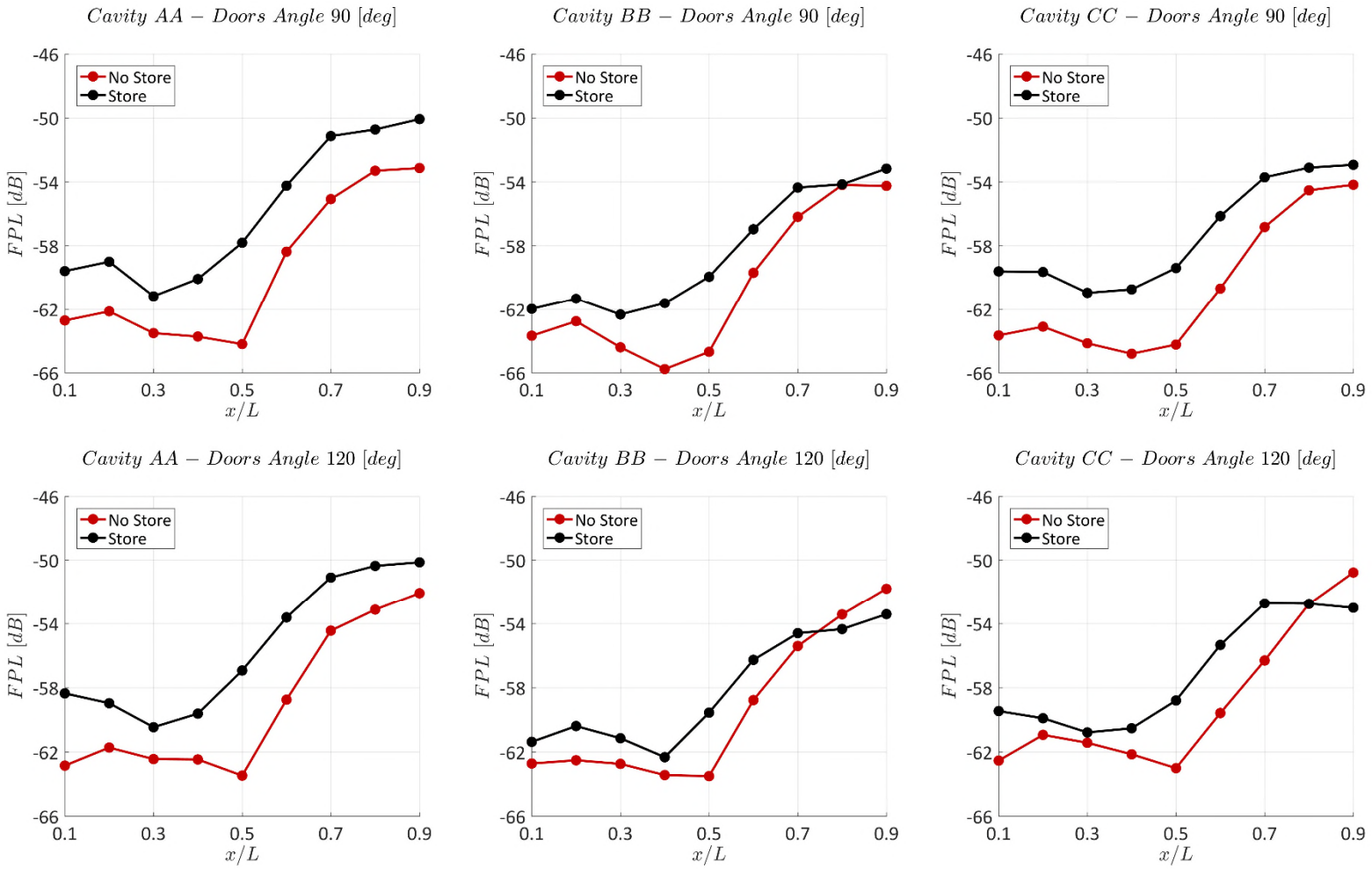

Figure 7.5 - M1 longitudinal trend. *Data refers to the cavity centreline.*

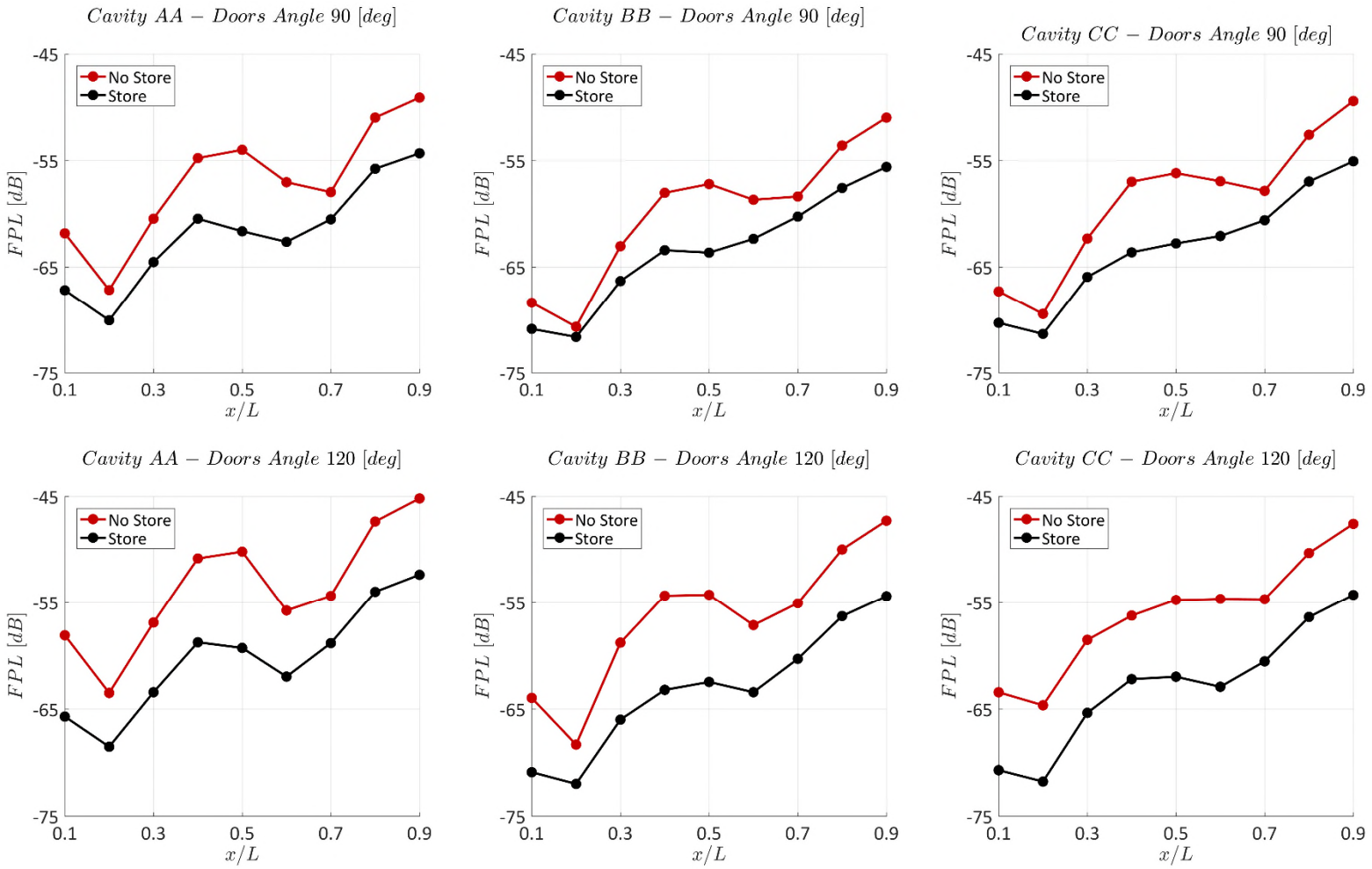

Figure 7.6 - M2 longitudinal trend. *Data refers to the cavity centreline.*

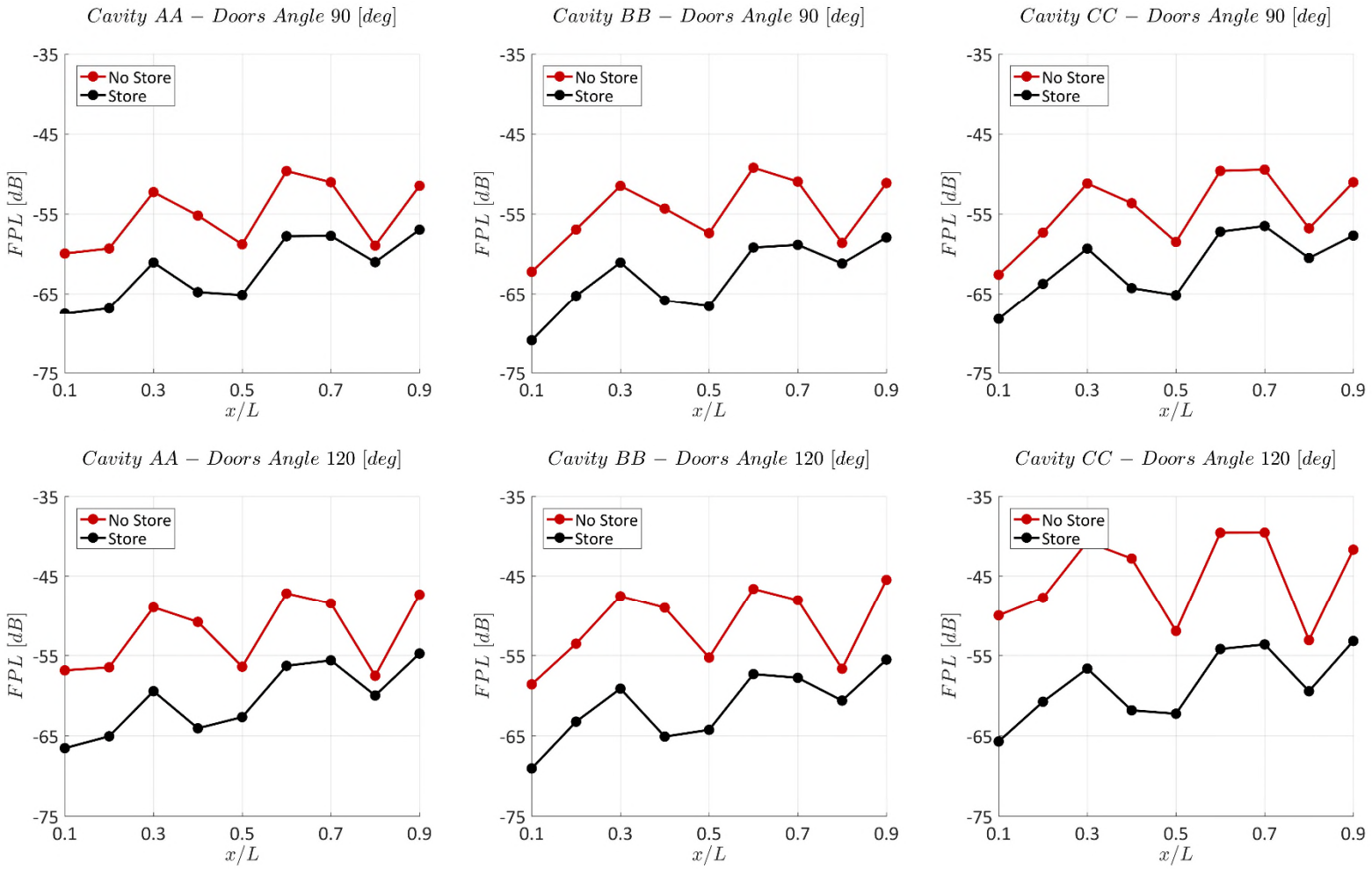

Figure 7.7 - M3 longitudinal trend. *Data refers to the cavity centreline.*

M2 had a different response, according to the geometry considered (see Figure 7.6). For the reference configuration (type AA), the double "V" shape was maintained and the only observed effect of the introduction of the store was a reduction in the FPL at all stations considered, regardless of the door opening angle. The reduction in decibels varied from station to station in a non-regular trend. With geometry BB, the store altered the shape of the curve. With doors opened at 90 degrees the curve, beyond the minimum at station x/L = 0.2, became an almost straight line up to x/L = 0.4, and then assumed a constant-positive-value gradient for the rest of the cavity length. For the 120 degree door-opening angle, the double "V" shape was maintained, although the peak and dips were less pronounced than the no-store case. The CC-type cavity showed a similar behaviour, indicating that, from the perspective of M2, the major influence of the mode power level attained, at different cavity stations, was influenced by the arrangement of the vorticity ejected in the shear layer at the bay's leading edge.

Finally, M3 had a similar response for all configurations considered (see Figure 7.7). Independently from the door opening angle, the double "V" shape was maintained and the sole store influence was a change in the reduction of power levels from 5 dB (AA and BB geometries) to 10 dB (CC Geometry), except for the particular case at station x/L = 0.8, in which the mode FPL values underwent a reduction from 1 dB (AA geometry) to 3 dB (BB and CC geometries).

The main change observed from the time-frequency domain analysis was the high variation of the persistence index of M1. Taking cavity type AA as an example with the doors at 90 degrees, M1's PR increased from 48.06% with no store to 76.61% with the store. By comparison, on the same geometry, M2 and M3 slightly reduced their values, from 96.66% to 94.32%, and from 98.33% to 92.03% respectively.

Since from the STFT it was not possible to discern any appreciable variation introduced in the time frequency map by the presence of the store, it was decided to switch to wavelet analysis, to check for any characteristic change in the mode footprint. Introducing the equivalent of WAVT for the STFT, i.e. the average variance trend (AVT), defined in Equation (7-1), it was possible to determine, for the non-store case and the store case (still considering the Type-AA cavity with doors-opening angle of 90 degrees), the instant in which signals assumed the maximum absolute power value.

$$AVT(n) = 10 \cdot \log_{10}\left(\frac{1}{K \cdot \sigma^2} \cdot \sum_{k=0}^{K} \widehat{SX}(k,n) \cdot \widehat{SX}^*(k,n)\right) \quad \textbf{(7-1)}$$

The result obtained (see Figure 7.8) identified the respective instants corresponding to time equal to 1 second for the non-store case and time equal to 3 seconds for the store case. Time intervals of duration equal to 0.2 seconds, and centred at these values, were then extracted and processed with the wavelet transform.

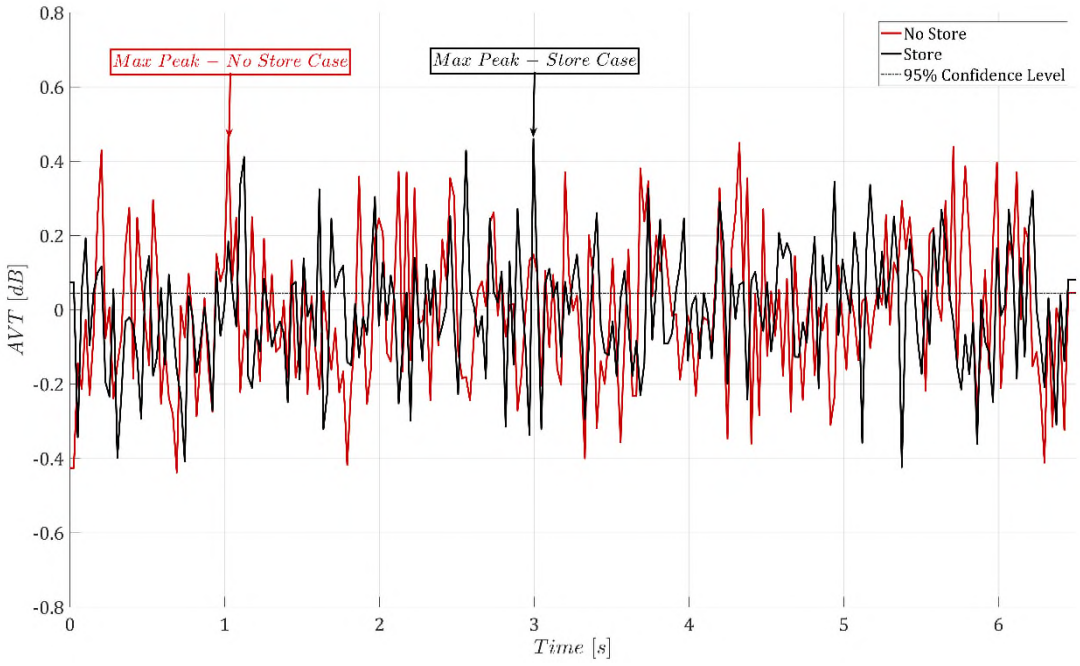

Figure 7.8 - Store effects on AVT of pressure signal at x/L = 0.9, $2y/W$ = 0.0, z/D = 1.0.

Data refers to configuration AA, doors open 90 degrees.

Comparing the outcomes (Figure 7.9), the main difference was identified by the appearance, in the store-case time-frequency map, of peaks classifiable as true features in the Strouhal band containing M1. Such a result was in accordance with the increased PR index of M1 calculated in the STFT analysis, whose increase gave the on/off cycle of this mode a shorter period. The characteristics of the other main modes, M2, M3, M4 and Mt remained nearly identical in both cases. Of significance was the fact that wavelet analysis made it possible to identify, with higher precision, the time of maximum AVT activity in both signals. This corresponded to 1.02 s for the no-store case, and 3.01 s for the store case. In both configurations, such instants were characterised by the co-existence of all the modes, while for the greater part of the signal a mode-switching behaviour was more common.

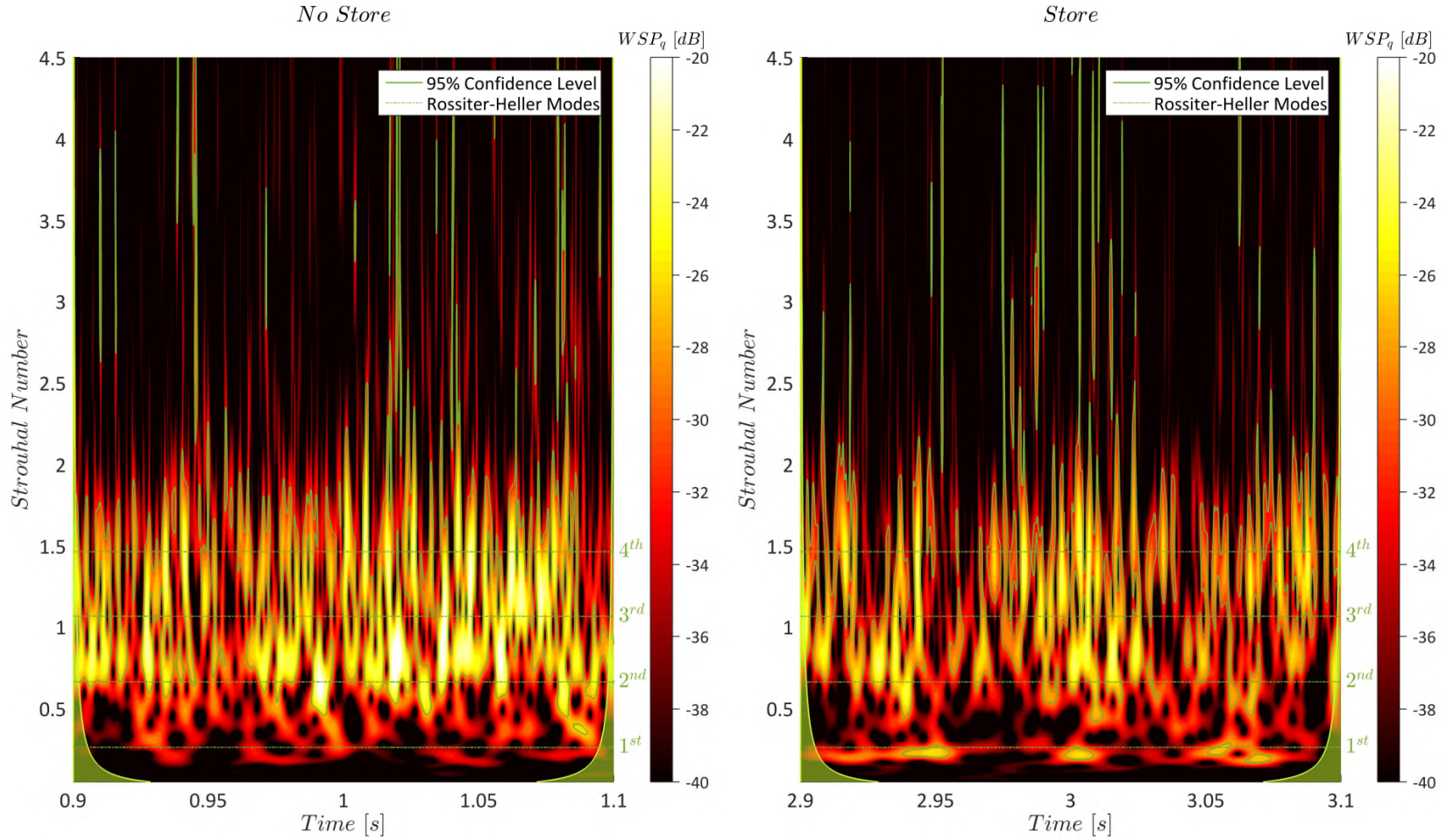

Figure 7.9 - Store effects on wavelet analysis of the pressure signal at x/L = 0.9, $2y/W$ = 0.0, z/D = 1.0. *Data refers to configuration AA, doors open 90 degrees. The time intervals are centred at the instant of absolute maximum of the signals' AVT.*

7.2 COLLAR EFFECTS

The analysis of the collars was divided into two phases. The first was dedicated to the determination of the best arrangement between the four versions proposed (see Paragraph 3.1.5). In this case, all configurations were tested with the type AA cavity geometry, with the doors opened at 90 degrees. Once the optimum configuration was determined, the second phase was launched. Here the most promising arrangement was tested with the other cavity geometries to check for any performance variations. In all cases, each arrangement was tested with and without the store placed inside the cavity, while only the 90 degree door opening angle was examined.

7.2.1 OPTIMUM CONFIGURATION DETERMINATION

The determination of the optimum configuration aimed to select the collar arrangement with the best performance in terms of the aero-acoustic properties of the cavity. This procedure had as its target the ideally desired characteristics of a cavity. The longitudinal mean pressure coefficient should assume a curve as flat as possible especially with the store installed, otherwise there is a penalty due to an induced pitching moment on the payload. Complementary to this was a reduction in the OAFPL and FPL values, with special attention in the latter case to the suppression, if possible of the resonant mode.

MEAN FLOW ANALYSIS

In the analysis of the mean pressure coefficient, attention was focussed on the store case. Within all the configurations tested, Version-0 (collars at 5%, 15%, 25%, 35%, 45%, 55%, 65%, 75%, 85%, and 95% of cavity length) had the best performance (see Figure 7.10). Despite the abrupt pressure rise from x/L = 0.2 to x/L = 0.3, this version assumed a nearly flat trend for the rest of the cavity. Version-1 (collars at 15%, 35%, 55%, 75%, and 95% of cavity length) had a similar performance, although in this case the rise was located between x/L = 0.3 and x/L = 0.4. Version-2 (collars at 5%, 25%, 45%, 65%, and 85% of cavity length) and Version-3 (collars at 5%, 15%, 45%, 55%, 85%, and 95% of cavity length) were inferior since they failed to attain the required pressure distribution. When the store was removed, in every version tested, the collars performed worse than the empty-cavity case. Nevertheless, this aspect was considered secondary to the requirement on the mean pressure coefficient, as an acceptable payoff for the better performance with the store installed.

The store-installed results correlated with the maximum spacing between the collars. V0, which was the best configuration, had a maximum distance between collars equal to 10% of the cavity length. In the other versions, performance degraded according to the increase in collar spacing (the maximum distance between collars was 20% of cavity length for V1 and V2, and 30% of cavity length for V3). V3 particularly, had a behaviour similar to the empty cavity, indicating that the collars largely failed to prevent the internal formation of the vortex system causing the typical concave-convex shape of the mean pressure coefficient. It was also noted that the pressure rise on the cavity floor occurred just before the position of the collar where the store reached its maximum diameter. This gave the additional indication that the gap between the store and the collar should be kept to a minimum for the configuration to work.

The sharp rises observed in the mean pressure coefficient plots were induced by the impact of the shear layer on the collar. In fact the introduction of these transverse obstacles had the effect of slitting the cavity in smaller sub-cavity, with each one having a longitudinal pressure trend similar to the empty cavity case. This was particular true for the first sub-cavity in which the collars divide the main bay, which usually experienced the highest pressure rise. Moving downward, the effect was less pronounced, since the shear layer coming had less energy due to the previous impact. This also explained the reason for V0 having the best performances. The splitting of the volume in many smaller sub-elements avoided the formation of sharp pressure rises and continuously disrupted the coherence of the shear layer.

The OAFPL curves (Figure 6.11) also indicated that V0 was the best configuration, with the store installed inside the cavity. Such an arrangement, with respect to the no-collars case, showed reductions of 5 dB in the front of the bay and 8 dB in the rear. In the middle of the cavity the reduction was as low as 1 dB, at station x/L = 0.3, and then began to increase again. A similar trend was observed for configuration V3 even if, excluding the first 30% of the cavity, its performance was generally between 1 to 2 dB inferior to V0. V1 continued to offer an improved situation with respect to the no-collars case, especially in the rear part of the cavity. Nevertheless, it performance up to x/L = 0.3 was inferior. V2 showed an abrupt rise in power level in the front half of the cavity. It did improve the overall situation with respect to the no-collars case, but only from x/L = 0.6 onwards. Its maximum OAFPL reduction was around 3 dB.

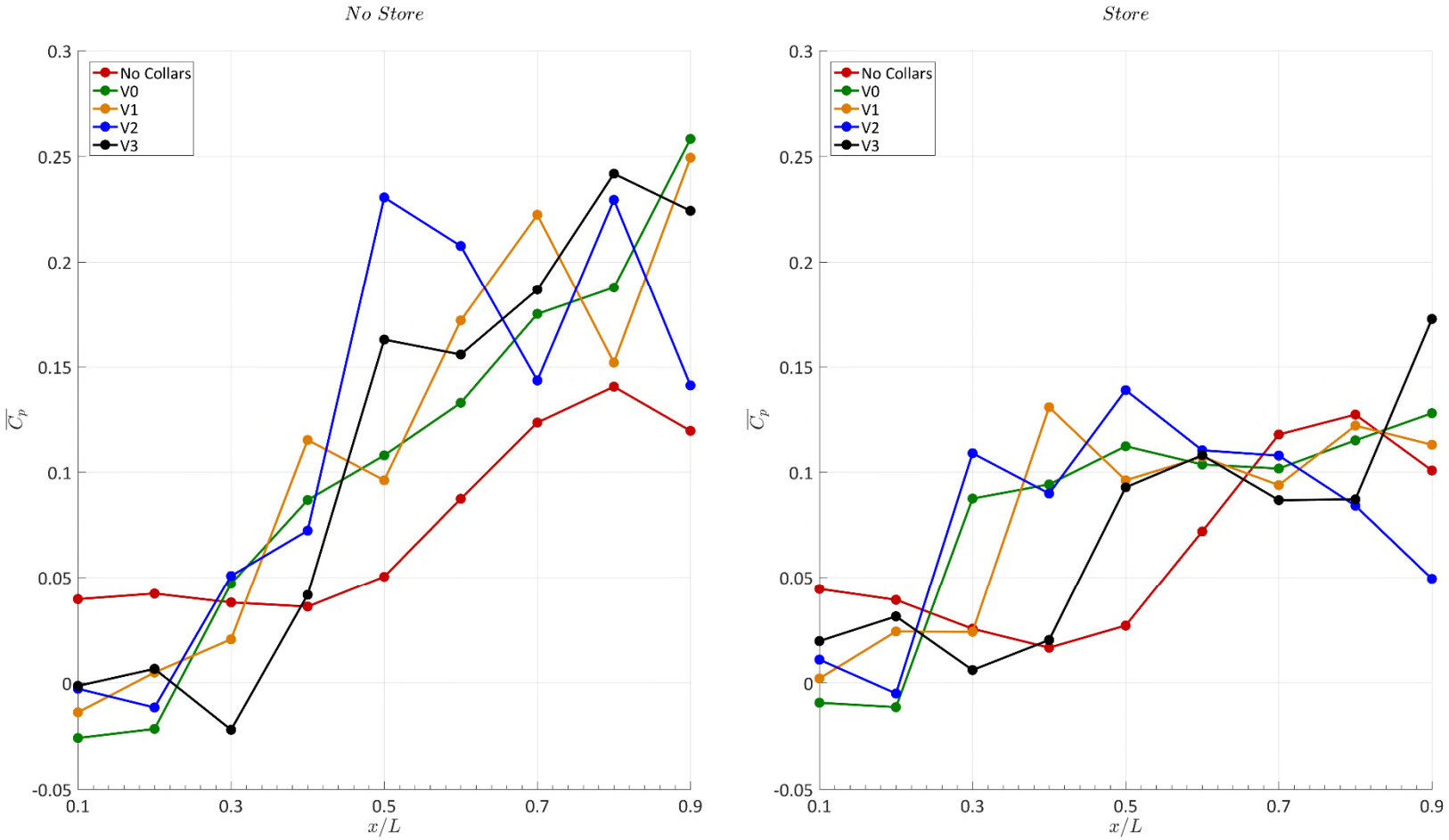

Figure 7.10 - Collar effect on the mean pressure coefficient. *Data refers to the central rake. Cavity Type AA. Doors open 90 degrees.*

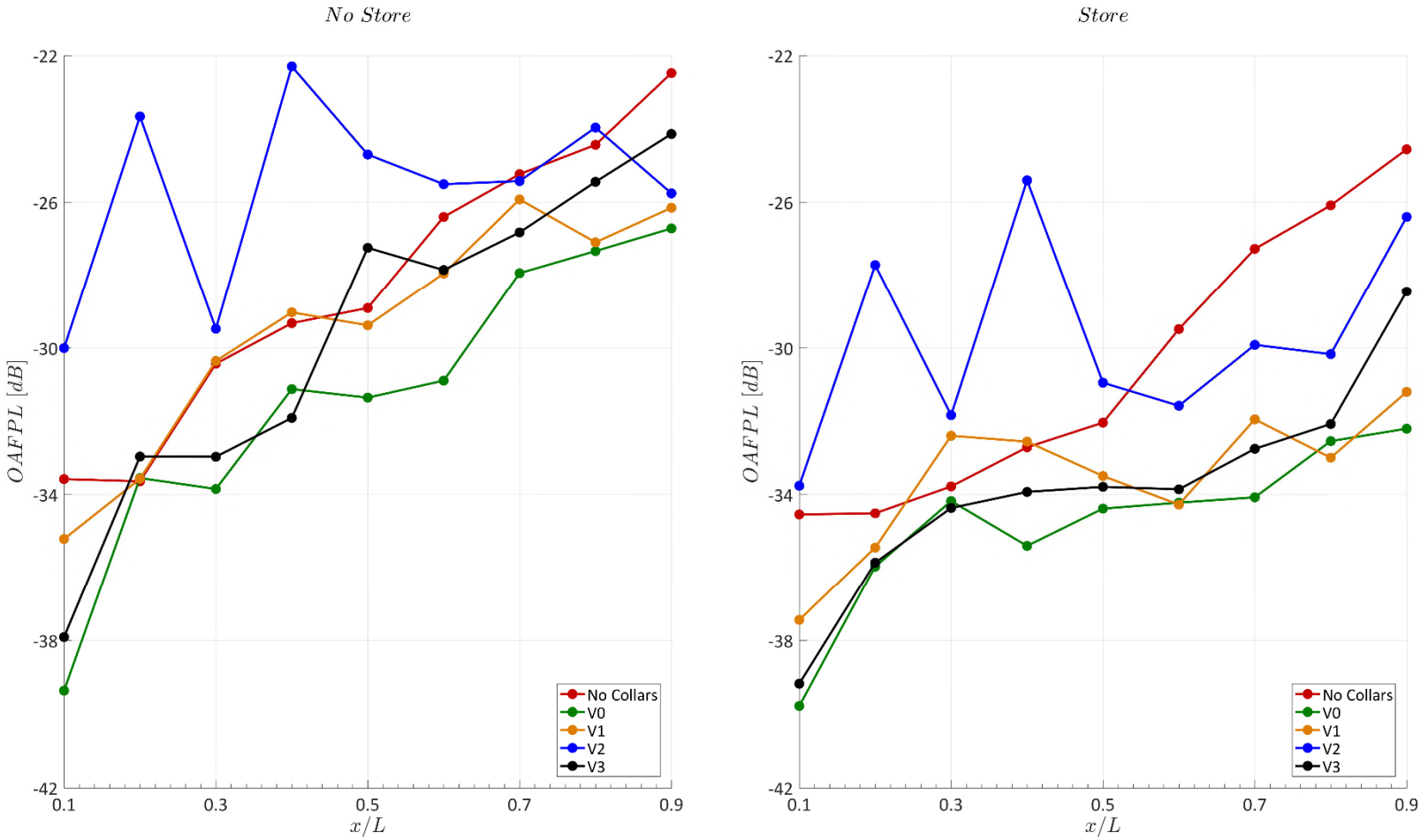

Figure 7.11 - Collar effect on the OAFPL. *Data refers to the central rake. Cavity Type AA. Doors open 90 degrees.*

When the store was removed the level of OAFPL reduction decreased. V0 continued to be the best solution, and offered an overall decrease in power levels of around 2 dB. V3 and V1 maintained good performance, while V2 again performed the worst.

NON-STATIONARY FLOW ANALYSIS

FPL plots at three longitudinal positions were produced to analyse the collar performance in the whole cavity. At the front wall, (x/L = 0.1, Figure 7.12) when the store was not installed, very good performance was achieved with Version-0. With respect to the reference case, M1 and M2 disappeared, leaving space for a tone centred at St = 0.5, but with a power 10 dB lower than the no-collar case at the same Strouhal number. M3 dropped by 18 dB while M4 experienced a reduction of 7 dB. Mt as well was reduced, in this case by 5 dB. V0 was also capable of reducing broadband noise up to a Strouhal number of 2.5.

Other collar configurations also showed good performance, but in these cases the reduction in power was less compared to V0. In particular, V1 and V2 experienced high peaks of power at St of 2.319 and 1.57 respectively. In the latter case especially, the increase of power was very large and reached a value of -49.04 dB, approximately 11 dB higher than the FPL value of the dominant mode in the reference configuration (M3). These tones corresponded, in the case of V1, to approximately the first Rossiter-Heller mode of the sub-cavity created by the bay's front wall and the first downstream collar and, in the case of V2, the first and second collars moving downstream from the cavity's leading edge. Curiously, neither V0 nor V3 had similar peaks, possibly indicating a sub-cavity with length equal to 10% of the overall cavity length had an L/D too small to develop Rossiter-Heller-like tones.

If the store was added, all spectra experienced a beneficial reduction of the power recorded. The collar characteristics were similar to the no-store case, with V0 still offering the best performance in terms of tone suppression and broadband noise reduction.

The situation at station x/L = 0.5, for the no-store case, was slightly different (see Figure 7.13). V0 was again the best configuration suppressing M1, M2 and M3; nevertheless, it introduced the adverse effect of increasing the power of M4 by 7 dB and the overall broadband noise, at Strouhal numbers above 1.8, by 5 dB, although it reduced the power of Mt by 5 dB. The other collar versions offered a picture similar to the one obtained at x/L = 0.1, with V2 again exacerbating the power of M4.

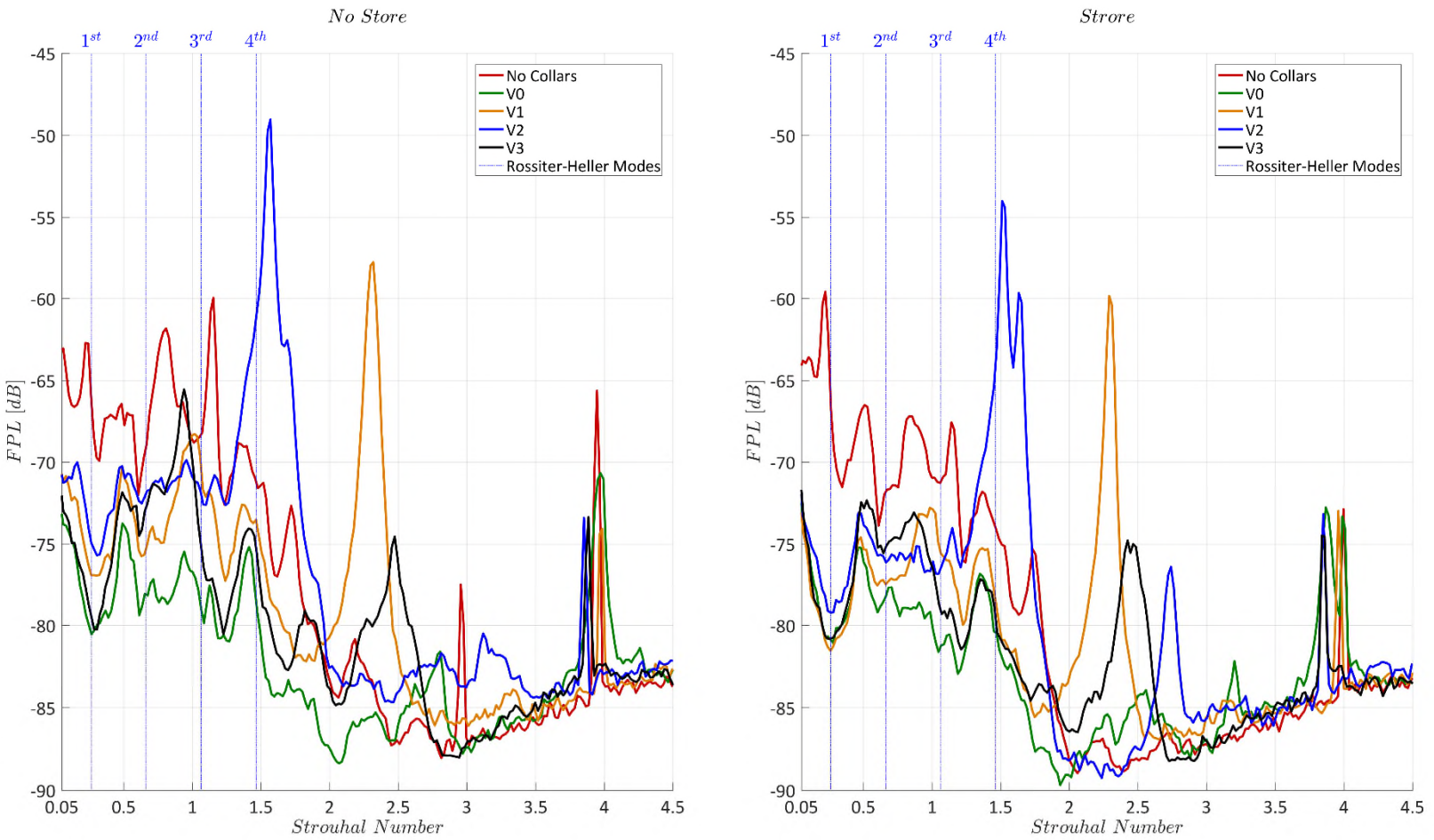

Figure 7.12 - Collar effects on FPL. *Data refers to the pressure probe located at x/L = 0.1, 2y/W = 0.0, z/D = 1.0. Cavity Type AA. Doors open 90 degrees.*

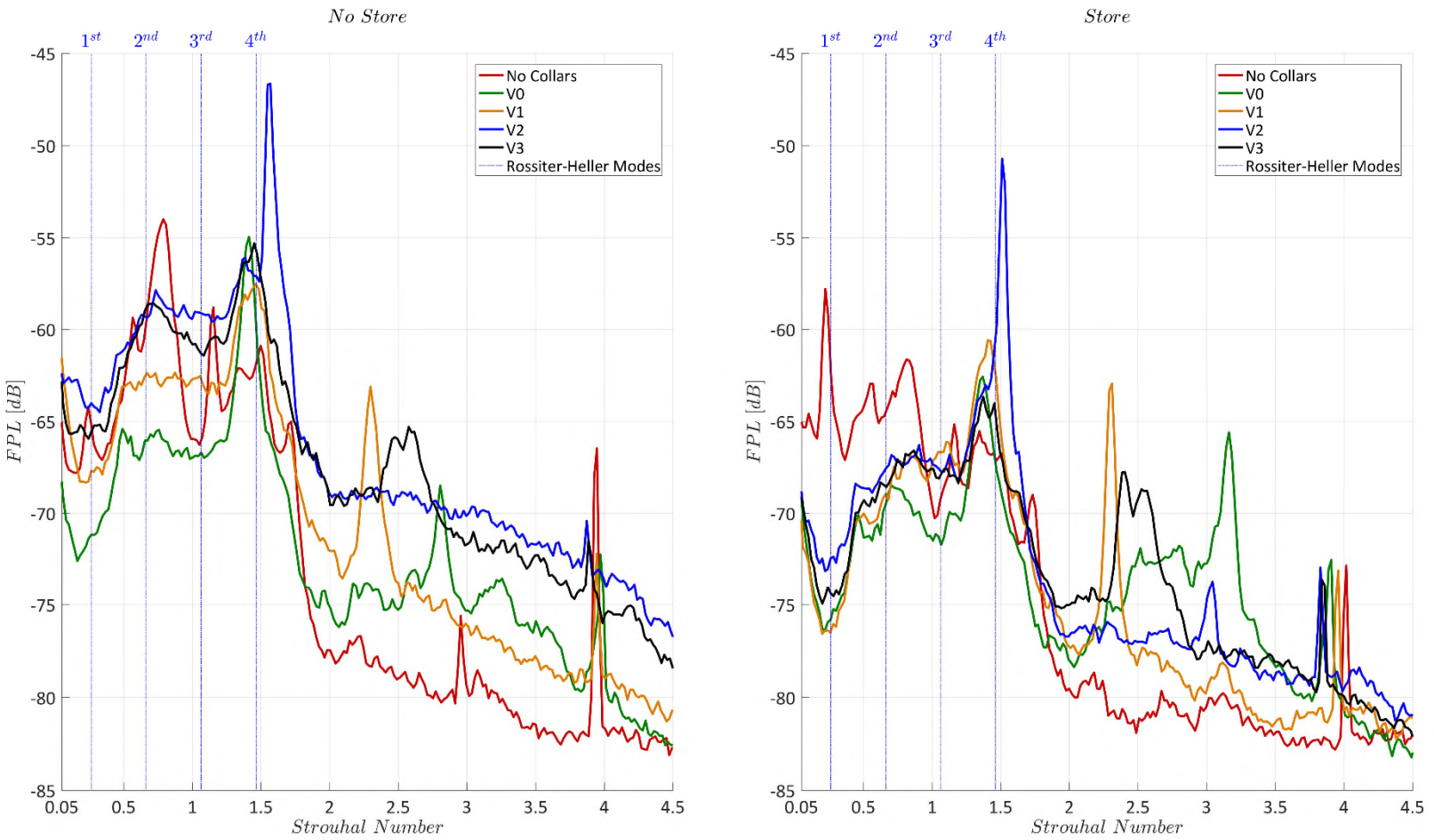

Figure 7.13 - Collar effects on FPL. *Data refers to the pressure probe located at x/L = 0.5, 2y/W = 0.0, z/D = 1.0. Cavity Type AA. Doors open 90 degrees.*

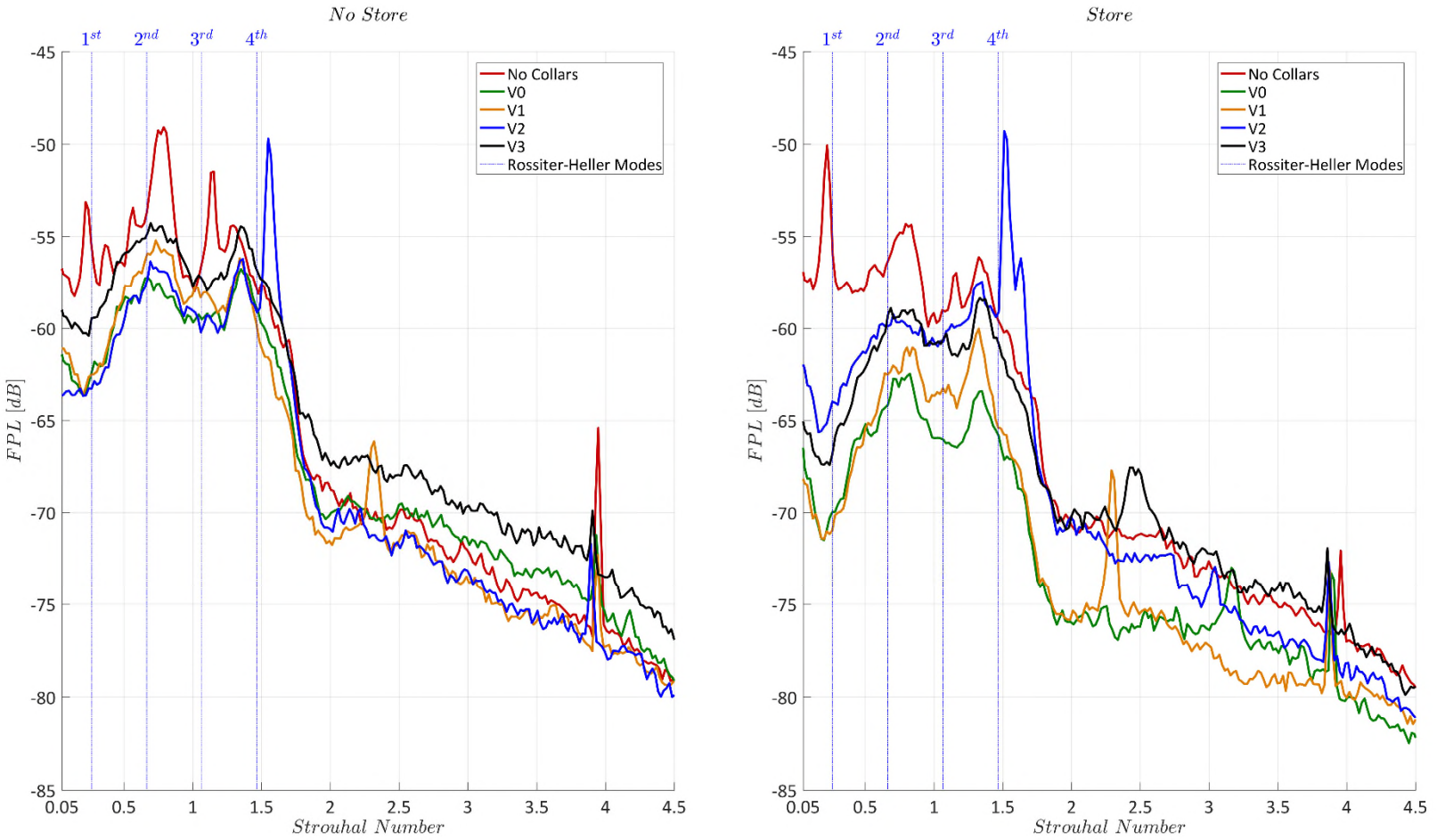

Figure 7.14 - Collar effects on FPL. *Data refers to the pressure probe located at x/L = 0.9, 2y/W = 0.0, z/D = 1.0. Cavity Type AA. Doors open 90 degrees*

With the introduction of the store, it was observed that the curve of the spectrum of V0, above St = 1.8, was increased instead of being reduced, as was the case of V1, V2, V3 and the reference configuration. However, the reason of this behaviour was not determined.

The situation at the rear wall (x/L = 0.9, Figure 7.14) indicated that V0 had the best performance when the store was installed inside the cavity. V1 also offered good noise suppression capabilities, while V2 and V3 could not be considered as good. Again, removing the store increased the power level at all stations. Finally, all collar versions, at this longitudinal location, were capable of suppressing completely M1 and M3. The tests indicated that Version-0 was superior to all other collar arrangements. Even if in very specific parts of the cavity this was not true, from a global point of view the performance of V0 in the mean flow and the non-stationary flow characteristics made it eligible as the best collar version between all those tested, and, encouraged the adoption of this configuration as a tool to improve the aero-acoustics of the basic cavity.

7.2.2 OPTIMUM CONFIGURATION ANALYSIS

The decision to analyse the optimum configuration when installed in cavity BB and CC type was driven by the necessity to identify any possible interaction capable of influencing the collar suppression capability.

MEAN FLOW ANALYSIS

Analysing the longitudinal trend of the mean pressure coefficient (Figure 7.15) some differences were noticed when comparing the effects of the installation of the collars Version-0 into the various cavity geometries. When the store was installed, the type-BB cavity displayed the same $\bar{C}_p$ trend as type AA, with a sharp pressure rise between x/L = 0.2 and x/L = 0.3, followed by an almost flat trend for the rest of the bay. Nevertheless, in the former case, the coefficient was always positive and maintained in the interval between 0.008 and 0.096, while in the latter case these boundaries expanded to -0.011 and 0.128. Similar results were obtained with the cavity CC.

When the store was removed, the straight-line trend observed in cavity AA was maintained for both the BB and CC geometries, however, the difference between the maximum and minimum $\bar{C}_p$ values was reduced. In the case of cavity BB the range was -0.026 to 0.258, and for CC -0.09 to 0.225. The conclusion was that, from the mean coefficient perspective, indentation of leading and trailing edges improved the performance of the collars.

Similar findings were obtained analysing the OAFPL curves (Figure 7.16). The introduction of the saw-tooth geometries BB and CC, offered a slightly better performance, usually not above 2 dB, and only observed in the store-present cases. When the store was removed from the cavity, no differences with respect to the reference geometry were recorded.

NON-STATIONARY FLOW ANALYSIS

When collar Version-0 was installed in the type-BB and type-CC cavities, an influence on the pressure spectra was observed.

At station x/L = 0.1 (Figure 7.17), with the store not installed, both BB and CC configurations experienced an increase in the power of Mt, with an increase of 7 dB for the former and 11 dB for the latter. Due to this common result, it is proposed that the mode linked to the status of the vorticity injected into the shear layer, which for Type-BB and Type-CC cavities had a similar arrangement due to the common saw-tooth profile present at the leading edge.

With Version-0 introduced into the Type-BB cavity a reduction of the power of M2 by 2 dB, a complete suppression of M3, and an increase of M4's FPL by 2 dB was also observed. Introducing the store reduced by 1 dB all power content up to St = 1.8 but in both the BB and CC geometries the power of Mt was increased.

A different situation was instead observed at x/L = 0.5 (Figure 7.18). In this case, geometry BB always offered better performance than the reference configuration, especially in reducing the broadband noise in the Strouhal number interval between 1.8 and 3.8. Type-CC also improved the situation with respect to Type-AA, even if its performance was not as good as Type-BB.

At station x/L = 0.9, (Figure 7.19) the introduction of the derived geometries offered a marginal improvement in the spectral response of the cavity, reducing the power content by between 1 dB and 2 dB. No appreciable variations were observed between the three cavity geometries when the store was not installed.

Spectral analysis confirmed the capability of the collars to improve the aero-acoustic properties of the cavity even with Type-BB and Type-CC geometries at the expense of an increase of the response of Mt in the whole cavity length. Improved performance was confirmed with the store both installed and absent from the bay. This outcome cleared the

adoption of this innovative adverse-phenomena-suppression technique in more complex geometries with respect to a simple rectangular cavity.

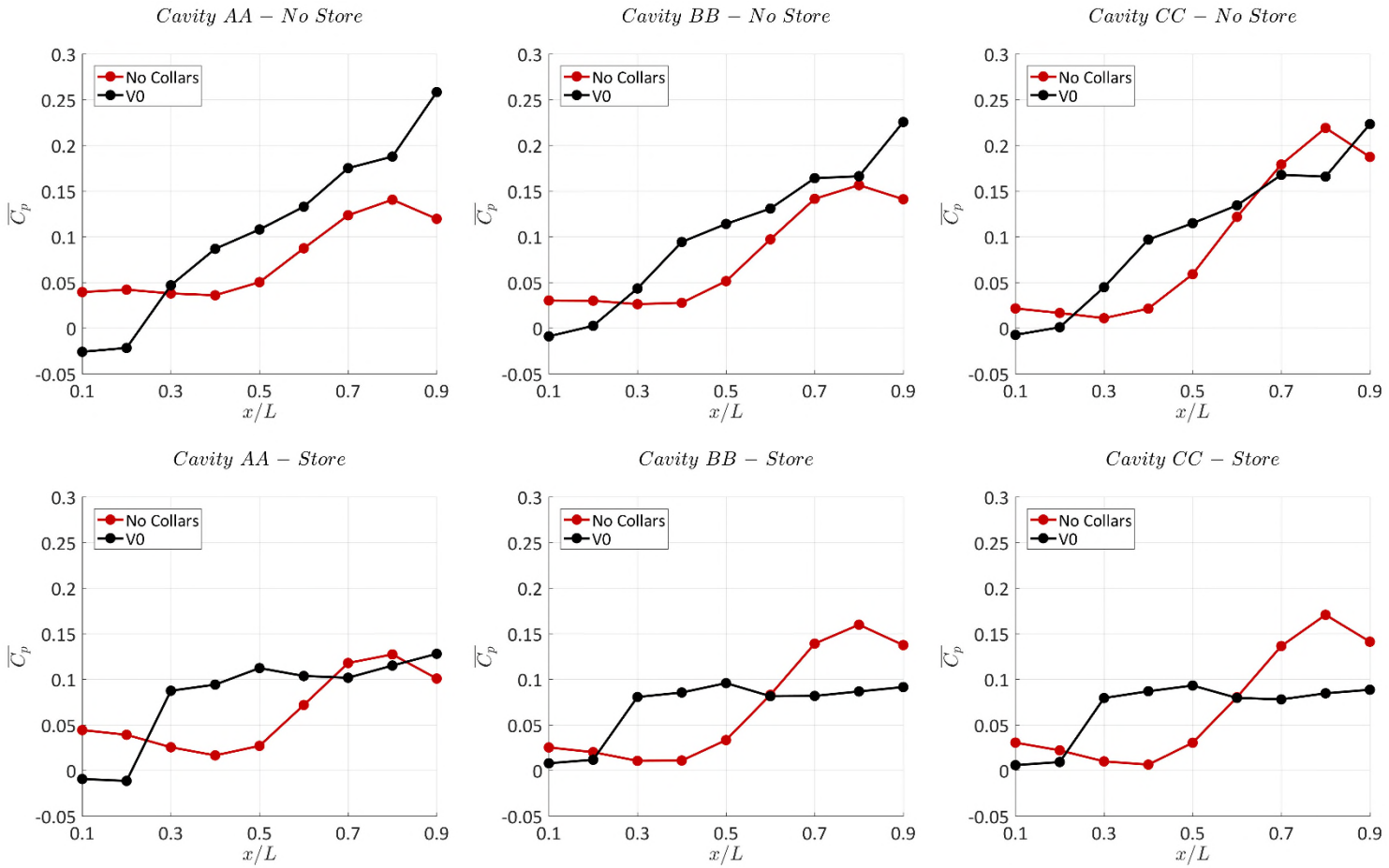

Figure 7.15 - Collar Version-0 effects on mean pressure coefficient of all cavity types. *Data refers to the central rake. Doors open 90 degrees.*

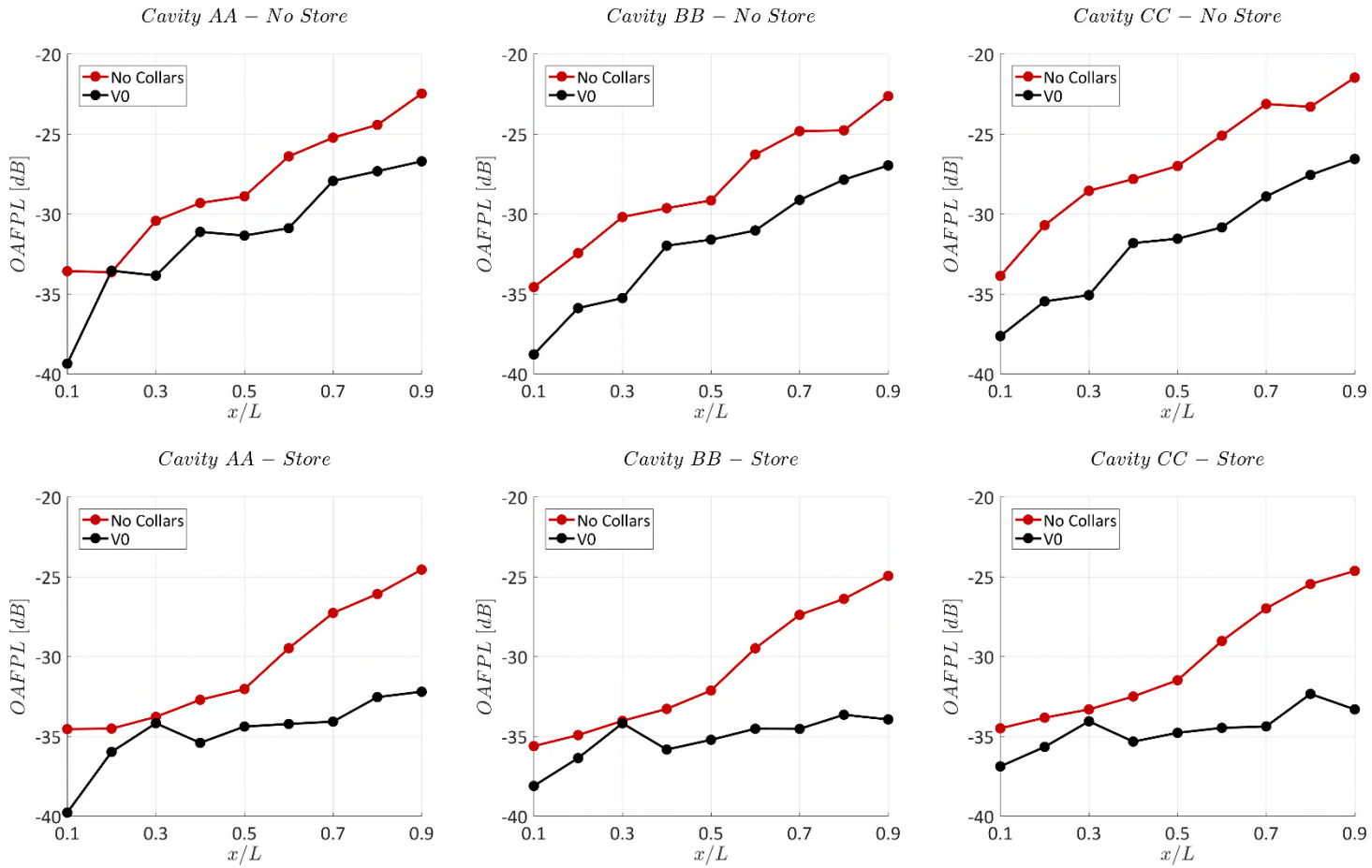

Figure 7.16 - Collar Version-0 effects on OAFPL of all cavity types. *Data refers to the central rake. Doors open 90 degrees.*

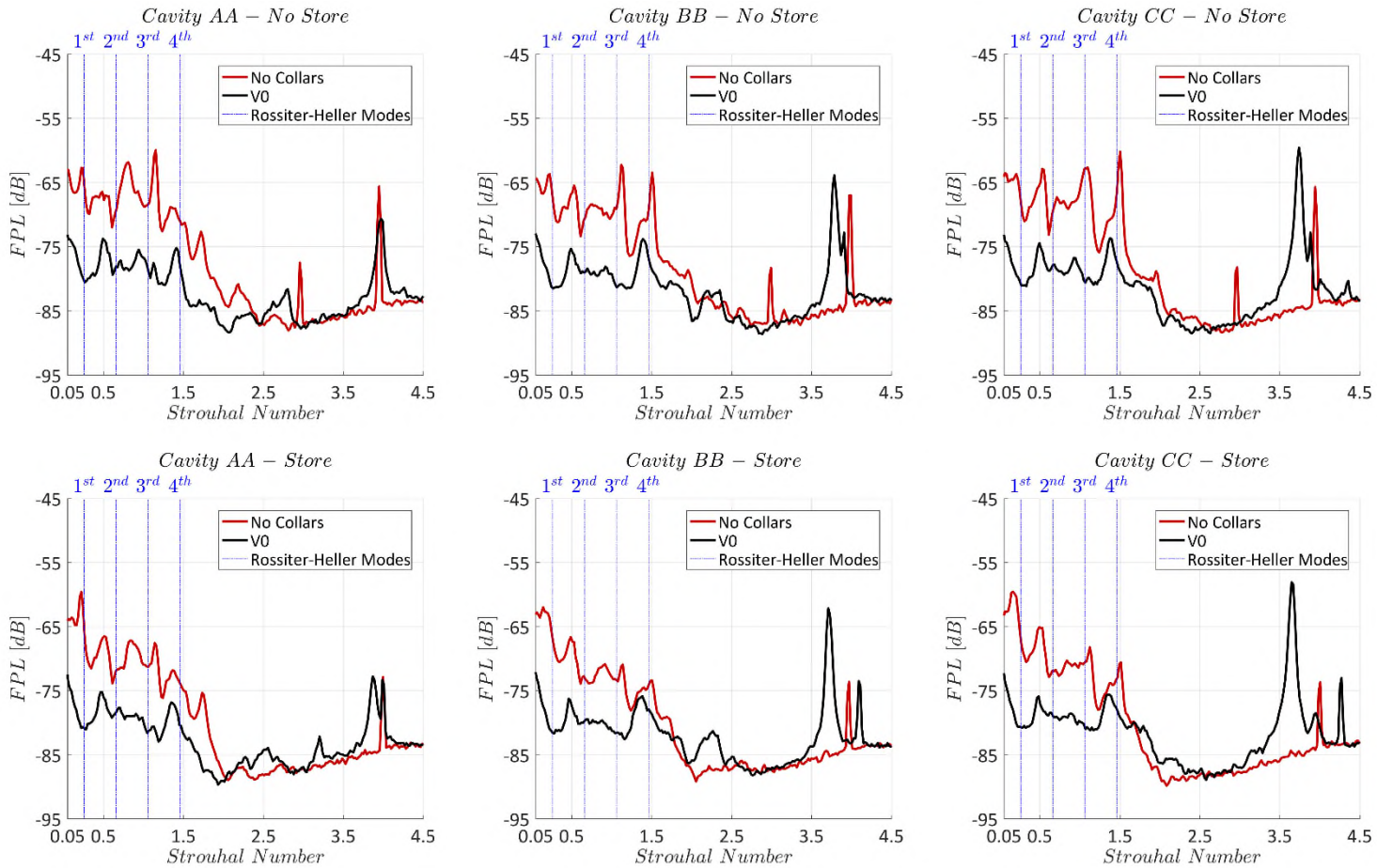

Figure 7.17 - Collar Version-0 effects on FPL of all cavity types. *Data refers to the probe located at x/L = 0.1, 2y/W = 0.0, z/D = 1.0. Doors open 90 degrees.*

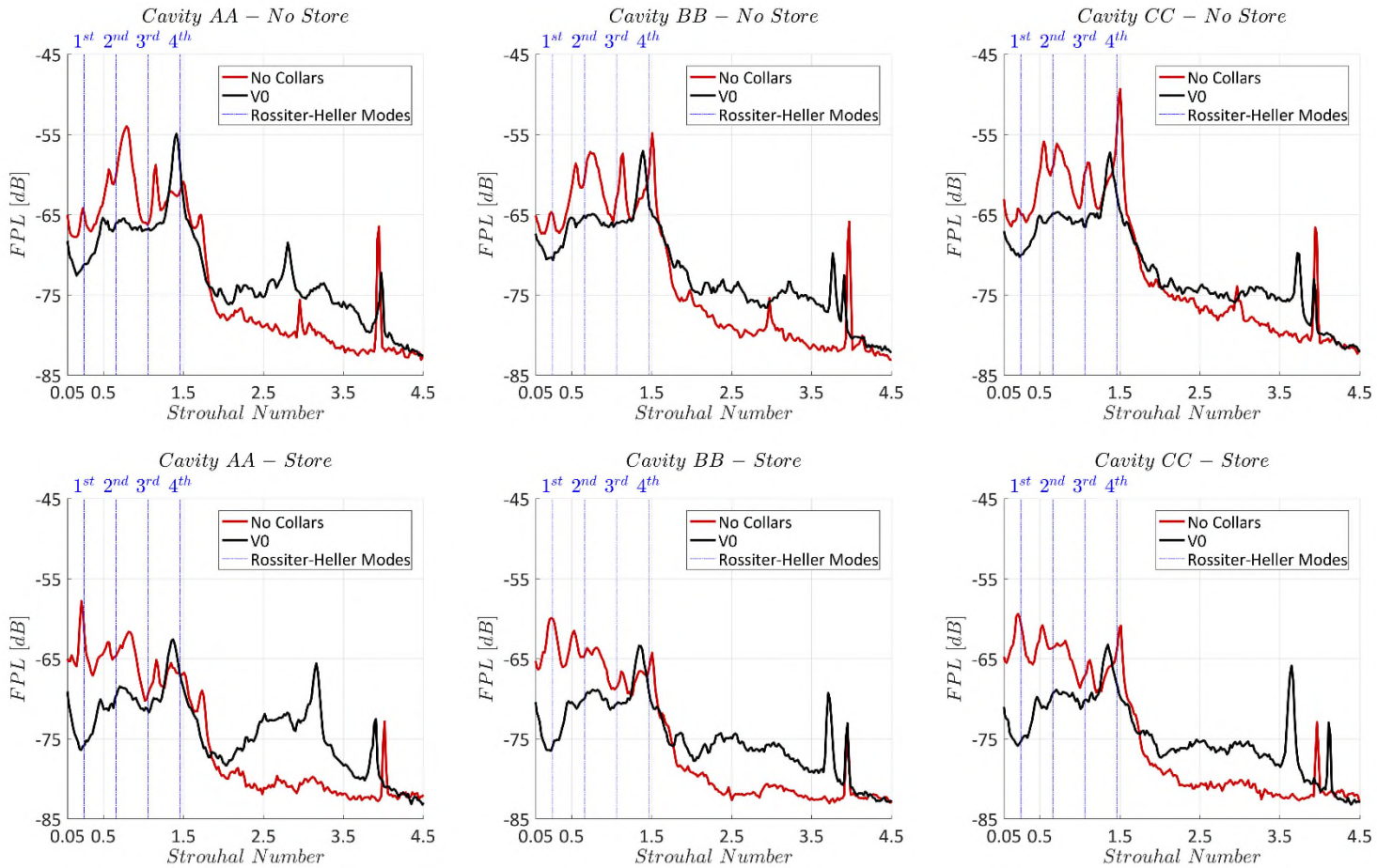

Figure 7.18 - Collar Version-0 effects on FPL of all cavity types. *Data refers to the probe located at x/L = 0.5, 2y/W = 0.0, z/D = 1.0. Doors open 90 degrees.*

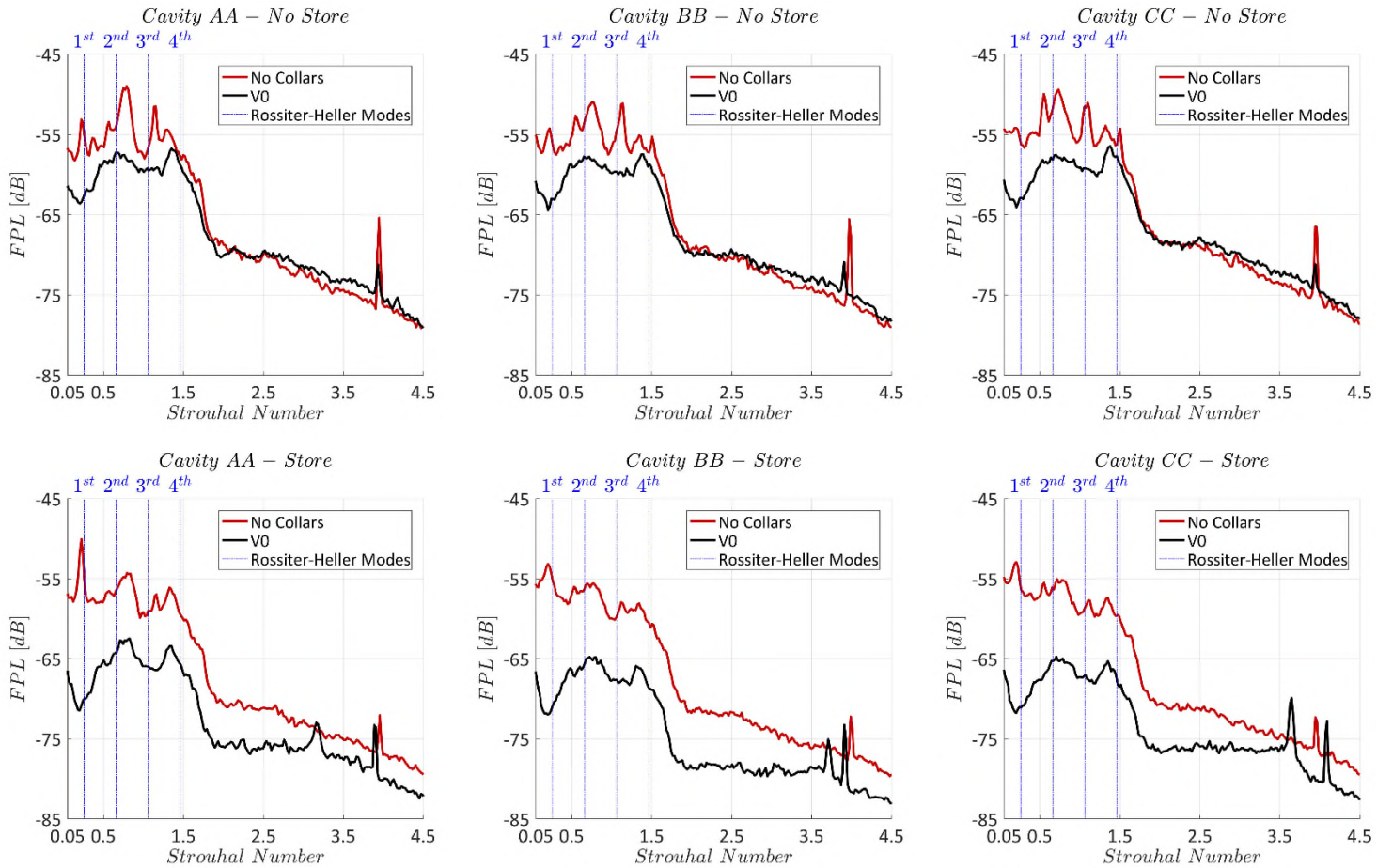

Figure 7.19 - Collar Version-0 effects on FPL of all cavity types. *Data refers to probe located at x/L = 0.9, 2y/W = 0.0, z/D = 1.0. Doors open 90 degrees.*

7.3 CHAPTER CONCLUSIONS

A wind tunnel campaign on the three cavity geometries (Type-AA, Type-BB, and Type-CC) was conducted to explore the effects of the installation inside the bay of a store and of various collar arrangements, the latter being a system developed to overcome the adverse effects of cavity flows.

The introduction of the store made the aero-acoustic response of the cavity nearly independent to door-opening angle and geometry variations. Additionally, OAFPL and FPL curves slightly reduced their values at all longitudinal stations, with the latter adopting a spectrum dominated by M1, with the other modes present in the empty-cavity cases reduced in power. These results indicated that the store had a shielding effect on the cavity, and since it was positioned at z/D = 0.45, it might have protected the bay's floor from the negative influence of shear layer oscillations.

The analysis of collars placed inside the cavity showed Version-0 (collars at 5%, 15%, 25%, 35%, 45%, 55%, 65%, 75%, 85% and 95% of cavity length) to have the best performance. This collar disposition was capable to lowering the mean longitudinal pressure gradient, when the store was installed, reduced the OAFPL power levels, no matter which cavity geometry was considered, and altered the spectral response, reducing and/or suppressing the tones characterising the reference geometry. Of particular interest was the response of the collars when tested with Type-BB cavity, with doors open 90 degrees. Such a configuration was a good representation of a real weapon bay, due to its leading and trailing edge scheme and door configuration. The only drawback was an increase of the power response of Mt. Such an aspect was considered acceptable since it had not enough relevance to overcome all other beneficial effects.

8 CONCLUSIONS

An experimental and computational campaign was designed to understand some of the differences between the well-known transonic cavity flow phenomenon and its direct application to military aircraft, weapon bays. The experiments were designed to analyse the effects of military aircraft design requirements on weapons bays. Store effects were investigated as well. Finally, the performance of a passive control method (collars) was investigated, and an attempt was made to define an optimum configuration.

Three cavity geometries (Type-AA, Type-BB and Type-CC) along with two door opening angles (90 and 120 degrees) were tested in wind tunnel experiments, assuming as the reference, configuration Type-AA with the doors at 90 degrees. This configuration had the typical trend of a transitional-open cavity, with the spectrum characterised by four Rossiter-Heller modes (M1, M2, M3, and M4), a non-linear induced mode created by the interactions of the sub-harmonics of M2, and an additional tone, characterised by a high Strouhal number value, whose origins were in the transverse oscillations of the shear layer. The analysis on the indented-transverse-edge geometries (Type-BB and Type-CC cavities) indicated that these configurations affected quantitatively only the aero-acoustic properties of the flow. While the longitudinal trend of the mean pressure coefficient had a higher gradient compared to the Type-AA for both of the derived geometries, OAFPL values were increased only in the Type-CC cavity, while the trend for Type-BB was nearly identical to the reference configuration. A similar result was obtained in the spectral analysis, with the performance of Type-AA and Type-BB assuming similar values and Type-CC experiencing higher amplitudes.

The door-opening angle strongly influenced the aero-acoustic properties of the cavity and it was observed that increasing the aperture from 90 to 120 degrees, increased the gradient of the longitudinal mean pressure gradient and increased the level of the OAFPL and FPL power in all cavity geometries. The cause was found to be the gap between the doors and the surface surrounding the cavity. Such a gap was open with the doors at 90 degrees and closed with doors at 120 degrees. Closing the gap obstructed the spillage of air through it, which had beneficial effects on the overall aero-acoustic characteristics.

The properties of the three cavity geometries were tested with CFD simulations, when installed on a typical military airframe, the Boeing UCAV1303, with doors open at an angle of 90 degrees. Mean flow analysis indicated that the cavity leading- and trailing-edge geometry had a small effect on the trend and the values of the pressure and velocity field,

with small local variations induced by the configuration details, but an overall trend similar for all three types. A different outcome was obtained from the spectral analysis, in which the Type-BB and Type-CC cavities differed from Type-AA. While in the former case up to five Rossiter-Heller modes were present, in the latter only M1, M2, and M3 characterised the spectrum. Such a difference was correlated to the nature of the shear layer detaching from the cavity's leading edge, which iso-surfaces of Q-criterion showed to be influenced by the leading edge of the Type-BB and Type-CC geometries.

The changes observed with respect to wind tunnel results[38] underlined the importance of the length of the time histories recorded compared to the characteristic time of the cavity itself, with simulations usually an order of magnitude shorter than experiments, but with the former usually more representative of the duration of a typical weapon bay duty-cycle.

The exploration of angle of attack effects revealed a strong dependence of cavity flow on that parameter. Both mean and non-stationary flow properties varied coherently (an increase in $\bar{C}_p$ values, an increase in OASPL values, and an increase of the tones' power) up to 3.0 degrees of incidence and reflecting the increase in airflow directed towards the bay. At 4.5 degrees however, the flow underwent changes, with aero-acoustic power levels experiencing an unexpected fall. This implied the existence of a change in the overall arrangement of the flow, which was indeed observed by analysing the mean velocity vector field. The main clockwise vortex, that occupied the greater part of the cavity, and had an elliptical shape, rotated its major axis by 30 degrees clockwise between the 3.0 and 4.5 degree angle-of-attack cases. Beyond 4.5 degrees the flow resumed the trend observed for zero and three degrees angle-of-attack, with an increase of the acoustic loads as incidence was increased.

The introduction of the store made the aero-acoustic response of the cavity nearly independent of door-opening angle and geometry variations. Additionally, OAFPL and FPL curves slightly reduced their values at all longitudinal stations, with the latter changing its pattern and adopting a spectrum dominated by M1. This indicated that the store had a shielding effect on the cavity floor making it insensitive to shear layer variations.

[38] Note: In comparing wind tunnel and CFD results, no corrections were applied for the different free-stream Mach numbers (0.81 and 0.85 respectively), since the effects were secondary (see Tracy & Plentovich (1997)) with respect to the changes induced by the different geometrical set-up.

In the analysis of the four collar arrangements proposed, it was found that Version-0 (collars at 5%, 15%, 25%, 35%, 45%, 55%, 65%, 75%, 85% and 95% of cavity length) had the best performance. Combining this geometry with the store installed inside the cavity, a nearly zero gradient pressure gradient and a reduction of OAFPL values were observed. The spectral analysis indicated a reduction and/or suppression of the tones, with the only drawback being an increase in the power response of Mt. Such an aspect was considered acceptable since it was not significant enough to overcome the beneficial effects. The results obtained underlined the potential advantages of this approach over methods that involve external spoilers, deflectors, or blowing, in that no actuation is required. Moreover, this configuration could reveal to be superior regarding the impact on airframe drag since, unlike spoilers, the collars do not extend in to the undisturbed flow. Finally, collars, as shown in Knowles, et al. (2017, 27-28-29 of March), can be simply produced by 3D printing with plastic materials, reducing the production cost and the weight increase of the aircraft.

The final experiments conducted on the doors' dynamic effects, even if basic and at an embryonic stage, were able to offer interesting information on the flow. It was observed that the modes were quick to respond to the movement of the doors, with the tone's adaption speed (i.e. velocity in the response to changing boundary conditions) increasing with increasing Strouhal number of the mode. Also of interest was the observed apparent correlation between the actuation speed of the doors and the cavity modes' adaption speed.

9 FUTURE WORK

From the airframe installation point of view, little is yet known about the influence of internal structures, and additional studies should be done in examine the effects of multiple ribs, tubing, and door hinges. Moreover, the impact of the surface surrounding the cavity, represented by the belly of the aircraft, may strongly influence the aero-acoustic response and further details should be gathered. Additionally, other RCS-suppression geometries, common to stealth aircraft, should be investigated. Finally, it is always recommended to perform real-scale simulations during the design process, to ensure that results obtained in the wind tunnel and/or with simplified geometries will be confirmed in flying activities.

A detailed study of the effects of typical combat engagement conditions is also strongly recommended. It has already been shown that incidence has a profound influence on the aero-acoustic response of a weapons bay, hence an additional step forward should be the analysis of angle of sideslip effects, and combinations of angle of attack and sideslip effects on the weapon bay aero-acoustic response. A typical analysis matrix could be a sweep of angle of sideslip (for example up to a value of 6 degrees) at null angle of attack, followed by sweeps of angle of sideslip at angles of attack greater different from zero (for example the 3.0, 4.5, and 6.0 values explored in this study). This approach should enable to build up a dataset capable to underline the major effects of on the aero-acoustic properties of a weapon bay, when the carrying airframe varies it flight profile in the transonic regime.

Airframe dynamics should be investigated too. Aircraft, especially air-to-air superiority platforms, usually deploy stores whilst they are manoeuvring, and the effect of body-axis angular rates may strongly influence cavity flow.

A weapons bay is typically exposed to duty cycles of the order of seconds, with doors opening and closing. As shown in the basic experiments conducted in this study, there is an influence, and the doors' actuation speed can affect the flow response. It is suggested that a more thorough analysis of duty cycles, in which the cavity is opened and then closed, and in which store release procedures are also investigated. It is strongly suggested to analyse the flow with JFTFA techniques due to their capacity to detect non-linear and statistically non-stationary properties.

Finally, collars have proven to be a simple and effective technique to address the aero-acoustic issues related to cavity flows. Their capacity to adapt to the cavity geometry, and

their ease of manufacturing, offers potential advantages with respect to other methods such as spoilers, actuators, and blowing. Obviously, their performance can be improved by local geometry modifications, and their capacities should be analysed as well with effects induced by incidence, sideslip, and aircraft dynamics. A further recommendation will be to analyse also the effect of collar installation on the overall drag produced by cavity. Passive cavity-tones suppression mechanism like spoilers, when deployed in the airflow, increase the overall drag of the cavity. Being collars buried inside the bay, they might not suffer of this unwanted side effects, or at least have a drag increase lower compared to a spoiler mechanism.

REFERENCES

Ahuja, K. K., & Mendoza, J. (1995). *Effects of Cavity Dimensions Boundary Layer and Temperature on Cavity Noise with Emphasis on Benchmark Data to Validate Computational Aeroacoustic Codes.* NASA CR-4653.

Bruun, H. H. (1996). *Hot-Wire Anemometry Principles and Signal Analysis.* Oxford, England: Oxford University Press. ISBN 9780198563426.

Cabral, B., & Leedom, L. C. (1993). Imaging Vector Fields Using Line Integral Convolution. *SIGGRAPH 93 - 20th Annual Conference and Exhibition on Computer Graphics and Interactive Techniques*, (pp. 263-272). Anaheim, California, USA.

Casper, K. M., Wagner, J. L., Beresh, S. J., Henfling, J. F., Spillers, R. W., & Brian, O. M. (2016). Complex Geometry Effects on Cavity Resonance. *AIAA Journal, 54*(1), pp. 320-330.

Chaplin, R. A., & Birch, T. J. (2012). Aero-acoustic Environment Within the Weapons Bay of a Generic UCAV. *30th AIAA Applied Aerodynamics Conference*, (pp. 1-26). New Orleans.

Clark, R. L. (1979). *Evaluation of F-111 Weapon Bay Aeroacoustic and Weapon Separation Improvement Techniques.* AFFDL-TR-79-3003, Air Force Flights Dynamic Laboratories.

Davidson, P. A. (2004). *Turbulence: An Introduction for Scientist and Engineers.* Oxford University Press. Oxford. ISBN 9780198529491.

Dawdy, D. R., & Matalas, N. C. (1964). *Statistical and Probability analysis of Hydrologic data, Part III: Analysis of Variance, Covariance and Time Series.* New York, United States of America: McGraw-Hill Book Company.

Farge, M. (1992). Wavelet Transforms and their Application to Turbulence. *Annual Review of Fluid Mechanics, 24*, pp. 355-457.

Gilman, D. L., Fuglister, F. J., & Mitchell, J. M. (1963). On the Power Spectrum of Red Noise. *Journal of Atmospheric Science, 20*, pp. 182-184.

Grinsted, A., Moore, J. C., & Jevrejeva, S. (2004). Application of the Cross Wavelet Transform and Wavelet Coherence to Geophysical Time Series. *Nonlinear Processes in Geophysics, 11*, pp. 561-566.

Hallissy, B. P., & Hariharan, N. S. (2014). Prediction of Unsteady Flow in UCAV Weapon's Bay Using CREATE-AV Kestrel. *52nd Aerospace Science Meeting*. National Harbor, Maryland, USA.

Heller, H. H., Holmes, D. G., & Covert, E. E. (1971). Flow Induced Oscillations in Shallow Cavities. *Journal of Sound and Vibration, 18*, pp. 545-553.

Helmholtz, H. (1895). *On the Sensations of Tone as a Physiological Basis for the Theory of Music, 3rd Edition*. Cambridge: Cambridge University Press. ISBN 9780511701801.

Hussain, A. K. (1986). Coherent Structures and Turbulence. *Journal of Fluid Mechanics, 173*, pp. 303-356.

Kannepalli, C., Chartrand, C., Birbeck, R., & Sinha, N. (2011). Computational Modeling of Geometrically Complex Weapon Bays. *17th AIAA/CEAS Aeroacoustic Conference*. Portland, Oregon, USA.

Kergerise, M. A., Spina, E. F., Garg, S., Cattafesa III, L., & N. (2004). Mode-Switching and Nonlinear Effects in Compressible Flow over Cavity. *Physics of Fluids, 16*(103), pp. 678-687.

Kergerise, M., Cattafesa III, L., & Ha, C. (2002). *Adaptive Identification and Control Flow Induced Cavity Oscillations*. NASA, Langley Research Center. Langley, Virginia, USA: CASI.

Khanal, B. (2010). A Numerical Investigation of the Aerodynamic Noise Generation Mechanism in Transonic Cavity Flows. PhD Thesis. Cranfield University.

Kim, Y. C., & Powers, E. J. (1979). Digital Bispectral Analysis and Its Applications to Nonlinear Wave Interactions. *IEEE Transactions on Plasma Science, 7*(2), pp. 120-131.

Knowles, K., Bacci, D., Saddington, A. J., Newby, B., & Taylor, N. J. (2017, 27-28-29 of March). Controlling Unsteady Cavity Flows Using Internal Structures. In 3AF (Ed.), *52nd 3AF International Conference on Applied Aerodynamics*, (pp. Paper FP38-March 2017). Lyon - France.

Knowles, K., Finnis, M. V., & Sapsford, L. D. (2015, 30-31 of March & 1 of April). Effects of Internal Structures on Unsteady Cavity Flows. *50th International Conference on Applied Aerodynamics* (pp. Paper FP23-2015). Toulouse: 3AF.

Larcheveque, L., Sagaut, P., Mary, I., Labbè, O., & Comte, P. (2003). Large Eddy Simulation of a Compressible Flow Past a Deep Cavity. *Physics of Fluids, 15*, 193-210.

Lawson, S. J., & Barakos, G. N. (2009, May-June). Assessment of Passive Flow Control for Transonic Cavity Flow Using Detached-Eddy Simulation. *Journal of Aircraft, 46*(3), pp. 1009-1029.

Lawson, S. J., & Barakos, G. N. (2010). Evaluation of DES for Weapon Bays in UCAV. *Aerospace Science and Technology, 14*, pp. 397-414.

Lawson, S. J., & Barakos, G. N. (2012). Influence of Stores on the Flow Inside UCAV Weapon Bays. *The Aeronautical Journal, 116*.

Lawson, S., & Barakos, G. (2011). Review of Numerical Simulations of High-Speed Turbulent Cavity Flows. *Progress in Aerospace Sciences, 47*, pp. 186-216.

Maccarone, J. M. (2013). The Biphase Explained - Understanding the Asymmetries in Coupled Fourier Components of Astronomical Time Series. *Monthly Notices of the Royal Astronomical Society, 435*(4), 1-14.

Maraun, D., & Kurths, J. (2004). Cross Wavelet Analysis: Significance Testing and Pitfalls. *Nonlinear Processes in Geophysics, 11*, 505-514.

Menter, F. R. (2012). *Best Practice for Scale Resolving Simulations in ANSYS CFD.* ANSYS.

Morton, M. H., Cox, J. T., & Powell, E. A. (2012). Initial Assessment of a CFD Application for Predicting F22 Cavity Bay Acoustics for Subsonic and Supersonic Aircraft States. In AIAA (Ed.), *53rd AIAA/ASME/ASCE/AHS/ASC Conference*, (pp. AIAA March 2012 - 1624). Honolulu, Hawaii, USA.

Murray, N. E., & Jansen, B. J. (2012). Effect of Door Configuration on Cavity Flow Modulation Process. *AIAA Journal, 50*(12), pp. 2932-2937.

Newland, D. E. (1993). *An Introduction to Random Vibrations, Spectral & Wavelet Analysis.* Harlow, Essex, England: Longman Group Limited. ISBN 9780486442747.

Okada, A., & Kao, D. (1996). *Enhanced Line Integral Convolution with Flow Feature Detection.* NASA, Ames Research Center. Moffert Field, California, USA: NAS - M/S T27A-2.

Peake, D. J., & Tobak, M. (1980). *Three-Dimensional Interactions and Vortical Flows with Emphasis on High Speeds*. NASA, Ames Research Center. Moffed Field, California, USA: AGARD Fluid Dynamics Panel.

Plentovich, E. B., Stallings, R. L., & Tracy, M. B. (1993). *Experimental Cavity Pressure Measurements at Subsonic and Transonic Speeds*. NASA Technical Paper 3358, Langley Research Center, Hampton, Virginia.

Roberts, D. (2013). Analysis and Control of Resonant Cavity Flows. PhD Thesis. Cranfield University.

Rockwell, D., & Naudasher, E. (1978). Review of Self Sustaining Oscillation of Flow Past Cavities. *Journal of Fluids Engineering, 100*, pp. 152-165.

Rossiter, J. (1966). *Wind Tunnel Experiments on the Flow Over Rectangular Cavities at Subsonic and Transonic Speeds*. Aeronautical Research Council Reports and Memoranda. TR-3438.

Sarno, R., & Franke, M. (1994). Suppression of Flow Induced Pressure Oscillations in Cavities. *Journal of Aircraft, 31*, pp. 90-96.

Shur, M. L., Spalart, P. R., Strelets, M., & Travin, A. K. (2008). A Hybrid RANS-LES Approach with Delayed-DES and Wall-Modelled LES Capabilities. *International Journal of Heat and Fluid Flow, 29*, pp. 1638-1649.

Spalart, P. R. (2001). *Young Person Guide to DES Grids*. NASA CR-2001-211032, Langley Research Center, Hampton, Virginia.

Spalart, P. R., & Rumsey, C. L. (2007). Effective Inflow Conditions for Turbulence Models in Aerodynamic Calculations. *AIAA Journal, 45*(10), pp. 2544-2553.

Spalart, P. R., Jou, W. H., Strelets, M., & Allmaras, S. (1997). Comments on the Feasibility of LES for Wings, and on a Hybrid RANS/LES Approach. *Advances in DNS/LES*, pp. 4-8.

Stalling, D., & Hege, H.-C. (1995). Fast and Resolution Indipendent Line Integral Convolution. *Computer Graphics 29*, (pp. 249-256).

Thangamani, V., Knowles, K., & Saddington, A. J. (2013). An Investigation of Passive Control Methods for a Large Scale Cavity Model in High Subsonic Flow. *19th AIAA/CEAS Aeroacoustic Conference*. Berlin, Germany.

Thangamani, V., Knowles, K., & Saddington, A. J. (2014). Effects of Scaling on High Subsonic Cavity Flow Oscillations and Control. *Journal of Aircraft, 52*(2).

Torrence, C., & Compo, G. P. (1998). A Practical Guide to Wavelet Analysis. *American Meteorogical Society, 79*(1), pp. 61-78.

Tracy, M. B., & Plentovich, E. B. (1993). *Characterisation of Cavity Flow Fields Using Pressure Data Obatained in the Langley 0.3-Meter Transonic Cryogenic Tunnel.* NASA Technical Memorandum 4436, Langley Research Center, Hampton, Virginia.

Tracy, M. B., & Plentovich, E. B. (1997). *Cavity Unsteady Pressure Measurements at Subsonic and Transonic Speeds.* NASA Technical Paper 3669, Langley Research Center, Hampton, Virginia.

Tracy, M. B., Plentovich, E. B., Hemsch, M. J., & Wilcox, F. J. (2012). *Effect of Sweep on Cavity Flow Fields at Subsonic and Transonic Speeds.* NASA TM-201221-217577, Langley Research Center, Hampton, Virginia.

Tripton, A. G. (1980). *Weapon Bay Cavity Noise Environments Data Correlation and Prediction for the B-1 Aircraft.* AFWAL-TR-80-3050, Air Force Wright Aeronautical Laboratories.

Ukeiley, L., Arunajatesan, S., & Jansen, B. J. (2008). Control of Pressure Loeads in Geometrically Complex Cavities. *Journal of Aircraft, 45*(3), pp. 1014-1024.

Wilcox, D. C. (2006). *Turbulence Modeling for CFD, 3rd Edition.* DCW Industries - ISBN 9781928729082.

Yen, N. (1971). *Subharmonic Generation in Acoustic Systems.* Harvard University, Acoustic Research Laboratory. Cambridge, Massachusetts, USA: Office of Naval Research. Technical Memorandum 65.

APPENDICES

APPENDIX A. CFD MODEL DRAFTING

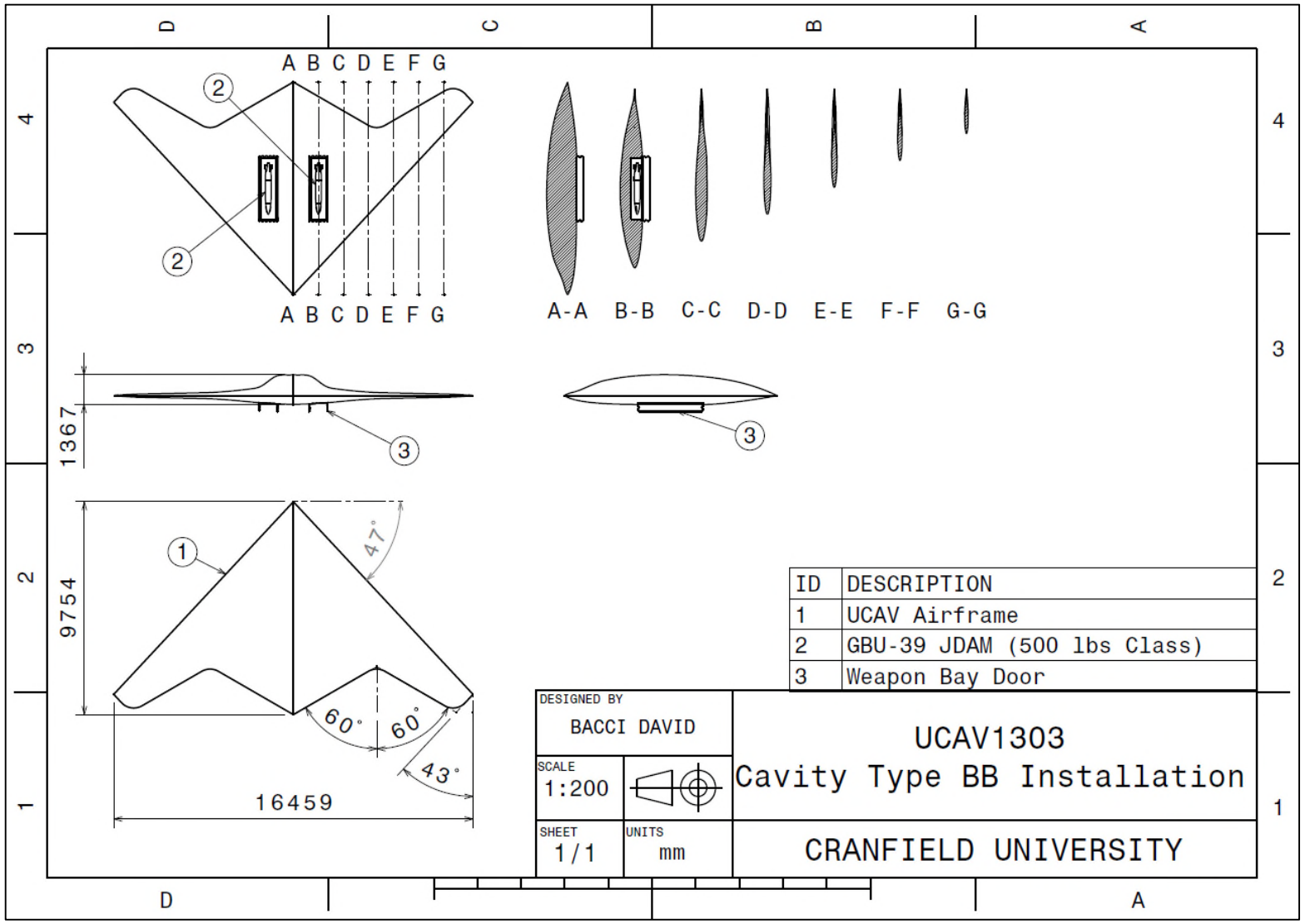

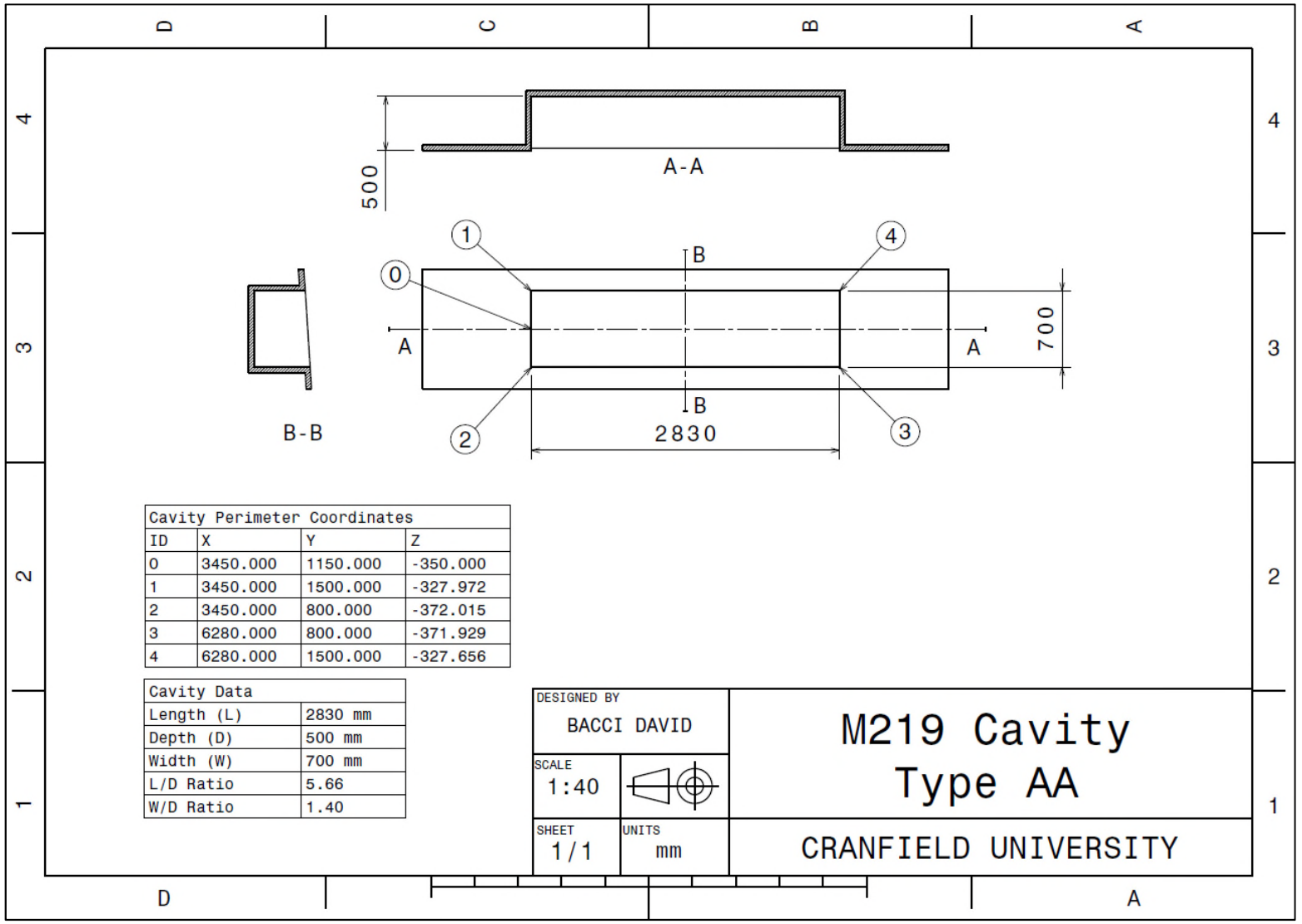

Cavity Perimeter Coordinates			
ID	X	Y	Z
0	3450.000	1150.000	-350.000
1	3450.000	1500.000	-327.972
2	3450.000	800.000	-372.015
3	6280.000	800.000	-371.929
4	6280.000	1500.000	-327.656

Cavity Data	
Length (L)	2830 mm
Depth (D)	500 mm
Width (W)	700 mm
L/D Ratio	5.66
W/D Ratio	1.40

DESIGNED BY: BACCI DAVID

SCALE: 1:40

SHEET: 1/1

UNITS: mm

M219 Cavity Type AA

CRANFIELD UNIVERSITY

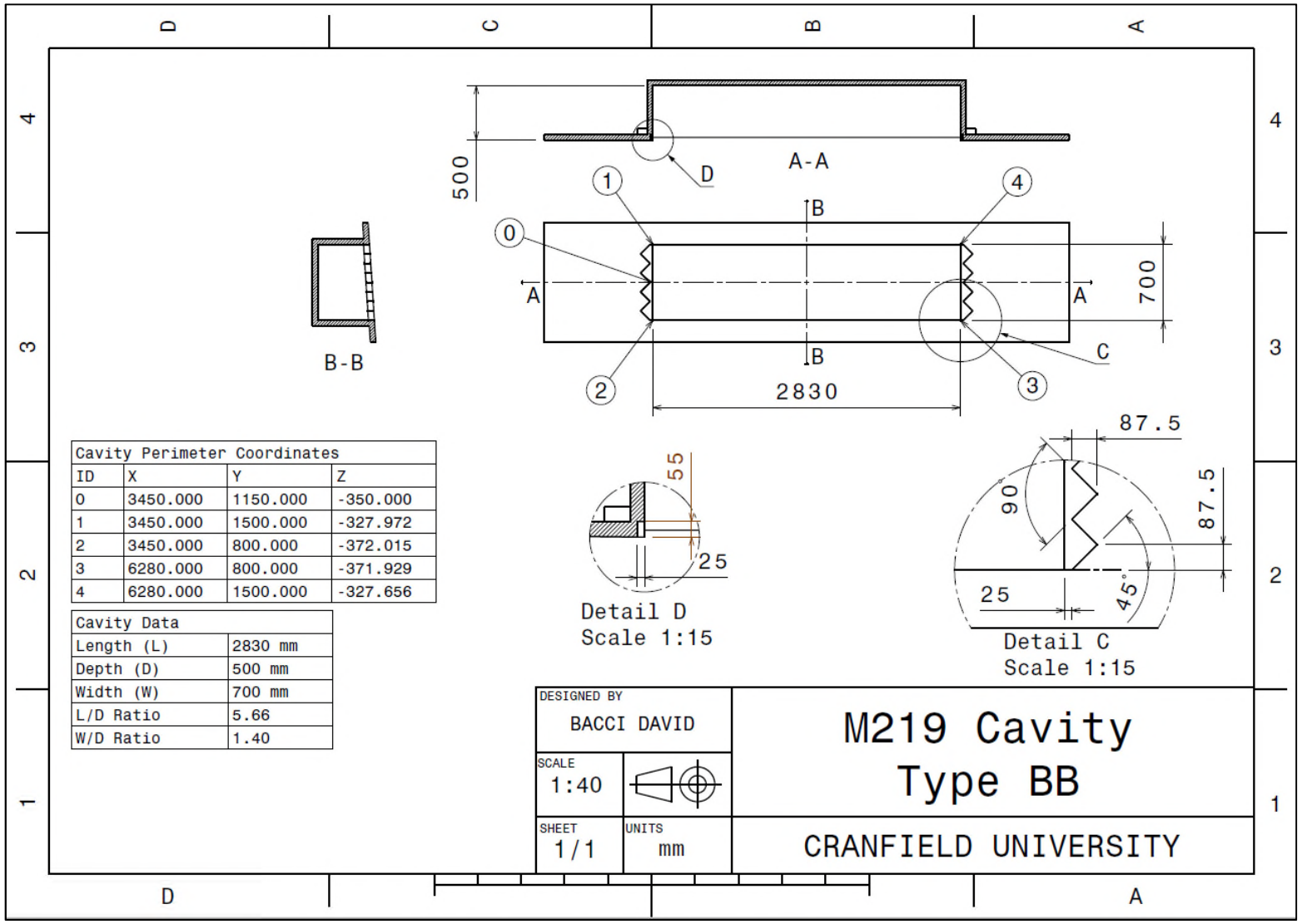

Cavity Perimeter Coordinates			
ID	X	Y	Z
0	3450.000	1150.000	-350.000
1	3450.000	1500.000	-327.972
2	3450.000	800.000	-372.015
3	6280.000	800.000	-371.929
4	6280.000	1500.000	-327.656

Cavity Data	
Length (L)	2830 mm
Depth (D)	500 mm
Width (W)	700 mm
L/D Ratio	5.66
W/D Ratio	1.40

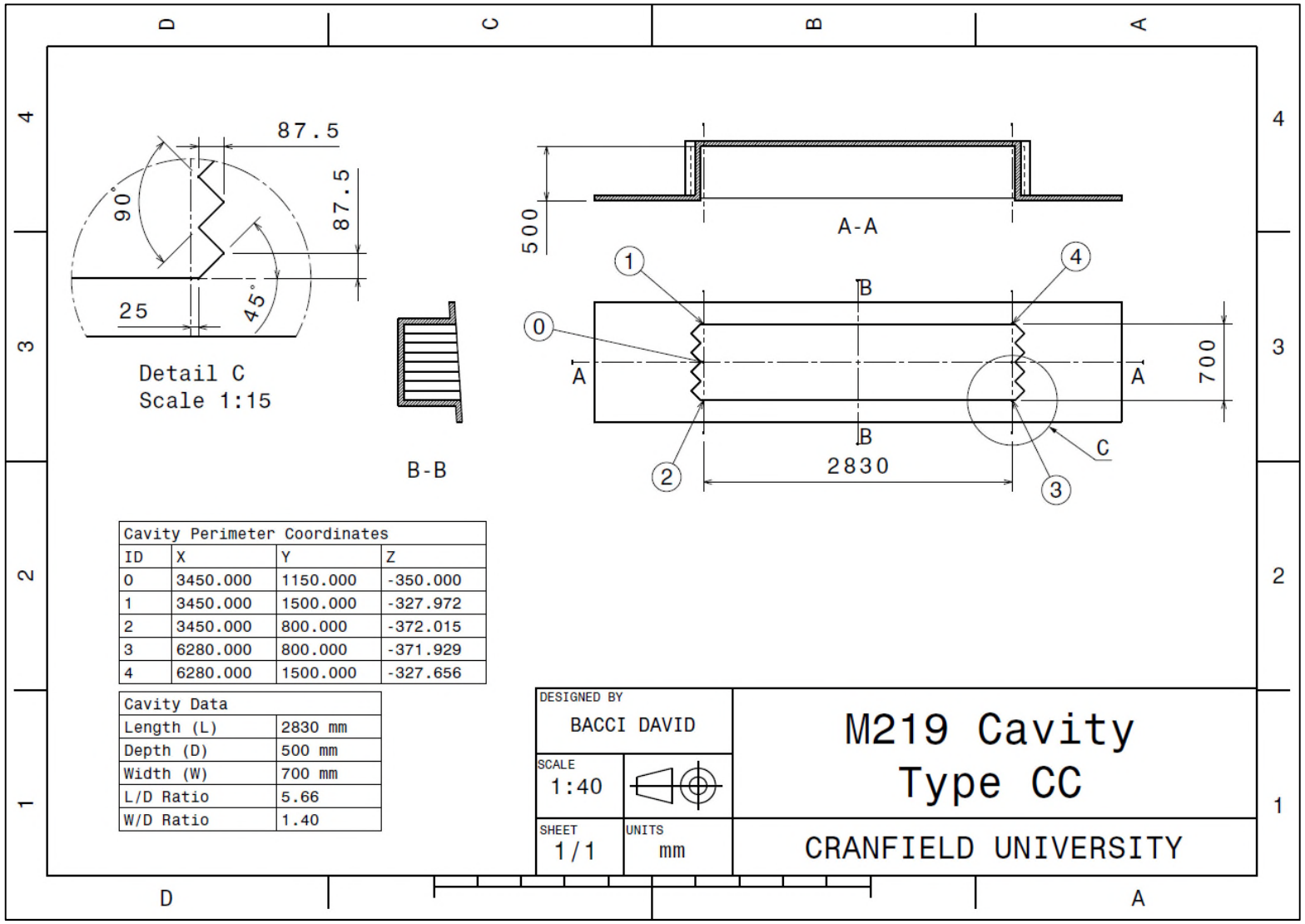

Cavity Perimeter Coordinates			
ID	X	Y	Z
0	3450.000	1150.000	-350.000
1	3450.000	1500.000	-327.972
2	3450.000	800.000	-372.015
3	6280.000	800.000	-371.929
4	6280.000	1500.000	-327.656

Cavity Data	
Length (L)	2830 mm
Depth (D)	500 mm
Width (W)	700 mm
L/D Ratio	5.66
W/D Ratio	1.40

DESIGNED BY BACCI DAVID		M219 Cavity Type CC
SCALE 1:40		
SHEET 1/1	UNITS mm	CRANFIELD UNIVERSITY

APPENDIX B. PUBLICATIONS BASED ON THIS WORK

CONFERENCE PROCEEDINGS

► Bacci D., Saddington A.J., Bray D. "*Transient Aerodynamics and Aeroacoustics of Complex-Geometry Weapon Bays*". 50th 3AF International Conference on Applied Aerodynamics. Toulouse. France. 2015.

► Bacci D., Saddington A.J., Bray D. "*Wavelet Analysis of Complex-Geometry Transonic Cavity Flows*". 34th AIAA Applied Aerodynamics Conference. Washington. United States. 2016.

► Bacci D., Saddington A.J., Bray D. "*UCAV1303/M219 Weapon Bay Analysis in Transonic Flow Regime*". RAeS 2016 Applied Aerodynamics Conference. Bristol. United Kingdom. 2016.

► Knowles K., Bacci D., Saddington, A.J., Newby B., Taylor, N.J. "*Controlling Unsteady Cavity Flows Using Internal Structures*". 52nd 3AF International Conference on Applied Aerodynamics. Lyon. France. 2017.

► Bacci D. "*Design of Weapons Bay for Stealth Aircrafts*". 1st Defence Education Conference. Athens. Greece. 2017.

PUBLICATIONS

► Bacci D., Saddington A.J., Bray D. "*Joint Frequency and Time-Frequency Domain Analysis of Transonic Cavity Flows*". Aerospace Science and Technology. (Paper submitted and awaiting review).

► Bacci D., Saddington A.J., Bray D. "*UCAV1303/M219 Weapon Bay Analysis in Transonic Flow Regime Part I – Mean Flow Analysis*". The Aeronautical Journal (RAeS). (Paper under preparation).

► Bacci D., Saddington A.J., Bray D. "*UCAV1303/M219 Weapon Bay Analysis in Transonic Flow Regime Part II – Non-Stationary Flow Analysis*". The Aeronautical Journal (RAeS). (Paper under preparation).

► Bacci D., Saddington A.J., Bray D. "*Wavelet Analysis of Complex-Geometry Transonic Cavity Flows*". Journal of Aircraft (AIAA). (Paper under preparation).

► Bacci D., Saddington A.J., Bray D. "*Angle of Attack Effects on Transonic Cavity Flows*". AIAA Journal (AIAA). (Paper under preparation).

APPENDIX C. WIND TUNNELS EXPERIMENTS ON BAY DOOR DYNAMIC EFFECTS

As stated in Paragraph 3.1.2, the wind-tunnel cavity model comprised two controllable bay doors with 45 degree saw-toothed leading and trailing edges. The structure of the door was complemented by a moving mechanism that was designed with the intention of linking the doors to an automatic actuator, to test the effect of the weapons bay's duty-cycles[39] on the cavity flow. The aperture of the doors, which varied from 0 degrees (doors closed) to 120 degrees (door at maximum allowable aperture), was controlled by the mechanism depicted in Figure C1.1. Due to the limited space available it was necessary to include a two gear mechanism (Figure C1.1-3 and Figure C1.1-5), with a transmission ratio of 3.12, which enabled the full 120 degrees of door opening motion in 39 degrees of rotation of the main shaft (Figure C1.1-6). The main gear was then connected to a rack (Figure C1.1-7) supported by a slide (Figure C1.1-8) connected to the mechanism. The rotational motion was then converted into a linear one, transforming the full opening movement of 120 degrees in a translation of 6.8 millimetres. At the end of the rack a piston was mounted (Figure C1.1-9), whose up and down movement controlled the door opening angle.

Even if with the mechanism installed it was theoretically possible to test the effect of moving the doors during wind tunnel experiments,, measurements with a spring balance indicated that, to actuate the doors in the wind tunnel, forces in excess of 150 N were required to drive each piston. Such a high load was beyond the capability of compact electric-driven motors and the adoption of a hydraulic actuator became mandatory. Such system complexity was not available at the time of the research; hence, the intended experimental campaign on door dynamic effects could not be conducted. Nevertheless, it was decided to conduct some qualitative assessments to begin to explore this new aspect of cavity flows. It was decided to actuate the doors manually[40], since the push movement (to open the cavity) and the pull movement (to close the cavity) could be easily conducted by an external operator. While this solution did not permit the acquisition of data in a

[39] A bay duty cycle is a sequence in which the doors are initially closed, are opened, and then closed again. This represents the typical duty cycle of a weapons bay when a store is released.

[40] It was possible to determine that the operator required less than 1 second to close/open the doors. However, due to the lack of repeatability of the operation it was not possible to have a more precise time-of-door actuation.

rigorous experimental procedure, some qualitative information on the flow could be obtained.

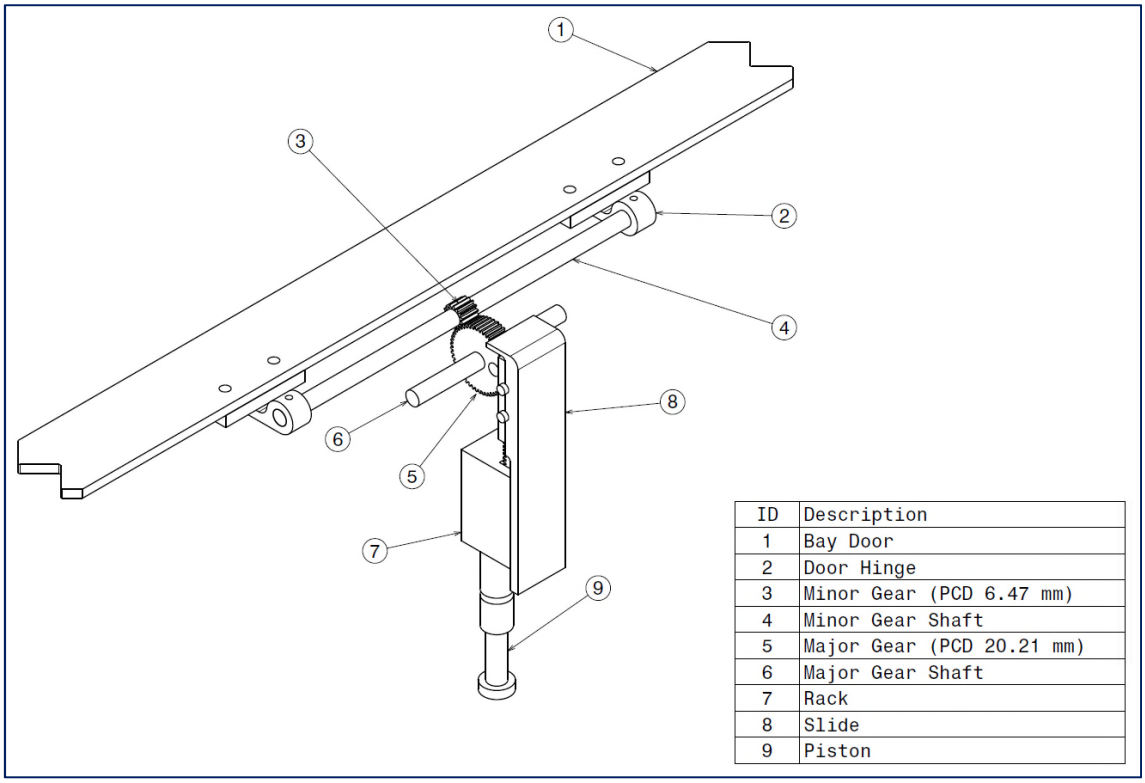

ID	Description
1	Bay Door
2	Door Hinge
3	Minor Gear (PCD 6.47 mm)
4	Minor Gear Shaft
5	Major Gear (PCD 20.21 mm)
6	Major Gear Shaft
7	Rack
8	Slide
9	Piston

Figure C1.1 - Bay door with the relative moving mechanism

Tests were conducted on cavity type BB, with the door maximum opening angle fixed at 90 degrees[41]. This geometry allowed the doors to be fully closed and previous work indicated it as the best configuration in terms of aero-acoustic properties. Two different situations were tested. In the first one, the doors, starting from a closed position, were open to an angle of 90 degrees and held fixed until the end of the run. In the second, a full door cycle was attempted. Both experiments were repeated five times. Actuation times were indicative and considered of secondary importance. The main objective of this analysis was directed towards the study of the effect of the door movement on the pressure signals.

CLOSED-OPEN CYCLE

The closed-open cycle was the easiest to execute, since the door operator had just to push on the pistons. It was decided to monitor data for two seconds and then open the doors.

[41] By careful re-assembly of the door moving mechanism it was possible to halt the door opening at 90 degrees, which reduced the operator task to a simple push/pull process.

Analyses focussed on a single port, located at x/L = 0.9, $2y/W$ = 0.0, z/D = 1.0, since repeatability of the experiments was not reliable. Data gathered was compared with the static-doors case to determine any differences.

The spectral analysis (Figure C1.2) indicated a small difference between the doors-moving and doors-static case. The two curves were identical in shape, with the former translated approximately 1 dB below the latter. The only significant difference was Mt, which the moving doors attenuated by 10 dB and shifted to a higher Strouhal number.

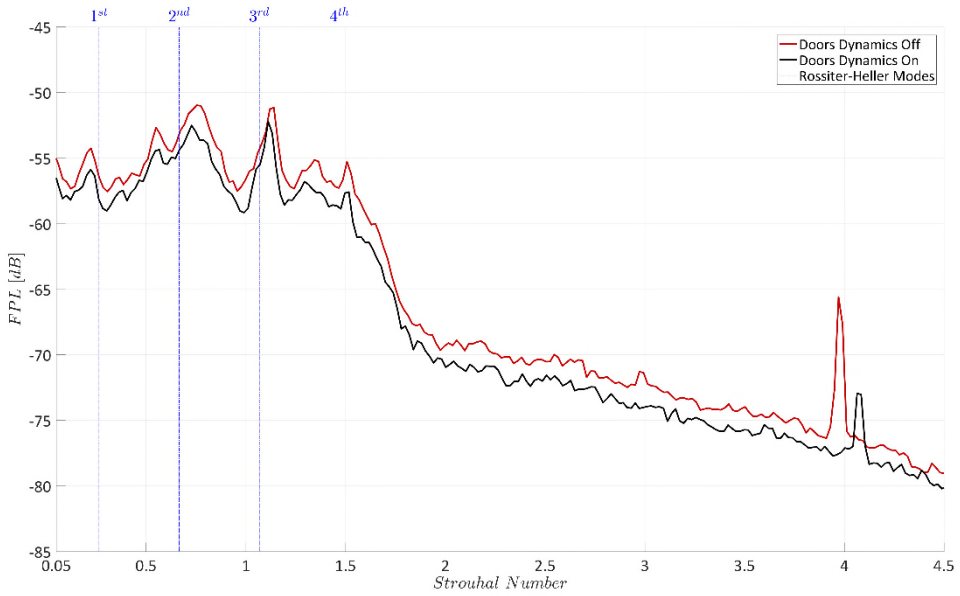

Figure C1.2 - Doors dynamics effects on FPL of the pressure signal at x/L = 0.9, $2y/W$ = 0.0, z/D = 1.0. *Configuration BB. Doors-opening angle 90 degrees. Close-open cycle.*

This outcome probably indicated that transient effects were minimal on the longer temporal scales in which data was gathered, i.e. the length of the sample was enough to hide the difference between the two cases from a pure frequency-domain analysis.

The difference between the two cases was clearly evidenced by the STFT analysis of the pressure signal (Figure C1.3). In the time-frequency map of the doors-moving case the activation of the modes due to the door opening was easily recognisable in the time interval between two and three seconds. Moreover, it was possible to observe that dynamic temporal scales were fast enough to be considered instantaneous from the STFT transform.

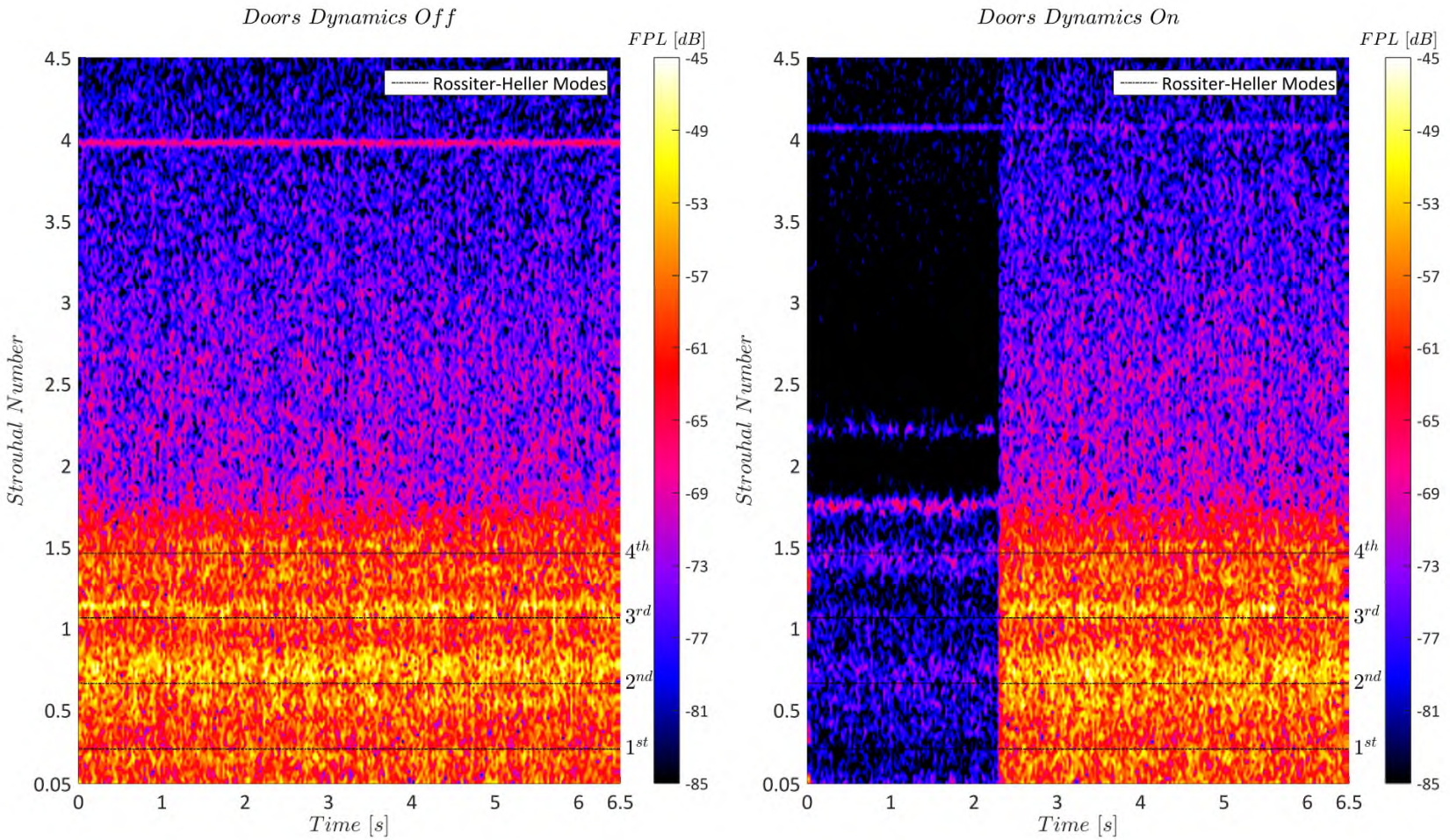

Figure C1.3 - STFT comparison of the door dynamic effects on the pressure signal at x/L = 0.9, $2y/W$ = 0.0, z/D = 1.0. *Configuration BB. Doors open 90 degrees. Closed-open cycle. Confidence level contours not displayed for ease of visualisation.*

Beyond the point at which the doors opened the time-frequency mapping became essentially identical to the doors-static case, apart for Mt, which from being located at a Strouhal number of 3.97 was now located at a Strouhal number of 4.25, and had a 8 dB lower FPL value. Another interesting feature could be recognised in the doors-closed part of the time-varying spectrum. Here, a considerable amount of noise was present between Strouhal numbers of 0.05 and 2.0. Moreover, two tones were recognisable, one at St of 1.759 and the other at St of 2.224. Finally, Mt was still present even if the doors were closed. The appearance of an ordered acoustic loading even when the doors were in their closed position was an expected outcome, because, as shown in Figure C1.4, to allow the simple rotary movement of the doors, the introduction of gaps (details B and C) between the doors and the cavity surface was necessary. Such apertures allowed air to spill inside the bay and to create the noise recorded in the STFT analysis. Unfortunately, a proper identification of the origin of these waves was not possible given the amount of data available, since a correct identification of the phenomenon would have required flow-visualisation techniques, not available in these experiments. Of course Mt, whose properties did not vary for the whole duration of the experiment, could still be tied to the fluctuation of air between the doors and the side surfaces of the cavity.

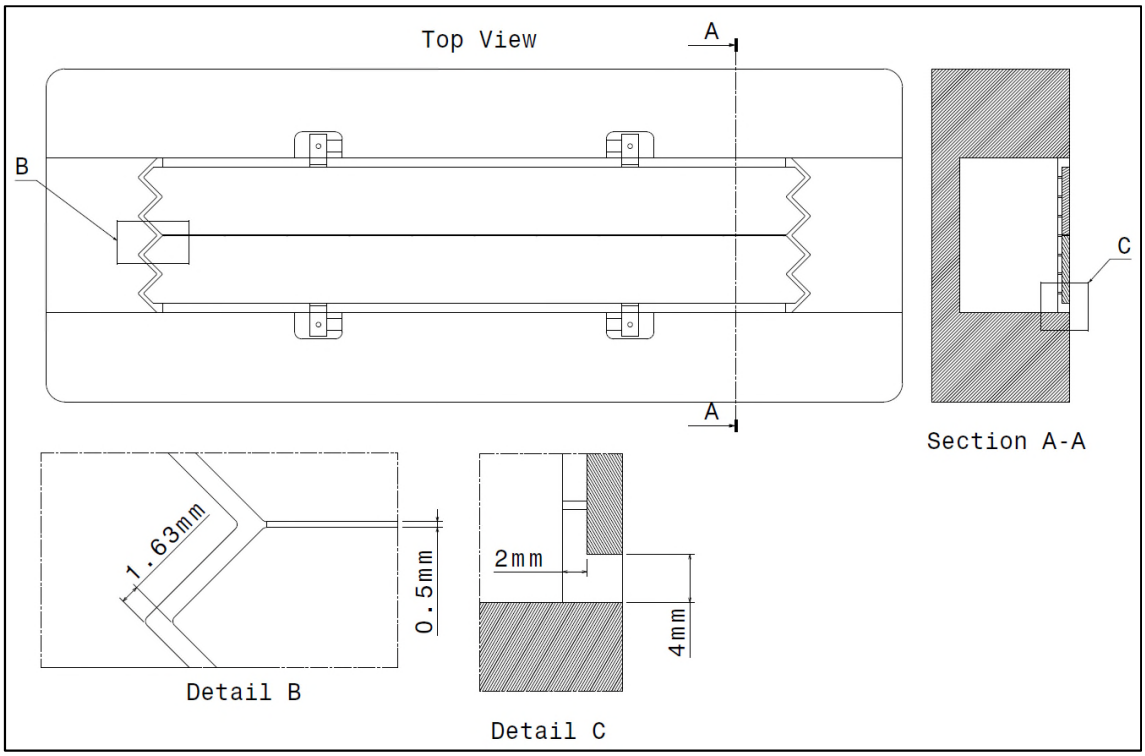

Figure C1.4 - Sketch of gaps between doors and cavity surfaces.

The two other tones identified may have a similar origin but were not encountered before because, as shown in Figure C1.3, once the doors were open their power was not sufficient to overcome the background noise, and the wave disappeared from the spectrum.

To obtain a better understanding of the dynamics of the flow during the door opening phase, it was decided to zoom the time-frequency map in the temporal axis using the wavelet transform. The time interval from 2.24 to 2.41 seconds was then extracted and processed. Figure C1.5 shows the comparison of the WAVT trend between the doors-static and doors-moving cases[42]. In this plot, it was possible to identify three significant events, labelled t_0, t_1, and t_2.[43] Time t_0 identified the beginning of the doors opening. This event was marked by an increase in signal power following the ingress of high-speed flow inside the cavity. Time t_1 indicated the time at which the door motion was completed, since the power of the signal interrupted its steep growth.

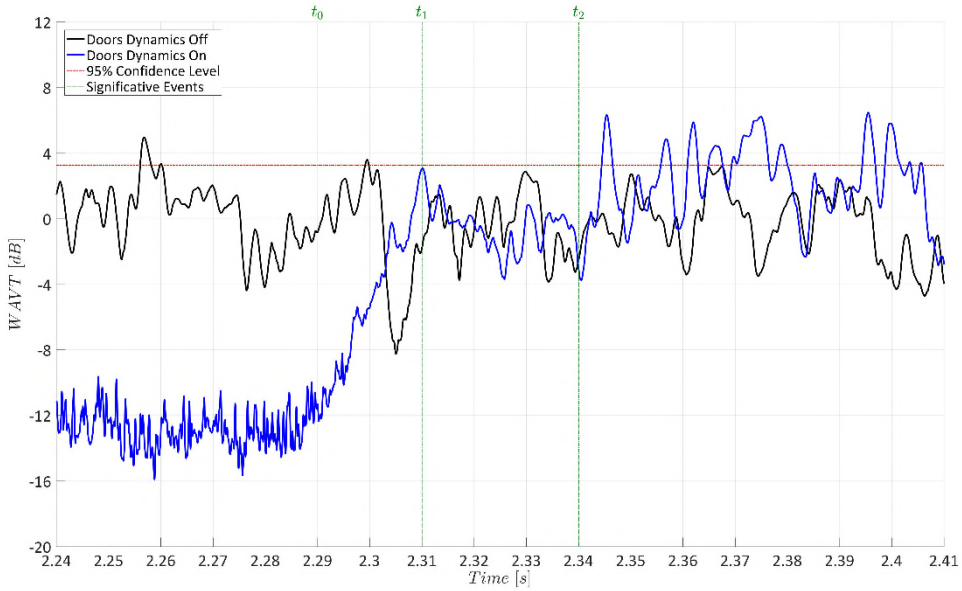

Figure C1.5 - Doors dynamics effects on WAVT of the pressure signal at x/L = 0.9, $2y/W$ = 0.0, z/D = 1.0. *Configuration BB. Doors open 90 degrees. Closed-open cycle.*

[42] While a quantitative comparison is not possible, since the two datasets were obtained in distinct experiments, the doors-static WAVT trend was used as a qualitative reference to locate the temporally-significant events in the door-moving experiment.

[43] The criteria used in the selection of this temporal gate consisted in the analysis of the WAVT signal filtered with a $100 \cdot t_{Char}$ width window. Gates were chosen whenever the gradient of the resulting curve assumed a variation of 10%.

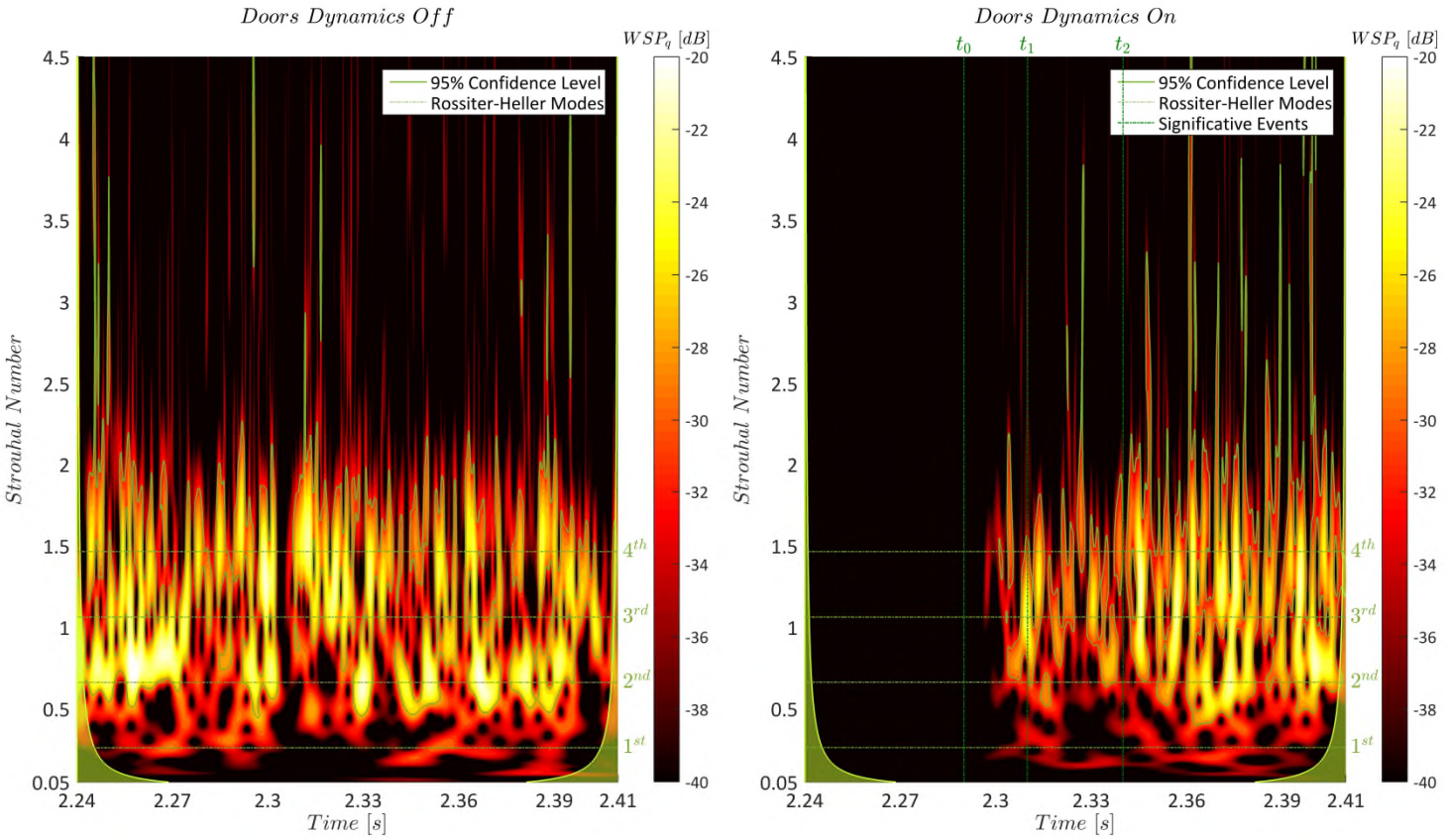

Figure C1.6 - Wavelet comparison of the door dynamic effects on the pressure signal at x/L = 0.9, $2y/W$ = 0.0, z/D = 1.0. *Configuration BB. Doors open 90 degrees. Closed-open cycle. The wavelet maps are time-zoomed at the door-opening event.*

The interval from t_1 to t_2 was considered as a settling phase in which the dynamics inside the cavity adjusted and reached their regime features recognisable by a WAVT footprint similar to the doors-static case. Of particular interest was the duration of the settling phase, estimated to last approximately 0.03 seconds, equivalent to 29 times cavity t_{Char}, indicating a fast dynamic of the flow. Such an outcome was even more evident in the time-frequency map obtained by wavelet analysis (see Figure C1.6). During the door-opening phase, energy began to accumulate, around Strouhal bands containing M3 and M4[44]. This trend continued for the settling phase, in which M3 and M4 raised their energetic content assuming an intermittent behaviour. M2 began to appear only at the beginning of the quasi-steady phase, while M1 failed to present any significant event. By contrast Mt appeared in randomised bursts of energy just after the start of the quasi-steady phase. The reason for the nature of such dynamics was unclear; nevertheless, a hypothesis could be identified in the fact that M3 and M4, having a shorter wavelength might have had higher chances to establish during the transitory phase. Longer wavelength tones like M1 and M2 could, instead, require larger temporal scales to settle, with respect to the faster dynamics involved in a door-opening activity. Obviously, this could also be correlated in the speed at which doors were opened; the speed considered to be realistic for the scale of experiments conducted. Comparing the characteristic times of the wind tunnel experiment and the CFD simulations, an opening duration of 0.02 seconds, as obtained in this study and equal to 19 times t_{Char} implied that, in the full-scale model, doors would have completed their opening in about 0.21 seconds, a value many times less than the few seconds typical of current aircraft.

CLOSE-OPEN-CLOSE CYCLE

The closed-open-closed cycle was more difficult to simulate since closing the doors required a high demand on the operator, who had to apply a pull force of 150 N with each arm. Hence, the door-closing motion was not as smooth as the opening one. Again, the analysis was concentrated on the pressure signal recorded at x/L = 0.9, $2y/W$ = 0.0, z/D = 1.0. Figure C1.7 reports the FPL analysis. As in the closed-open case, the closed-open-closed experiment produced a spectrum curve nearly identical in shape to the corresponding doors-static experiment. In this case, however, the decrease in power was higher, around 4 dB. Mt appeared at a lower Strouhal number with respect to the static

[44] Note that the door-static experiment results indicated that the spectrum was characterised by four Rossiter-Heller tones (M1, M2, M3, and M4) and the additional mode Mt.

case (in the door closed-open experiment the opposite was true), while the reduction of approximately 10 dB was maintained. It was also observed that there was a peak at a Strouhal number of 1.759, probably because the time during which the doors were fully open was not sufficient to make the background noise acquire enough energy to obscure this mode as in the doors-static experiments.

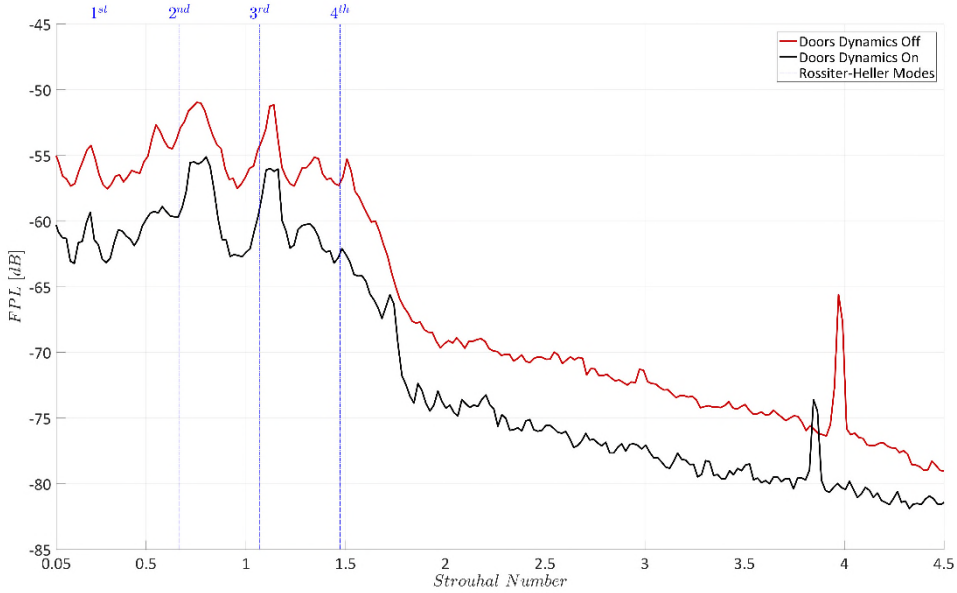

Figure C1.7 - Door dynamic effects on the FPL of pressure signal at x/L = 0.9, $2y/W$ = 0.0, z/D = 1.0. *Configuration BB. Doors open 90 degrees. Closed-open-closed cycle.*

A better view of the dynamics was obtained with the STFT analysis (Figure C1.9). The events of opening and closing of the doors were clearly identifiable and at such temporal resolution considered instantaneous. Once the cavity was opened, the structure of the flow was similar to the door-static case. Again, as in the closed-open experiments, during the phase in which the cavity was closed some noise did exist, and the organised tone Mt, as well as the waves at St of 1.759 and St 2.224, were present. Since during the opening phase no significant differences were observed with respect to the previous experiment of closed-open dynamics, it was decided to focus on the doors' closing stage.

A temporal zoom in the interval between 4.20 and 4.37 seconds was performed using the wavelet transform. WAVT curve analysis (Figure C1.8) revealed the exact time at which the doors began to close (t_0). In this case, however, due to the difficulty in maintaining a door speed equivalent to the opening case, it was not possible to discern between a phase, in which doors ended their movement, and the following settling stage. Only the event at

which the flow returned to its low noise behaviour, typical of a closed cavity, could be identified (t_1). The closing procedure lasted for an interval equivalent to 53 times t_{Char}, or 0.58 seconds in a full-scale model, longer than the opening phase, but still small compared to real aircraft applications.

Wavelet analysis (Figure C1.10) identified the shut-off order of the modes during the closing phase. M1, as in the closed-open case had a temporal scale bigger than the interval analysed and did not appear, even if a burst of energy erupted for some seconds just after the beginning of the door movement. Mt and M4 were the first tones to disappear, fading completely after t_0 + 0.011 seconds. A different trend was observed for M2 and M3, which survived up to t_0 + 0.035 seconds. Their fading probably indicated the time at which the doors were completely closed, and the following part of the signal was hence characterised by the disappearance of the remaining noise, which settled at its final value beyond t_1.

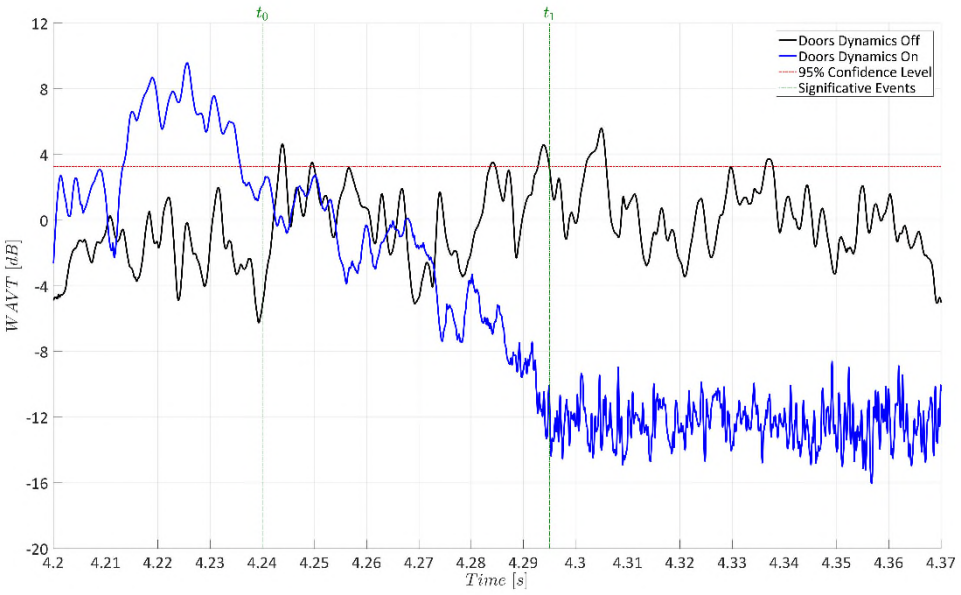

Figure C1.8 - Door dynamic effects on WAVT of the pressure signal at x/L = 0.9, $2y/W$ = 0.0, z/D = 1.0. *Configuration BB. Doors open 90 degrees. Closed-open-closed cycle.*

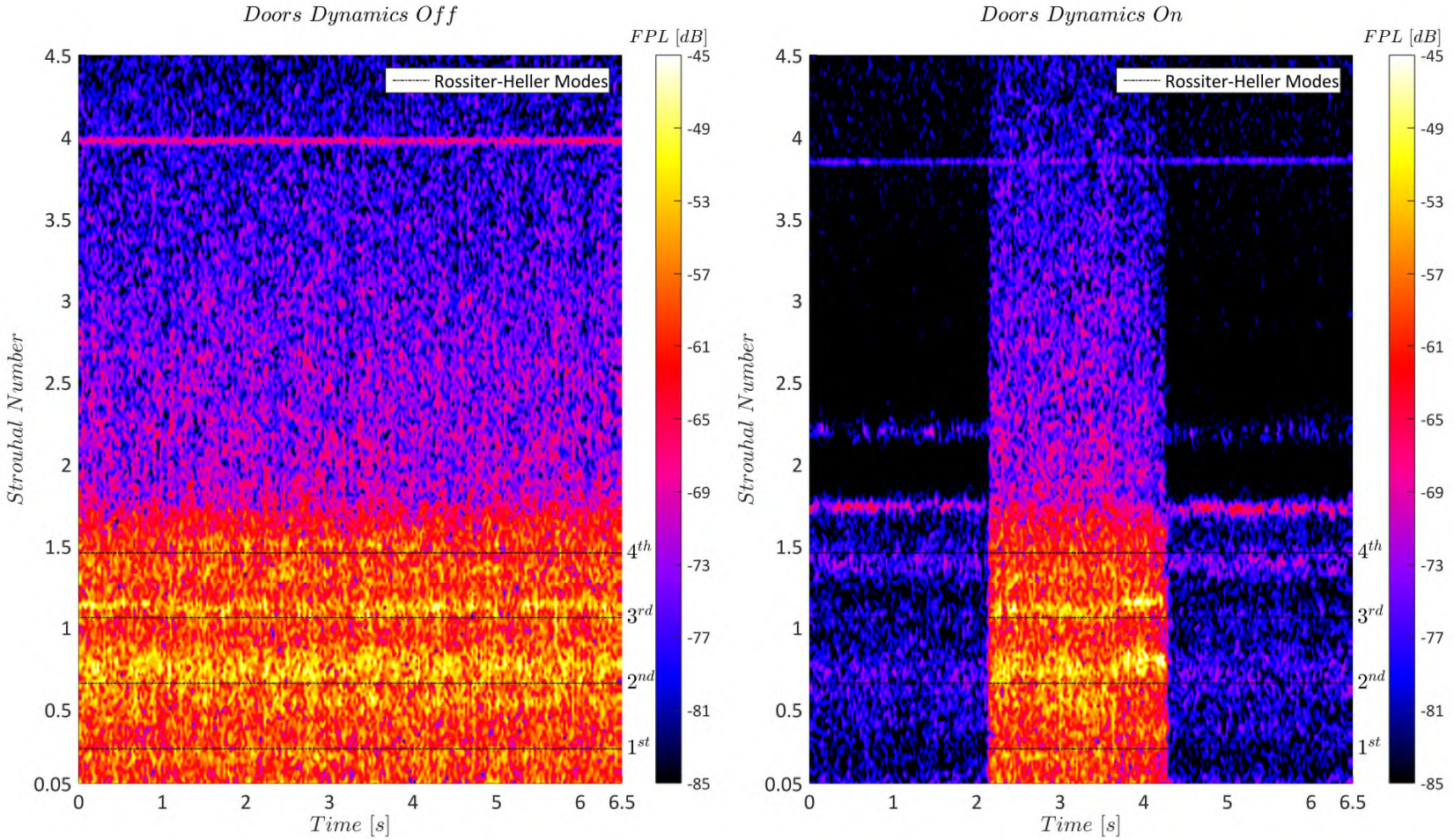

Figure C1.9 - STFT comparison of the door dynamic effects on the pressure signal at x/L = 0.9, $2y/W$ = 0.0, z/D = 1.0. *Configuration BB. Doors open 90 degrees. Closed-open-closed cycle. Confidence level contours not displayed for ease of visualisation.*

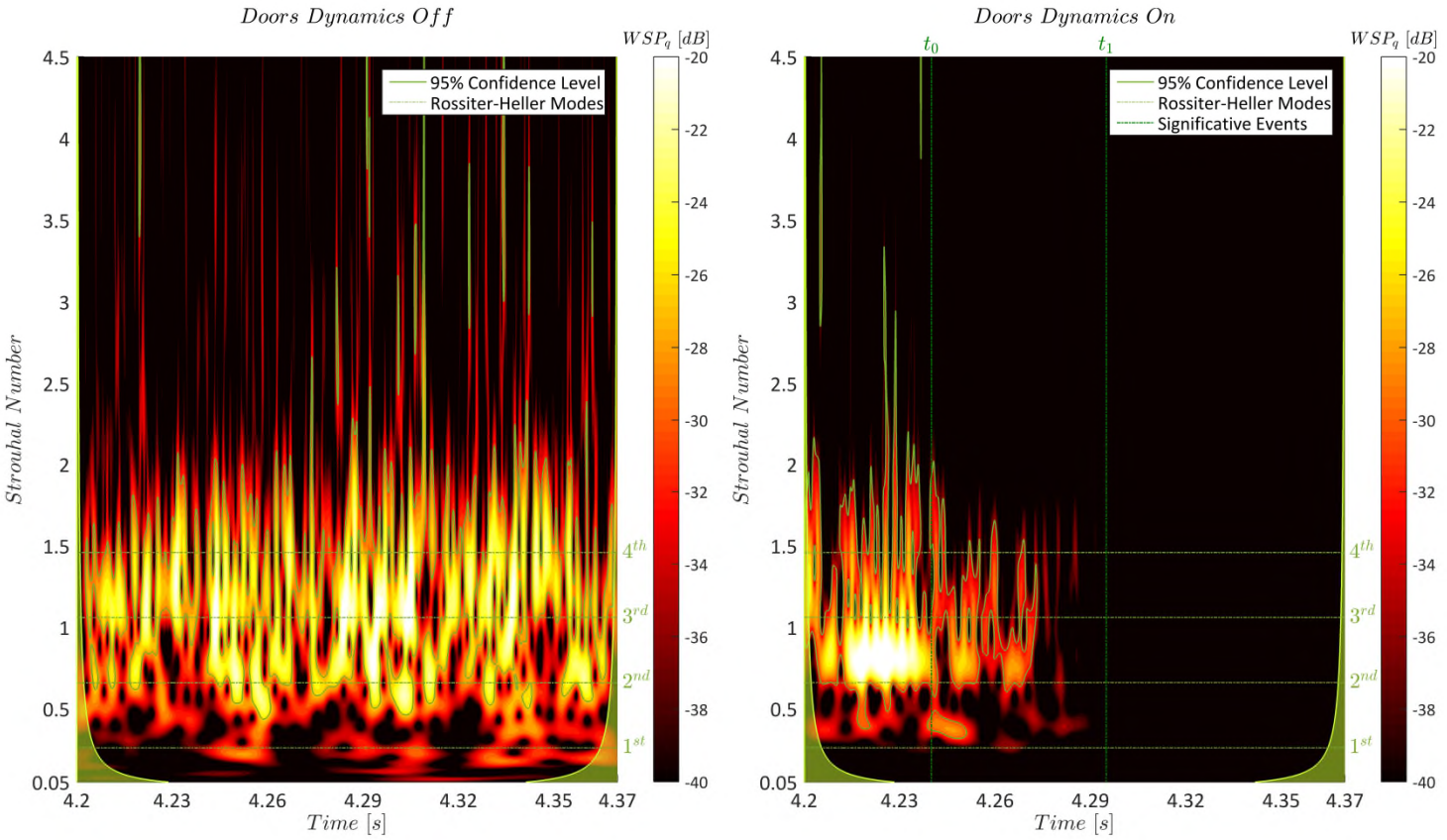

Figure C1.10 - Wavelet comparison of the door dynamic effects on the pressure signal at x/L = 0.9, $2y/W$ = 0.0, z/D = 1.0. *Configuration BB. Doors open 90 degrees. Closed-open-closed cycle. The wavelet maps are time-zoomed at the doors-closing event.*

CONCLUSIONS

The basic experiments conducted on the door dynamic effects on cavity flow, albeit with manual operation, were capable of offering some interesting qualitative results on the flow. The main outcome was the extremely quick time response of the flow when the boundary conditions were changed, especially during the opening phase of the doors. From the wavelet analysis it was possible to observe that, once the doors established their final open position, and the solid boundaries ceased to move, the spectral structure of the pressure fluctuations attained their characteristics in an interval equal to just 29 times the characteristic time of the cavity. It was also revealed that high frequency tones were the first to appear while lower frequency ones, such as M2 and M1 required more time. During the closing phase, similar temporal scales were observed and the last modes to disappear during the transitory motion were M3 and M2. From these experiments there also appeared to be a link between the doors' actuation speed and the modes' transitory temporal scales. However, the condition at which tests were conducted prevented a detailed study of the correlated physics.